Electron Beam Induced Damage and Helium Accumulation in Lithium Metatitanate Ceramic Breeder Materials

Samuel J. Waters

A thesis submitted in partial fulfilment of the requirements for the degree of Doctor of Philosophy

The University of Sheffield

Faculty of Engineering

Department of Materials Science and Engineering

April 2021

Table of Contents

2

Acknowledgements

Special thanks to Daniel Geddes and Joshua Radford, for sharing the happy times, tolerating me at my worst, and carrying me through when I'd hit rock bottom. I'm afraid you're stuck with me now chaps!... but I look forward to being further entertained by our future ham-fisted antics and inebriated ramblings.

To Rita Vasconcelos, thank you for being the ever-smiling office buddy who never failed to brighten my day. You are an absolute ray of sunshine and positivity.

Last but by no means least, thanks to Niki Stehling for being the life of a night out, and the uplifting influence of your care-free dancing style!

Sincerely, thank you very much indeed to you all.

List of Figures

List of Tables

Abstract

Polycrystalline lithium metatitanate (Li_2TiO_3) is an attractive material for a range of applications including battery materials and microwave dielectrics, it has also attracted a great deal of attention as proposed tritium breeder material for use in nuclear fusion reactors. During the continued development of Li_2TiO_3, and similar Li-containing ceramics, for these advanced applications, transmission electron microscopy (TEM) is likely to be employed to study the nano-structure of these materials and, in the case of nuclear fusion applications, their response to radiation induced damage.

In this project, the effects of ceramic processing conditions on the microstructure of Li_2TiO_3 ceramics was first identified. The effects of ceramic microstructure on the behaviour of Li_2TiO_3 under electron irradiation was subsequently investigated. Results show that electron irradiation in a conventional TEM results in the formation of nanometre sized vacancy-type defects at room temperature, and that the size and number density of the vacancy-type defects are linked to ceramic microstructure and crystallographic disorder. Electron beam induced vacancy-type defect formation is discussed in terms of electron beam heating, electron beam induced radiolysis and electron beam induced displacement damage; the displacement of Li and O lattice atoms is proposed to be primarily responsible for the observed damage. Results suggest that the formation and growth of vacancy-type defects is initially driven by the supersaturation of vacancies due to the preferential loss of interstitials to the surfaces of thin film TEM specimens, followed by coalescence of larger vacancy-type defects, which leads to cavity growth. Results from X-ray diffraction suggest that growth at room temperature may be facilitated by the presence of CO_2, produced by the decomposition of a Li_2CO_3 surface reaction layer under the electron beam. These results highlight that care must be taken when interpreting TEM data and undertaking the associated analysis, especially in Li-containing oxides.

Following the discovery of electron beam induced cavity formation in Li_2TiO_3, the thermal evolution of these cavities at temperatures relevant to fusion breeder blanket operating conditions was investigated using in-situ thermal annealing experiments, which were carried out under electron irradiation in a TEM. The effects of temperature, electron beam exposure time, and ceramic microstructure on cavity growth dynamics are discussed. The rate and extent of cavity growth was found to be significantly enhanced at elevated temperature, this is primarily attributed to the increased mobility of defects introduced as a result of electron beam induced displacement damage. Minimising exposure of thin-film TEM specimens to the electron beam was found to significantly

reduce the extent of cavity growth, particularly at high temperatures, indicating that cavity growth is strongly dependent on electron fluence. The microstructural properties of low porosity and large grain size may increase the resistance of Li_2TiO_3 to electron beam damage. This is attributed to the longer diffusion path to defect sinks associated with large grain size and low porosity, resulting in a reduction of preferential interstitial loss and increased probability of defect recombination; thus reducing the excess vacancy concentration responsible for cavity growth in the bulk. A distinct correlation between the temperature at which significant quantities of CO_2 were released from bulk Li_2TiO_3 samples (revealed by the results of thermal desorption spectroscopy (TDS) experiments) and accelerated cavity growth in thin film specimens was identified. Hence it is proposed that enhanced cavity growth under electron irradiation at elevated temperature in Li_2TiO_3 may be facilitated by CO_2 gas produced as a result of the thermal decomposition of an Li_2CO_3 surface reaction layer.

The accumulation of helium in Li_2TiO_3 samples with different microstructural properties was investigated using in-situ helium ion implantation. The influence of the interactions of implanted helium with electron beam induced radiation defects on cavity / gas bubble growth at elevated temperatures was investigated using complimentary in-situ thermal annealing experiments. Helium was found to accumulate to a greater extent in samples of low porosity and large grain size. The extent of cavity / bubble growth was found to be significantly exacerbated at elevated temperatures in samples which exhibited high helium retention. Such cavities have the potential to trap tritium in a working breeder blanket, thereby impeding its release and increasing tritium inventory, both of which would be detrimental to material performance. In the absence of implanted helium, the microstructural properties of large grain size and low porosity appear to increase the radiation tolerance of Li_2TiO_3 to displacement damage induced by electron irradiation. However, since the presence of helium has been shown to severely exacerbate cavity growth in Li_2TiO_3, the increased helium retention by specimens of low porosity and large grain size in fact resulted in a greater extent of cavity growth in such specimens at temperatures relevant to breeder blanket operating conditions. As such, the properties of high porosity and small grain size are likely to be beneficial for the optimisation of the performance of Li_2TiO_3 ceramic breeder materials from the perspective of reducing cavity formation at breeder blanket operating temperatures when the effects of helium are taken into account.

Chapter 1 - Introduction and aims

With ever increasing population, a dwindling supply of fossil fuels and increasing pressure to reduce carbon emissions, meeting the global demand for energy in an environmentally responsible manner is a challenge which cannot be ignored. Harvesting energy from nuclear fusion is a viable alternative to fossil fuels; in conjunction with conventional nuclear fission and renewable energy sources, fusion could make a major contribution towards solving the issue of the ever increasing global energy demand.

Advantages of nuclear fusion include [1]:

- Fundamentally safe – There will be insufficient fuel in the plasma chamber for a potentially dangerous runaway reaction to occur. Reactor design minimises the amount of radioactive isotopes present at any one time.
- Sustainable – Fuel sources are plentiful. Deuterium can be recovered from water, and tritium can be bred from lithium, which is sufficiently abundant on land to supply several hundred years of energy generation (after which extraction of lithium from sea water is a possibility).
- Environmentally friendly – No carbon emissions are directly associated with the process. No long lived radioactive isotopes are produced in the reaction; and while structural reactor materials will become radioactive, they are expected to be safe to be recycled within around 100 years following removal from the reactor.
- Efficient – 1 kg of lithium could produce enough tritium to supply 3×10^{13} J of energy (equivalent to 900,000 l of petrol, or ~100,000 kg of coal).

The fusion reaction currently proposed for power generation is the reaction between two isotopes of hydrogen, namely deuterium (D) and tritium (T), which fuse to form helium, and a high energy neutron is ejected:

^{2}H (D) + ^{3}H (T) → ^{4}He + ^{1}n   (17.6 MeV)
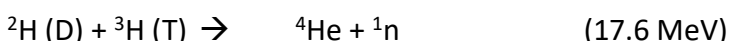
The energy is liberated in the form of kinetic energy, which is distributed between the neutron (14.1 MeV) and the helium nucleus (3.5 MeV) [2].

D and T have been selected as the fuels for fusion as the reaction cross section (a measure of the probability of fusion) is the largest of any fusion reaction of interest for power generation, and hence

the most easily achievable fusion reaction with a net energy gain [1, 2]. ^{4}He is very tightly bound; it is this difference in binding energy between nucleons in the fuel nuclei (D and T) and the ^{4}He product that is responsible for the energy liberated (see Figure 1.1).
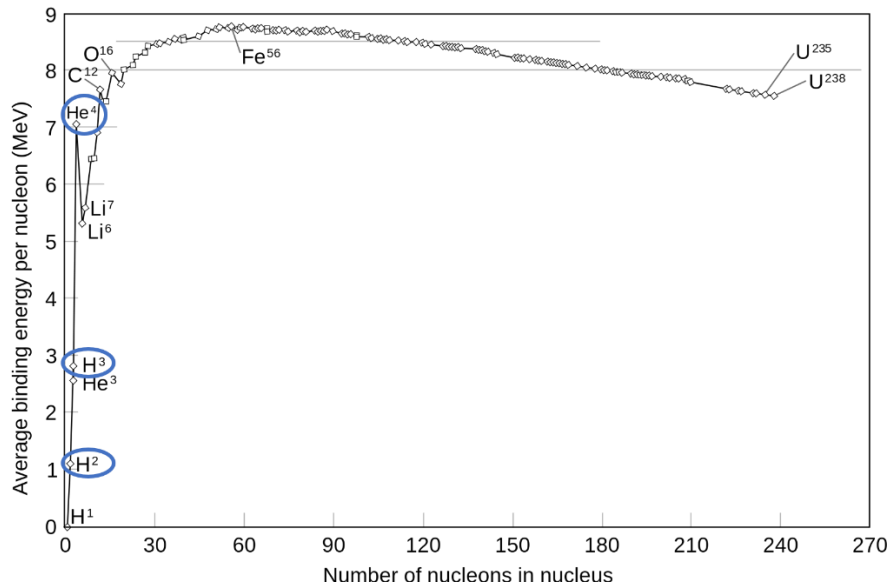
Figure 1.1: Average binding energy per nucleon vs. number of nucleons in nucleus. Adapted from Wikimedia Commons. (https://commons.wikimedia.org/wiki/File:Binding_energy_curve_-_common_isotopes.svg)

While deuterium can be recovered from water, tritium is inherently unstable ($t_{\frac{1}{2}}$ = ~12 years), and hence must be generated in-situ. Tritium can be "bred" from lithium by transmutation reaction, which occurs following capture of neutrons produced by the fusion reaction by lithium atoms [1]:

^{6}Li (n, α): ^{6}Li + ^{1}n   →   T + ^{4}He   (+ 4.8 MeV)

^{7}Li (n, α n): ^{7}Li + ^{1}n   →   T + ^{4}He + ^{1}n   (-2.47 MeV)
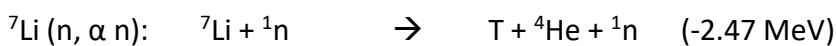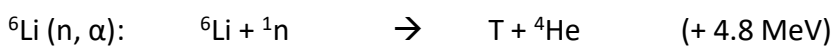
This is the primary function of the breeder blanket, which is composed of a lithium-containing material located in the first wall surrounding the plasma chamber (Figure 1.2, top). Its secondary function is to convert the kinetic energy of neutrons produced during fusion to recoverable heat.

A number of different breeder blanket concept designs have been developed. These include Helium Cooled Lithium Lead (HCLL), Water Cooled Lithium Lead (WCLL) and Dual Coolant Lithium Lead (DCLL) designs [3], all of which utilise a molten lithium-lead eutectic (~$Pb_{16}Li$) as a breeder material, the lead component of which functions as a neutron multiplier; the former two designs utilise helium and water as coolants respectively, while the latter utilises a combination of the two.

16

The research carried out in this project is concerned with solid breeder materials in the form of lithium containing ternary ceramics, which will be used in conjunction with a neutron multiplier material. The function of the neutron multiplier (the EU reference material for which takes the form of beryllium metal pebbles [4] while current designs are proposed to employ $Be_{12}Ti$ beryllide or molten lead [5]) is to increase the number of neutrons available for capture by lithium in the blanket; thereby increasing the number of lithium transmutation events per fusion neutron produced and in turn increasing the tritium breeding ratio (TBR), which is the ratio of tritium atoms produced per fusion neutron. For the fusion reaction to be sustainable, the TBR must be greater than 1; current design targets specify a TBR value ≥ 1.05 [6].

Inside the EU, ceramic breeder materials are proposed to be used in the so called HCPB (Helium Cooled Pebble Bed) concept. In the EU reference HCPB blanket design, a schematic of which is shown in Figure 1.2, both the ceramic breeder and beryllium multiplier take the form of pebbles, which are arranged in alternating layers in a number of breeder units surrounding the plasma chamber. Helium, with a small addition of hydrogen, acts as both a coolant (for heat recovery) and a purge gas for tritium extraction [3, 7].
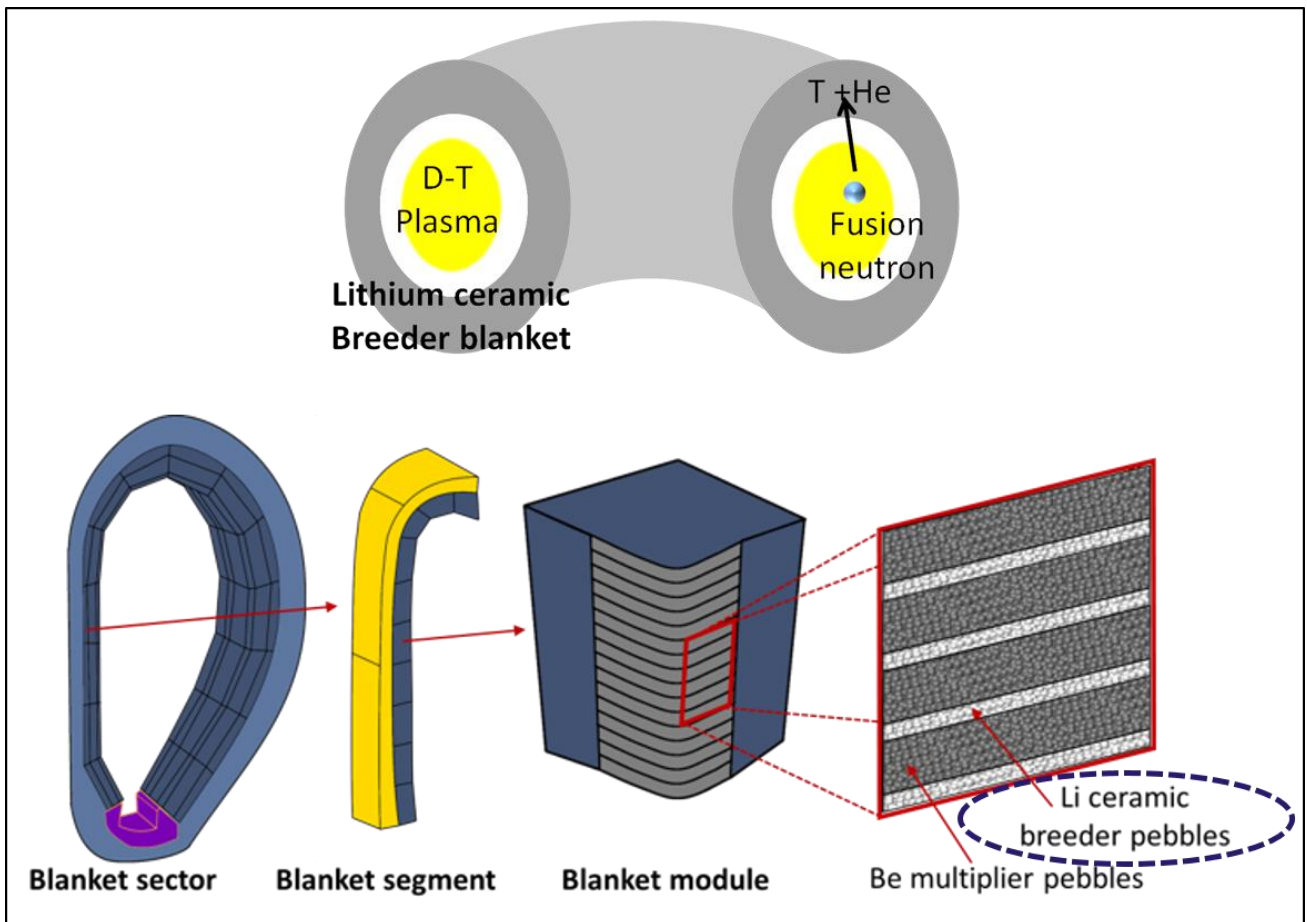
Figure 1.2: Top: Schematic of breeder blanket surrounding the plasma chamber in a fusion reactor. Bottom: Reference HCPB blanket module design circa. 2015, adapted from [3].

The latest proposed HCPB design [5], shown in Figure 1.3, utilises "fuel-breeder pins" which house lithium ceramic breeder pebbles, surrounded by hexagonal blocks of $Be_{12}Ti$ neutron multiplier as opposed to the layered configuration of the reference design. This design is reported to reduce the risk of structural materials overheating, and a variant of this design allows the use of a molten lead neutron multiplier in place of beryllium; thus circumventing inherent issues associated with the use of beryllium as a neutron multiplier material such as its toxicity, reactivity and relatively low abundance.
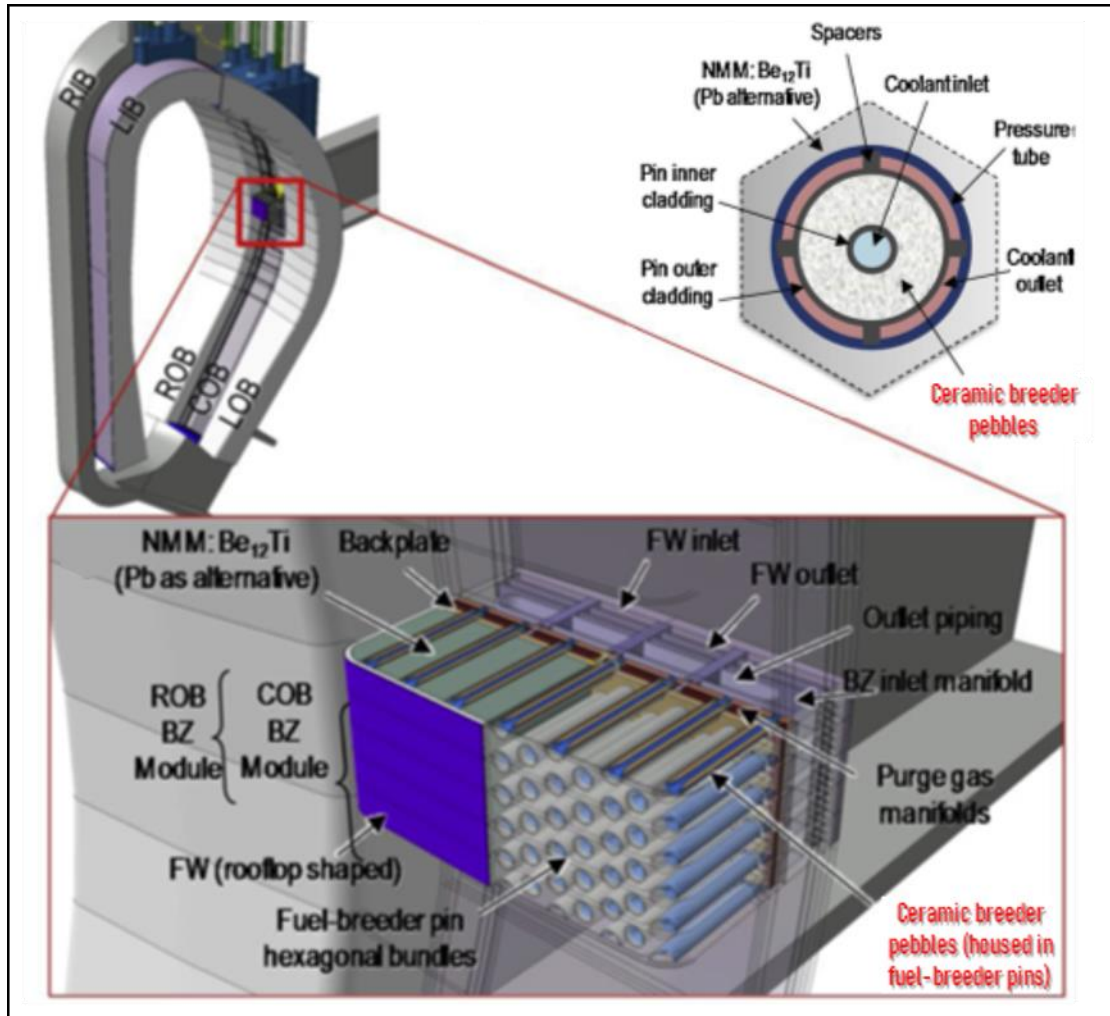
Figure 1.3: "Enhanced" HCPB blanket configuration, adapted from [5].

The material studied in this project was lithium metatitanate (Li_2TiO_3), which is considered to be one of the leading candidate ceramic breeder materials; indeed, Li_2TiO_3 is incorporated into the latest generation of ceramic breeder materials being developed for use with the aforementioned EU HCPB concept, which are composed primarily of lithium orthosilicate (Li_4SiO_4) with additions of Li_2TiO_3 as a secondary phase [8]. Li_2TiO_3 has also been proposed for use in the various breeder blanket concept designs being investigated by wider international research groups [9-11].

During operation, ceramic breeder materials must withstand the extreme conditions associated with nuclear fusion, including high temperatures and thermal gradients, and high magnetic fields. Breeder materials must also be compatible with structural reactor materials, and remain stable for their operational lifetime [12].

Possibly the most demanding condition however, is the high levels of radiation damage which will be induced by exposure to a high flux of high energy neutrons (14.1 MeV c.f. ~2 MeV for conventional fission). The estimated neutron flux at the first wall of the DEMO pilot plant is 1.75 MW m^{-2}, rising to 2.2 MW m^{-2} in the first industrial plant; this equates to 9.86x10^{17} 14.1 MeV neutrons m^{-2} s^{-1}, or approximately 150-200 displacements per atom (dpa) in first-wall steel over the lifetime of the blanket (based on an approximation for Fe) [13].

Neutron irradiation damage will result in the displacement of lattice atoms in ceramic breeder materials from their equilibrium positions, introducing defects in the form of vacancies and interstitials (Frenkel pairs); the correlation between defect annihilation and tritium release behaviour suggests that these defects may act as trapping sites for tritium [14-16], and as such impede tritium release and recovery, which is detrimental to the material's performance. The aggregation of like defects can also result in the formation of extended defects such as voids, cavities, and dislocation loops [17, 18]; tritium could potentially become trapped in such cavities, impeding its recovery and increasing the tritium inventory of the blanket material. Excessive tritium retention in the breeder blanket poses a potential safety risk at the blanket End-of-Life due to the inherent radioactivity of tritium [6].

A second key issue associated with tritium production is the large quantities of helium produced within the breeder material as a result of lithium transmutation. Due to its insolubility in most solids [19], accumulation of helium can result in the formation of gas bubbles in irradiated materials [20]. Furthermore, it has long been established that the nucleation and growth of irradiation induced voids and cavities is facilitated by the presence of gas atoms [21-23]. As such, in addition to accumulating to form bubbles which could act as trapping sites for tritium, the helium produced as a result of lithium transmutation has the potential to exacerbate the formation and growth of extended radiation defects such as voids and cavities; this could be detrimental to the mechanical integrity of ceramic breeder pebbles, and further impede tritium release and recovery. To date however, relatively little research has been carried out regarding the role of helium in ceramic breeder materials; despite this, there exists some limited evidence in the literature which suggests that the presence of helium could have a detrimental effect on the tritium release characteristics of Li$_2$TiO$_3$ [24].

Microstructural properties such as grain size are known to affect the irradiation behaviour of materials. Enhanced radiation tolerance, attributed to increased interfacial area associated with grain boundaries which act as efficient defect sinks, has been reported in numerous nanocrystalline materials [25-29]. Aggregation of defects in larger grained analogues, leading to the formation of defect clusters, has previously been attributed to the longer diffusion path to sinks at grain boundaries [25, 30]. Conversely, some materials exhibit higher radiation tolerance when they are composed of larger grains; for example, UO_2, ThO_2 and CeO_2 are all reported to exhibit a greater degree of volumetric swelling as a result of heavy ion implantation in nanocrystalline format than their analogous microcrystalline counterparts [31]. Helium retention and gas bubble formation has also been shown to be affected by microstructure; for example, Huang *et al.* [29] reported that a higher fluence of helium was required to induce bubble formation in $Gd_2Zr_2O_7$ ceramics with smaller grain size. Similarly, according to El-Atwani *et al. [32]*, no helium bubbles were observed in helium implanted iron with grain sizes less than 400 nm, but helium bubble density was reported to increase with increasing grain size in specimens with grain sizes up to 3 μm. The microstructural properties of high porosity and small grain size have also been reported to be beneficial for tritium release for ceramic breeder materials [33].

Ion implantation and electron irradiation are commonly used to "simulate" radiation damage and fission gas production in materials [34, 35]. Transmission Electron Microscopy (TEM) is one of the key techniques used to investigate the effects of externally induced damage introduced as a result of neutron irradiation or ion implantation [36, 37]. However, one factor that is often overlooked is the effect of the electron beams utilised in TEM, which are also capable of inducing damage, on the specimen being examined. The mechanisms by which damage is induced by electron beams are likely to differ from those of neutron damage owing to a significant difference in mass, and the charge associated with electrons. However, given that electron irradiation in a TEM has the potential to introduce defects which are similar in nature (i.e. atomic displacement) to those induced by neutron irradiation and ion implantation, it is important to determine how examination of ion implanted / irradiated materials using TEM techniques will affect the nano-structure of the material being examined in order to avoid the erroneous interpretation of results.

In addition to being the subject of extensive research for application as a ceramic breeder material, Li_2TiO_3 has been proposed for use in a multitude of other applications including electrode materials for use in lithium ion batteries [38-44], microwave dielectrics [45-47], and supercapattery

applications [48]. Since a number of the applications for which Li_2TiO_3 and similar lithium-containing ceramics have been proposed utilise materials with sub-micron or nanoscale microstructural properties [38, 41, 43-45, 48], TEM is likely to be used to examine their microstructure on the nano-scale. Hence, an understanding of the behaviour of Li_2TiO_3 under electron irradiation in a TEM may also assist in the explanation of unexpected phenomena observed during TEM examination of analogous materials developed for wider applications; thus avoiding the potential for erroneous findings being made and reported.

The aims of this project were:

- To determine the effects of the interactions of conventional TEM electron beams with Li_2TiO_3 ceramics.
- To investigate the influence of ceramic microstructure and processing conditions on the susceptibility of Li_2TiO_3 to electron beam damage.
- To investigate the effects of ceramic microstructure on helium accumulation in Li_2TiO_3, and identify the influence of implanted helium on the thermal evolution of irradiation defects therein at temperatures relevant to breeder blanket operating conditions.

In order to achieve the above aims, the effects of ceramic processing conditions on the microstructure of Li_2TiO_3 ceramics produced by solid state synthesis and conventional sintering methods were firstly investigated. Thereafter, in-situ transmission electron microscopy was used to observe the effects of electron beam irradiation on polycrystalline Li_2TiO_3 at room temperature. We report, for the first time, the observation of electron beam induced cavity formation in Li_2TiO_3. The effects of electron irradiation time and the microstructure of the ceramic in its as-prepared state on the formation and growth of cavities are identified, and the possible mechanisms responsible for the observed cavity formation under electron irradiation are discussed. Subsequently, in-situ thermal annealing experiments under electron irradiation in a TEM were used to investigate the thermal evolution of electron beam induced cavities in Li_2TiO_3 ceramics with different microstructural properties; such that the effects of the electron beam could be taken into account when interpreting the results of the ion implantation experiments which followed. Finally, in-situ helium ion implantation and complimentary in-situ thermal annealing experiments were used to investigate the effects of ceramic microstructure on the extent of helium accumulation and bubble formation in Li_2TiO_3, and to determine the influence of helium on cavity and bubble growth therein at temperatures relevant to breeder blanket operating conditions.

Chapter 2 - Literature review

2.1 Candidate ceramic breeder materials

To be suitable for application as breeder blanket materials, lithium ceramics must possess [49]:

(i)   High lithium atom density in order to maximise tritium breeding ratio (TBR), which is the number of tritium atoms produced per fusion neutron. The TBR must be >1 to achieve tritium self-sufficiency.

(ii)   Low tritium solubility for efficient tritium release and recovery.

(iii)   High thermal conductivity for efficient heat recovery.

(iv)   Good thermal, chemical and mechanical stability.

(v)   Good compatibility with structural reactor materials.

(vi)   Desirable irradiation behaviour

In addition, current activation targets dictate that activity levels of fusion reactor materials should be sufficiently low that they can be safely recycled within 100 years following removal from the reactor [50]; as such, the residual tritium inventory of candidate ceramic breeder materials should ideally be low, and the elemental composition should be such that no long-lived radioactive isotopes are produced as a result of neutron irradiation.

Early investigations focused on Li_2O due to its high lithium atom density (0.93 g cm^{-3}) and thermal conductivity (3.4 Wm^{-1}K^{-1}) [49]. However, it has since been eliminated due to concerns regarding its chemical reactivity with water (Li_2O reacts readily with water to form caustic LiOH) and structural reactor materials, and mechanical stability [51]. Hence, ceramic breeder materials research shifted towards the ternary lithium ceramics Li_4SiO_4, Li_2TiO_3, Li_2ZrO_3 and $LiAlO_2$. $LiAlO_2$ has since been eliminated due to its low lithium content and concerns about the activation of aluminium [52]. Internationally, Li_2TiO_3 and Li_4SiO_4 are currently favoured over Li_2ZrO_3, presumably because of the lower lithium atom density of the latter and the potential for zirconium activation.

Li_2TiO_3 is currently the material of choice for use with blanket designs utilising ceramic breeder materials in India [10], Korea [53] and Japan [54], who are also developing so-called 'super advanced' tritium breeders composed of a solid solution of Li_2TiO_3 and Li_2ZrO_3 [55]. The EU reference material, which is scheduled to be tested in Test Blanket Modules at the International Thermonuclear Experimental Reactor (ITER TBM) is composed of hyperstoichiometric Li_4SiO_4 with minor inclusions

of Li$_2$SiO$_3$ [56]; recent studies however, have shown that incorporating Li$_2$TiO$_3$ as a secondary phase enhanced the mechanical properties of the latest generation of 'advanced' bi-phasic ceramic breeder pebbles [8], which are currently being developed for use with the EU DEMO HCPB concept [5].

The crystal structures and compositional chemistry of current candidate ceramic breeder materials are discussed below, selected properties are listed in Table 2.1. The research carried out in this project focussed on single phase Li$_2$TiO$_3$; the structures and compositional details of Li$_4$SiO$_4$ and Li$_2$ZrO$_3$ are included for comparison.

2.1.2 Lithium metatitanate (Li$_2$TiO$_3$)

According to the phase diagram of the Li$_2$O-TiO$_2$ system [57] (as shown in Figure 2.1), three polymorphs of Li$_2$TiO$_3$ exist. At low temperatures a metastable cubic phase (α-Li$_2$TiO$_3$) exists, which can be prepared under hydrothermal conditions [58]; above 300°C α-Li$_2$TiO$_3$ is progressively and irreversibly converted to the β-phase over a wide temperature range. The stable polymorph under ambient conditions is monoclinic β-Li$_2$TiO$_3$, which has a narrow homogeneity range, forming solid solutions between ~48 and ~51 mol% TiO$_2$ [57, 59].

The phase of interest for application as a ceramic breeder material is the β-polymorph, since it is stable across the entire range of expected blanket operating temperatures (~400 °C – 920 °C [60]).

Stoichiometric β-Li$_2$TiO$_3$ is stable up to ~1155°C [57], at which point a rapid, reversible transition to the high-temperature cubic phase (γ – Li$_2$TiO$_3$) takes place [59]. The high-temperature cubic phase adopts a disordered rock salt structure and forms solid solutions over a wide range of compositions (44 - 60 mol% depending on temperature); non-stoichiometric solid solutions remain stable in the cubic structure to lower temperatures (~1050°C and ~930°C at lithia-rich and titania-rich limits respectively) than stoichiometric Li$_2$TiO$_3$ [57, 59], which melts congruently at ~1533°C.
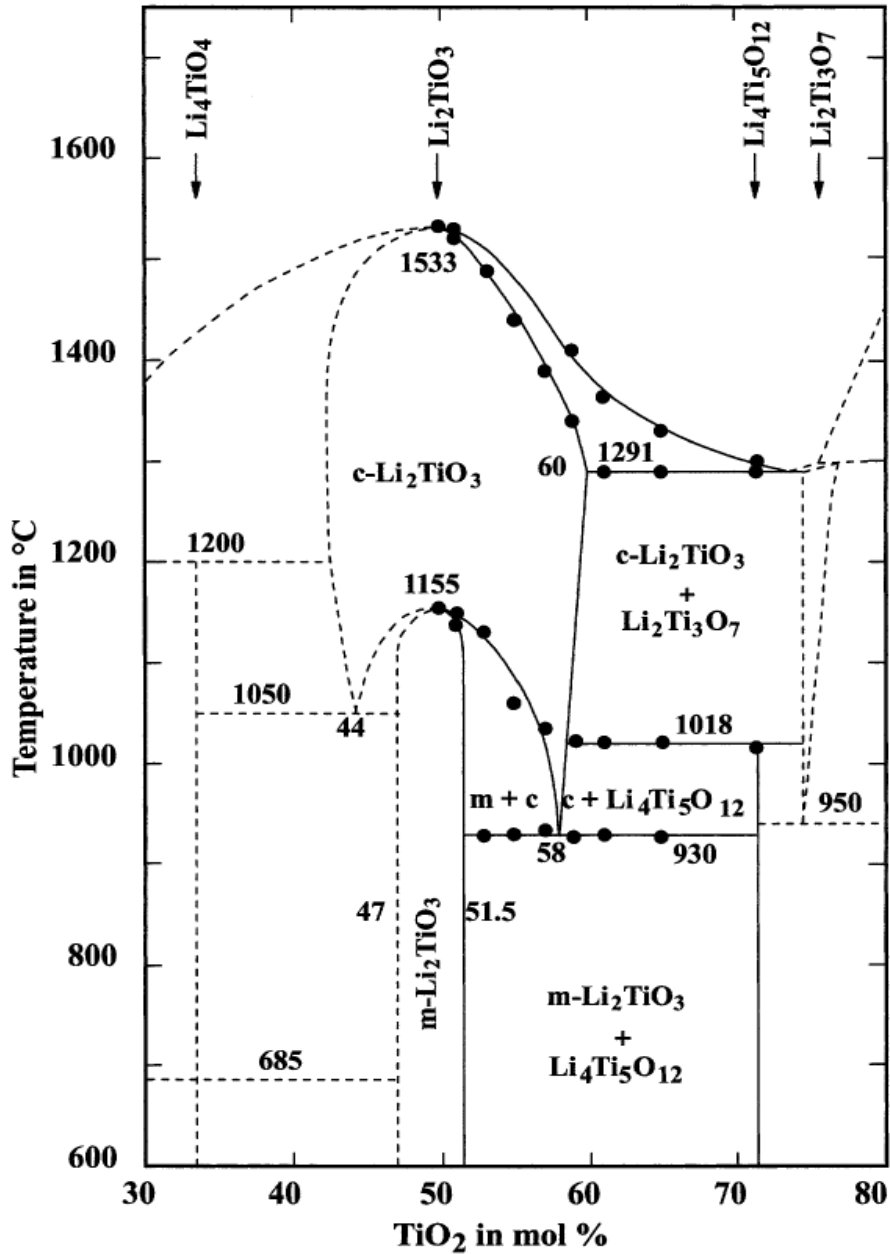
Figure 2.1 Phase diagram for the Li_2O-TiO_2 system. Taken from [57].

Monoclinic β-Li_2TiO_3 belongs to space group C2/c and crystallises in a distorted rock salt structure similar to Li_2SnO_3 [61]. The layered structure is constructed from edge-sharing LiO_6 and TiO_6 octahedra. Hexagonal close packed cation layers in the 004 planes are occupied alternately by layers exclusively composed of lithium, and layers composed of a 2:1 ratio of titanium and lithium [62]. In the mixed cation layers, lithium atoms occupy the centres of the hexagons, while titanium atoms occupy the vertices. Oxygen atoms lie between the layers of cations. The structure according to Kataoka *et al.* [61] is shown in Figure 2.2.
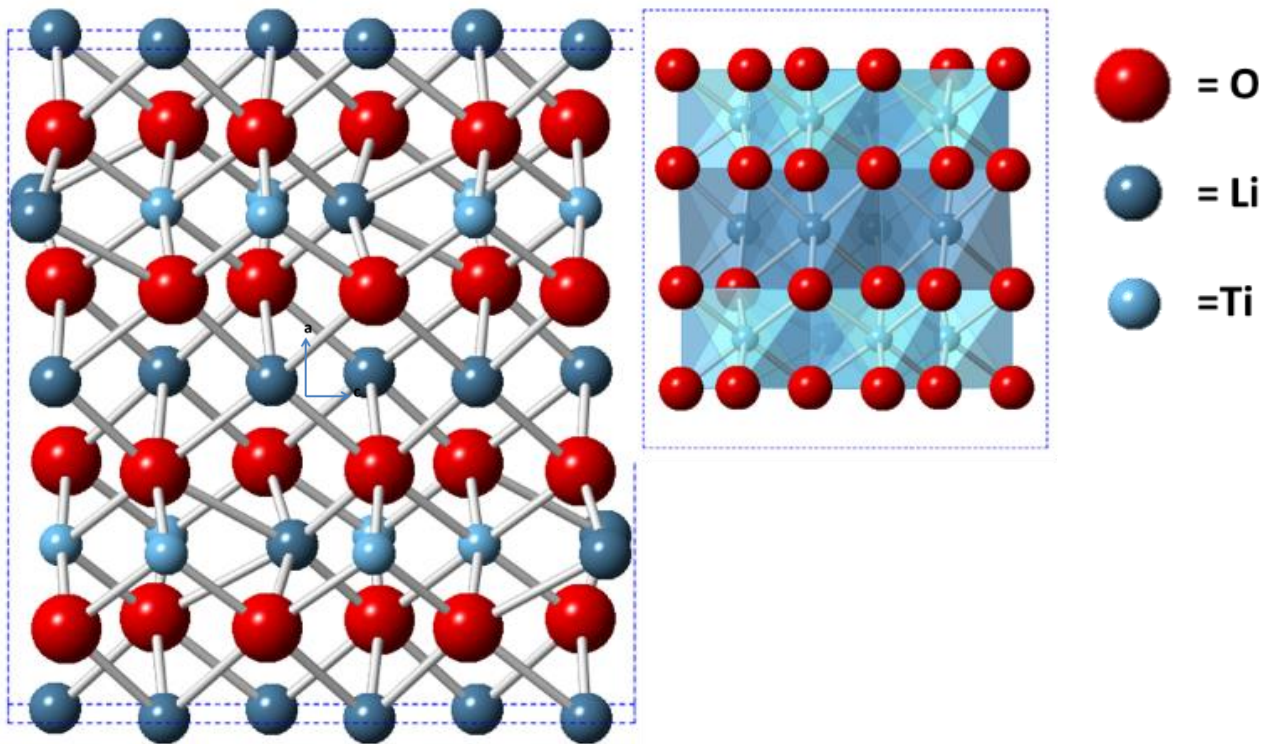
Figure 2.2: Structure of β- Li_2TiO_3 according to Katakoa *et al.*[61] . Images generated using CrystalMaker® [63].

2.1.1 Lithium orthosilicate (Li_4SiO_4)

Under ambient conditions, the crystal structure of Li_4SiO_4 is reported to be monoclinic, with space group $P2_1/m$. The Li_4SiO_4 unit cell contains 14 formula units and can be described as a supercell consisting of seven smaller subcell units, each containing two formula units [64].

The structure according to De Jong *et al*. [65] is shown in Figure 2.3. The majority of lithium atoms are tetrahedrally coordinated by oxygen atoms, although fivefold and sixfold coordination of lithium is also observed in the structure. Some partial occupancy of lithium atom sites is also reported. Silicon is exclusively tetrahedrally coordinated. The SiO_4, LiO_4, LiO_5, and LiO_6 polyhedra form a three dimensional network by a combination of corner- and edge-sharing.
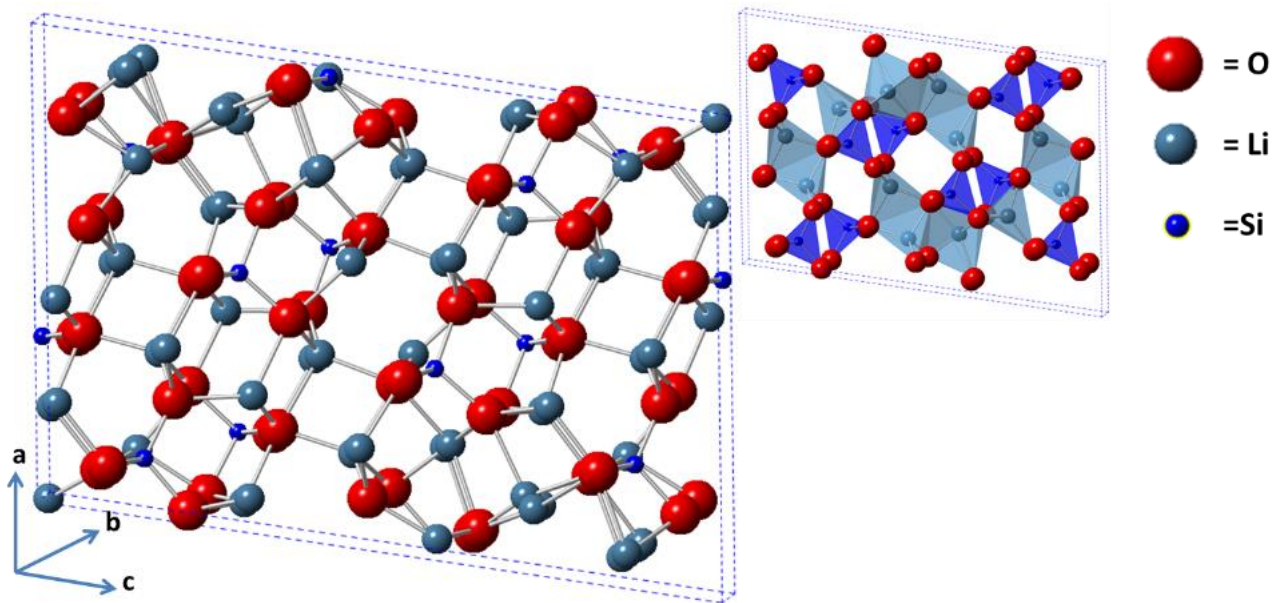
Figure 2.3: Structure of Li_4SiO_4 according to De Jong *et al.*[65] Images generated using CrystalMaker® [63].

Li_4SiO_4 melts congruently at 1255°C [66]. A reversible displacive transition involving a slight contraction of the crystal lattice in the c-axis with concurrent expansion in the a- and b-axes is reported to occur at 666°C, which results in a small overall increase in unit cell volume [67]. Since no change in crystal system or space group is associated with this transition, the high temperature structure is assumed to be a slightly distorted version of the room temperature structure.

According to the binary phase diagram for the Li_2O-SiO_2 system [66, 68] several lithium silicates exist in the region between 20 mol% and 50 mol% SiO_2. Single phase Li_4SiO_4 is only obtained at precisely stoichiometric composition (33.3 mol% SiO_2).

In lithium rich regions (20 < mol% SiO_2 < 33.3) Li_8SiO_6 forms as a stable secondary phase below 832°C; above this temperature Li_8SiO_6 decomposes to Li_2O and Li_4SiO_4. Further heating results in the formation of a lithium-rich liquid secondary phase at 992°C. In silica rich regions (33.3 < mol% SiO_2 < 50) lithium metasilicate (Li_2SiO_3) forms as a secondary phase below 1024°C. Above this temperature, either side of the eutectic point at ~38 mol% SiO_2, either Li_4SiO_4 or Li_2SiO_3 coexists with a liquid phase. Two other, possibly metastable phases (Li_6SiO_5 [69] and $Li_6Si_2O_7$ [70]) have also been reported.

The EU breeder blanket reference material is based on Li_4SiO_4 with a small excess of silica, such that Li_4SiO_4 is the major phase (90 mol%) and Li_2SiO_3 is present as a minor phase (10 mol%) [71]. Incorporation of Li_2SiO_3 secondary phase is reported to enhance mechanical properties [72]. The

structure of Li_2SiO_3 is orthorhombic with space group $Cmc2_1$. Chains of corner-sharing SiO_4 tetrahedra parallel to the (001) plane are in turn corner-linked to chains of corner-sharing LiO_4 tetrahedra parallel to the same plane, such that Li atoms lie between SiO_4 chains [73].

2.1.3 Lithium metazirconate (Li_2ZrO_3)

Similarly to Li_4SiO_4, Li_2ZrO_3 is a so called 'line phase' (i.e. it is not known to form non-stoichiometric solid solutions with excess Li_2O or ZrO_2) and as such pure Li_2ZrO_3 is only obtained at precisely stoichiometric composition (50 mol% Li_2O).

At stoichiometric composition, pure phase Li_2ZrO_3 exists as one of two polymorphs. At lower temperatures, Li_2ZrO_3 adopts a tetragonal structure (t-Li_2ZrO_3) [74] which undergoes a progressive, irreversible transformation to the stable monoclinic form (m-Li_2ZrO_3) at elevated temperatures [75]. The precise temperature at which this transition occurs is not clear from the available literature; it is noted however that all of the samples examined by Wyers and Cordfunke [75] which initially contained t-Li_2ZrO_3 at lower temperatures were found to consist exclusively of m-Li_2ZrO_3 following heat treatments exceeding 975K (~701°C), indicating that the transition to the monoclinic form is complete at this temperature.

In lithium deficient regions (< 50 mol% Li_2O) Li_2ZrO_3 is found to coexist with either of two polymorphs of ZrO_2 depending on the temperature of the system; with a monoclinic to tetragonal transition of ZrO_2 occurring at ~1177°C. In lithium rich regions close to stoichiometric composition (50 < mol% Li_2O < 60) Li_2ZrO_3 coexists with $Li_6Zr_2O_7$ up to the melting point of the latter (~1269 °C) at which point $Li_6Zr_2O_7$ melts incongruently into a lithia-rich liquid and solid Li_2ZrO_3 [75].

m-Li_2ZrO_3 is the phase of interest for breeder blanket applications. This phase is reported to be stable up to its estimated melting point at 1695±15°C [75], although decomposition due to lithia losses has been reported at temperatures exceeding 900°C [76].

The structure of m-Li_2ZrO_3, as reported by Hodeau *et al*. [77], is shown in Figure 2.4; it belongs to space group C2/c and crystallises in a distorted rock salt structure similar to Li_2SnO_3 and β-Li_2TiO_3.
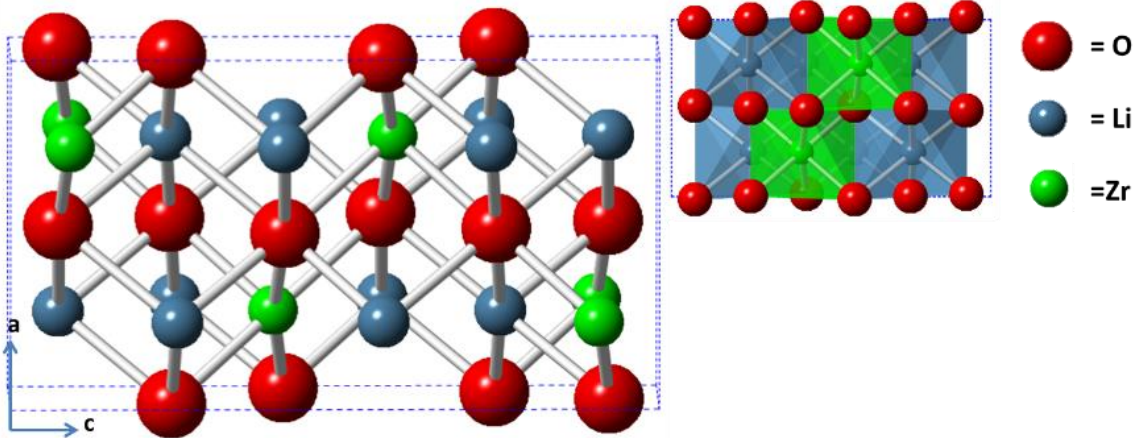
Figure 2.4: Structure of m-Li_2ZrO_3 according to Hodeau *et al.*[77]. Images generated using CrystalMaker®.

Similarly to the structure of β-Li_2TiO_3, the layered structure is constructed from edge-sharing LiO_6 and ZrO_6 octahedra with cations occupying hexagonal close packed layers in 004 planes; the difference being that in the case of Li_2ZrO_3, all cation layers are composed of lithium and zirconium in a ratio of 2:1. In each cation layer zirconium atoms occupy the centres of the hexagons, while lithium atoms occupy the vertices [77] (effectively the reverse of the mixed cation layers observed in β-Li_2TiO_3). Oxygen atoms lie between the layers of cations.

Table 2.1: Basic properties of candidate ceramic breeder materials Li_4SiO_4, Li_2TiO_3 and Li_2ZrO_3.

Candidate Material:	Li_4SiO_4 [49, 65]	β- Li_2TiO_3 [61, 78]	m- Li_2ZrO_3 [77, 78]
Empirical Formula:	Li_4SiO_4	Li_2TiO_3	Li_2ZrO_3
Formula Weight / g mol^{-1}:	119.85	109.76	153.10
Bulk Density / g cm^{-1}	2.35	3.43	4.15
Lithium atom density / g cm^{-1}	0.54	0.43	0.33
Melting point / °C	1255	1533	1695
Crystal System:	Monoclinic	Monoclinic	Monoclinic
Space Group:	$P2_1/m$	C2/c	C2/c

2.2 Synthesis methods

2.2.1 Solid state synthesis

The oldest and simplest method employed for ceramic synthesis is the Solid State Reaction method, in which stoichiometric amounts of reactant materials in powder form are mixed together, pressed into the desired shape and heated at high temperature for prolonged periods such that reaction occurs at the interface between reactant particles [79]. This technique is still widely used today and, according to literature [80-83], it remains the conventional method for the preparation of Li_2TiO_3. Titania (TiO_2) is commonly used as a titanium source, while lithium carbonate (Li_2CO_3) is the favoured source of lithium.

Mandal *et al. [82]* reported that solid state reaction between anatase TiO_2 and Li_2CO_3 begins at around 600°C, but found that pure Li_2CO_3 does not begin to decompose until ~740 °C. Hence they proposed that formation of Li_2TiO_3 must occur without prior decomposition of the carbonate via the following reaction:

$$Li_2CO_3 + TiO_2 \rightarrow Li_2TiO_3 + CO_2$$

A slight variation on this mechanism is proposed by Sonak *et al*. [84] who suggest that TiO_2 particles have a catalytic effect on the decomposition of Li_2CO_3; as such the carbonate decomposes at the surface of TiO_2 particles and the resulting oxide reacts rapidly with TiO_2 to form Li_2TiO_3:

$$Li_2CO_3 \rightarrow Li_2O + CO_2 \quad \text{(surface contact with } TiO_2 \text{ particle)}$$

$$Li_2O + TiO_2 \rightarrow Li_2TiO_3$$
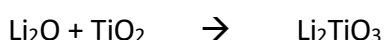
Growth of the resulting Li_2TiO_3 phase is then proposed to proceed by the diffusion of Li and O through the Li_2TiO_3 layer and subsequent reaction with TiO_2. The authors reported no evidence of intermediate phases in X-ray diffraction (XRD) patterns of partially reacted powders.

Since solid state reaction is, by definition, reliant on the diffusion of ions through solid materials, therefore high temperatures and long thermal soaking times are often required. Reducing the particle size, thereby reducing the diffusion distance required for reactants to come into contact, can aid the process of solid state synthesis. This can be achieved by milling the reactant materials together prior to calcination, which also ensures that reactants are well mixed.

Zhukov *et al.* [85] investigated the effect of so-called mechanoactivation of TiO_2-Li_2CO_3 mixtures by high energy ball milling. They found that increased milling time resulted in more successful conversion of reactant powders to the desired phase upon heat treatment under the same conditions. Optimum parameters for the synthesis of Li_2TiO_3 are reported to be 30 minutes planetary ball milling followed by heat treatment at 650°C with an isothermal soaking time of two hours; although longer milling time and higher calcination temperatures are more commonly adopted [82, 86, 87].

While milling may facilitate the formation of the desired phase by solid state reaction at lowered temperature and/or reduced thermal soaking time, sintering at relatively high temperatures is usually required to fabricate Li_2TiO_3 ceramics of high density.

Maximising the bulk density of ceramic breeder materials is considered desirable as the overall lithium atom density will be greater in a dense ceramic than a porous equivalent; hence the probability of fusion neutrons interacting with lithium atoms in the breeder blanket will be increased in a dense ceramic, which in turn increases the tritium breeding ratio. Densification of ceramics is commonly achieved by solid state sintering, where ceramic powders are compacted under high pressure and subsequently heat treated at temperatures typically ranging from 50-90% of the melting point of the material [88]. At such temperatures, diffusion of atoms from grain boundaries and dislocations to neck regions between contacting particles results in densification by the filling of pores. It is widely accepted that the process of densification is driven by the reduction in surface free energy associated with the reduction of internal surface area attributed to pores.

However, due to the inherent volatility of lithium, sintering of lithium-containing ceramics can be problematic; the high temperatures required can result in the loss of lithium species. High temperature vapourisation and thermal stability studies have been carried out on numerous candidate breeder materials including Li_2O [89], lithium aluminates [90], lithium zirconates [76, 91] and lithium titanate [92]; Li and Li_2O are usually the predominant species detected in the vapour phase, with LiO and Li_3O present in smaller quantities in some cases.

For example, the thermal stability of lithium silicates has been investigated by Cruz *et al.* [93] who found that Li_4SiO_4 decomposes to Li_2SiO_3 due to sublimation of lithium in the form of Li_2O according to the process:

$$Li_4SiO_{4(s)} \rightarrow Li_2SiO_{3(s)} + Li_2O_{(g)}$$
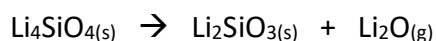
Since the formation of Li_2SiO_3 attributed to the sublimation of lithium species is observed across the entire temperature range investigated in their study (900°C - 1400°C), it is unclear at what temperature the onset of lithium sublimation takes place. It is clear however, that the rate of lithium sublimation increases significantly with increased temperature. While lithium vaporisation has been reported in Li_2TiO_3 at temperatures in excess of 900 °C [92], its structure is likely to be reasonably tolerant of the associated lithium deficiency due to the homogeneous range of solid solutions around the stoichiometric composition of Li_2TiO_3 in the Li_2O-TiO_2 system. Nonetheless, lowering sintering temperature as far as reasonably possible is considered beneficial from the perspective of maximising lithium retention.

Densification during sintering is accompanied by grain growth, the driving force for which is the associated reduction in total surface (or interfacial) area, thus reducing the total interfacial energy of a polycrystalline system. Densification and grain growth in Li_2TiO_3 has been shown to be strongly dependent on sintering conditions (e.g. temperature and duration) [94, 95]; as such, a degree of microstructural control can be afforded by systematic variation of sintering conditions.

2.2.3 Sol-gel methods

Sol gel methods feature regularly in the literature concerned with synthesis of ceramic breeder materials. The key advantage of sol-gel methods over traditional solid state reaction is the increased homogeneity of reagents (afforded by the use of solution state precursors) which facilitates lower processing temperatures and greater control over particle size and morphology [96].

Traditionally, sol-gel synthesis relies upon hydrolysis and condensation of metal alkoxides by reaction with water in an organic co-solvent. Hydrolysis results in polymerisation of the metal alkoxide via formation of metaloxane bonds. Initially, this leads to partial condensation (forming the 'sol'); as the condensation reaction proceeds, cross-linking occurs between polymer chains (forming a 'gel') [96, 97]. The solvent is then removed and the gel calcined to yield the final product.

The reaction is often acid- or base-catalysed. Choice of alkoxide precursor, type and concentration of catalyst employed and alkoxide:water ratio can all have significant effects on the structure of the gel obtained. Li_2TiO_3 and Li_4SiO_4 with well-controlled near-identical microstructures have been synthesised by this method by Renoult *et al*. [98].

Modern sol-gel techniques however, are not limited to reactions employing alkoxide precursors and organic solvents. Water-based systems - where the sol consists of a colloidal suspension of precursors which gel due to intermolecular forces (van der Waals/ hydrogen bonding) or interaction between metal complexes [96] - are increasingly utilised. Relevant examples of this include methods employed by Yu *et al*. [99] and Wu *et al* [100], in the synthesis of Li_4SiO_4 and Li_2TiO_3 respectively using water-based sol-gel methods employing citric acid as a chelating agent.

2.2.4 Melt spraying

A method which has attracted major attention is the melt-based KALOS (Karlsruhe Lithium Orthosilicate) process, originally developed by a leading fusion ceramics research group at the Karlsruhe Institute of Technology (KIT) for the production of Li_4SiO_4 [101]. The process has since been further developed for the production of dual-phase "advanced" ceramic breeder pebbles composed of Li_4SiO_4 and Li_2TiO_3 [8]; the addition the lithium titanate secondary phase is reported to enhance the mechanical properties of the resulting ceramics. In this process, lithium hydroxide hydrate, silica, and titania powders are mixed together and co-melted. The resulting melt is allowed to pass through a pinhole nozzle at the base of the crucible; after passing through the nozzle, droplets are formed as a result of the decay of the jet of liquid as it falls through the air beneath. The resulting droplets are dropped into liquid nitrogen to reduce deformation and inhibit microstructural changes. This rapid quenching is reportedly responsible for the dendritic microstructure of the resulting ceramic pebbles, which exhibit densities $\geq$ 95% of theoretical density (TD) depending on Li_2TiO_3 content.

For its simplicity, in conjunction with the microstructure control afforded by variation of sintering conditions, solid state synthesis and solid state sintering were the methods utilised in the synthesis and microstructure engineering aspects of this project.

2.3 Radiation damage

2.3.1 Radiation damage mechanisms

The energy transferred to lattice atoms as a result of the interactions of crystalline materials with particulate radiation (defined here as neutrons or charged particles such as ions and electrons) can cause structural damage in the form of atomic displacements. The mechanisms of energy transfer can be split into two major categories; electronic stopping and nuclear stopping [102]. In electronic stopping, the energy of the incident particle is transferred to the electron cloud associated with atoms in the material via inelastic interactions, resulting in electronic excitation and ionisation. Electronic stopping mechanisms result in low levels of damage over a long range. Nuclear stopping, where energy of the incident particle is transferred to target nuclei via elastic collisions, can result in much higher levels of displacement damage over a shorter range. Neutrons, being neutral particles, transfer energy to lattice atoms via elastic interactions with atomic nuclei. With the exception of low energy heavy ions, the majority of energy transferred by charged particles (i.e. electrons and ions), which interact with both atomic electrons and nuclei in a Coulombic manner, occurs via inelastic interactions with atomic electrons.

Several models designed to calculate the maximum kinetic energy transferred to a lattice atom by incident particles exist (which are further discussed in Chapter 5), the simplest approximation of this is the binary collision model, which is based on a "hard sphere" ballistic interaction between two particles, which takes no account of relativistic effects. For an incident particle of energy E and mass m, the maximum kinetic energy T_{max} transferred to a lattice atom of mass M is given by [103]:

$$T_{max} = E \frac{4Mm}{(M+m)^2}$$

From this relationship, it is clear that the proportion of the energy of the incident particle which is transferred to target atoms by ballistic interactions is strongly dependent on the difference in mass between the incident particle and the target nuclei; i.e. a larger proportion of incident particle energy is transferred to target nuclei by incident particles of similar mass. Nonetheless, sufficient energy can be transferred from high energy particles of significantly different mass to that of target nuclei (such as the beams of accelerated electrons utilised in electron microscopy) to induce 'knock-on' displacement of lattice atoms via ballistic interactions [104].

Atomic displacements result in the production of point defects in the form of vacancies and interstitials, known as a Frenkel pairs, a basic 2D schematic is shown in Figure 2.5.
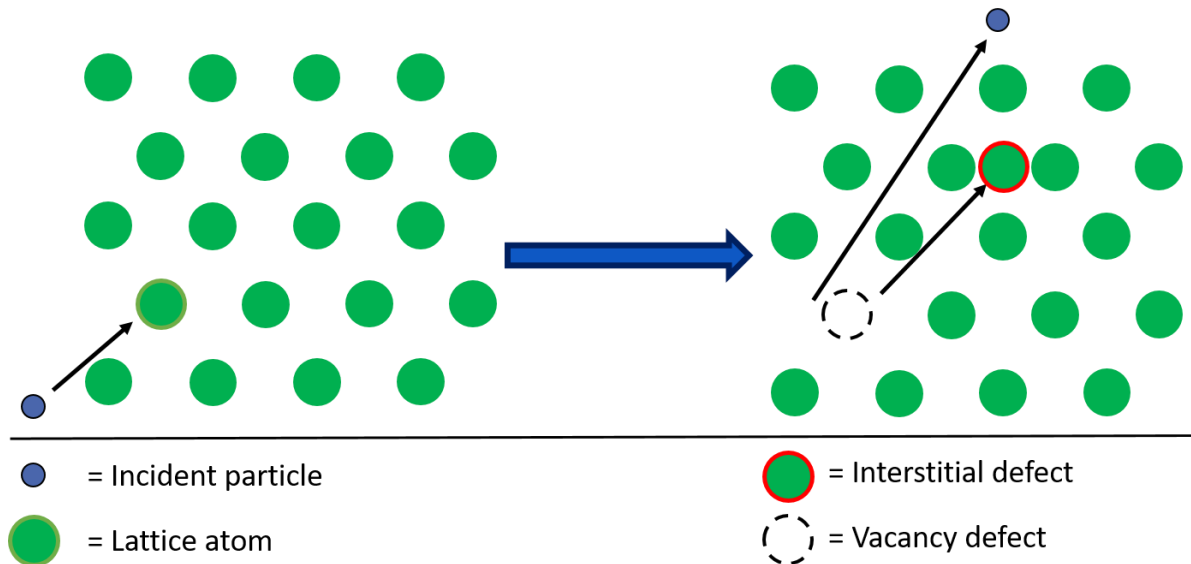
Figure 2.5: 2D Schematic of atomic displacement resulting in the production of a vacancy defect and an interstitial defect (Frenkel pair).

The displacement energy (E_d) of an atom in a crystalline structure is defined as the energy required to displace the atom from its lattice site. If the energy transferred to the lattice atom by the incident particle is greater than E_d, the atom will be displaced, creating a primary knock-on atom (PKA) which may then displace further atoms in a so called damage cascade. Incident particles and the resulting knock-on atoms will continue to displace further atoms until their respective energies are reduced below E_d. The amount of damage produced in a material as a result of interactions with radiation is often quantified in terms of displacements per atom (dpa); defined as the average number of times an atom in a given system has been displaced.

Knock-on displacement damage can occur directly, as a result of elastic collisions of incident particles (charged or neutral) with atomic nuclei. For knock-on displacement to occur, the kinetic energy transferred to the lattice atom by incident particles must be sufficient to exceed the displacement energy (E_d); thus, if the maximum possible kinetic energy transfer to lattice atoms exceeds E_d, lattice atoms can be permanently displaced. Radiation induced point defects in ceramic breeder materials can originate from interactions of lattice atoms with (i) incident neutrons produced by the fusion

reaction, (ii) recoil ^{4}He or T atoms resulting from lithium transmutation, (iii) knock on atoms, or (iv) creation of lithium vacancies due to Li burnup resulting from lithium transmutation [105].

Charged particles (such as electrons and ions) can also induce displacements indirectly as a result of radiolysis due to inelastic interactions with atomic electrons. A major part of the research carried out in this project was concerned with the investigation of the effects of displacement damage induced as a result of electron irradiation in Li_2TiO_3 ceramics under a conventional TEM electron beam. In addition to knock-on displacements due to elastic interactions with beam electrons, a number of inorganic materials are known to be susceptible to electron beam induced displacement damage as a result of radiolytic mechanisms; examples include alkali halides [106-108], alkaline earth fluorides [109, 110] and silicates [111, 112]. For displacement to occur via radiolysis, a sufficiently localised excitation of energy greater than E_d and sufficient excitation lifetime (>1 ps) must be induced, and a mechanism for the conversion of excitation energy to momentum must exist [113]. One such mechanism was proposed by Knotek and Fiebelman [114] to explain the phenomenon of electron stimulated desorption of oxygen from maximum valency ionic compounds (where the cation is ionised to its maximum oxidation state such that its outer electron shell is nominally empty). According to this mechanism, externally induced electronic excitation (e.g. by an electron beam) resulting in ionisation of a core electron of the cation results in an inter-atomic Auger process whereby the core electron hole on the cation is filled by a valence electron from a neighbouring oxygen anion. The energy released in this decay process is transferred to other electrons in the oxygen anion, resulting in Auger emission of one or two Auger electrons; thus, Auger decays can remove sufficient electrons from oxygen anions to render them positively charged. The resulting Coulombic repulsion between positively charged oxygen ions and surrounding metal cations subsequently leads to displacement (or desorption if located at the surface) of the oxygen ion.

2.3.2 Ion implantation

Currently, no neutron source is capable of producing a sufficiently high flux of 14.1 MeV neutrons to replicate the irradiation conditions of the first wall in a fusion reactor. While a number of neutron irradiation campaigns have been carried out on ceramic breeder materials [115-121], the relatively low flux of neutrons results in slow accumulation of damage, which limits practically achievable dose levels in a reasonable time frame. As such the number of studies in which ceramic breeders have

been neutron irradiated to fluences corresponding to levels of lithium burnup which are representative of an operational fusion reactor are relatively few.

Ion beam accelerators are commonly used to induce displacement damage and simulate the production of gases in irradiated materials. Heavy ions such as Au [35] and Xe [122] are often employed in studies concerned with inducing high levels of displacement damage since the proportion of energy deposited by nuclear stopping mechanisms is greater for heavy ions. The production of gaseous transmutation products such as helium [123] can be simulated by implantation of the relevant species; deuterium is commonly used as a tritium surrogate in studies concerned with tritium transport [124-126]. Ion beam accelerators allow for simultaneous dual (or multiple) ion implantation, such that the effects of displacement damage and gas accumulation can be studied simultaneously [127]. Some facilities, like the MIAMI-II system [128] at the University of Huddersfield (part of the UK National Ion Beam Centre) which was extensively used in this project, allow in-situ examination of the effects of ion implantation using TEM; such facilities have been used to study the nucleation and growth of gas bubbles in irradiated materials at controlled temperatures [19, 129].

The main advantage ion implantation is that high dose levels can be achieved in a short time frame [130]. Additionally, ion implantation offers a high level of control with respect to experimental parameters such as ion energy, flux, fluence and species [131]; these parameters can be tuned, often according to the results of simulations using the software package SRIM [132] (Stopping Range of Ions in Matter), such that ions are implanted to an appropriate depth and the effects of individual parameters can be studied. However, typical implantation depths are limited to an approximately 1 µm layer close to the sample surface; as such, it is difficult to determine whether the damage induced and / or behaviour of implanted gases in this limited irradiation volume are representative of bulk radiation behaviour. The higher proportion of low energy PKA's produced by ion irradiation compared to those induced by neutron irradiation results in smaller defect clusters in the damage cascade, and a higher surviving defect fraction [131]; additionally, sub-threshold collisions and ionisation effects can cause increased point defect diffusion in ion irradiated materials. Surface effects are of particular importance to in-situ TEM experiments, which call for very thin specimens with high surface area to volume ratio. Free surfaces act as a planar sink for point defects; defect-depleted or denuded zones attributed to the reduction in point defect supersaturation in the vicinity of the free surface has been reported [133, 134]; conversely, localised void swelling may occur close to free surfaces due to the biased loss of interstitials to the surface sink [135].

2.3.3 Extended defects: Formation and growth of cavities and gas bubbles

While the vast majority of Frenkel defects induced as a result of displacement damage by the various forms of irradiation recombine and annihilate, the aggregation of like defects can lead to the formation of larger, more stable extended defects such as voids, cavities and dislocation loops [17, 18, 136-138].

Nucleation of voids and cavities is generally attributed the aggregation of vacancies, which form clusters as a result of vacancy supersaturation (an excess concentration of vacancies over and above the equilibrium vacancy concentration of a material at a given temperature). Several theories regarding the causes of vacancy supersaturation have been proposed. One long-standing theory is the "Dislocation Bias" model, the basis of which is that, following initial displacement and the associated formation of a Frenkel pair, interstitial defects are preferentially absorbed at dislocations due to the high elastic strains associated with self-interstitial atoms [18], thus leaving behind an excess concentration of vacancies. An atomic scale HRTEM experiment by Xu *et al*. [136] unequivocally showed the nucleation and growth of voids in the vicinity of self-interstitial atom (SIA) loops in Mg under electron irradiation. Void nucleation in this case was attributed to vacancy supersaturation adjacent to SIA loops which acted as biased sinks for interstitial atoms.

Alternatively, the "Production Bias" model suggests that the intra-cascade production of thermally stable, mobile SIA clusters in addition to thermally unstable vacancy clusters can result in high levels of vacancy supersaturation; following the diffusion of mobile SIA clusters by one-dimensional glide, subsequent (partial) absorption of SIA clusters by sinks at dislocations and grain boundaries results supersaturation of the corresponding vacancies [139].

In the absence of dislocations, cavity formation due to vacancy supersaturation has also been attributed to the preferential loss of interstitial defects at free surfaces of thin film TEM specimens as a result of the higher mobility of interstitials compared to that of vacancies [140]. Under conditions where a vacancy supersaturation has been established, the resultant net influx of mobile vacancies to the walls of existing vacancy clusters results in cavity growth [18].

However, given that small vacancy clusters readily collapse into dislocation loops or stacking fault tetrahedra [141-144], the homogeneous nucleation of voids by random coalescence of mobile vacancies is generally considered unlikely [21]; as such it has long been theorised that the presence of gas atoms is essential for void / cavity nucleation and subsequent growth [18, 22]. The presence

of gas atoms reduces the surface energy associated with vacancy clusters, voids and cavities [145], thereby stabilising the internal surfaces, and in turn preventing the collapse of small voids and facilitating growth. Void number density has been reported to increase with gas concentration in irradiated metals, indicating that the gas acts as an efficient nucleating agent [146]. In addition to aiding nucleation, void embryos containing a sufficient quantity of gas have been reported to experience preferential growth, where void number density was significantly reduced or entirely absent in degassed specimens of the same material [145]. Hence, the nucleation and growth of voids and cavities is generally believed to occur by the absorption of vacancies *and* gas atoms [18, 23]; the extent of (volumetric) growth is primarily dictated by the supply of vacancies, the net absorption of which may be driven by the internal pressure of the stabilising gas [147].

According to Mayer *et al.* [146]*,* any gas is capable of stabilising voids and cavities. Helium is known to be particularly efficient in this aspect; indeed, vacancy defects have been described as an insaturable trap for helium due to the positive binding energy between interstitial helium atoms and helium-vacancy clusters [147]. As such, helium trapped within cavities can reach very high gas pressures, which in turn increases the driving force for vacancy absorption. Additionally, due to its insolubility in most solids [19], combined with high mobility and a strong affinity for vacancy defects [148] helium readily agglomerates to form bubbles in irradiated materials. Helium bubble formation has been observed in numerous classes of materials including metals [19, 149], ceramics [20, 123, 150, 151] and glasses [152].

Once nucleated, the growth and coarsening (i.e. an average increase in size and concurrent reduction of number density) of cavities and gas bubbles occurs by a number of different mechanisms [153]:

(i)   Vacancy collection - the net absorption of vacancies by cavities, driven by the excess pressure inside the cavities (exerted by gas atoms contained therein).

(ii)   Migration and coalescence (MC) – Long range driving forces such as temperature or stress gradients can result in the migration of cavities, which subsequently leads to coalescence and growth. Migration of cavities has also been shown to occur by Brownian motion in the absence of long range driving force [154].

(iii)   Ostwald Ripening (OR) – Exchange of vacancies and gas atoms between cavities / bubbles by thermally activated dissociation (re-dissolution into the matrix) of vacancies and gas

atoms from small cavities / bubbles, and subsequent re-deposition at larger ones. This process is driven by the difference in pressures within small and large bubbles.

The efficiency of cavity and bubble growth is known to be temperature dependent. The growth of cavities and bubbles can be enhanced at elevated temperatures as a result of the associated increase in the mobility of point defects (i.e. vacancies), gas atoms, and the cavities / bubbles themselves [155, 156]. Hence, the frequency of coalescence events is increased due to the enhanced mobility of stable cavities and bubbles, increasing the efficiency of MC. Under conditions where a vacancy supersaturation is present, the flux of vacancies to existing bubbles / cavities is increased; thereby accelerating growth by vacancy collection. Additionally, since the migration energy of vacancies is generally greater than that of interstitials in oxide ceramics [157], vacancies are less mobile than interstitials. As such, at low temperatures where vacancies remain relatively immobile, mutual recombination with mobile interstitials may be favoured over the vacancy aggregation processes, limiting cavity growth. In the case of Ostwald Ripening, this mechanism relies on the thermally activated dissociation of vacancies and gas atoms from existing vacancy-gas complexes. As such, the activation energy for OR where helium is present is equal to the activation energy for helium (and vacancy) dissociation from existing bubbles, which is reported to be much higher than that of migration and coalescence [156]; hence MC is expected to dominate at lower temperatures, where OR mechanisms may contribute to growth to a greater extent at relatively higher temperatures. Indeed, a transition from MC to OR in helium implanted metals has been suggested by Shroeder and Fichner [158]. Comparison of MC and OR "void" coarsening mechanisms in helium implanted silicon was discussed by Evans [159], who concluded that, under conditions where growth by Ostwald Ripening mechanisms would be appreciable, loss of vacancies to the surface would inhibit growth to such an extent that it would not be possible to reach the cavity sizes observed in specimens annealed in the temperature range of 700 - 1000 °C; whereas the migration and coalescence model fitted experimental data very well. Hence it was suggested that OR mechanisms did not contribute to void growth at such temperatures. The pressure exerted by gases contained within cavities is reported to reduce the thermal emission of vacancies, which would also inhibit OR growth mechanisms [140].

Thermal annealing experiments are commonly used to investigate the effect of temperature on the growth of cavities and gas bubbles. Enhanced growth is often attributed to the increased mobility of defects, gas atoms, and the bubbles / cavities themselves. Ono *et al.* [129] reported that the growth of helium bubbles as a result of coalescence by random migration in helium implanted silicon became

more significant at temperatures in excess of 870 °C; no shrinkage of smaller bubbles was observed, as such they conclude that OR mechanisms were not a contributing factor. Sasajima *et al.* [37] attributed the preferential formation of helium bubbles in the vicinity of dislocation loop planes in Al_2O_3 at elevated temperature (1073 K) to the increased mobility of helium and vacancies, and the de-trapping of helium from vacancies at higher temperature. Zinkle *et al* [20] suggested that the reduction in the helium fluence required to produce resolvable cavities in $MgAl_2O_4$, MgO and Al_2O_3 at elevated temperatures was due to the increased mobility of helium-vacancy clusters, they also suggest that the decrease in cavity density in hydrogen and helium implanted $MgAl_2O_4$ at peak implantation depth was due to the coalescence of neighbouring bubbles at 650 °C. Helium bubble growth in $MgAl_2O_4$ and Al_2O_3 during thermal annealing was also attributed to coalescence mechanisms by Furuno *et al.* [160]. Ofan *et al. [161]* ascribed the aggregation of implanted helium into bubble strings in $LiNbO_3$ to increased mobility of helium at elevated temperature, subsequent growth of helium bubbles was again attributed to coalescence. Vacancy-type defects in helium implanted zirconia were shown by Yang *et al. [150]* to increase in size with increasing helium fluence at room temperature; preferential accumulation of helium at grain boundaries followed by coalescence of the resulting bubbles was reported to result in the formation of a connected channel along the grain boundary. Taylor *et al. [162]* reported that helium implantation into palladium metal at 400 °C resulted in the rapid migration of helium and implantation-induced vacancies to existing cavities, indicating the high mobility of the aforementioned species at such temperatures. Subsequent cavity growth at temperatures in excess of 500 °C was attributed to coalescence. According to Chernikov *et al.,* [163] the coarsening of helium bubbles in helium implanted nickel was faster close to the surface of thin-film specimens during thermal annealing in the temperature range of 873-1273 K. The authors ascribe this to enhanced relaxation of bubbles facilitated by the greater supply of vacancies in near-surface regions, which are reportedly transferred between bubbles by an OR type mechanism. In the bulk however, bubble growth was proposed to occur via MC mechanisms since an insufficient supply of vacancies (provided from dislocations in the bulk) prevents OR. Bubble growth during the thermal annealing of helium implanted nickel has also shown to occur by coalescence in the work of Muntifering [26], who also reported that the increased grain boundary area in nanocrystalline nickel had a negligible ability to limit the growth of cavities. Their work also showed that specimens which had been pre-damaged by heavy-ion implantation prior to helium implantation exhibited a higher, uniform, number density of helium bubbles in the bulk of the grains than those which had not been pre-damaged; suggesting that existing defects can act as nucleation

sites for gas bubbles. Growth of cavities in TiO_2 by coalescence under electron irradiation has also been reported [164], which was shown by McCartney and Smith to be significantly exacerbated at elevated temperatures [165].

2.3.4 Effect of microstructure on radiation tolerance and helium accumulation

The influence of microstructural properties such as grain size on radiation induced damage accumulation and recovery has been investigated for numerous materials, many of these studies are concerned with nanocrystalline oxide ceramics. The contrasting results of selected studies are briefly discussed forthwith.

A number of materials have been reported to have superior radiation stability in nanocrystalline form compared to their larger grained analogues. This effect was first highlighted by Rose *et al.* [25] who reported a linear correlation between grain size and defect number density in nanocrystalline ZrO_2 in the grain size range 18 - ~70 nm, saturation of defect number density was apparently observed in grains 70 – 100 nm in size. They proposed that, since no resolvable defects were observed in grains smaller than 15nm, all point defects were absorbed at grain boundaries, which act as efficient defect sinks. Agglomeration of defects in larger grains, leading to cluster formation, was attributed to the increased diffusion path length to grain boundaries. Enhanced radiation stability in the context of defect accumulation and amorphisation has also been reported for nanocrystalline $MgGa_2O_4$ [28], which was reported to remain crystalline at Kr^+ fluences approximately a factor of eight higher than the onset of amorphisation in large grained (~10 µm) polycrystalline counterparts; and $Gd_2Zr_2O_7$ [29], where a lesser proportion of samples consisting of 55 nm grains was reported to have amorphised than those consisting of 221 nm grains under He^+ irradiation. Dey *et al.[30]* reported that larger grained (220 nm) samples of yttria stabilised zirconia exhibited a higher number density of defects than those with smaller grains (25 – 38 nm) under Kr^+ irradiation; adding that both vacancy and interstitial clusters were observed in larger grained samples, where only vacancy-type defect clusters were observed in smaller grained samples. They attribute this observation to the preferential migration of interstitial defects to defect sinks at grain boundaries during the cascade. However, aside from the increased availability of defect sinks associated with the increased grain boundary area of smaller grained materials, their irradiation response can also be affected by competing effects which are detrimental to radiation damage tolerance. High surface energy associated with increased interfacial area enhances the driving force for structural modifications which reduce the free energy

of the system, such as grain growth and phase transformations, which can reduce radiation stability [166]. The highly localised energy deposition resulting from the increased confinement of excited phonons and electrons in small grains, where the dissipation of energy is impeded due to scattering at grain boundaries, can result in thermal spikes. In conjunction with the excess free energy of grain interfaces, these two factors reduce the energy difference between amorphous (disordered) and crystalline (ordered) states, lowering radiation damage resistance; as proposed by Lu *et al.* to explain the amorphisation of nanocrystalline monoclinic ZrO_2 under U^+ irradiation [167] when bulk ZrO_2 with ~ 0.2 μm grains could not be amorphised under similar irradiation conditions [168]. Other materials where larger grain size has been reported to improve radiation tolerance include ZrO_2-MgO composite ceramics [169], where larger grained samples exhibited increased resistance to phase transitions under Xe^+ irradiation; and UO_2, ThO_2 and CeO_2 [31], all of which showed increased volumetric swelling of unit cell parameters in nanocrystalline form (~20 nm grain size) as a result of Au^+ irradiation compared to microcrystalline analogues (~2 μm grain size). With reference to helium accumulation, Huang *et al.* [29] reported that a higher fluence of helium was required to induce bubble formation in $Gd_2Zr_2O_7$ ceramics with smaller grain size. Similarly, according to El-Atwani *et al.* *[32]*, no helium bubbles were observed in helium implanted iron with grain sizes less than 400 nm, but helium bubble density was reported to increase with increasing grain size in specimens with grain sizes up to 3μm.

2.4 Radiation damage studies on Li_2TiO_3 (and other candidate ceramic breeder materials) and its implications for material performance

The effect of Xe^+ ion irradiation on the structure of Li_2TiO_3 has been investigated by Nakazawa *et al.* [122, 170] using a combination of XRD and Raman spectroscopy. Evidence of the breakdown of long range order as a result of irradiation induced damage was demonstrated by observed reduction in XRD peak intensity with increased ion fluence. Reduction of intensity and eventual disappearance of peaks observed in Raman spectra with increased ion energy was also reported, indicating disruption to short-range order in structural units as a result of ion implantation; the authors suggest that structural disorder as a result of irradiations is more dependent on electronic stopping mechanisms than nuclear stopping. Similar observations (significant reduction in Raman and XRD peak intensities) have been made by Zhou *et al.* [171] in the results of Ar^+ irradiation experiments carried out on Li_2TiO_3 with grain size <5μm.

In addition to introducing structural disorder, and the formation of extended defects such as dislocation loops and cavities discussed previously, radiation damage can lead to the formation of secondary phases; colloidal Li metal has been detected in neutron irradiated Li_2O [172], presumably due to radiation induced segregation caused by preferential migration of particular types of defect. Lithium burnup during operation will also result in compositional changes, potentially causing precipitation of secondary phases.

Tiliks *et al*. [173] detected colloidal lithium in Li_4SiO_4 irradiated with fast electrons at an absorbed dose of 10-20 MGy between 400-600 K, but argue that Li_4SiO_4 is sufficiently radiation stable for application as a breeder material as the degree of radiolysis (the number of radiation induced defects per structural unit) was 0.1-1% and does not exceed Li burn-up. Under the same conditions, no colloidal Li was detected in Li_2TiO_3 up to a dose of 500 MGy, and the limit of thermal stability for localised defects is reported to be 550-600 K; hence the authors state that Li_2TiO_3 has very high radiation stability. Zarins *et al*. [174] conducted a similar experiment on Li_4SiO_4 using 5 MeV electron irradiation (10.56 GGy dose); the results suggest that samples with small grain size (1 μm) are more stable under irradiation than samples with larger grain sizes. No publications concerned with electron irradiation of ceramic breeder materials using TEM electron beams, nor the stability of thin-film specimens thereof under such beams has been discovered in this literature survey.

The aforementioned paper by Zarins *et al*. is however, one of the very few which has shown direct correlation between as-prepared microstructure on irradiation stability. In many cases key microstructural details (particularly morphological information) are omitted from papers concerned with radiation damage performance. It is also apparent that, in cases where microstructural details are provided, the microstructures of different candidate materials subjected to similar experimental investigation are often not comparable, thereby rendering true comparison of irradiation performance problematic. There is a clear need to approach this area of research in a more systematic fashion; this view appears to be shared by some of the leading researchers in the field: "The effects of pebble microstructure on tritium release and mechanical integrity and stability need to be verified" [72].

Gas bubbles attributed to helium accumulation have been observed in Li_2O [175]. Macroscopic swelling in irradiated Li_2O has also been attributed to retained helium [176]. While there exists a preponderance of evidence that gas bubble formation can occur in ceramics as a result of neutron

irradiation or ion implantation, very little effort has been made to understand the mechanisms of helium accommodation in lithium ceramics for application as breeder materials. Nano-scale examination of irradiated or helium / hydrogen isotope implanted ceramic breeder materials appears to be rarely carried out; Carella *et al*. [177] examined He implanted Li_2TiO_3 under a TEM, and suggest that precipitated helium forms nanocavities in the damage cascade during implantation; no follow-up paper appears to have been published to date.

It is generally agreed in the literature that the mechanism for tritium release from lithium ceramics is a complex process involving (i) diffusion through the bulk of the grain, (ii) grain boundary diffusion, (iii) surface diffusion (iv) surface reaction (adsorption/desorption/ion exchange), (v) gas phase percolation through pore structure, and (vi) trapping/detrapping of tritium by irradiation defects. It is recognised that bulk diffusion is generally the rate determining step for large-grained samples, while surface interactions can dominate in smaller grained samples [178-181]. Trapping of tritium on defect sites becomes significant at high levels of displacement damage [15].

It is often stated that small grain size and open porosity are beneficial for efficient tritium release [33, 182]; Wedemeyer *et al* found that tritium release from small-grained Li_4SiO_4 was faster than that of samples with larger grains [183]. Increased pebble density has been shown to increase tritium residence time in Li_2TiO_3 [184]. Furthermore, the results of recent neutron irradiation experiments on Li_4SiO_4 breeder pebbles suggest that tritium release behaviour is dominated by the recombination of tritium species at the sample surfaces [185]; such surface processes could be significantly altered according to the porosity and grain size of ceramic breeder materials.

The extent of radiation damage is also proposed to affect tritium release characteristics. A thermal desorption spectroscopy (TDS) study by Kobayashi *et al*. [186] showed a reduction in tritium release rate and concurrent increase in peak tritium release temperature with increased neutron fluence in Li_2TiO_3. They propose that increased neutron fluence results in a higher concentration of defect sites, which trap tritium and inhibit its release from the material. A similar shift in tritium release temperature was observed in the case of neutron irradiated Li_4SiO_4, where samples which had been irradiated to higher Li burn-up exhibited peak tritium release at higher temperature [116]. Further evidence that radiation induced defects have a significant effect on tritium release performance is the correlation defect annihilation and the rate of tritium release observed in neutron irradiated Li_2TiO_3 and Li_4SiO_4 [14].

Numerous studies concerning tritium diffusion and release have been carried out; the influence of the presence of helium on tritium diffusion however, has not been thoroughly investigated. One of the few publications which directly investigates the influence of helium on tritium release from ceramic breeder materials was carried out by Kobayashi *et al*. [24], who found that that the amount of tritium released from Li_2TiO_3 was reduced in samples which had been pre-implanted with helium. Initially they proposed this to be due to trapping of tritium in helium bubbles, but also note that the level of residual tritium detected was low, and suggest that helium may displace tritium from trapping sites, aiding its release. Although they appear to have reached conflicting conclusions, the results of this study indicate that the presence of helium effects tritium release; as such their findings warrant further investigation of the behaviour of helium in ceramic breeder materials.

Chapter 3 - Materials and methods

This chapter describes the methods used to synthesise, process and characterise the materials studied in this project in their pristine ("un-irradiated") state. The methods used thereafter to investigate the effects of the microstructural properties of the materials fabricated on their behaviour under electron irradiation, the behaviour of implanted helium therein, and the thermal evolution of irradiation / implantation induced defects at temperatures relevant to breeder blanket operating conditions are also detailed here.

3.1 Ceramic synthesis and processing

3.1.1 Solid state synthesis of Li_2TiO_3 powders

Lithium metatitanate (Li_2TiO_3) powders were synthesised via the solid state reaction method according to the following reaction:

$$Li_2CO_{3\,(s)} + TiO_{2\,(s)} \rightarrow Li_2TiO_{3\,(s)} + CO_{2\,(g)}$$
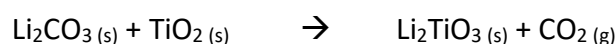
The phase purity of commercially available reagent powders Li_2CO_3 (Acros Organics Li_2CO_3 99+ % ACS Reagent) and TiO_2 (Aldrich Titanium (IV) oxide, ~325 mesh, >99% trace metals basis) was confirmed by X-ray diffraction as detailed in section 3.2.2 below. Reagents were dried (180 °C and 900 °C respectively) for a minimum of 12 h prior to synthesis. The dried reagent powders were mixed together in stoichiometric ratios and ball milled for 24 h under isopropanol with 10 mm yttria-stabilised zirconia (YSZ) media. The resulting slurry was dried overnight (80 °C) to remove the isopropanol, and sieved using a mesh size of 250 µm.

3.1.2 Thermogravimetric analysis (TGA) of milled reagent powders

TGA can be used to monitor the mass loss associated with the decomposition of reagent powders during solid state reaction as a function of temperature. In the case of the formation of Li_2TiO_3 by reaction of TiO_2 with Li_2CO_3, the reaction is considered to be complete at such a temperature where no further mass loss associated with the evolution of CO_2 as a result of Li_2CO_3 decomposition is observed. Hence, in order to identify an appropriate calcination temperature, a Perkin Elmer TGA4000 thermogravimetric analyser was employed to carry out TGA on a portion (~40 mg) of the milled reagent powders prior to calcination. TGA was performed under flowing air (30 ml min^{-1}) from 30 °C – 855 °C using a heating rate of 10 °C min^{-1}.

Based on the results of thermogravimetric analysis (detailed in Chapter 4), the milled reagent powders were calcined under atmospheric air in a box furnace using the two-stage calcination program shown in Figure 3.1 (RT to 700 °C, heating rate of 5 °C min^{-1}, 4 h dwell; and 700 to 730 °C, 5 °C min^{-1} heating rate, 4 h dwell). The two-stage calcination program was adopted in order to allow the reaction to progress as far as reasonably possible below the melting point of Li_2CO_3 during the first stage, thus mitigating the extent of possible particle agglomeration; the second stage ensured that the reaction reached completion. The calcined product was ball milled for 24 h under isopropanol with 10 mm YSZ media, dried overnight at 80 °C, and sieved using a mesh size of 250 µm.
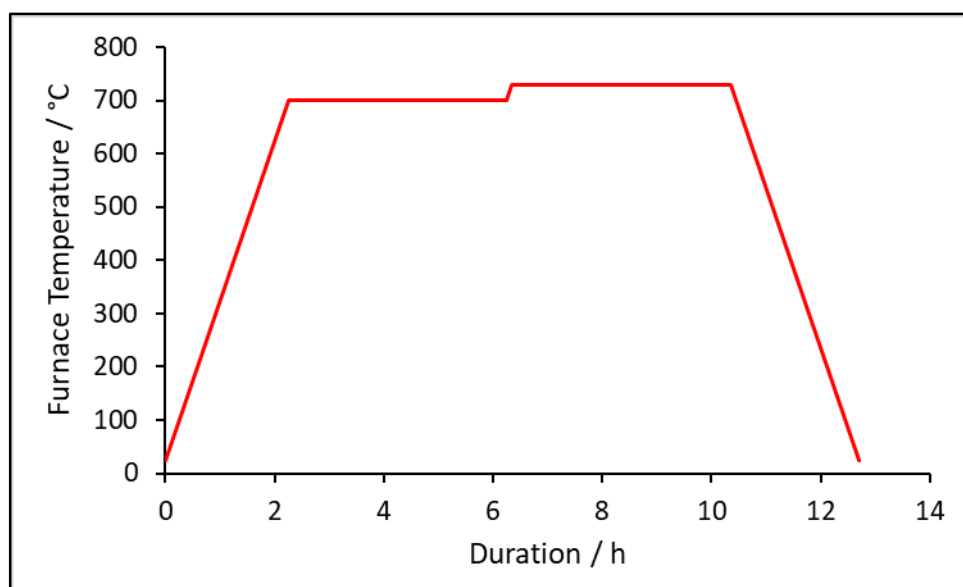
Figure 3.1: Temperature profile of the two-stage calcination programme adopted for the solid state synthesis of Li_2TiO_3 powders from Li_2CO_3 and TiO_2 reagents.

3.1.3 Sintering – Densification and microstructural manipulation

Portions of Li_2TiO_3 powder (~0.3 g), synthesised as per section 3.1.1, were uniaxially pressed into pellets (10 mm diameter, 0.8 Ton load ≈ 100 MPa, 1 min hold) to form "green bodies", which were subsequently sintered under atmospheric air in a tube furnace. One of the main aims of this project was to investigate the effect of grain size and porosity on helium accommodation mechanisms; hence, in order to investigate this, suites of samples with varying grain size and porosity were produced. In order to determine the processing conditions required to produce the desired microstructures, a sintering study was initially undertaken; sintering conditions were systematically varied in order to determine the effects of sintering (i) temperature and (ii) duration, on the density and microstructure of the resulting ceramics.

Initially, green bodies were sintered at systematically increasing temperature (750 °C – 1150 °C, 50 °C increments, 6 h dwell) in order to investigate the effect of sintering temperature on densification behaviour, and thus identify appropriate sintering temperatures for the production of Li_2TiO_3 ceramics of different densities. Based on the results of the aforementioned initial study, further green bodies were sintered at two different temperatures for systematically increasing durations (900 °C, 3 h - 9 h, 3 h increments; and 1000 °C, 2 h - 8 h, 2 h increments) to produce two suites of ceramic samples - a high porosity suite and a low porosity suite – comprising a range of grain sizes. This allowed the investigation of the effects of sintering duration on ceramic grain size at the temperatures adopted. A longer duration increment was employed during sintering of the porous suite as the rate of grain growth was expected to be lesser at lower temperature. In each case, two pellets were sintered simultaneously at each incremental temperature / duration.

3.2 Characterisation of reagents and pristine Li_2TiO_3 samples

3.2.1 Preparation of sintered pellets

One face of all sintered Li_2TiO_3 pellets was progressively polished to a 1 μm finish using silicon carbide grit paper followed by non-aqueous diamond suspensions, and thermally etched under atmospheric air at 90% of the respective sintering temperature for 30 min prior to characterisation.

3.2.2 X-ray diffraction (XRD) – phase analysis

XRD is commonly used to probe the structure of crystalline materials, allowing the determination of unit cell (the smallest repeating unit representative of the full symmetry of the crystal structure of a material) parameters, space group, and the position of atoms which make up the respective unit cell. Phase identification is commonly achieved by comparison of XRD patterns to entries corresponding to known structures in the International Centre for Diffraction Data (ICDD) database.

Given that the atoms in crystalline materials are, by definition, ordered in a regular repeating array, the structure of crystalline materials can be visualised as sets of uniformly spaced planes of atoms separated by a distance *d*. The orientation of a given set of crystal planes in relation to the unit cell is conventionally represented by fractions of unit cell vertices denoted Miller Indices.
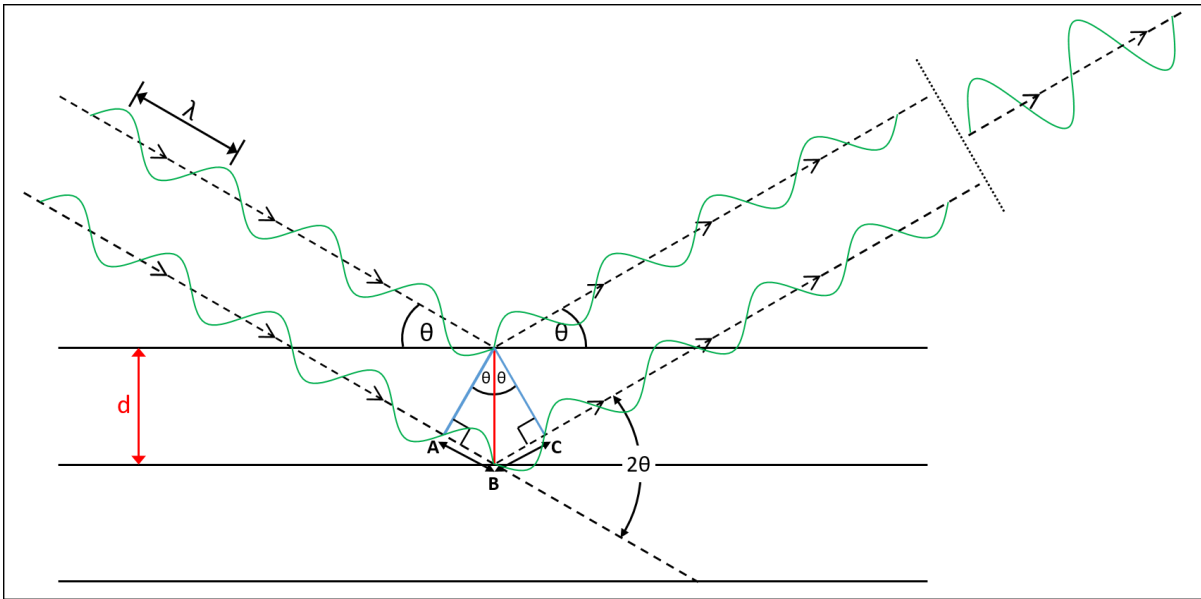
Figure 3.2 (Adapted from [187]): Schematic diagram portraying diffraction of X-rays, as described by Bragg's law. Crystal planes are represented by horizontal lines shown in black, X-rays are represented by waves shown in green.

X-rays are a class of electromagnetic radiation, as such incident X-rays are scattered by atomic electrons. Scattering of X-rays at consecutive planes within the penetration depth of the incident beam results in interference, which can be either constructive or destructive. The majority of scattering events result in destructive interference; however, when the path length of X-rays scattered at consecutive planes differs by an integer number of wavelengths, constructive interference occurs, increasing the cumulative amplitude of the scattered wave. This constructive interference gives rise to peaks in the diffraction patterns of crystalline materials. Diffraction peaks are directly related to the interplanar spacing *d* of a given set of crystal planes according to Bragg's law:

$$n\lambda = 2d \sin \theta$$

Where *n* is an integer, λ is the X-ray wavelength and θ is the incident angle of X-rays.

Using the scenario depicted in Figure 3.2, in which incident X-rays are scattered by an angle equal to 2θ at a set of crystal planes such that the path difference of X-rays scattered at consecutive planes differs by 1λ (resulting in coherent scattering due to constructive interference of "in phase" scattered waves); the origin of Bragg's law can be demonstrated using trigonometry. The total path difference of X-rays scattered at consecutive crystal planes is equal to the sum of the (equal) distances **AB** and **BC,** which is in turn equal to **2 · (AB)**. Therefore $n\lambda = 2\,AB$.

Using trigonometry: $\quad sin\,\theta = \dfrac{AB}{d}$ $\qquad\qquad \therefore \qquad AB = d\,sin\,\theta$

Substituting AB for $n\lambda$ / 2: $\quad \dfrac{n\lambda}{2} = d\,sin\,\theta$ $\qquad\rightarrow\qquad n\lambda = 2d\,sin\,\theta$

X-rays are widely utilised for diffraction studies since the wavelength of X-ray radiation is typically the same order of magnitude as the d spacing of crystal planes; thus X-rays are of a suitable wavelength to allow the diffraction peaks corresponding to the d spacing of planes of atoms in a crystalline material to be resolved.

Diffraction patterns for simple (cubic) systems can be indexed (i.e. Miller Indices can be assigned to each diffraction peak) using equations relating interplanar spacing, *d*, to the unit cell parameter, *a,* and possible values of Miller Indices, *h, k, l,* in conjunction with Bragg's law. i.e. for a cubic system:

$$\dfrac{1}{d^2} = \dfrac{(h^2+k^2+l^2)}{a^2} \qquad\qquad \therefore \qquad \theta = \dfrac{n^2\lambda^2}{4a^2}\cdot(h^2+k^2+l^2)$$

Once indexed, approximate unit cell parameters can be calculated from the d spacing of peaks with known *hkl* values. However, such equations become significantly more complicated to solve where more complex (less symmetric) systems are concerned; e.g. for monoclinic crystal systems such as that of Li_2TiO_3, the above equation for 1 / d² becomes:

$$\dfrac{1}{d^2} = \dfrac{h^2}{a^2\beta} + \dfrac{k^2}{b^2} + \dfrac{l^2}{c^2\beta} - \dfrac{2\,hl\,cos\,\beta}{ac\beta}$$

Hence indexing and unit cell refinement are often carried out with the aid of appropriate software packages when dealing with more complex systems.

In this work, XRD was used to confirm phase purity of reagent powders, as well as the phase assemblage of the as-synthesised Li_2TiO_3 powder and the sintered ceramic pellets. Powder samples were ground to a fine, visually uniform texture using a pestle and mortar prior to data collection. All XRD data were collected in Bragg Brentano geometry using Cu Kα radiation (λ = 1.5418 Å). Bruker D2 Phaser or PANalytical X'Pert[3] Powder diffractometers were utilised. Phase identification was achieved by comparison of observed diffraction patterns to entries in the ICDD PDF4+ database with the aid of EVA 3.1 (Bruker Diffrac Suite) and PDF4+ (ICDD) software packages.

3.2.3 Density measurement

The dimensions of each sintered pellet were measured using Vernier callipers (precision: 0.01 ± 0.005 mm). The mass of each pellet was measured using a mass balance (precision: 0.0001 ± 0.00005 g). Modelling each pellet as a cylinder, the absolute density (ρ) of each of the sintered pellets was calculated from its mass (m) and the mean values (obtained from six measurements) of diameter (D) and depth (d) according to Eq. (3.1). The error $(\delta\rho)$ associated with the density of each individual pellet was calculated by propagating the maximum deviation and instrumental error associated with each measured dimension through to density according to Eq. (3.2).

$$\rho = \frac{m}{V} = \frac{m}{A_s \cdot d} = \frac{m}{\pi r^2 \cdot d} = \frac{m}{\pi\left(\frac{D}{2}\right)^2 \cdot d} \qquad (3.1)$$

$$\delta\rho = \rho \cdot \sqrt{\left(2 \cdot \frac{\delta D}{D}\right)^2 + \left(\frac{\delta d}{d}\right)^2} \qquad (3.2)$$

where V is the volume of the pellet, A_s is the surface area of the circular pellet face, r is the pellet radius, and δD and δd are the absolute errors associated with diameter and depth respectively (taken as half of the range of six measurements, plus the instrumental error). Full details of how Eq. (3.2) was constructed are given below:

$$\rho = \frac{m}{V} \qquad\qquad \therefore \frac{\delta\rho}{\rho} = \sqrt{\left(\frac{\delta m}{m}\right)^2 + \left(\frac{\delta V}{V}\right)^2}$$

Neglecting $\frac{\delta m}{m}$ (negligibly small by comparison to $\frac{\delta V}{V}$):

$$\frac{\delta\rho}{\rho} = \left(\frac{\delta V}{V}\right) \qquad\qquad V = A_s \cdot d \qquad \therefore \frac{\delta\rho}{\rho} = \sqrt{\left(\frac{\delta A_s}{A_s}\right)^2 + \left(\frac{\delta d}{d}\right)^2}$$

$$A_s = \pi r^2 \qquad \therefore \frac{\delta A_s}{A_s} = 2 \cdot \frac{\delta r}{r} = 2 \cdot \frac{\delta D}{D}$$

$$\therefore \frac{\delta\rho}{\rho} = \sqrt{\left(2 \cdot \frac{\delta D}{D}\right)^2 + \left(\frac{\delta d}{d}\right)^2}$$

$$\therefore \delta\rho = \rho \cdot \sqrt{\left(2 \cdot \frac{\delta D}{D}\right)^2 + \left(\frac{\delta d}{d}\right)^2}$$

Final values of density were calculated from the mean average values of the absolute density obtained from two pellets prepared under identical conditions. The final values of associated errors

($\delta\rho_{Tot}$) are quoted as the sum of the errors calculated for each individual pellet propagated through to the mean, and half of the range of the absolute density values obtained (Eq. (3.3)):

$$\delta\rho_{Tot} = \left(\frac{\sqrt{(\delta\rho_1)^2 + (\delta\rho_2)^2}}{2} + \frac{|\rho_1 - \rho_2|}{2} \right) \quad (3.3)$$

3.2.4 Scanning electron microscopy (SEM) – grain size analysis

SEM was used to examine the morphology of the milled Li_2TiO_3 powder, give an estimation of powder particle size prior to sintering, and to obtain a micro-scale overview of the microstructure of the sintered ceramic pellets. SEM micrographs also provided visual verification of the nature and extent of porosity, and the extent of grain growth, exhibited by samples sintered under different conditions.
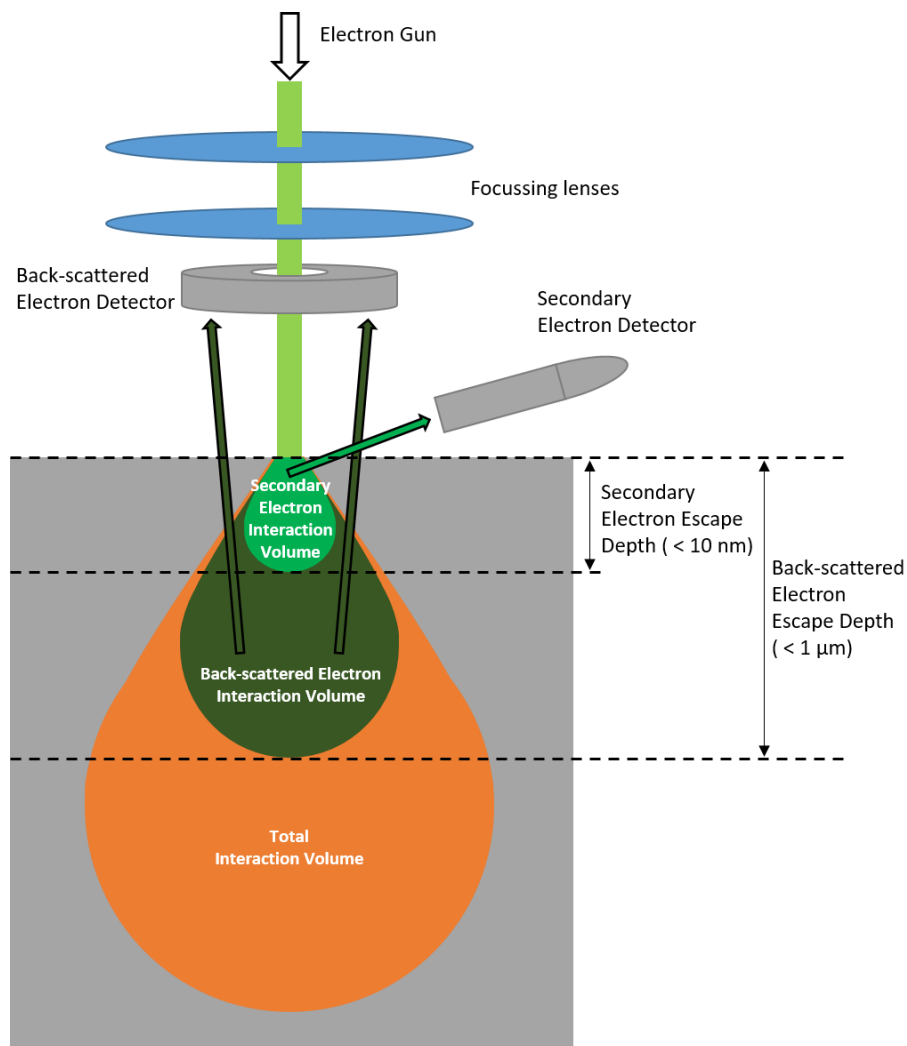
Figure 3.3: Basic schematic of a typical SEM setup showing the escape depth of the secondary and backscattered electrons which can be used for imaging.

A basic schematic of a typical SEM setup is shown in Figure 3.3. A beam of accelerated electrons (typically <30 keV) is focussed to a small probe (typically 1-10 nm in diameter) on the surface of a sample by a set of electromagnetic lenses. The probe is rastered across the sample surface. Secondary electrons (SE) are produced as a result of inelastic scattering interactions of beam electrons with weakly bound outer-shell (valence or conduction) atomic electrons. If sufficient energy is transferred from incident beam electrons to outer-shell atomic electrons to overcome the Coulombic forces which confine them to a particular atom, a secondary electron is released; any excess energy transferred to the released electron is retained in the form of kinetic energy. Most secondary electrons come to rest within the interaction volume (the three-dimensional region of the sample in which most of the scattered beam electrons are contained), but those very close to the surface may escape to the vacuum where they can be detected by the secondary electron detector. Since detectable secondary electrons originate from very close to the surface, SE imaging is used to obtain topographical information about the sample.

Beam electrons can also be backscattered (scattered through an angle greater than 90°) as a result of elastic interactions with positively charged atomic nuclei. Due to the elastic nature of such interactions, the kinetic energy of backscattered electrons (BSE) is comparable to that of the incident beam, and significantly greater than that of secondary electrons; as such the escape depth of BSE is much greater than that of SE. As a result of this, much of the topographical information is lost, but since the cross section for high-angle elastic scattering is proportional to atomic number (Z), more electrons are backscattered by elements of higher atomic number. Hence, the contrast observed in BSE images can provide information corresponding to variations in the elemental composition of the sample.

In this work, powder / pellet samples were mounted to aluminium stubs using self-adhesive carbon pads. The upward-facing surfaces (polished and thermally etched in the case of pellet samples) of samples were sputter-coated with gold (15 mA, 2-3 minutes) prior to imaging in order to reduce specimen charging. All SEM micrographs were collected in SE imaging mode using FEI Inspect F or FEI Inspect F50 electron microscopes operated at 20 kV. Both microscopes are equipped with field emission gun electron sources.

The SE SEM micrographs obtained were subsequently used to determine the grain size distribution and mean average grain size exhibited by Li_2TiO_3 samples sintered under the different conditions

detailed in section 3.1. Using the image processing package ImageJ [188], the longest available dimension of 450 grains per sample was measured, and the corresponding mean average grain size calculated. Errors associated with the mean grain size are quoted as the estimated standard deviation (ESD) of the 450 grain population measured.

3.3 (In-situ) transmission electron microscopy (TEM)

In a TEM, a beam of accelerated electrons is focussed onto a thin (~100 nm) specimen by a series of electromagnetic lenses. As the beam of electrons passes through the specimen, they are scattered as a result of interactions (which may be elastic and inelastic) with atomic nuclei and atomic electrons associated with the specimen material. Forward-scattered beam electrons are subsequently collected, magnified, and focussed onto a fluorescent screen or a CCD detector by further sets of electromagnetic lenses to form either an image or a diffraction pattern depending on the strength of the second set of lenses. A simplified schematic detailing the basic components of a conventional TEM is shown in Figure 3.4.
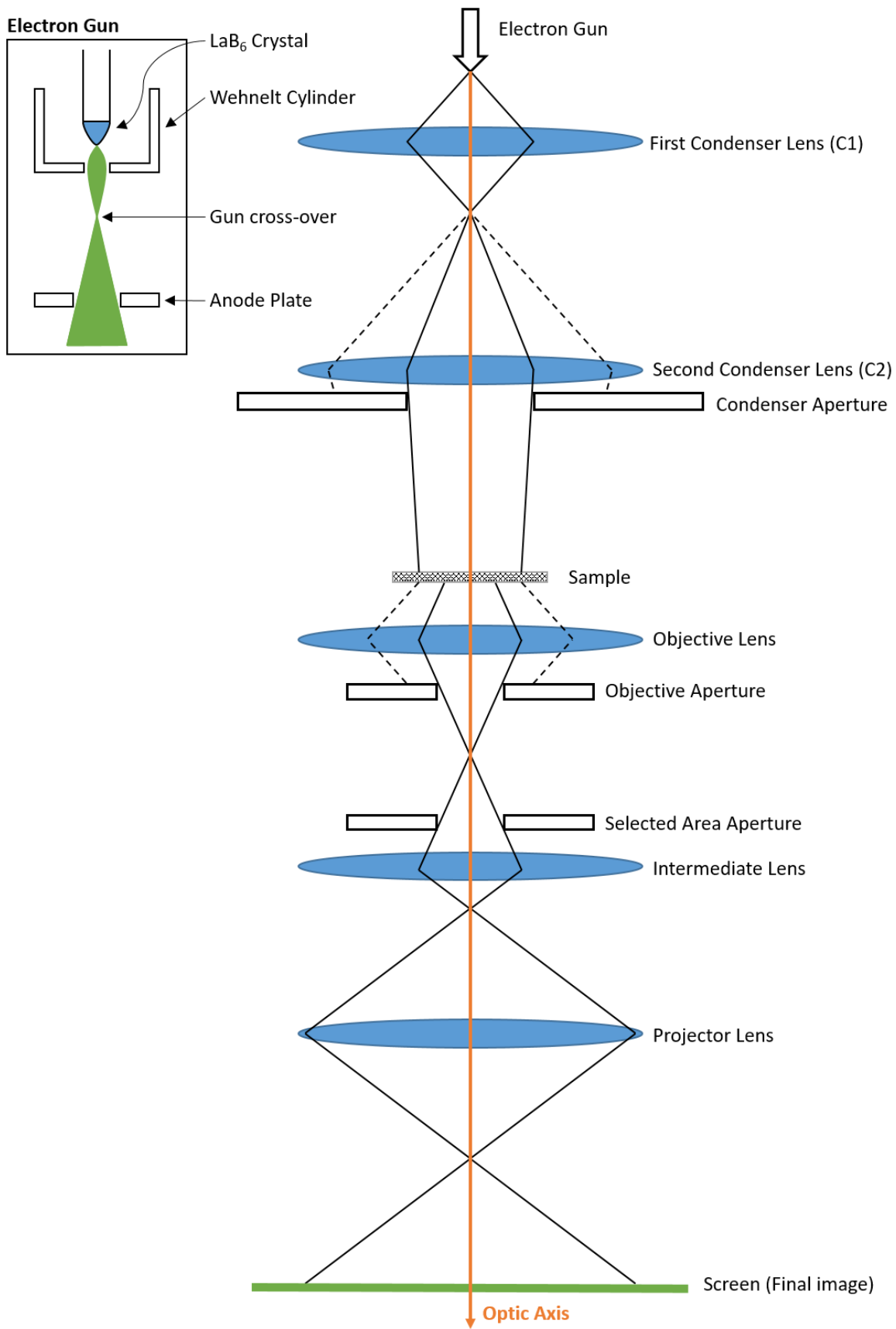
Figure 3.4 (Adapted from [189]): Simplified schematic showing the basic components of a conventional TEM. Schematic of an electron gun with a thermionic emission source inset top left.

The Hitachi H-9500 microscope used in this work, utilises a LaB$_6$ crystal electron source, where electrons are produced by thermionic emission as a result of ohmic heating. Within the electron gun, the LaB$_6$ source is housed in a Wehnelt cylinder, where it acts as the cathode, and the electrons produced are accelerated towards the earthed anode of the cylinder due to the difference in applied potential. This difference in applied potential is known as the accelerating voltage. A slight negative bias is applied to the Wehnelt cylinder; the resulting electric field focuses the accelerated electrons into a crossover, and directs them through a hole in the anode into the microscope itself. The electrons from the gun are transferred to the specimen by a series of condenser lenses (four in the case of the microscope used here) and an aperture. The first condenser lens (C1) creates a demagnified image of the gun-crossover; the strength of subsequent condenser lenses are adjusted to produce an under-focussed image of the C1 crossover at the plane of the specimen such that a "parallel beam" is incident on the specimen. The condenser aperture reduces the convergence angle of the electrons which reach the specimen, thereby producing a more parallel beam.

After passing through the sample, scattered beams of electrons are collected by the objective lens, and magnified by a series of intermediate lenses (3 in the case of the Hitachi H-9500) before being projected on the screen / detector by the final (projector) lens. The strength of the intermediate lenses can be adjusted in order to produce an image or a diffraction pattern, and control magnification. If the strength of the uppermost intermediate lens is adjusted such that its object plane coincides with the image plane of the objective lens, an image is produced on the screen / detector; if the strength of the intermediate lens is such that its object plane coincides with the back-focal plane (BFP) of the objective lens, a diffraction pattern is produced. Respectively, the objective and selected area apertures are used to limit the collection angle of scattered electrons exiting the specimen, and dictate the area from which a diffraction pattern is obtained.

The TEM micrographs featured in this work were taken exclusively in bright-field (BF) imaging mode. For the formation of BF TEM micrographs, the objective aperture (located at the BFP of the objective lens) is centred around the direct beam on the optic axis. In BF imaging mode, the contrast observed in TEM micrographs is generally dominated by amplitude contrast arising from:

(i) Mass / thickness contrast – Atoms of greater atomic number (Z) and/or thicker regions of the specimen inelastically scatter electrons to a greater extent than atoms of lower Z / thinner regions. Thus a larger number of electrons are scattered off-axis (and blocked by

57

the objective aperture) by higher Z / thicker regions of the specimen and as such these regions appear darker in a BF image.

(ii)   Diffraction contrast – Regions of the specimen which are oriented such that they diffract the incident beam away from the optic axis sufficiently for the diffracted beam to be blocked by the objective aperture appear darker in a BF image; this is because the electrons originating from the diffracting region of the specimen are intercepted by the objective aperture, and hence do not contribute to the final image.

Fresnel contrast, utilised extensively in this work according to the Fresnel contrast analysis method described in section 3.3.2, is a phase contrast effect arising as a result of an abrupt change of inner potential between a feature (such as an edge, void, bubble or cavity) and the matrix material. Interference patterns due to the difference in path length of spherical waves scattered from the edge of the feature with those that are scattered to a lesser extent (i.e. those passing through the void/cavity or the vacuum immediately beyond the edge of the specimen) results in the formation of fringes at the edges of the feature.

In this work, four sample types, two from the high porosity suite and two from the low porosity suite detailed in section 3.1.3, were selected for TEM experiments on the basis that:

(i)   Samples from different suites exhibited a significant difference in density (and hence by association the degree of porosity).

(ii)   Within their respective suite, samples exhibited comparable density and a significant difference in grain size.

Thus allowing the effects of porosity and grain size to be investigated in the following in-situ TEM experiments.

All TEM experiments were carried out at the University of Huddersfield MIAMI Facility [128] using a modified Hitachi H-9500 TEM equipped with a lanthanum hexaboride (LaB_6) electron gun, operated in bright field (BF) TEM mode at 300 kV. Beam current was recorded at 55 nA. Images and videos were captured by a Gatan OneView CMOS camera with resolution of 16 MPx.

TEM was initially used to characterise the microstructure of the selected Li_2TiO_3 ceramic samples on the nanoscale. In-situ electron irradiation experiments were used to investigate the formation and growth of electron beam induced cavities in Li_2TiO_3 samples with different microstructural properties

at room temperature. The effects of temperature and electron beam exposure time on the thermal evolution of electron beam induced cavities were investigated in in-situ thermal annealing experiments.

3.3.1 TEM sample preparation

To produce thin film specimens for use in TEM experiments, selected sintered pellets were sectioned into cubes (~ 2 mm^3) using a slow saw equipped with a diamond cutting disk. The resulting cubes of ceramic were mechanically thinned to a thickness of 60 µm ± 10 µm using silicon carbide grit paper (P1200 - P4000), the opposing faces were subsequently polished to a 1 µm finish using non-aqueous diamond suspension. A Gatan model 656 dimple grinder was utilised to achieve a final thickness of ~ 20 µm in a hemispherical region (polished to a 0.25 µm finish) in the centre of each sample. Samples were subsequently mounted to molybdenum TEM grids using Gatan G1 epoxy (cured at 80 °C, 1 h). Electron transparent regions were produced using a Precision Ion Polishing System (Gatan PIPS II - dual beam modulation, automatic gas flow rate); Ar$^+$ ion energy was gradually reduced (5 keV at 6°, 3 keV at 4°, 1 keV at 4°) during the ion milling process in order to minimise surface damage and contamination, and to produce a greater area of electron transparency.

3.3.2 Room temperature in-situ electron irradiation

In order to investigate the formation and growth of electron beam induced cavities in Li$_2$TiO$_3$ at room temperature, an area of selected thin-film specimens was exposed a 300 keV TEM electron beam and the exposure time (defined as the time elapsed while an area of specimen was exposed to the TEM electron beam) was recorded. Live video was captured during in-situ electron irradiation, and bright field TEM micrographs were taken at regular intervals. Fresnel contrast analysis was used to identify vacancy-type defects. In this technique, BF TEM micrographs are defocussed by ± 500 – 1000 nm in order to observe the appearance and change in intensity distribution of Fresnel fringes which form around vacancy-type defects such as small voids, cavities, vacancy clusters or gas bubbles. In under-focus images, vacancy-type defects appear bright with a dark fringe, while in over-focus images they appear dark with a bright fringe. Small (< 5 nm) vacancy-type defects are invisible when the TEM image is in focus; thus the observation of a change in Fresnel contrast when the objective lens is defocussed also allows a distinction to be made between vacancy-type defects and secondary phase precipitates as the contrast associated with precipitates does not vary in this way, and often remains the same irrespective of focus. In this work, bright field through-focal-series micrographs (± 500 nm

objective lens defocus) were taken at 10 minute intervals of beam exposure to monitor the formation and evolution of TEM resolvable vacancy-type defects. Condenser lens settings were altered according to the optimal conditions for imaging each individual specimen, as such it was not possible to consistently monitor electron fluence; this has been taken into consideration when discussing the effects of electron beam exposure on Li_2TiO_3.

3.3.3 In-situ thermal annealing of Li_2TiO_3 under electron irradiation

In order to investigate the effects of temperature on the thermal evolution of electron beam induced cavities in Li_2TiO_3, a thin film specimen was initially thermally annealed in-situ under constant electron irradiation by a 300 keV TEM electron beam. Using a Gatan Model 652 double-tilt heating holder equipped with a water-fed cooling system, the specimen was heated from 30 °C to 1000 °C in 100 °C increments; a 10 min dwell was incorporated into the heating program at each incremental temperature. Live video was captured throughout the annealing process under constant electron irradiation, bright field through-focal series micrographs (± 500 nm objective lens defocus) were taken at the end of the dwell time at each incremental temperature.

In order to investigate the effects of minimising electron beam exposure time (and thus reduced electron fluence) on the thermal evolution of electron beam induced cavities in Li_2TiO_3, the experiment described immediately above was repeated with the gun valve closed (i.e. the electron beam was effectively "switched off") during the dwell time at each incremental temperature. The same heating program as that specified above was adopted (30 °C – 1000 °C, 100 °C increments, 10 min dwell / temperature increment). The gun valve was only briefly opened at the end of the dwell time associated with each temperature increment in order to capture bright field through-focal-series micrographs, thereby minimising electron beam exposure time as much as reasonably possible. The electron beam exposure time corresponding to through focal-series micrographs captured at each incremental temperature was recorded.

In order to investigate the effects of ceramic microstructure and processing conditions on the formation and thermal evolution of electron beam induced cavities in Li_2TiO_3, subsequent analogous experiments were conducted on selected Li_2TiO_3 samples with different microstructural properties (produced according to the procedure detailed in section 3.1.3). The previously described method for minimising electron beam exposure time was adopted throughout; the electron beam exposure

time corresponding to through focal-series micrographs captured at each incremental temperature was recorded in each case.

3.3.4 In-situ helium ion implantation and thermal annealing

In-situ helium ion implantation was used to investigate the accumulation of helium in Li_2TiO_3 ceramics with different microstructural properties at room temperature. Subsequent in-situ annealing experiments were used to investigate the thermal evolution of helium bubbles, and the effect of the interaction of electron beam induced defects with implanted helium on the thermal evolution of cavities / helium bubbles.

To simulate the production of helium in Li_2TiO_3 as a result of lithium transmutation following neutron capture, thin film specimens were implanted with helium ions in-situ in a TEM using the MIAMI-II system [128] at the University of Huddersfield MIAMI Facility.
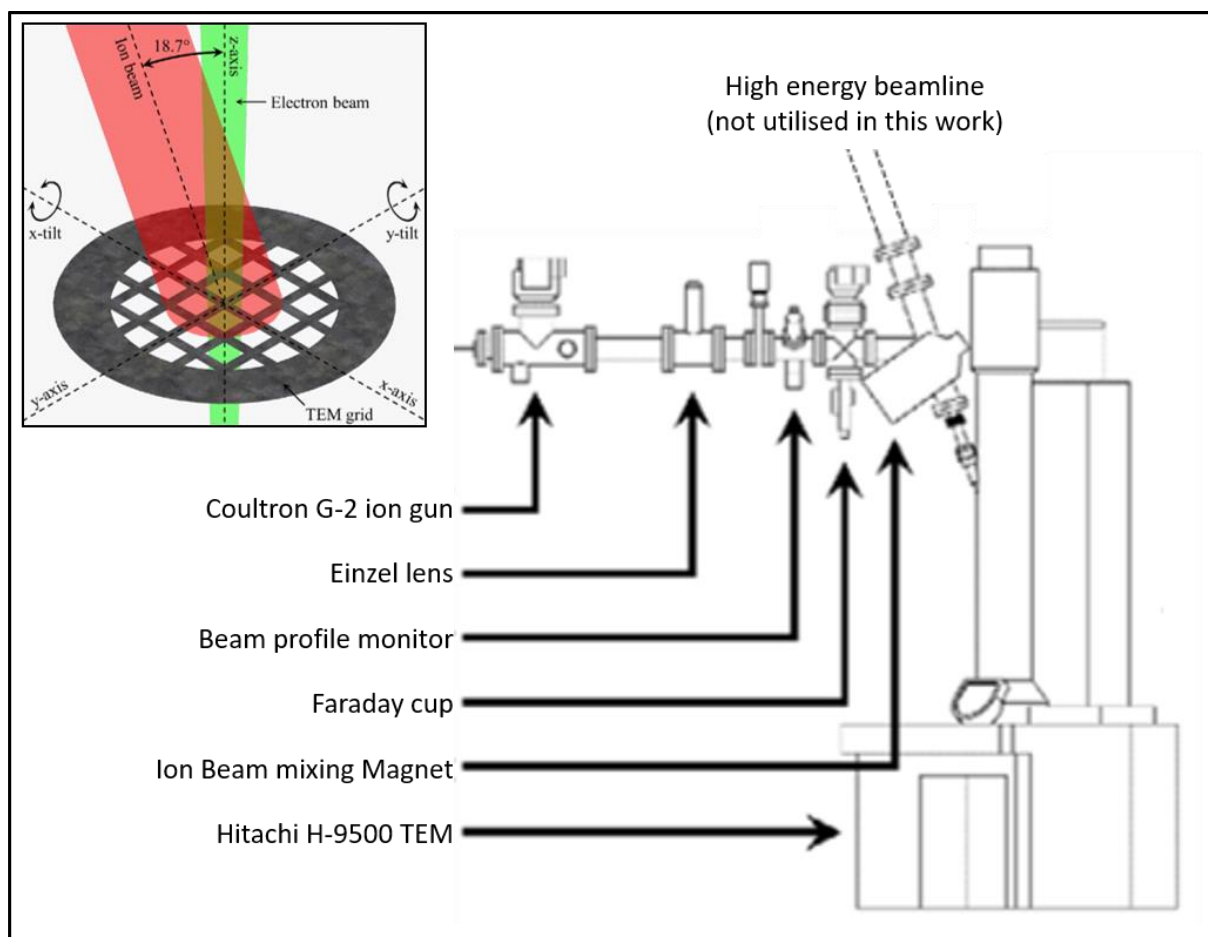
Figure 3.5 (Adapted from [128]): Schematic of the layout low energy beamline of the MIAMI – II system. Inset top left shows the geometry of the incident ion beam relative to the TEM electron beam and the axes of the goniometer / sample holder.

Figure 3.5 shows a schematic of the layout of the low energy (≤ 20 kV) beamline of the MIAMI-II system utilised in this study; the system is also equipped with a medium energy (≤ 350 kV) beamline which was not used here. The low energy beamline utilises a Coultron G-2 ion gun to produce high ion currents from light gaseous species. The helium ion energy utilised in this work was tuned according to the results of SRIM [132] simulations such that the majority of helium was deposited within the thin film specimens, and peak helium concentration coincided approximately with the centre of each specimen. The thickness of electron transparent regions of the specimen was estimated to be ~100 nm. In order to investigate the effects of ceramic microstructure and processing conditions on helium accumulation in Li_2TiO_3, selected thin film specimens with different microstructural properties (produced according to the procedure detailed in section 3.1.3) were implanted in-situ with 5.5 keV He^+ ions. Implantation was carried out at room temperature using a He^+ ion fluence of approximately 4×10^{13} ions cm^{-2} s^{-1}. Specimens were implanted in 10 min 15 s intervals (such that each interval corresponded to a fluence of ~2.5×10^{16} ions cm^2), to a total fluence of 1×10^{17} ions cm^2. In order to circumvent any synergistic effects between the electron and ion beams during implantation, the electron beam was not incident on the sample during implantation. Bright field through-focal-series micrographs were captured at each fluence interval. The electron beam exposure time associated with the acquisition of micrographs at each interval, which was minimised as far and reasonably possible, was recorded.

In order to investigate the thermal evolution behaviour of implanted helium in Li_2TiO_3 with different microstructural properties, and the interactions of helium with electron beam induced defects, the helium implanted specimens were subsequently annealed in-situ using the same temperature profile as was detailed in section 3.3.3 above (30 °C – 1000 °C, 100 °C increments, 10 min dwell / temperature increment). Bright field through-focal-series micrographs were captured at the end of the dwell time at each incremental temperature. Electron beam exposure time was minimised throughout according to the procedure detailed in section 3.3.3; the electron beam exposure time corresponding to through focal-series micrographs captured at each incremental temperature was recorded in each case. At the end of each experiment, areas of the specimen which had not been previously exposed to the electron beam were examined in order to independently determine the behaviour of implanted helium at elevated temperatures in the absence of electron beam induced damage; thus

enabling the effects the interactions of electron beam induced defects with implanted helium on the thermal evolution of cavities / helium bubbles in Li_2TiO_3 to be evaluated.

3.3.5 Image analysis

After acquisition, image processing was performed using the image editing software ImageJ [188]. A bandpass filter (3-50 pixels) was applied to each 4K image (horizontal resolution ≈ 4080 pixels) to suppress features of low spatial resolution, and the contrast adjusted to enhance features of interest. Processed under- and over-focus micrographs corresponding to each through-focus-series were subsequently aligned and stacked.

As detailed in section 3.3.2, vacancy-type defects (used here to describe voids, cavities or gas bubbles) appear bright with a dark fringe in under-focus micrographs, and dark with a bright fringe in over-focus images due to Fresnel contrast. Vacancy-type defects were considered resolvable only if the fringes associated therewith could be observed in both under- and over-focus micrographs after processing.

The number density of vacancy-type defects was calculated by taking the mean average of the number of resolvable defects observed in three different regions of equal area (25 x 25 nm or 50 x 50 nm depending on defect size), associated errors are quoted as ± half of the range of the values obtained over three areas. Vacancy-type defect size was determined using the "Intensity Profile" and "Multi Plot" tools incorporated into the software package ImageJ [188] in conjunction with a purpose-built Excel spreadsheet. Greyscale intensity profiles of linescans across the longest available dimension of individual vacancy-type defects with well resolved fringes on opposing edges were obtained using the line intensity profile and multi plot tools in ImageJ [188]. The distance between fringes was extracted from intensity profiles in a semi-automated fashion using a purpose-built Excel spreadsheet which yields: (i) individual cavity diameters (taken as the average distance between fringes of the same cavity measured in equivalent under- and over-focus images), (ii) the mean average cavity diameter (calculated from the extracted diameter of 50 cavities), (iii) Estimated errors in the form of the ESD and the standard error of the mean, and (iv) a population distribution of the measured cavities according to size in graphical format.

Values of defect size reported here are given as the mean average value calculated from the extracted diameter of 50 cavities; associated errors are quoted as the standard error of the mean. Examples of the graphical outputs obtained from the purpose-built Excel spreadsheet are shown in Figure 3.6.
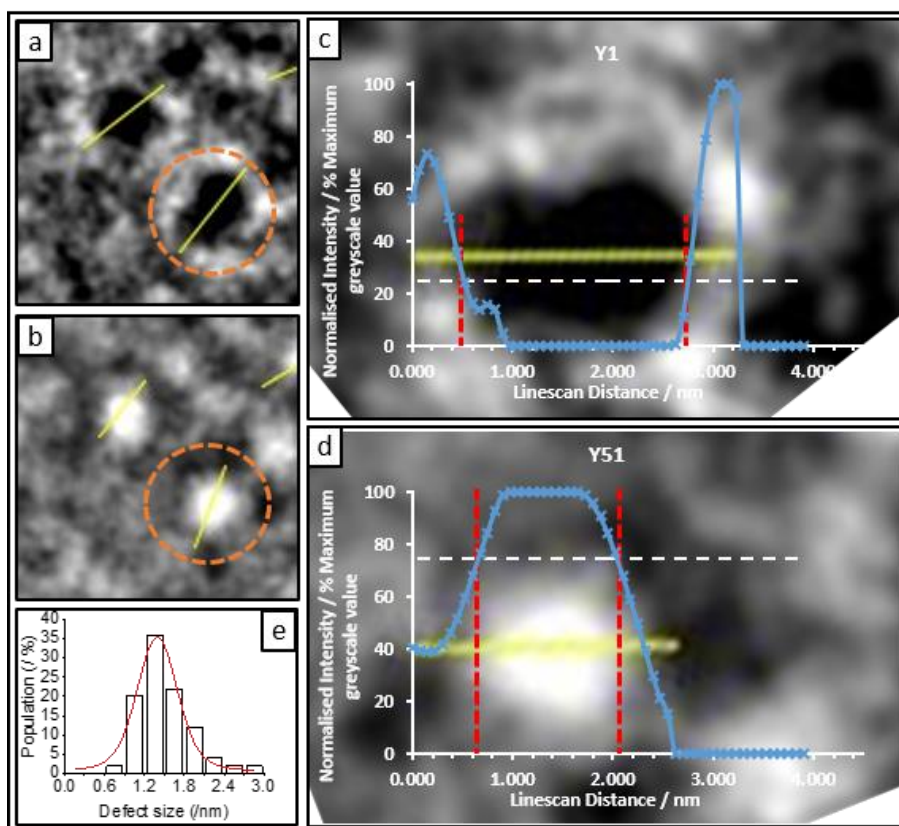
Figure 3.6: Example of semi-automated measurement of defects in (a) over- and (b) under-focus micrographs, and the respective graphical outputs (c and d) obtained from Excel defect size measurement spreadsheet (superimposed over corresponding BF TEM micrographs). (e) Example histogram of defect size distribution constructed using output generated from Excel defect size measurement spreadsheet; fitted distribution curve added using OriginPro [190].

An outline of the process by which feature sizes (in this case cavity diameters) are extracted from raw greyscale intensity profile data exported from ImageJ by the purpose-built spreadsheet is detailed below. Note that the spreadsheet is designed such that the only input required from the user is to paste the data (in the default .csv format from ImageJ) into a master sheet, and select an appropriate threshold intensity; all outputs are automated. This is a novel process, developed during this PhD and is therefore described in detail below. The spreadsheet will be made publically available via the publication presented in Chapter 5:

1. Greyscale intensity values for each linescan are automatically normalised to their respective maximum.

2. Individual graphical representations of each linescan (Linescan Distance vs. Normalised Intensity) are automatically plotted. On each graph a horizontal "threshold" line, and corresponding vertical intersects at the maximum and minimum intersection points of intensity data with the threshold line is automatically generated. This provides the user with a visual representation of how the measurement is being extracted, thus the cause of any errors in output values can be easily identified.

3. The (%) intensity value at which the threshold line intersects the Y axis is adjusted (by the user) to an appropriate value such that the corresponding vertical intersects are representative of the position of the opposing edges of the fringes of the features of interest. The horizontal threshold and corresponding vertical intersect lines displayed on all graphs are simultaneously updated automatically with the input of the desired intensity threshold percentage into a single cell by the user.

4. The lesser of the two linescan distance values corresponding to the vertical intersects on each graph is automatically subtracted from the greater to yield the distance between fringes and thus the diameter of the feature across which each linescan was drawn. The diameter of each feature is output and automatically transposed to a table in the form of a list.

5. The mean diameter of the same feature in under- and over-focus images is automatically calculated to give a final value of diameter for each individual feature, and added to the table.

6. The mean average defect diameter of the population, an ESD, and the standard error of the mean are automatically calculated from the final values of diameter measured from 50 defects. The diameter distribution is automatically displayed in the form of a customisable histogram.

A copy of this spreadsheet *al*ong with a user guide can be found in supplementary file 1a.

3.3.6 Thermal Desorption Spectroscopy (TDS)

TDS was used to investigate the release characteristics of gaseous species from Li_2TiO_3 samples with different microstructural properties as a function of temperature. All TDS experiments were carried out at the UK Atomic Energy Authority Materials Research Facility, located at the Culham Centre for Fusion Energy. The TDS system employed was a TPD Workstation type 640100 manufactured by Hiden Analytical, shown in Figure 3.7; the system is equipped with a Hiden Analytical HAL/3F RC 1051-9 PIC quadrupole mass spectrometer (MS).
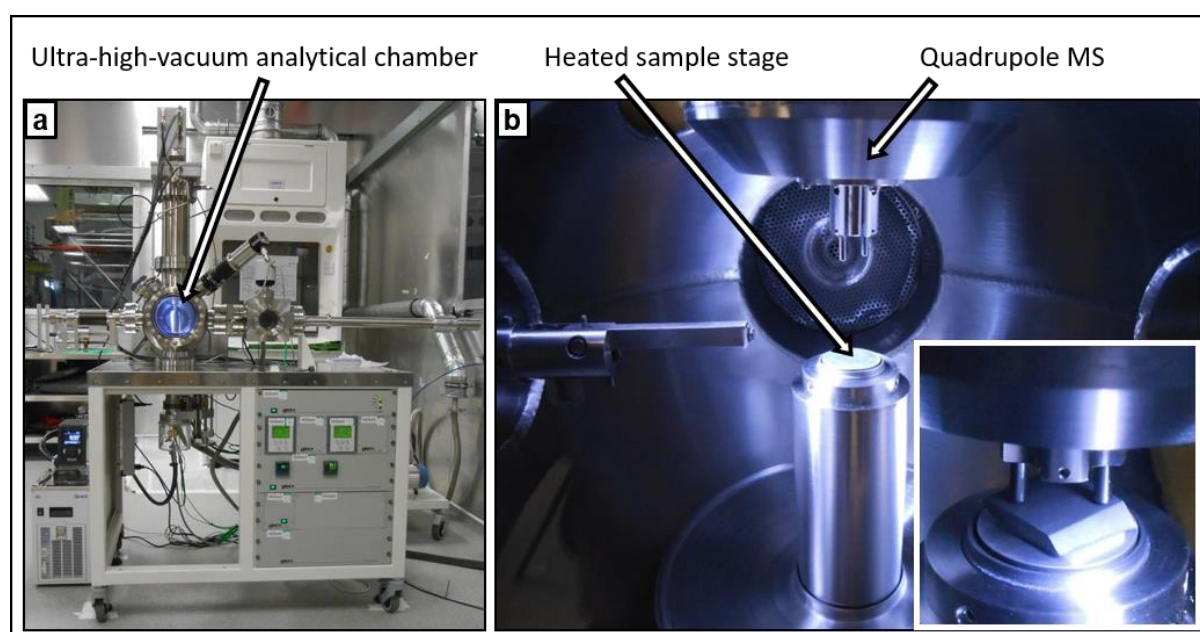
Figure 3.7: (Adapted from [191, 192]): (a) Photograph showing the layout of the TDS system utilised in this work (Hiden Analytical Workstation type 640100). (b) Photograph of the Internal layout of the UHV analytical chamber showing the position of the MS relative to the heated sample stage; inset shows an example of the configuration of the sample, stage and MS during operation.

In this TDS system, the main analytical chamber is under ultra-high vacuum (UHV) during data collection. The sample is heated from below by the ohmically heated sample stage, the temperature of which is controlled by an embedded thermocouple. Gaseous species evolved from the sample during the heating programme are recorded by a quadruple MS positioned directly above the sample, in line of sight of the sample surface. Upon entering the MS, the desorbed gaseous species are initially positively ionised by electron bombardment, and subsequently extracted to the quadrupole mass analyser by a set of electrostatic lenses which accelerate and focus the gas ions.
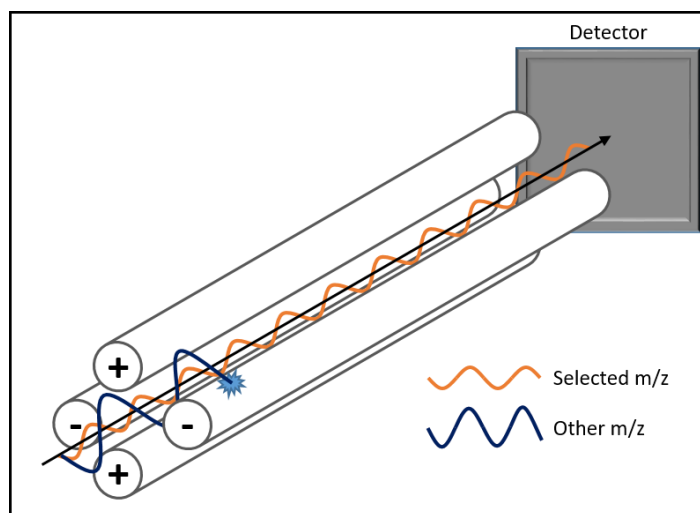
Figure 3.8: Schematic representation of a quadrupole mass analyser.

The quadrupole mass analyser itself (depicted in Figure 3.8) consists of four parallel rods where opposite rods are electrically connected. A voltage of opposite polarity, consisting of both direct current (DC) and radio frequency (RF) components, is applied to adjacent rods. The electric field produced by the biased rods causes the ions to oscillate as they travel through the central region between the rods, the amplitude of these oscillations is dependent on the mass to charge ratio of the ion (m/z). If the oscillations become too large or unstable, the ion will strike the rods and become neutralised, as such only ions within a very narrow range of m/z will traverse the rods and reach the detector; hence the ions which enter the MS are separated according to the mass to charge ratio. Incrementally scanning through the voltage applied to the rods allows ions with sequentially larger values of m/z to pass through the rods to the detector.

In this work, sintered pellets were individually loaded into the TDS system and manipulated onto the sample stage in the main chamber. An aluminium nitride ceramic plate was placed between the sample and the stage itself to prevent contamination/reaction with the stage.

Each sample was heated by the sample stage under ultra-high vacuum ($1.8 \times 10^{-9} \pm 0.5 \times 10^{-9}$ Torr when heating was initiated) from room temperature to 900 °C using a heating rate of 5°C min^{-1}; a 30 minute dwell was incorporated into the heating programme at the maximum temperature. The vacuum pump was running throughout each experiment, the maximum pressure reached within the main chamber, which increases during the heating programme due to outgassing of gaseous species from the sample, was ~ 5×10^{-6} Torr. The release profiles of desorbed gaseous species of masses 1-50 amu were recorded by the MS as a function of the stage temperature.

3.4 Potential bias in the measurement of grain, cavity and bubble size

Line-based measurements are commonly used to measure the size and distribution of microstructural features such as grain size from two dimensional (2D) micrographs. Lineal intercept methods, such as those described in the ASTM E112 standard for metallic materials [193], have been devised to streamline the process of manually measuring average grain size based on linear intercepts with line segments. In these methods, a line is superimposed over a 2D micrograph, and the average grain size is calculated from the known length of the superimposed line and the number of intercepts between the line and grain boundaries. However, it is recognised that measurements take from 2D images are inherently biased towards underestimating the dimensions of 3D features since the imaged surface is an indiscriminate cross-section through 3D volume. As such, the probability of this cross-section coinciding with the longest dimension of a randomly oriented three-dimensional particle is small; thus the actual measurement often corresponds to a dimension which is shorter than the longest dimension of the particle. Correction factors such as those calculated by Mendelson [194] (recently corrected by Gerlt [195]), where grains are modelled as tetrakaidecahedral in morphology with log-normal size distribution, and grain size is interpreted as the mean perpendicular distance between two parallel tangent planes averaged over all orientations, can be used to take account for this experimental artefact. However, as pointed out by Wurst [196], these corrections are based on a fully dense microstructure consisting of equiaxed grains. Hence, in light of the significant degree of porosity exhibited by the Li_2TiO_3 ceramics studied in this work, it was concluded that the use of conventional lineal intercept methods for the measurement of grain size would not be appropriate here. Instead, a variation of a lineal intercept method was used in which well-defined, individual grains were manually selected and linear measurements were taken along the longest available dimension on the basis that grain morphology was not typically significantly anisotropic. While this method had the potential to introduce bias due to the somewhat subjective nature of defining the longest dimension and the precise position of grain boundaries, it allowed the measurement of only well-defined grains while simultaneously counteracting the inherent bias of 2D measurement to underestimate 3D grain size to some degree.

A similar method, as described in section 3.3.5, was used to measure cavity and bubble sizes in electron irradiated and / or helium implanted Li_2TiO_3 ceramics using the longest available linear dimension of manually selected features. While this method had the potential to introduce similar biases as those discussed above with respect to grain size, as well as the potential to overestimate

cavity and bubble sizes where larger, more anisotropic features were concerned, this method allowed the measurement of only well-resolved features; thereby reducing the uncertainty arising from overlapping features or lack of resolution in regions of poor contrast which would otherwise have been included if a conventional lineal intersect methodology had been adopted.

Measurement of each grain, cavity or bubble across multiple dimensions would have afforded a greater degree of accuracy and reduced the extent of any overestimation of the size of anisotropic features, but this was deemed overly labour intensive given the number of samples / conditions studied and the number of measurements involved. It is recognised that the accuracy of the absolute values quoted with respect to grain, cavity and bubble size in this work may not, quantitatively speaking, be an exact representation of the features from which the measurements were obtained, and are likely to be underestimates of the true values where approximately equiaxed features are concerned, and potentially overestimates where anisotropic features are concerned. Nonetheless, the methods employed for the measurement of grain, cavity and bubble size throughout this work were deemed sufficiently consistent to make valid comparison between the results obtained from the samples studied.

Chapter 4 - Pristine characterisation and microstructure manipulation

In this chapter, the results of solid state synthesis experiments and the characterisation of Li_2TiO_3 powder are presented. The effect of post-synthesis sintering conditions on the microstructure of the resulting ceramic pellets is discussed.

4.1 Solid state synthesis and characterisation of Li_2TiO_3 powder

Li_2TiO_3 was synthesised from Li_2CO_3 and TiO_2 as detailed in section 3.1.1 according to the reaction:

$$Li_2CO_{3\,(s)} + TiO_{2\,(s)} \quad \rightarrow \quad Li_2TiO_{3\,(s)} + CO_{2\,(g)}$$
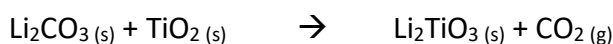
In order to identify a suitable calcination temperature for the preparation of Li_2TiO_3 powder, Thermogravimetric Analysis (TGA) was carried out on the milled reagent powder mixture prepared according to the procedure described in section 3.1.2. The results of this study are shown in Figure 4.1. It is noted that mass loss associated with CO_2 evolution begins to occur at ~470 °C, well below the decomposition temperature of pure lithium carbonate in the absence of contacting TiO_2 particles (reported to commence at ~740 °C by Mandal *et al.* [82]). As proposed by Sonak *et al.* [84], this may indicate that the decomposition of Li_2CO_3, and subsequent reaction of the resulting Li_2O with TiO_2 to form Li_2TiO_3, may be catalysed at the surface of TiO_2 particles.
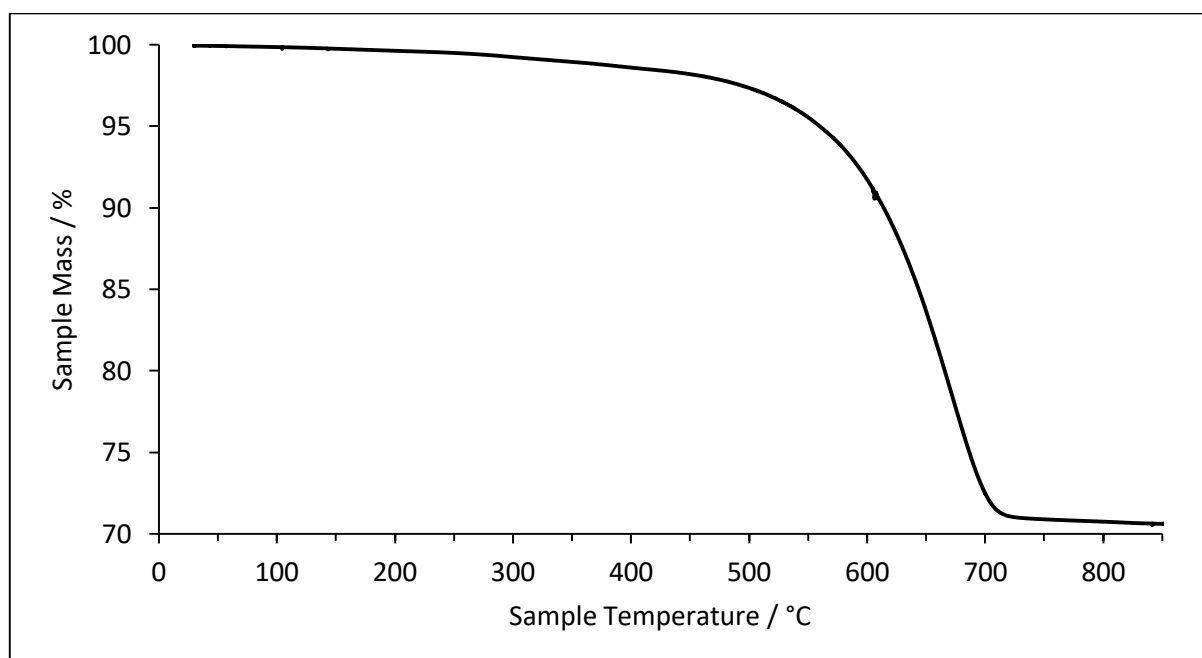
Figure 4.1: TGA data collected from milled Li_2CO_3 / TiO_2 reagent powder mixture under flowing air. Data collected using a Perkin Elmer TGA4000 thermogravimetric analyser over a temperature range of 30 – 855 °C; heating rate 10 °C min^{-1}.

No further significant mass loss associated with CO_2 evolution is observed above 730°C; as such it can be concluded that the reaction is complete at this temperature. Hence a maximum temperature of 730°C was defined for batch reagent powder calcination in order to minimise lithium vapourisation and maintain small particle size in the Li_2TiO_3 product.

A powder X-ray diffraction (PXRD) pattern obtained from the powder prepared according to the procedure detailed in section 3.1.1 (using a maximum calcination temperature of 730 °C according to the TGA results) is shown in Figure 4.2. Phase analysis carried out using the ICDD database in conjunction with Bruker Diffrac Eva 3.1 software showed that the pattern indexed well to the monoclinic β-Li_2TiO_3 structure reported by Kataoka *et al.* [61]. Only peaks consistent with this structure were observed, confirming that the powder obtained was single phase β-Li_2TiO_3. Miller indices were assigned according to the corresponding ICDD Powder Diffraction File (ICDD PDF no. 01-077-8280).
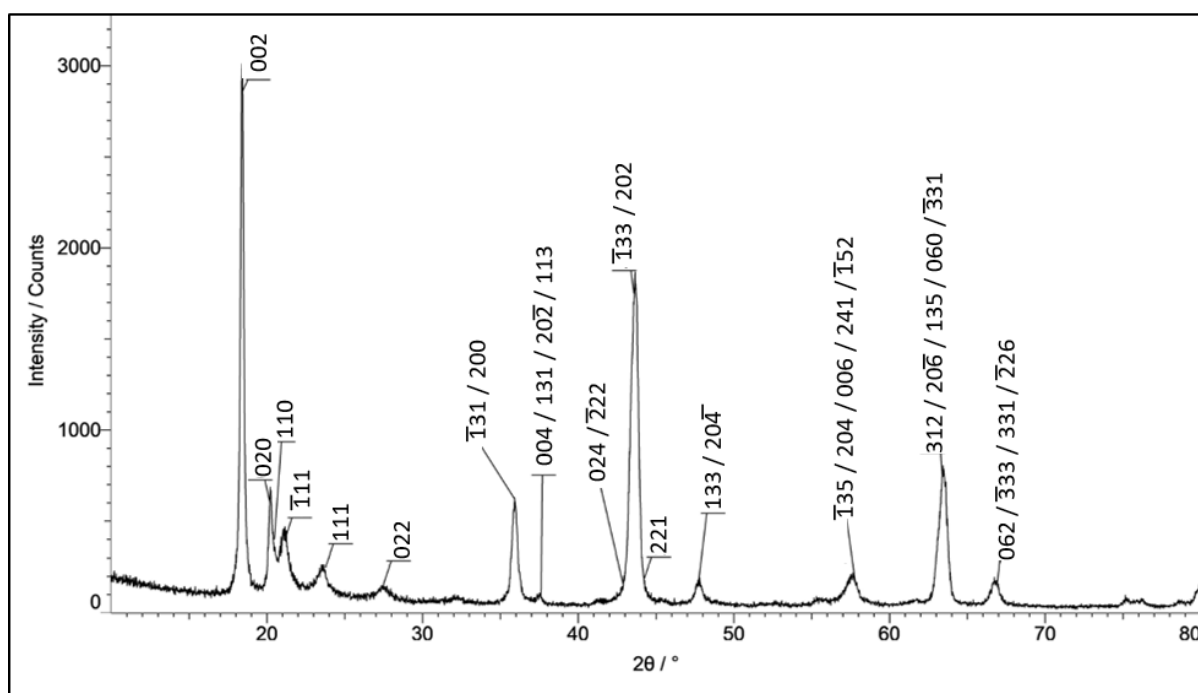
Figure 4.2: Powder XRD pattern obtained from Li_2TiO_3 powder prepared by solid state synthesis. Data collected using a Bruker D2 Phaser diffractometer using Cu K_α radiation; 10-80° 2θ, 0.02° step, 0.2 s / point. Indexed according to ICDD PDF no. 01-077-8280 [61]. *Some hkl labels omitted for clarity.

Figure 4.3 shows secondary electron SEM micrographs of the milled Li_2TiO_3 powder from which sintered pellets were fabricated in subsequent ceramic processing experiments. The rounded powder particles generally exhibit relatively spherical (as opposed to angular) morphology and low aspect

71

ratio; the powder agglomerates observed in SEM micrographs were found to be composed of particles estimated to be in the range of 0.2-1.5 µm in size, with a typical particle size of approximately 0.5 µm.
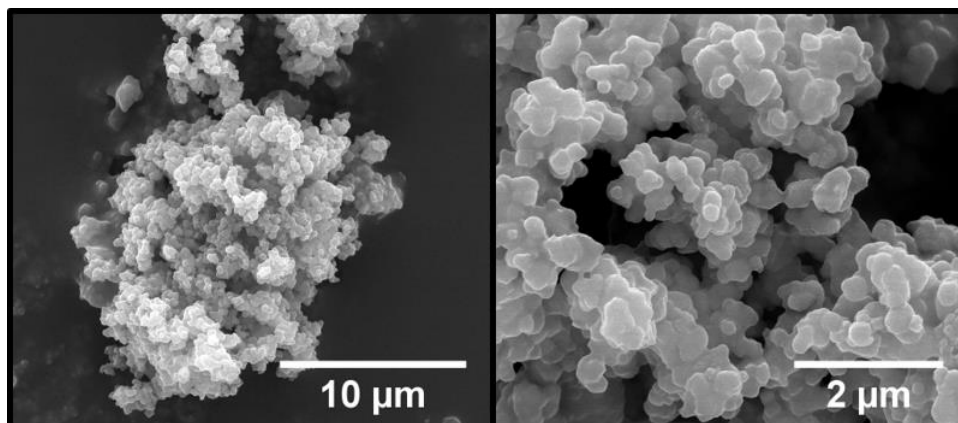
Figure 4.3: Secondary Electron SEM micrographs, captured using an FEI Inspect F50 electron microscope operated at 20 kV, showing the particle size and morphology of milled Li_2TiO_3 ceramic powder prepared by solid state synthesis.

The small crystallite size associated with sub-micron particle size is likely to be a contributing factor to the relatively broad peak profiles observed in the PXRD pattern, which is in turn responsible for the lack of resolution where peaks corresponding to crystal planes of similar *d*-spacing are concerned. As such, many of the peaks observed in the diffraction pattern shown in Figure 4.2 represent a convolution of the contributions of X-rays diffracted at several different crystal planes of similar *d*-spacing.

The Li_2TiO_3 powder described above was used to form the green bodies for use in subsequent sintering experiments, the results of which are discussed in the following section.

4.2 Densification and microstructure manipulation

Maximising the bulk density of ceramic breeder materials is considered desirable as the overall lithium atom density will be greater in a dense ceramic than a porous equivalent; hence the probability of fusion neutrons interacting with lithium atoms in the breeder blanket will be increased in a dense ceramic, which in turn increases tritium breeding ratio (TBR). However, the reduction in surface area and open porosity associated with densification may have a detrimental effect on tritium transport and release characteristics [197]. Furthermore, ceramic microstructure could have significant effects on radiation damage resistance and helium accommodation mechanisms of

ceramic breeder materials. Hence, the effects of ceramic processing conditions on ceramic density and grain size in Li_2TiO_3 were investigated and subsequently tailored in order to produce two suites of samples – of high and low porosity respectively – which exhibited different grain sizes in order to independently identify the effects of ceramic density and grain size on material performance in subsequent electron irradiation and ion-implantation experiments. The results below show the effects of sintering green bodies at different temperatures (between 750 and 1150 °C) for different durations (between 2 and 9 hours), carried out to determine appropriate sintering conditions to produce the two suites of samples required for the implantation / irradiation experiments.

Figure 4.4 shows the measured density of Li_2TiO_3 ceramic pellets sintered for 6 hours under atmospheric air at incrementally increasing temperature. Data points shown are the mean average value of the absolute measured densities obtained from two pellets prepared under identical conditions, error bars were calculated according to Eqn. (3.3) as detailed in section 3.2.3.
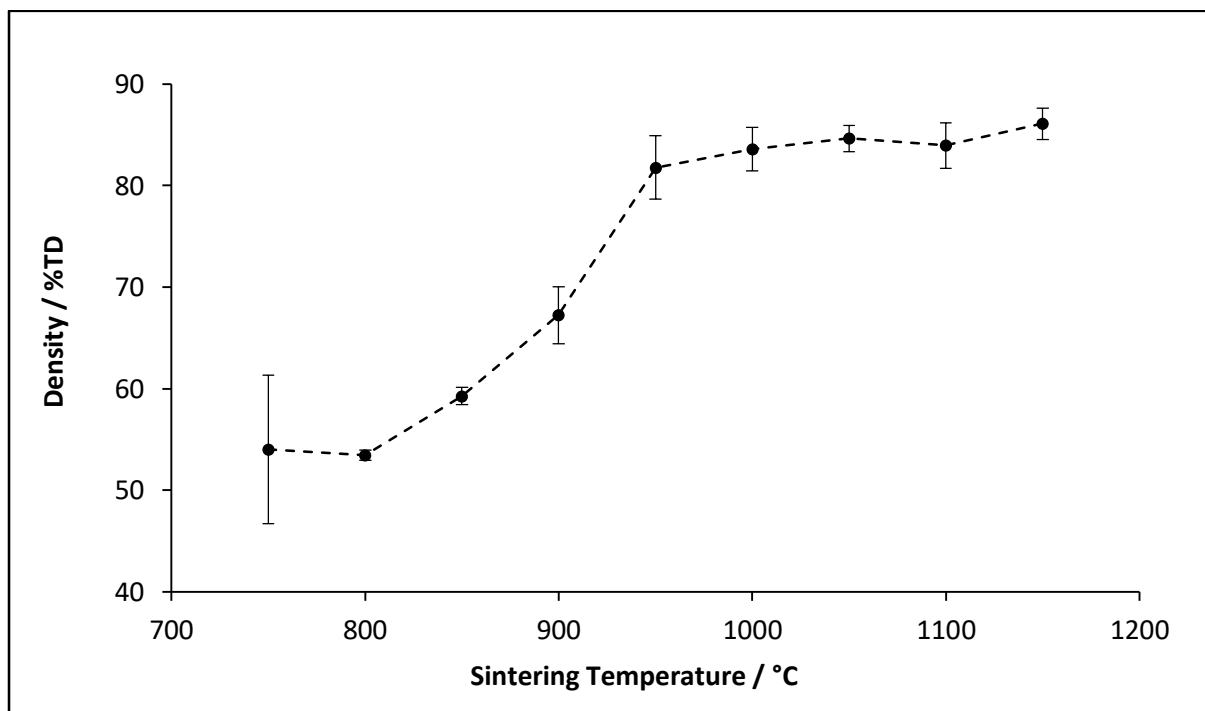
Figure 4.4: Measured density of Li_2TiO_3 ceramic pellets sintered under atmospheric air for 6 hours duration at incrementally increasing temperature.

The densification behaviour of Li_2TiO_3 was shown to be strongly dependent on sintering temperature. A significant increase in densification efficiency was observed between 800 °C and 950 °C, clearly indicating an increase in the rate of the thermally activated atomic diffusion processes responsible for densification in this temperature range. At temperatures in excess of 950 °C, the observed

increase in density with temperature was markedly reduced; the density of pellets sintered between 1000 °C and 1150 °C became effectively constant within the error associated with density measurement. Hence, sintering temperatures of 900 °C and 1000 - 1100 °C were subsequently employed to produce suites of Li_2TiO_3 ceramics which exhibited "high" and "low" porosity respectively.

Secondary electron SEM micrographs showing the microstructure of the polished surfaces of Li_2TiO_3 ceramic pellets, sintered at 900 – 1100 °C for various durations in order to produce samples with different grain sizes, are shown in Figure 4.5. In agreement with the results of the preceding sintering temperature study, it was visually apparent from SEM micrographs that the porosity of samples sintered at 1000 °C and above was markedly reduced compared to those sintered at 900 °C; thus confirming the strong dependence of densification efficiency on temperature.
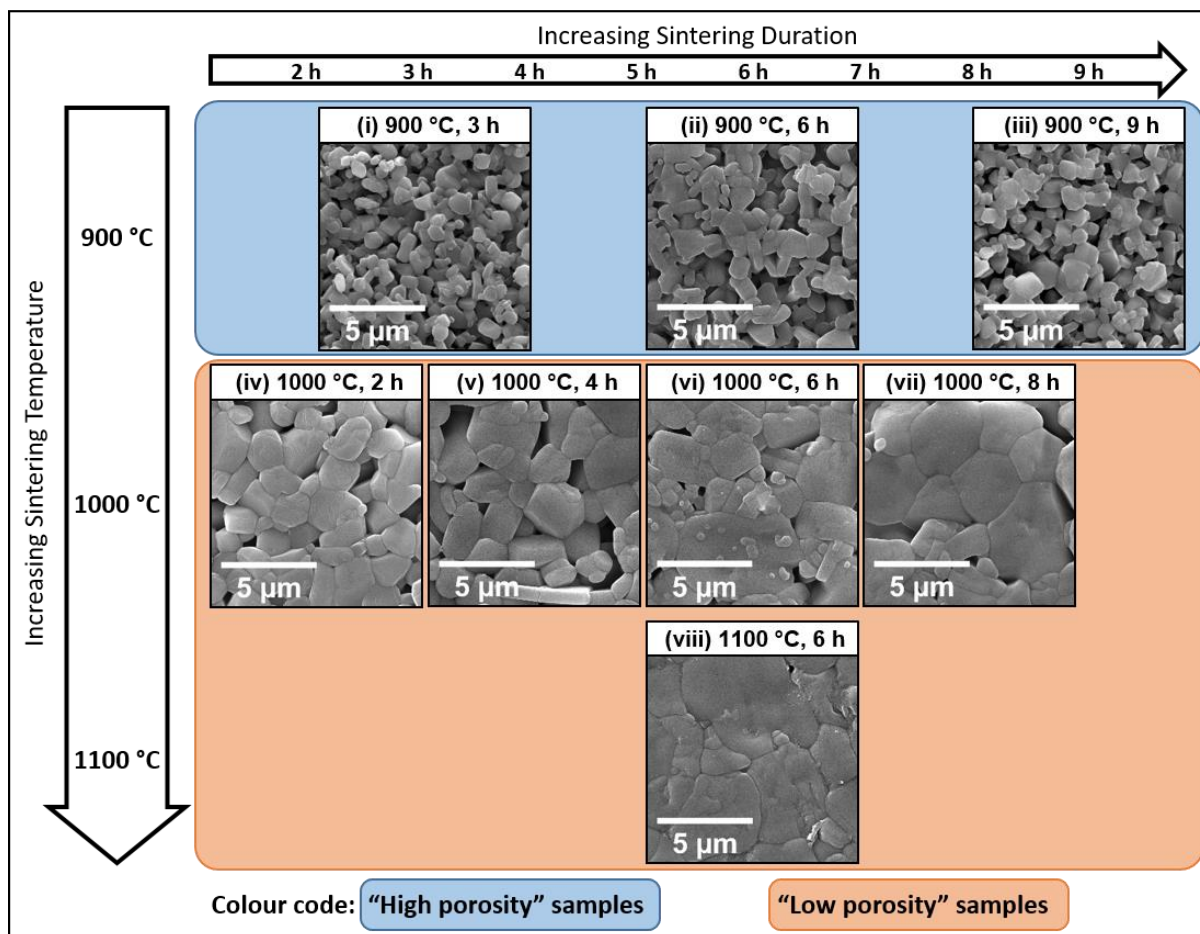
Figure 4.5: Secondary Electron SEM micrographs showing the polished and thermally etched surfaces of Li_2TiO_3 ceramic pellets sintered 900 – 1100 °C for various durations (2 – 9 hours), captured using an FEI Inspect F50 electron microscope operated at 20 kV. "High porosity" samples shown on blue background (top row), "low porosity" samples shown on orange background (lower two rows).

On the basis of visual inspection, the effect of sintering duration on densification at constant temperature appeared to be minimal, although a slight reduction in the porosity of samples sintered at 1000 °C may be evident at longer sintering durations. Grain growth was also shown to be more strongly dependant on temperature than sintering duration under the conditions studied; significant non-uniform grain growth was observed with increasing sintering temperature (see Figure 4.5 (ii), (vi) and (viii) for example). Grain morphology initially became more angular during densification and grain growth, presumably due to the reduction in surface energy associated with reducing the average surface curvature of the rounded powder particles and maximising the contacting surfaces of adjacent particles. As densification and grain growth progressed, grain boundaries were found to become less angular which is proposed to be due to the reduction of interfacial energy associated with grain boundaries of lower angle. While it is apparent that the effect of sintering duration on the extent of grain growth was comparably lesser than that of temperature, a subtle increase in grain size was generally observed with increasing sintering duration at a given temperature; thus a broad range of grain sizes was produced across the two suites of samples. The non-uniformity of the observed grain growth resulted in a concurrent widening of grain size distributions as shown in Figure 4.6, which shows the grain size distributions obtained from each sample shown in Figure 4.5 based on measurement of the longest dimension of 450 grains per sample observed in 2D secondary electron SEM micrographs. Quoted errors associated with the mean average grain size are equal to one ESD.
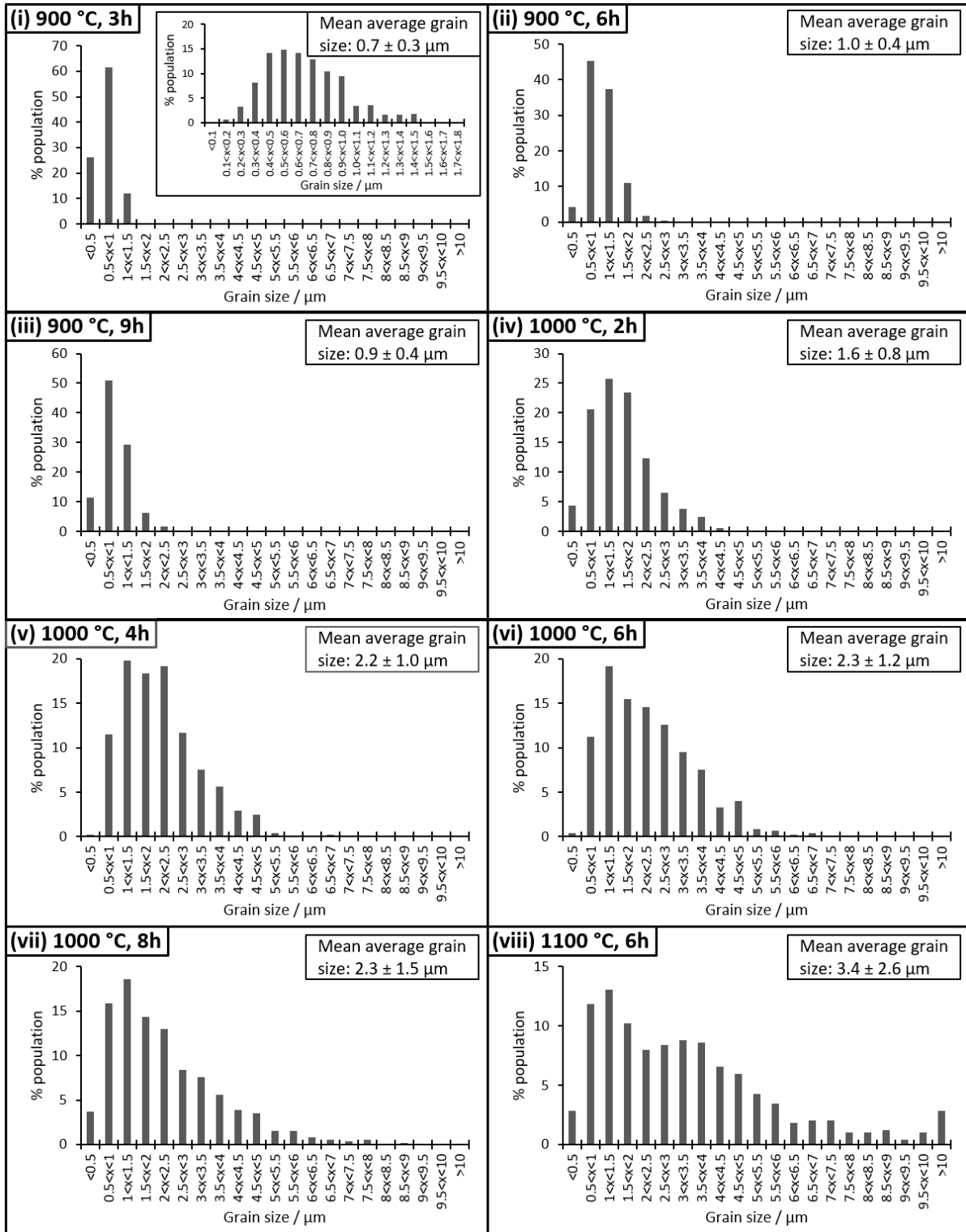
Figure 4.6: Grain size distributions of Li₂TiO₃ ceramic pellets sintered at 900 – 1100 °C for various durations (2 – 9 hours). Statistics shown are based on measurement of the longest dimension of 450 grains per sample observed in 2D secondary electron SEM micrographs. Quoted errors associated with the mean average grain size are equal to one ESD. The inset figure in (i) shows the grain size distribution obtained from the sample as the main figure over a narrower range.

Grain size distribution was found to be relatively narrow in samples sintered at low temperature (900 °C; Figure 4.6 (i)-(iii)). The sample sintered at low temperature for the shortest duration (900°C, 3h) exhibited a grain size range of less than 1.5 μm, which broadens to 2.5 μm after extended sintering duration. In each case the population deviated slightly from a normal distribution of grain sizes, the modal value was found to be slightly skewed towards a value slightly smaller than the mean average grain size. Consistent with non-uniform grain growth, this deviation from a normal distribution was shown to increase in samples sintered at higher temperatures (≥ 1000 °C); the distribution of grain sizes becomes increasingly skewed towards values smaller than the mean with increasing sintering duration / temperature. While the modal size of the grains measured was consistently between 1 μm and 2.5 μm, the range of grain sizes was found to increase significantly with increasing sintering duration at higher temperatures, rising from ~4 μm (1000 °C, 2h) to ~9 μm after 8 h of sintering at 1000 °C; further increasing to ~16 μm after 6 h at the maximum sintering temperature of 1100°C, where grain sizes appear to have approached a bimodal distribution. The observed increase in the range of grain sizes is accompanied by a general increase in mean grain size, suggesting that a relatively small number of large grains are growing at the expense of smaller ones, consistent with an Ostwald Ripening type grain growth mechanism. However, in contrast to the statistics obtained here, it is noted that this grain growth mechanism would theoretically result in a skew of the grain size distribution towards *larger* grain sizes during the intermediate stages of grain growth, as described by the Lifshitz-Slyozov-Wagner (LSW) model [198, 199], where an extended tail is expected at the *small* end of the particle diameter range. It is proposed that the high proportion of smaller grains observed in 2D SEM micrographs, which are responsible for the aforementioned skewing of grain size distribution to sizes smaller than the mean, is due (at least in part) to the method by which grain size measurements were obtained. Measurements taken from a two-dimensional "slice" represented in an SEM micrograph obtained from a sample surface are inherently biased towards underestimating grain size since the imaged surface is an indiscriminate cross-section through the grains. As such, the probability of this cross-section coinciding with the longest dimension of a randomly oriented three-dimensional particle is small; thus the actual measurement often corresponds to a dimension which is shorter than the longest dimension of the particle. This effect is exacerbated in the case of samples with large grains, since many of the "*small grains*" observed between larger grains in SEM micrographs are in fact likely to represent cross-sections through short dimensions of much larger grains, the longer dimensions of which are obscured by surrounding particles in two-dimensional images. This experimental artefact may explain the consistently small

modal grain size measured across all of the Li_2TiO_3 ceramics processed under the various sintering conditions, and the increasingly skewed grain size distributions observed with increasing mean grain size. It is also noted that the corresponding values of mean grain size calculated for each sample are likely to be an underestimate of their true value as a consequence.

The mean average grain size and corresponding density of all of the Li_2TiO_3 ceramics produced are detailed in Table 4.1; the corresponding graphical representation is shown in Figure 4.7. Density data points shown are the mean average value of the absolute measured densities obtained from two pellets prepared under identical conditions, density error bars were calculated according to Eqn. (3.3) as detailed in section 3.2.3. Grain size data points were calculated from the mean average value of the longest measured dimension of 450 grains analysed per sample, grain size error bars are equal to ± one estimated standard deviation (ESD). Values of density and mean grain size, and associated errors, quoted in Table 4.1 are rounded to the nearest 1 % TD and 0.1 μm respectively.

Table 4.1: Measured density and mean average grain size data (determined by SEM image analysis and manual density measurements respectively) of Li_2TiO_3 pellets sintered at 900 – 1100 °C for various durations (2 – 9 hours). Used to construct the graphical representation shown in Figure 4.7.

Assigned suite "High Porosity": HP "Low Porosity": LP	Sintering conditions	Density (%TD)	Mean grain size (μm) from SEM analysis	Sample ID for TEM experiments (where applicable)
HP	900 °C, 3 hours	65 ± 4	0.7 ± 0.3	A
HP	900 °C, 6 hours	67 ± 3	1.0 ± 0.4	B
HP	900 °C, 9 hours	72 ± 4	0.9 ± 0.4	-
LP	1000 °C, 2 hours	82 ± 2	1.6 ± 0.8	C
LP	1000 °C, 4 hours	84 ± 1	2.2 ± 1.0	-
LP	1000 °C, 6 hours	84 ± 2	2.3 ± 1.2	-
LP	1000 °C, 8 hours	87 ± 1	2.3 ± 1.5	-
LP	1100 °C, 6 hours	84 ± 2	3.4 ± 2.6	D
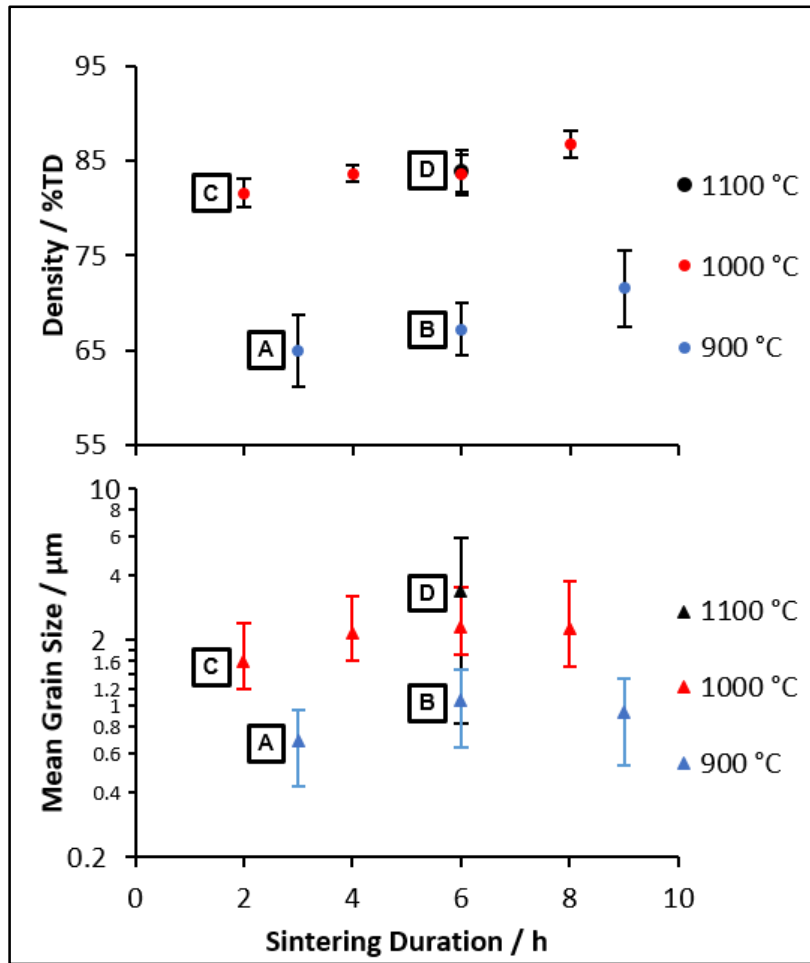
Figure 4.7: Top panel: Measured density of Li_2TiO_3 pellets sintered at 900 – 1100 °C as a function of sintering duration (in hours). Bottom panel: Mean average grain size measured from the longest dimension of 450 grains per sample observed in 2D secondary electron SEM micrographs. Samples (A – D) selected for use in TEM studies are marked with adjacent letters. *Note the log scale, used to highlight difference in grain sizes of the high porosity suite sintered at 900 °C.

Concurrent with the microstructure observations made from visual inspection of SEM micrographs, the effect of sintering duration at constant temperature on densification was shown to be significantly less pronounced than that of sintering temperature itself under the conditions studied (Figure 4.7, top panel). These results suggest that the majority of densification occurred during the first 2-3 hours of sintering. The absolute measured density of samples sintered at constant temperature was found to vary by ~ 7 % and ~ 5 % of theoretical density (TD) at 900 °C and 1000 °C respectively; whereas the difference in density between the two suites of samples (sintered at 900 °C and $\geq$ 1000 °C respectively) is in the region of 15 - 20 % TD. The density of the sample sintered at 1100 °C for 6h was found to be comparable to those sintered at 1000 °C. Thus a significant difference

in density, and hence porosity by association, exists between the "high porosity" suite (sintered at 900 °C) and the "low porosity" suite (sintered at ≥ 1000 °C); samples inside their respective suite exhibited relatively comparable density.

In conjunction with the grain size distributions shown in Figure 4.6, mean average grain size data (Figure 4.7, bottom panel) confirms that sintering temperature also had a more significant effect on grain growth than sintering duration. In the case of samples sintered at 900 °C, mean grain size initially increased from 0.7 µm ± 0.3 µm to 1.0 µm ± 0.4 µm at 3 hours and 6 hours sintering duration respectively; however, no further grain growth was observed at 9 hours sintering duration, indicating that the thermal energy provided is insufficient to promote further grain growth at this temperature. It is also noted that the rate of grain growth appeared to slow at sintering durations longer than 4 hours in samples sintered at 1000 °C. Comparatively, samples sintered for 6 hours at incrementally increasing temperature showed a significant increase in mean grain size (1.0 µm ± 0.4 µm, 2.3 µm ± 1.2 µm, and 3.4 µm ± 2.6 µm at 900 °C, 1000 °C and 1100 °C respectively).

Two samples from each suite (two high porosity [A and B] and two low porosity [C and D], marked by adjacent letters in Figure 4.7) were selected for subsequent TEM studies on the basis of exhibiting the most comparable density within their respective suite, in conjunction with the largest available difference in grain size. This allowed the effects of ceramic density and grain size on material performance to be investigated in subsequent electron irradiation and ion-implantation experiments detailed in the chapters which follow (Chapters 5 - 7).

A summary of the properties of the samples selected for TEM studies, including a brief discussion of the crystallographic differences between samples processed under different conditions (identified from XRD patterns), and the actual grain size of specific grains observed during TEM experiments is given as part of the following results chapter (Chapter 5), which is presented in the format of a manuscript prepared for publication.

4.3 Conclusions of pristine characterisation and microstructure manipulation experiments

The microstructural properties of Li_2TiO_3 ceramics prepared using solid state synthesis and conventional sintering methods were shown to be strongly dependant on post-synthetic processing conditions. The densification behaviour of Li_2TiO_3 was found to be strongly dependant on temperature, and relatively independent of sintering duration within the limits of the conditions studied. The extent of grain growth during sintering was shown to be affected by both the temperature and duration; hence, by adjusting the conditions employed, the microstructure of Li_2TiO_3 ceramics can be tuned in such a way that the contributions of porosity and grain size to the material's performance in different environments can be investigated. Temperature dependant crystallographic disorder, attributed to the presence of stacking faults and cation disorder has been identified in β- $Li2TiO3$ ceramics prepared by conventional solid state sintering; an inverse relationship between sintering temperature and the degree of deviation from the ideal structure was found to exist, suggesting that the concentration of intrinsic defects is likely to be greater in samples sintered at lower temperatures.

Chapter 5 - Room temperature electron beam induced cavity formation in Li$_2$TiO$_3$ ceramics

Chapter 5 details work carried out in order to observe the effects of electron beam irradiation on polycrystalline Li$_2$TiO$_3$ ceramics at room temperature using in-situ transmission electron microscopy (in-situ TEM). Details of the synthesis and characterisation of the bulk samples (which were selected from those described in Chapter 4) from which the thin-film TEM specimens used in this work were prepared prior to in-situ TEM experiments are included. This work is presented in the form of a manuscript which has been prepared for publication.

For ease of reference, the labels corresponding to figures and tables have been adapted in keeping with the format of this thesis. A separate reference list, which relates only to this chapter and the manuscript therein, is included at the end of this chapter.

Statement of contributions

Manuscript title: Room Temperature Electron Beam Induced Cavity Formation in Li$_2$TiO$_3$ Ceramics

Publication status: Currently in review by co-authors and funding body.

Authors: Samuel J. Waters, Nik Reeves McLaren, Yiqiang Wang, Graeme Greeves, Ray. F. Egerton and Amy S. Gandy.

Author contributions:

Samuel Waters conducted all experimental work and collected all experimental data regarding the synthesis, processing, preparation and characterisation of all of the materials used in this work prior to TEM experiments. The aforementioned elements of this work were carried out at the University of Sheffield Department of Materials Science and Engineering. All experimental data collected (including that which was obtained from TEM experiments) was analysed primarily by Samuel Waters, who also wrote the first draft of this manuscript and prepared all figures contained herein. The supplementary file 1a (a dedicated spreadsheet designed for the semi-automated measurement of features observed in TEM micrographs) was also constructed by Samuel Waters.

This work was supervised by Nik Reeves McLaren, Yiqiang Wang and Amy Gandy, who advised on the interpretation and presentation of experimental data. Amy Gandy also assisted with the mounting of TEM specimens prepared by Samuel Waters.

Graeme Greaves operated the transmission electron microscope and the ion beam equipment coupled to the MIAMI-II system used in this work. Graeme Greaves collected all raw data obtained from all TEM and ion implantation experiments. All TEM and ion implantation experiments were conducted at the University of Huddersfield MIAMI facility under the direction of Samuel Waters, who was present throughout all experimental work.

Ray Egerton has advised on the content of this manuscript and assisted in the understanding of electron beam induced radiolysis.

Room Temperature Electron Beam Induced Cavity Formation in Li$_2$TiO$_3$ Ceramics

Samuel J. Waters[1], Nik Reeves McLaren[1], Yiqiang Wang[2], Graeme Greeves[3], Ray. F. Egerton[4] and Amy S. Gandy[1]

Affiliations

1 Department of Materials Science and Engineering, University of Sheffield, S1 3JD, UK

2 UK Atomic Energy Authority, Culham Science Centre, Abingdon, Oxfordshire, OX14 3DB, UK

3 School of Computing and Engineering, University of Huddersfield, Huddersfield HD1 3DH, UK

4 Department of Physics, University of Alberta, Edmonton, Alberta, Canada,

Abstract

Polycrystalline lithium metatitanate (Li$_2$TiO$_3$) is an attractive material for a range of applications, including battery materials and microwave dielectrics, it has also attracted a great deal of attention as proposed tritium breeder material for use in nuclear fusion reactors. During the continued development of Li$_2$TiO$_3$, and similar Li-containing ceramics, for these advanced applications, transmission electron microscopy (TEM) is likely to be employed to study the nano-structure of these materials and, in the case of nuclear fusion applications, their response to radiation induced damage. In this work, we have shown that electron irradiation in a conventional TEM results in the formation of nanometre sized vacancy-type defects at room temperature, and that the size and number density of the vacancy-type defects are linked to ceramic microstructure and crystallographic disorder. Electron beam induced vacancy-type defect formation is discussed in terms of electron beam heating, electron beam induced radiolysis and electron beam induced displacement damage; the displacement of Li and O lattice atoms is proposed to be primarily responsible for the observed damage. Results suggest that the formation and growth of vacancy-type defects is a two-stage processes, initially driven by the supersaturation of vacancies due to the preferential loss of interstitials to the surfaces of thin film TEM specimens, followed by coalescence of larger vacancy-type defects, which leads to cavity growth. Furthermore, results from X-ray diffraction suggest that growth is facilitated by the presence of CO$_2$, produced by the decomposition of a Li$_2$CO$_3$ surface

reaction layer under the electron beam. These results highlight that care must be taken when interpreting TEM data and undertaking the associated analysis, especially in Li-containing oxides.

Introduction

Lithium metatitanate, Li_2TiO_3, has been the subject of research for a multitude of applications including electrode materials for use in lithium ion batteries [1-7], microwave dielectrics [8-10], and supercapattery applications [11]. Li_2TiO_3 has attracted particular interest in the field of tritium breeder materials research for nuclear fusion, and is currently considered to be one of the leading candidate ceramic breeder materials for use with various breeder blanket concept designs proposed by several international research groups [12-14].

The latest generation of ceramic breeder materials being developed for use with the EU DEMO concept design, known as the helium cooled pebble bed (HCPB) [15], are composed primarily of lithium orthosilicate (Li_4SiO_4) incorporating Li_2TiO_3 as a secondary phase [16]; addition of lithium titanate to the EU reference formulation, composed of hyperstoichiometric Li_4SiO_4 with minor inclusions of Li_2SiO_3 [17], was shown to enhance the mechanical stability of the ceramic pebbles. While the compatibility of these 'advanced' ceramic breeder pebbles may be cause for concern [18], the pebbles are reported to show excellent thermal stability [19], adequate thermal conductivity [20], appropriate tritium release characteristics [21], and reasonable tolerance to radiation [22].

During operation, ceramic breeder materials will be subjected to high levels of radiation, primarily from high energy (14.1 MeV) neutrons, which will induce high levels of displacement damage. Radiation induced displacement events introduce defects in the form of vacancies and interstitial atoms (known as Frenkel pairs); the correlation between defect annihilation and tritium release behaviour suggests that these defects may act as trapping sites for tritium [23-25], and as such impede tritium release and recovery, which is detrimental to the material's performance. Furthermore, aggregation of vacancy and/or interstitial defects can result in the formation of extended defects such as voids, cavities and dislocation loops [26-30].

Microstructural properties such as grain size are known to affect the irradiation behaviour of materials. Enhanced radiation tolerance, attributed to increased interfacial area associated with grain boundaries which act as efficient defect sinks, has been reported in numerous nanocrystalline

materials [31-35]. Aggregation of defects in larger grained analogues, leading to the formation of defect clusters, has previously been attributed to the longer diffusion path to sinks at grain boundaries[31, 36]. Conversely, other materials exhibit higher radiation tolerance when they are composed of larger grains; for example, UO_2, ThO_2 and CeO_2 are all reported to exhibit a greater degree of volumetric swelling as a result of heavy ion implantation in nanocrystalline format than their analogous microcrystalline counterparts [37]. While the increased availability of defect sinks associated with the increased grain boundary area of smaller grained materials may improve their radiation damage tolerance, competing effects such as the enhanced driving force for structural modifications associated with higher surface energy, and the increased localisation of energy deposition due to inefficient dissipation of energy as a result of phonon scattering at grain boundaries [37, 38] potentially reduces the radiation damage resistance of smaller grained materials.

Transmission Electron Microscopy (TEM) is routinely used to examine the effects of externally induced radiation damage, including void and cavity formation, in irradiated and ion-implanted materials [28, 39, 40]. Irrespective of the application, TEM is likely to be used to examine Li_2TiO_3 (and similar lithium-containing ceramics) on the nano-scale; particularly since a number of its proposed applications utilise materials with sub-micron or nanoscale microstructural properties [1, 4, 6-8, 11]. One factor that is often overlooked is the so called 'Observer Effect', i.e. *"An act of Observation is thus necessarily accompanied by some disturbance of the Object observed"* (P. A. M. Dirac, 1947) [41]; which, in this context, refers to the effects of the TEM electron beam itself on the specimen being examined. Electron beam induced damage can occur as a result of scattering interactions of incident (beam) electrons with the electrons or nuclei of the specimen material. Where elastic scattering interactions with nuclei can induce knock-on displacement of lattice atoms directly, inelastic interactions with atomic electrons can indirectly induce displacement damage via radiolytic mechanisms [42]. TEM electron beam damage has been reported in many inorganic materials, notably alkali halides [43-46], alkaline earth fluorides [47, 48], silicates [49, 50], zeolites [51], and maximum valency transition metal oxides [52-56].

Given that electron irradiation in a TEM has the potential to introduce defects which are similar in nature (i.e. atomic displacement) to those induced by neutron irradiation and ion implantation – both of which are commonly used to study / emulate radiation effects in materials - it is important to determine how examination of Li_2TiO_3 using TEM techniques will affect the nano-structure of the ceramic in order to avoid the erroneous interpretation of results. Such investigations allow the effects

of the electron beam to be taken into account in any future experiments which utilise TEM to investigate the effects of radiation damage in ceramic breeder materials containing Li_2TiO_3, and may assist in the explanation of unexpected phenomena observed during TEM examination of analogous materials developed for wider applications; thus avoiding the potential for erroneous findings being made and reported.

In this work, in-situ transmission electron microscopy was used to observe the effects of electron beam irradiation on polycrystalline Li_2TiO_3 at room temperature. The effects of electron irradiation time and the microstructure of the ceramic in its as-prepared state are identified, and the possible mechanisms responsible for the observed behaviour under electron irradiation are discussed.

Methods

Lithium metatitanate (Li_2TiO_3) powders were synthesised via the solid state reaction method. Commercially available reagents Li_2CO_3 (Acros Organics Li_2CO_3 99+ % ACS Reagent) and TiO_2 (Aldrich Titanium (IV) oxide, ~325 mesh, >99% trace metals basis) were dried (180 °C and 900 °C respectively) for a minimum of 12 h prior to synthesis. The dried reagent powders were mixed together in stoichiometric ratios and ball milled for 24 h under isopropanol with 10 mm yttria-stabilised zirconia (YSZ) media. The resulting slurry was dried overnight (80 °C) to remove the isopropanol, sieved using a mesh size of 250 μm, and calcined under atmospheric air in a box furnace using a two-stage calcination program (from RT to 700 °C, heating rate of 5 °C min^{-1}, 4 h dwell; and from 700 to 730 °C, 5 °C min^{-1} heating rate, 4 h dwell). The calcined product was ball milled for 24 h under isopropanol with 10 mm YSZ media, dried overnight at 80 °C, and sieved using a mesh size of 250 μm.

Portions of the resulting powder (~ 0.3 g) were uniaxially pressed into 10 mm pellets, (100 MPa, 1 min hold) to form "green bodies" and sintered under atmospheric air in a tube furnace. In this work, the relationship between ceramic grain size and electron beam induced damage was investigated. To investigate this, four pellets were sintered at different times and temperatures to produce a range of grain sizes and open volume porosity. Specifically, two high porosity samples were produced by sintering at 900 °C for 3 h or 900 °C for 6 h; and two low porosity samples were produced by sintering at 1000 °C for 2 h or 1100 °C for 6 h.

Due to the relatively high degree of open porosity exhibited by the pellets, and the propensity for Li_2TiO_3 and other lithium ceramics to react with air and water [57-62], density measurements using the Archimedes principle were not appropriate in this case. Therefore, the density of each sintered pellet was calculated from its respective mass, diameter and depth, modelling each pellet as a cylinder. The values of density reported here were calculated from the mean average values of the densities obtained from two pellets prepared under identical conditions.

One face of all sintered ceramic pellets was polished to a 1 μm finish using non-aqueous diamond suspension and thermally etched at 90% of the sintering temperature for 30 min prior to characterisation. X-ray diffraction (XRD) was used to confirm the identity and phase purity of the sintered ceramic pellets. XRD data were collected at room temperature in Bragg Brentano geometry using Cu Kα radiation (λ = 1.5418 Å) using a PANalytical X'Pert[3] Powder diffractometer. Phase identification was achieved by comparison of observed diffraction patterns to entries in the ICDD PDF-4+ database [63].

Scanning Electron Microscopy (SEM) was used to determine grain size, grain morphology and the nature of porosity in the sintered pellets. The pellets were mounted onto aluminium stubs using adhesive carbon discs and the polished surfaces were sputter coated with gold. Secondary electron SEM images were collected using an Inspect F50 SEM equipped with a field emission gun (FEG) electron source operated at 20 kV. Grain size statistics were calculated based on measurement of the longest dimension of 450 grains per sample observed in 2D SEM images, measured using ImageJ [64].

Transmission Electron Microscopy (TEM) was used to characterise the microstructure of the pristine specimens on the nano-scale, and to investigate the formation and growth of cavities due to exposure to the electron beam. To produce thin film specimens for use in TEM experiments, sintered pellets were sectioned into cubes (~2 mm^3) using a slow saw equipped with a diamond cutting disk. The resulting ceramic cubes were mechanically thinned to a thickness of 60 μm ± 10 μm and polished to a 1 μm finish using non-aqueous diamond suspension. A Gatan 656 dimple grinder was utilised to achieve a final thickness of ~20 μm in a hemispherical region (polished to a 0.25 μm finish) at the centre of each sample. Each sample was mounted to molybdenum TEM grids using Gatan G1 epoxy (cured at 80 °C for 1 h). Electron transparent regions were produced using a Precision Ion Polishing System (Gatan PIPS II - dual beam modulation, automatic gas flow rate). During the milling process,

the Ar$^+$ ion energy was gradually reduced from 5 keV at a milling angle of 6°, to 1 keV at a milling angle of 4° in order to minimise surface damage and contamination, and to produce a greater area of electron transparency. All TEM experiments were carried out using the MIAMI-II system [65], at the University of Huddersfield using a modified Hitachi H-9500 TEM equipped with a lanthanum hexaboride (LaB$_6$) electron gun, operated in bright field (BF) TEM mode at 300 kV. Images and videos were captured by a Gatan OneView CMOS camera with resolution of 16 MPx. In order to investigate the formation and growth of cavities in Li$_2$TiO$_3$ under the electron beam, the beam exposure time (defined as the time elapsed while an area of specimen was exposed to the TEM electron beam) was recorded throughout. Condenser lens settings were altered according to the optimal conditions for imaging each individual specimen, as such we were unable to consistently monitor electron fluence; this has been taken into consideration when discussing the effects of electron beam exposure on Li$_2$TiO$_3$. Where possible, live video was captured during in-situ experiments, and bright field TEM micrographs were taken at 10 minute intervals. Fresnel contrast analysis was used to identify vacancy-type defects in the samples. In this technique, BF TEM micrographs were defocussed by ± 500 – 1000 nm in order to observe the appearance and change in intensity distribution of Fresnel fringes which form around vacancy-type defects such as small voids, cavities, vacancy clusters or gas bubbles. In under-focus images, vacancy-type defects appear bright with a dark fringe, while in over-focus images they appear dark with a bright fringe. Small (< 5nm) vacancy-type defects are invisible when the TEM image is in focus; thus the observation of a change in Fresnel contrast when the objective lens is defocussed also allows a distinction to be made between vacancy-type defects and secondary phase precipitates as the contrast associated with precipitates does not vary in this way, and often remains the same irrespective of focus. In this work, bright field through-focal-series micrographs (± 500 nm objective lens defocus) were taken at 10 minute intervals of beam exposure to monitor the formation and evolution of TEM resolvable vacancy-type defects. After acquisition, image processing was performed using the image editing software ImageJ [64]. A bandpass filter (3-50 pixels) was applied to each 4K image (horizontal resolution ≈ 4080 pixels) to suppress features of low spatial resolution, and the contrast adjusted to enhance features of interest. Processed under- and over-focus images were subsequently aligned and stacked. Cavity number density was calculated by taking the mean average of the number of resolvable defects observed in three 25 x 25 nm areas. Greyscale intensity profiles of linescans across cavities were obtained using the "line intensity profile" and "multi plot" tools in ImageJ. The distance between fringes was extracted from intensity profiles in a semi-automated fashion using a purpose-built Excel spreadsheet which yields: (i) individual cavity

diameters (taken as the average distance between fringes of the same cavity measured in equivalent under- and over-focus images), (ii) the mean average cavity diameter (calculated from the extracted diameter of 50 cavities), and (iii) a population distribution of the measured cavities according to size. Examples of the graphical outputs obtained from the purpose-built Excel spreadsheet are shown in **Figure 5.1**.
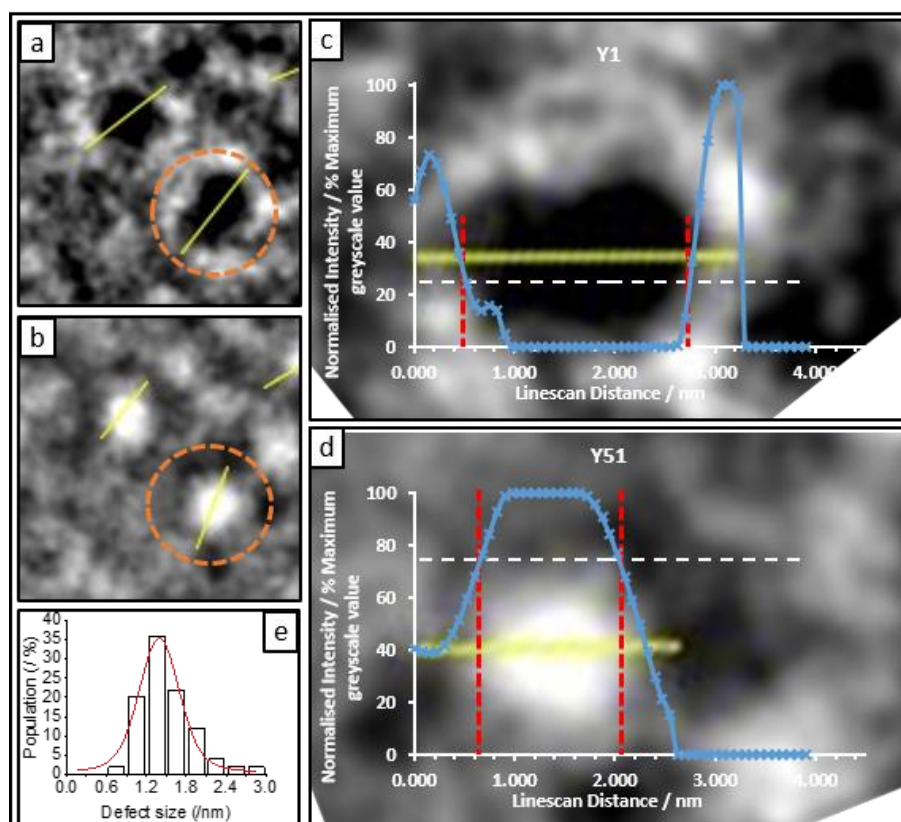
Figure 5.1: Example of semi-automated measurement of defects in (a) over- and (b) under-focus micrographs, and the respective graphical outputs (c and d) obtained from Excel defect size measurement spreadsheet (superimposed over corresponding BF TEM micrographs). Example histogram of defect size distribution (e) constructed using output generated from Excel defect size measurement spreadsheet; fitted distribution curve added using OriginPro.

The spreadsheet is designed such that the only input required from the user is to paste the data (in the default .csv format from ImageJ) into a master sheet, and select an appropriate threshold intensity (indicated by the white dashed line in **Figure 5.1**). All outputs are automated. A copy of this spreadsheet along with a user guide can be found in Supplementary file 1a.

Results and discussion

Microstructure and phase analysis

One of the aims of this work was to investigate the link between ceramic grain size and porosity, and electron beam induced damage. In order to separately investigate the effect of grain size and porosity, two suites of samples were produced, each with different densities; the samples within each suite exhibited similar ceramic densities but different grain sizes.

SEM and manual density measurements were used to determine the mean grain size and density of ceramic pellets. Figure 5.2 shows secondary electron SEM images of Li_2TiO_3 samples sintered at A) 900 °C for 3 hours, B) 900 °C for 6 hours, C) 1000 °C for 2 hours, and D) 1100 °C for 6 hours, and the corresponding low-magnification bright field TEM micrographs showing the specific grains examined during TEM electron irradiation.
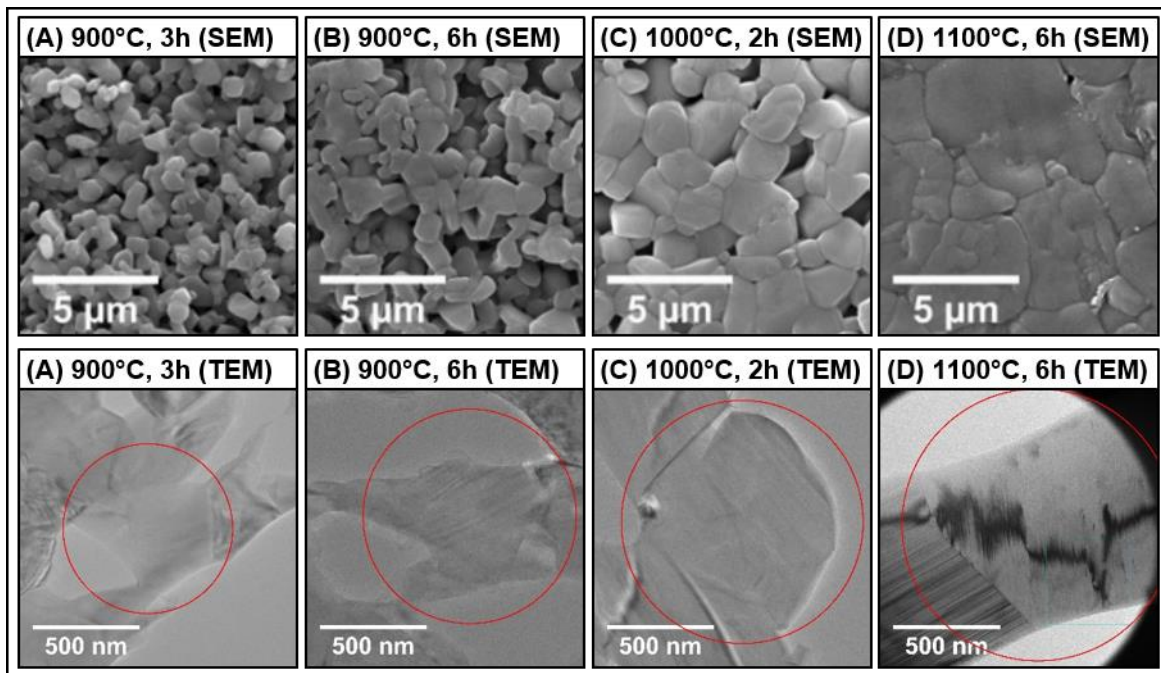
Figure 5.2: Upper row: Secondary electron SEM images showing an overview of the microstructure of four Li_2TiO_3 samples A-D, sintered for different durations at different temperatures in order to produce the suite of samples used in this study. Lower row: Corresponding low-magnification bright field TEM micrographs showing the specific grains examined during TEM electron irradiation.

Table 5.1 details the mean average grain size and density (determined by SEM image analysis and manual density measurements respectively) of each of the samples shown in Figure 5.2. Individual grain sizes were measured using the longest available dimension, the mean average grain size was

subsequently calculated from the longest measured dimension of 450 grains analysed per sample. Errors quoted for mean grain size are equal to one estimated standard deviation (ESD).

It is noted that, while there is a general increase in mean grain size from sample A to sample D, each sample exhibits a range of grain sizes. As indicated by the increase in the ESD associated with grain size distributions, the breadth of this range is shown to increase as mean grain size increases, consistent with a discontinuous (non-uniform) grain growth mechanism. Hence, in order to avoid ambiguity, the grain size of the specific grains investigated in TEM experiments was measured directly from TEM micrographs. The actual grain sizes used in TEM experiments, stated as the mean value of four measurements taken across each grain, are listed in Table 5.1; errors quoted are half the range of the four measurements taken across each grain.

The density values given in Table 5.1 were calculated from the mean average values of the densities obtained from two pellets prepared under identical conditions. The absolute density (ρ) of each cylindrical pellet was calculated from its mass, and the mean average values of diameter (D) and depth (d) obtained from six measurements. The error ($\delta\rho$) associated with the density of each pellet were calculated according to Eq. (1):

$$\delta\rho \ = \ \rho \ \cdot \sqrt{\left(2 \cdot \frac{\delta D}{D}\right)^2 + \left(\frac{\delta d}{d}\right)^2} \qquad (1)$$

where δD and δd are the absolute errors associated with diameter and depth respectively (taken as half of the range of six measurements, plus the instrumental error). The final errors quoted in Table 5.1 are the sum of the errors calculated for each individual pellet propagated though to the mean, and half of the range of the absolute density values obtained (Eq. (2)):

$$\delta\rho_{Tot} = \frac{\sqrt{(\delta\rho_1)^2 + (\delta\rho_2)^2}}{2} + \frac{|\rho_1 - \rho_2|}{2} \qquad (2)$$

Table 5.1: Mean average density and grain size (determined by SEM image analysis and manual density measurements respectively) of the Li_2TiO_3 samples shown in Figure 5.2, and the actual size of the specific grains examined during electron beam irradiation (determined from TEM micrographs). Errors quoted were calculated according to Eq. (2) for density, 1 ESD for mean grain size, and half of the range of four measurements across each grain for actual grain size used in TEM experiments.

Sample ID and sintering conditions	Density (%TD)	Mean grain size (µm) from SEM analysis	Actual grain size used in TEM experiments (µm)
A) 900 °C, 3 hours	65 ± 4	0.7 ± 0.3	0.58 ± 0.11
B) 900 °C, 6 hours	67 ± 3	1.0 ± 0.4	0.75 ± 0.12
C) 1000 °C, 2 hours	82 ± 2	1.6 ± 0.8	0.93 ± 0.12
D) 1100 °C, 6 hours	84 ± 2	3.4 ± 2.6	≥ 1.09 ± 0.08*

*Longest dimension of grain was larger than the field of view in the lowest available magnification image of this area; hence the figure quoted corresponds to the minimum possible grain size and is likely to be an underestimate of the actual grain size.

Figure 5.3 illustrates the variation in densities and grain sizes of the four samples studied. Samples A and B were determined to have comparable densities (65% of TD ± 4% and 67 % of TD ± 3%, respectively), but different grain sizes (0.7 µm ± 0.3 µm and 1.0 µm ± 0.4 µm, respectively). Similarly, samples C and D were determined to have comparable densities (82% of TD ± 2% and 84 % of TD ± 2%, respectively), but different grain sizes (1.6 µm ± 0.8 µm and 3.4 µm ± 2.6 µm, respectively). Owing to the difference in densities, and hence the degree of porosity by association, samples A and B are referred to as the "high porosity suite", and samples C and D referred to as the "low porosity suite".
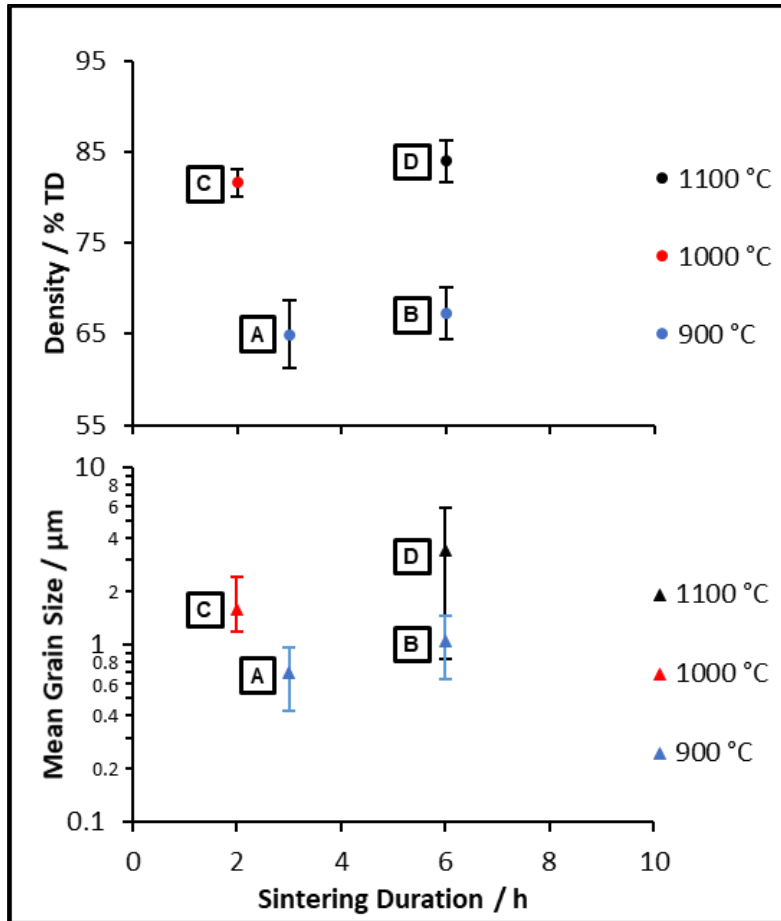
Figure 5.3: Top panel: Measured density of Li_2TiO_3 pellets (A), (B), (C) and (D) as a function of sintering duration, in hours. Bottom panel: Mean average grain size measured from the longest dimension of 450 grains per sample observed in 2D secondary electron SEM micrographs. *Note the log scale, used to highlight difference in grain size of 900 °C suite, samples (A) and (B).

Figure 5.4 shows normalised XRD patterns obtained from the polished and thermally etched surfaces of the sintered pellets. Phase analysis carried out using the ICDD PDF-4+ database showed that the structure indexed well to the monoclinic β-Li_2TiO_3 structure reported by Kataoka *et al.* [66] (ICDD PDF no. 01-077-8280). Only peaks consistent with this structure were observed in the diffraction patterns of all samples; hence, diffraction patterns were indexed according to this structure using space group *C2/c* and lattice parameters *a* = 5.0623(5) Å, *b* = 8.7876(9) Å, *c* = 9.7533(15) Å, and *β* = 100.212(11)° as reported by Kataoka *et al.*. It is noted that some peaks are entirely absent or unresolvable in the diffraction patterns of samples sintered at 900 °C (specifically (021) (023) (112) and ($\bar{1}$12) peaks), and some variation in relative peak intensities (i.e. inversion of (020) and (110) peaks, and loss of resolution of (111), ($\bar{1}$11) and (022) peaks) exists between samples sintered at different temperatures. Deviation from the ideal structure is apparently reduced with increased sintering temperature. Very similar peak broadening, loss of resolution and inversion of relative peak

94

intensities has been reported by Boulineau *et al.* in the crystalographically analogous material Li$_2$MnO$_3$ [67]; they ascribe these observations to cation disorder and the presence of stacking faults. Hence we propose that cation disorder (Li/Ti exchange) and the presence of stacking faults is likely to be largely responsible for the deviation of Li$_2$TiO$_3$ from the structure reported by Kataoka *et al.* particularly in the case of samples sintered at lower temperature where the thermal energy supplied may be insufficient to form the ideal, fully ordered structure.
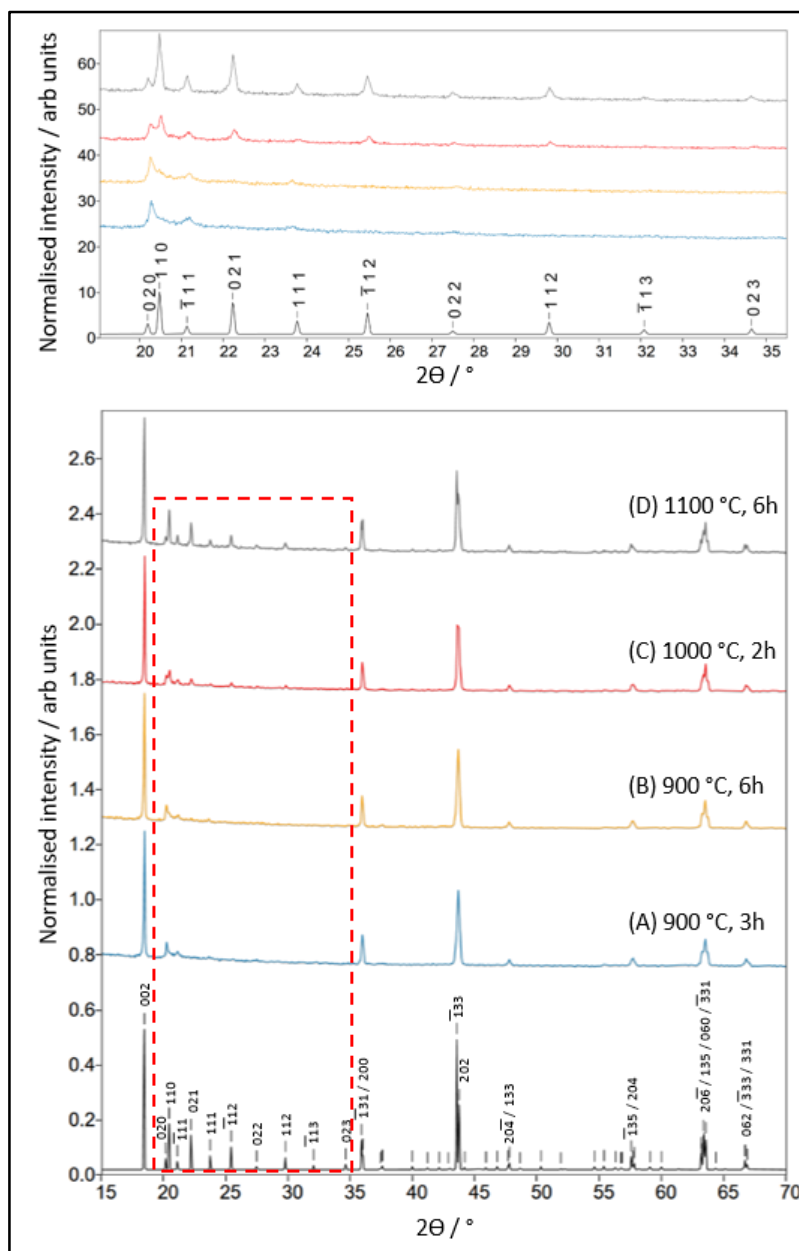
Figure 5.4: Bottom: XRD patterns of Li$_2$TiO$_3$ pellets sintered under different conditions. Indexed according to ICDD PDF no. 01-077-8280 [63, 66]. Lowermost pattern (shown in black) simulated from [66] (generated using CrystalDiffract® [68]), tick marks correspond to indexed peaks, some hkl labels omitted for clarity. Top: Expanded view of 19-36 ° 2θ range showing inversion of (020) and (110) peak intensity and loss of low angle peak resolution in samples sintered at lower temperature.

Electron beam induced damage – effect of exposure time

High porosity sample A (smallest grains, sintered at 900°C for 3 hours), was used to investigate the effect of electron beam exposure time on polycrystalline Li_2TiO_3. Figure 5.5 shows the formation and growth of defects in Li_2TiO_3 under a 300 kV TEM electron beam at ambient temperature as a function of exposure time. We define the "pristine" image in Figure 5.5 as being taken from a region of the sample which had only been exposed to the electron beam for the time it took to set the eucentric height and take the through-focal-series. In order to achieve this, the standard TEM calibration process was carried out on a different region of the sample. Vacancy-type defects were identified by analysis of bright-field through-focal-series micrographs according to the observation of the change in contrast of Fresnel fringes upon defocussing the objective lens. Inspection of the live video [Supplementary file 2], taken in under-focus condition during electron beam exposure, revealed the appearance of very small (~1 nm) bright features after approximately 6 to 7 minutes of exposure to the electron beam. After 10 minutes' beam exposure time, a distinct change in contrast of the Fresnel fringes around these features was observed in through-focal-series micrographs (shown inset in Figure 5.5), indicative of vacancy-type defects.
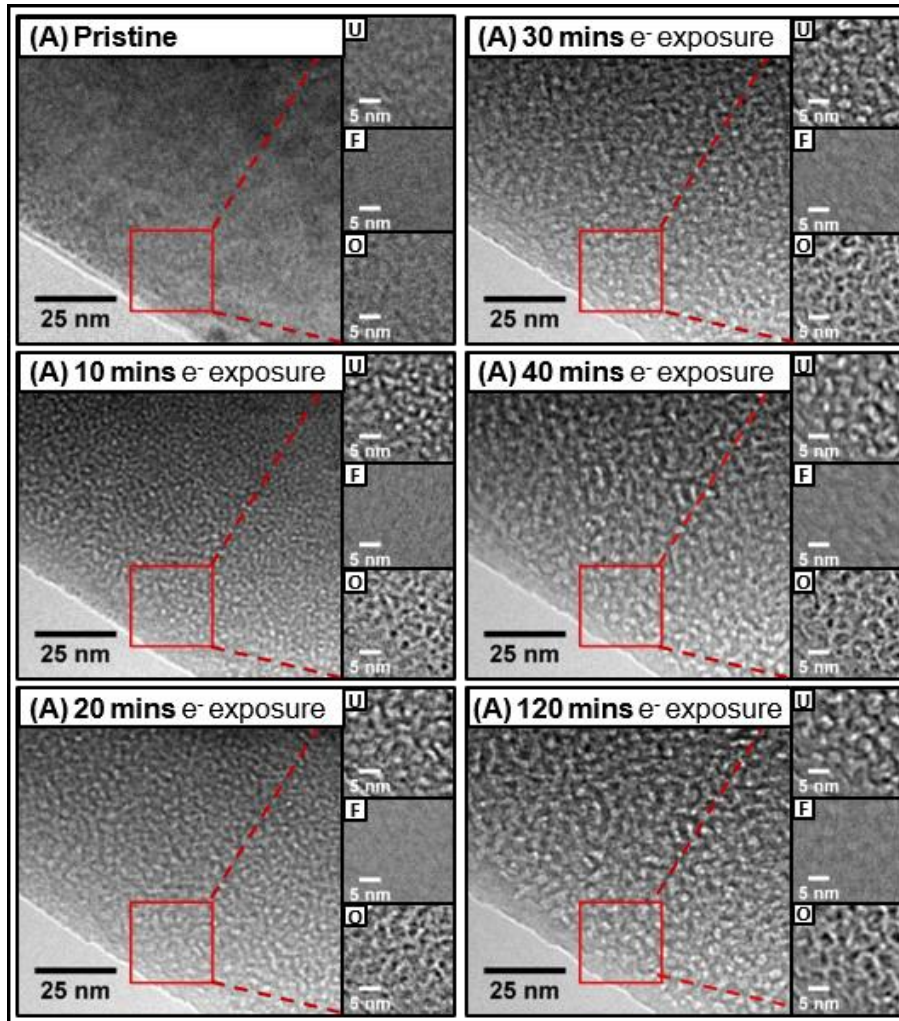
Figure 5.5: Under-focused bright field TEM micrographs of Li_2TiO_3 (sample A) taken at 10 minute intervals, with the corresponding through-focal-series inset. The contrast change observed in the under-focused (U), in-focus (F) and over-focused (O) micrographs is characteristic of vacancy-type defects.

As shown in Figure 5.5, the vacancy-type defects appear to nucleate relatively uniformly throughout the region observed, and increase in size with increasing electron beam exposure time. The defects exhibited irregular, non-spherical morphology, with rounded (as opposed to angular) edges in most cases. Non-spherical cavities attributed to the effects of ion irradiation have been observed to form in other oxide ceramics; for example in the work of Zinkle *et al.* [69]*,* irregularly shaped cavities were found to form in the vicinity of dislocation loops in H^+ implanted Al_2O_3, and in H^+ implanted $MgAl_2O_4$ where no distinct relationship between cavity morphology and the crystallographic orientation of the matrix material was identified*.*

Individual defect sizes were measured across the longest available dimension with well resolved fringes on opposing edges. Figure 5.6 shows the mean average defect size (calculated from 50 defects

per image) observed in Li$_2$TiO$_3$ measured at 10 minute intervals of beam exposure, and the corresponding mean average number density observed in three 25 x 25 nm (625 nm^2) areas. Error bars represent the standard error of the mean in the case of defect size, and the range over three areas in the case of number density. The mean average defect size was found to increase from ~1.4 nm after 10 minutes of beam exposure time, to ~2.3 nm after 120 minutes of beam exposure time. The most significant defect growth occurred in the first 40 minutes of electron beam exposure, where a near-linear increase in defect size was observed. Beyond 40 minutes of beam exposure the rate of defect growth was observed to decrease; mean average defect size was shown to stabilise after ~60 minutes, after which time the defect size was found to remain constant up to 120 minutes of beam exposure within the error associated with measurements.
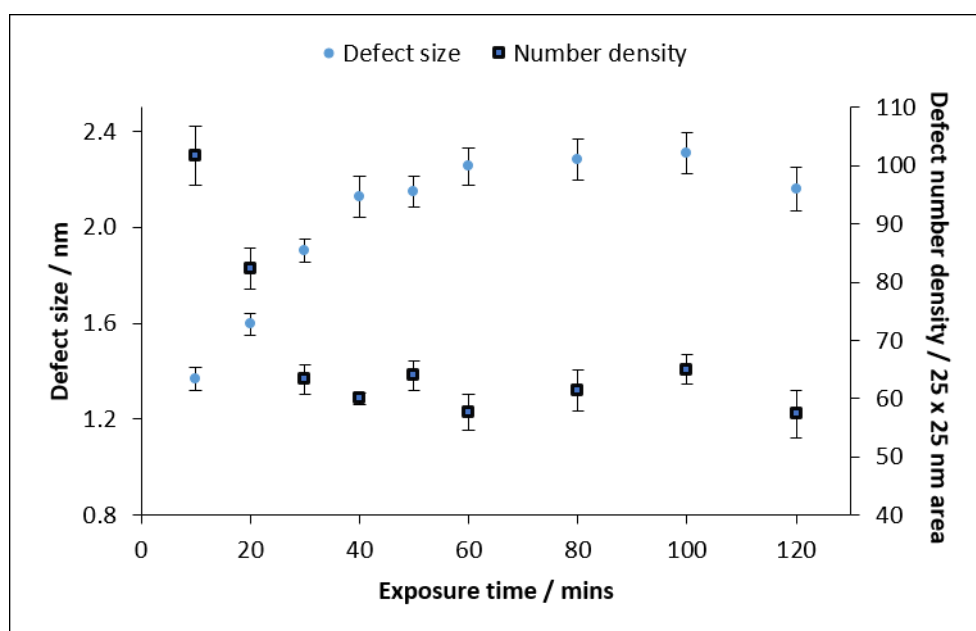
Figure 5.6: Mean average defect size and defect number density observed in Li$_2$TiO$_3$ (sample A) as a function of electron beam exposure time.

A concurrent decrease in defect number density was observed with defect growth; an approximately inverse relationship exists, characteristic of a coarsening process. During the first 40 minutes of exposure to the electron beam, where the highest rate of defect growth was observed, defect number density was shown to decrease rapidly from ~100 defects to ~60 defects per 625 nm^2 area, confirming that defect growth was accompanied by coarsening.

No TEM resolvable vacancy-type defects were observed regions of the sample far removed from the area that had been under irradiation. Since no vacancy-type defects were resolvable in the pristine specimen, nor in areas of the specimen which had not been previously exposed to the electron beam,

we conclude that these defects form as a direct result of exposure to the TEM electron beam. Next we will describe and discuss potential damage mechanisms that gave rise to the observed defect formation.

Electron beam damage can be broadly split into three categories, namely radiolysis (ionisation effects), knock-on damage (atomic displacement due to ballistic collisions) and beam heating.

Beam heating

Beam heating may occur due to inelastic interactions of beam electrons with the atomic electrons of the specimen. Due to the similar mass of the particles (electrons) involved in such interactions, a significant amount of energy can be transferred to atomic electrons; this energy may be dissipated in the form of heat, resulting in a localised increase in specimen temperature [70].

Building on the work of Fischer [71], Jenčič *et al.* [72] developed an equation (Eq. (3) below) designed to estimate the maximum rise in local specimen temperature, ΔT, induced by a TEM electron beam:

$$\Delta T = \frac{I}{\pi \kappa e} \left(\frac{\Delta E}{d}\right) ln\left(\frac{b}{r_0}\right) \quad (3)$$

Where *I* is the primary beam current, *κ* is the thermal conductivity of the specimen material, *e* is the charge on an electron, *b* is the radius of the heat sink (1.5 mm for a TEM specimen 3mm in diameter) and r_0 is the radius of the primary beam (estimated to be between 1.5 μm and 2.5μm in this work). *ΔE* is the total energy loss for a single electron over a distance *d* (sample thickness). According to Jenčič *et al.* [72], and later Edmondson *et. al.* [73], assuming the beam energy loss is constant throughout the sample, and negligibly small compared to the incident beam energy, the *ΔE/d* term in equation (3) can be substituted for the rate of energy loss by beam electrons (*-dE / dx*) due to interactions with atomic electrons. This can be calculated using the Bethe-Bloch formula, which, for electrons (including corrections for relativistic effects) is shown in Eq. (4). Note that the expression given by Jenčič *et al.* [72] requires that the density (*ρ*) of the specimen material is input in atoms m^{-3} to yield the correct result if all other input values are in SI units; here, N_A and *A* terms have been added to Eq. (4) such that if all input values are in SI units, the equation yields an output in J m^{-1} [72]:

$$-\langle\frac{dE}{dx}\rangle = \frac{2\pi Z N_A \rho}{m_0 v^2 A} \left(\frac{e^2}{4\pi\varepsilon_0}\right)^2 \left[ln\left(\frac{E(E+m_0c^2)^2\beta^2}{2I_e^2 m_0 c^2}\right) + (1+\beta^2) - (2-\sqrt{1-\beta^2}-1+\beta^2)ln2 \right.$$
$$\left. + \frac{1}{8}\left(1-\sqrt{1-\beta^2}\right)^2 \right] \quad (4)$$

Here Z, ρ and A are respectively the average atomic number, density (in kg m^{-3}), and molar mass (in kg mol^{-1}) of the specimen material, N_A is the Avogadro constant, m_0 is the rest mass of an electron, and v is the electron velocity. e is the charge on an electron, ε_0 is the vacuum permittivity, E is the primary beam energy, c is the speed of light in a vacuum, $\beta = v/c$, and I_e is the average excitation energy for electrons in the specimen material. v can be calculated according to equation (5) [74] where V is the accelerating voltage. A close approximation for I_e can be calculated from the weighted sum of the electron excitation of the elements from which specimen material is composed using Bragg's rule of additivity [75] (Eq. (6)):

$$v = c \left[1 - \frac{1}{\left(1 + \frac{eV}{m_0 c^2}\right)^2} \right]^{\frac{1}{2}} \qquad (5)$$

$$I_{e\,(Compound)} = exp\left(\frac{\sum_i n_i Z_i \ln(I_{ei})}{\sum_i n_i Z_i}\right) \qquad (6)$$

Where, in Eq. (6), n_i is the number of atoms of element i per formula unit in the specimen material, Z_i is the atomic number of element i, and I_{ei} is the mean excitation energy for electrons in element i.

As a brief aside, it is noted that there appears to be a printing error with respect to the Bethe-Bloch formula detailed in the paper by Edmondson *et al.* [74], where the exponent of the $(e^2 / 4\pi\varepsilon_0)^2$ term appears to be missing. It is also noted that, in the same paper, the ε_0 term is described as the dielectric constant as opposed to the vacuum permittivity; indeed, values of the dielectric constants of the materials with which the paper is concerned are listed in the corresponding table. Permittivity has units of F m^{-1} (*or C^2 s^2 kg^{-1} m^{-3}), which are required for Eq. (4) to yield an output in terms of energy per unit distance (J m^{-1} in SI); since the dielectric constant is a unitless ratio of the permittivity of a material relative to that of a vacuum, its use in place of the vacuum permittivity in Eq. (4) is not appropriate. While the use of the *permittivity* of the specimen material in place of the vacuum permittivity would yield an output in terms of energy per unit distance, the value of $-dE/dx$ obtained for the materials concerned would differ significantly from the values quoted (more than an order of magnitude at 200 keV). It is also noted that, for silicon at 200 keV, the value of $-dE/dx$ calculated using Eq. (4) (for comparison purposes only) was in good agreement with that reported by Jenčič *et al.*, but the values quoted by Edmondson *et al.* could not be obtained (differing by approximately a factor of two).

The thermal conductivity of a polycrystalline material is known to vary with porosity and grain size. Small grain size may reduce thermal conductivity due to increased phonon scattering at grain boundaries in cases where the mean free path of phonon scattering is less than the grain size [76]. The effect of porosity on the thermal conductivity of Li_2TiO_3 has been reported by Saito *el al.* [76] and Gierszewski [77]; both of whom provide equations, derived from experimental data, which allow the thermal conductivity of Li_2TiO_3 of a known porosity to be estimated. In this work, since the temperature rise induced by electron beam heating is inversely proportional to thermal conductivity, the equation given by Gierszewski [77] (Eq. (7)) was used, simply because it yielded the lesser of the two values obtained.

$$\kappa = (1 - P)^{2.9}[5.35 - (4.78 \times 10^{-3}T) + (2.87 \times 10^{-6}T^2)] \tag{7}$$

Where κ is the thermal conductivity, P is the porosity of the sample as a proportion of its theoretical density (1 – [measured density / theoretical density]), and T is the sample temperature.

In order to determine whether beam heating was likely to have contributed to the observed cavity formation and growth in Li_2TiO_3 under the TEM electron beam, the maximum local temperature increase due to beam heating was calculated for Li_2TiO_3 using equation (3). The primary beam current was recorded as 55 nA at the specimen position, the minimum beam radius was estimated to be 1.5 µm. The thermal conductivity of the highest porosity specimen at 300 K (~27 °C) was estimated using equation (7). $\Delta E/d$ was substituted for $-dE/dx$, which was calculated using equation (4). With respect to equation (4), the input value of I_e was calculated according to equation (6) using the elemental electron excitation energies reported by Seltzer *et al. [75]*, and the theoretical density of Li_2TiO_3 [78] was used as the input value for ρ as this yields the maximum value of $-dE/dx$, which in turn yielded the maximum value of ΔT. It is also valid to use the theoretical density in the calculation of $-dE/dx$ since regions of "porosity" in a thin film TEM sample are effectively empty space, as such no energy is deposited in the pores; whereas the sample grains themselves (where energy is deposited by the beam) are likely to exhibit densities close to the theoretical maximum. The results are summarised in Table 5.2.

Table 5.2: Energy loss of primary beam electrons (-dE/dx) and the corresponding maximum temperature rise (ΔT) attributable to electron beam heating effects in Li_2TiO_3. Key parameters used in calculations are included.

Material	Z	ρ (*Theoretical) / g cm^{-3}	E / keV	I_e / eV	- dE / dx / eV nm^{-1}	I / nA	P	κ / W m^{-1} K^{-1}	ΔT / K
Li_2TiO_3	8.6	3.43	300	132	0.115	55	0.35	1.2	11.6

The results of beam heating calculations show that the maximum local temperature rise in Li_2TiO_3 attributable to possible beam heating effects under the conditions employed here was approximately 12 °C. Hence it is concluded that the effects of beam heating on defect aggregation and subsequent cavity formation in Li_2TiO_3 under electron irradiation were negligible under the conditions employed here, since the maximum temperature rise induced by the TEM electron beam was insignificant in terms of the possible enhancement of defect mobility.

Radiolysis

Displacement damage however, often manifests itself in the form of vacancy clusters [79]; as such, it is probable that displacement damage is responsible for the formation of vacancy-type defects observed in Li_2TiO_3 under electron irradiation in a TEM.

Displacement damage can occur directly, as a result of elastic collisions of incident electrons with atomic nuclei, or indirectly as a result of radiolysis due to inelastic interactions with atomic electrons. In the case of the latter, electronic excitations and/or complete ionisation can lead to the production of exciton states and subsequent bond cleavage [80, 81]; examples of inorganic materials which exhibit radiolytic displacement damage mechanisms include alkali halides [43-45], alkaline earth fluorides [47, 48] and silicates [49, 50]. For displacement to occur via radiolysis, a sufficiently localised excitation of energy greater than the threshold displacement energy (E_d) and sufficient excitation lifetime (>1 ps) must be induced, and a mechanism for the conversion of excitation energy to momentum must exist [42]. One such mechanism was proposed by Knotek and Fiebelman [82] to explain the phenomenon of electron stimulated desorption of oxygen form maximum valency ionic compounds (where the cation is ionised to its maximum oxidation state such that its outer electron shell is nominally empty). According to this mechanism, externally induced electronic excitation (i.e.

by an electron beam) resulting in ionisation of a core electron of the cation results in an inter-atomic Auger process whereby the core electron hole on the cation is filled by a valence electron from a neighbouring oxygen anion. The energy released in this decay process is transferred to other electrons in the oxygen anion, resulting in Auger emission of one or two Auger electrons; thus, Auger decays can remove sufficient electrons from oxygen anions to render them positively charged. The resulting Coulombic repulsion between positively charged oxygen ions and surrounding metal cations subsequently leads to displacement (or desorption if located at the surface) of the oxygen ion.

It is not clear from the current literature whether such a mechanism exists in Li_2TiO_3 to efficiently convert the energy released as a result of the decay of electronic excitations into sufficient momentum to induce displacement. However, owing to its relatively low electronic conductivity (~10^{-6} S cm^{-1} [83, 84]) and the wide band gap responsible for its dielectric properties (reported as 3.49 eV by Wan *et al.* [85]) Li_2TiO_3 may satisfy all of the other criteria for radiolytic displacement; as such radiolysis cannot be ruled out as a possible cause of displacement damage in this case.

Knock-on damage

For knock-on displacement to occur, the kinetic energy transferred to the lattice atom by incident electrons must be sufficient to exceed the displacement energy (E_d); thus, if the maximum possible kinetic energy transfer to lattice atoms exceeds E_d, lattice atoms can be permanently displaced. Several different models exist which describe the maximum kinetic energy transfer from electrons to lattice atoms; commonly used models include an equation given by Hobbs [80] (Eq. (8)), the Sonder and Sibley equation [86] (Eq. (9)), the expression given by Lehmann [87] (Eq. (10)) and the binary collision model (Eq. 11). It is noted that, while the Hobbs, and Sonder and Sibley equations were derived experimentally, the binary collision model is based on ion-solid interactions using a hard-sphere approximation and as such is not strictly valid for interactions involving relativistic particles such as electrons. Nonetheless the binary collision model is still occasionally utilised with respect to electron-solid interactions [88].

$$T_{max} = \frac{5(20E+10)^2-100}{A} \qquad (8)$$

$$T_{max} = \frac{2147.7E(E+1.002)}{A} \qquad (9)$$

$$T_{max} = \frac{2E(E+2mc^2)}{Mc^2} \qquad (10)$$

$$T_{max} = E \frac{4Mm}{(M+m)^2} \qquad (11)$$

Where T_{max} is the maximum energy transferred (in eV) to a lattice atom of relative atomic mass A or mass M (in amu), by an electron of mass m (in amu). c is the speed of light in a vacuum (in ms^{-1}), and E is the primary beam energy (in MeV for equations (8) and (9), and eV for equations (10) and (11)). With respect to equations (10) and (11), in order to account for relativistic effects due to electron velocities in excess of 0.5c, the electron mass should be adjusted according to the equation [73]:

$$m = N_A m_0 (1 + Ve/m_0 c^2) \qquad (12)$$

where m_0 is the rest mass of the electron (in kg), V is the accelerating voltage (in V), and N_A is the Avogadro constant, to yield the relativistic mass of the electron, m (in amu).

The maximum kinetic energy transferred to lattice atoms in Li_2TiO_3 by 300 keV electrons, calculated from each model, are given in Table 5.3.

Table 5.3: Maximum kinetic energy transfer to lattice atoms (Li, Ti and O) in Li_2TiO_3 by 300 keV electrons. Calculated according to equations (8) - (11).

Lattice atom	Maximum Kinetic Energy Transfer / eV				Displacement Energy (E_d) / eV (Fischer *et al*. [71])
	Hobbs' (Eq. 8)	Sonder and Sibley (Eq. 9)	Lehmann (Eq. 10)	Binary collision (Eq. 11)	
O	73.75	52.43	65.31	65.30	23
Li	170.00	120.86	150.54	150.51	45
Ti	24.65	17.53	21.83	21.83	76

By comparing the calculated maximum kinetic energy transfer to the displacement threshold energies for each atom (Li, O and Ti), as reported by Fischer *et al*. [71], it can be concluded that, regardless of the model employed, sufficient energy is transferred to lattice atoms in Li_2TiO_3 by incident electrons to displace both lithium and oxygen atoms from their respective lattice sites at an operating voltage of 300 kV. Conversely, insufficient energy is transferred to titanium lattice atoms to induce displacement. Hence we propose that the vacancy-type defects observed in Li_2TiO_3 after electron irradiation in a TEM arise as a result of irradiation damage associated with the displacement of lithium and oxygen atoms.

Using the maximum kinetic energy transfer given by the above equations, the displacement cross section (i.e. the probability of a displacement event) for a direct interaction between incident electrons and lattice atoms can be estimated using the McKinley-Feshbach approximation [89] to the Mott expression [90]. A detailed explanation of how Eq. (14) is attained from the integral shown in Eq. (13) using this approximation can be found in the review by Reyes-Gasga *et al.* [91].

$$\sigma_d = \int_0^{T_{max}} P_d(T)\sigma(T, E)dT. \qquad (13)$$

$$\sigma_d = 4\pi \left(\frac{Za_0 U_R}{m_0 c^2}\right)^2 \frac{1-\beta^2}{\beta^4} \left[\left(\frac{T_{max}}{E_d} - 1\right) + \alpha\beta\pi \left\{2\left[\left(\frac{T_{max}}{E_d}\right)^{1/2} - 1\right] - ln\left(\frac{T_{max}}{E_d}\right)\right\} - \beta^2 ln\left(\frac{T_{max}}{E_d}\right)\right] \quad (14)$$

The displacement cross section, σ_d, is obtained by integrating the product of $\sigma(T, E)$ (the cross section for energy transfer T for an electron of energy E), and the probability of a displacement event due to the energy transferred, $P_d(T)$, over all possible values as per Eq. (13). For direct interaction only (i.e. not including cascade effects) the maximum and minimum limits of Eq. (13) become T_{max} and E_d respectively, and the $P_d(T)$ term has the conditions: (i) $P_d(T) = 0$ if $T < E_d$, and (ii) $P_d(T) = 1$ if $E_d < T < T_{max}$. $\sigma(T, E)$ is given by the McKinley-Freshbach approximation to the Mott expression to yield Eq. (14), where Z is the atomic number of the displaced nucleus, E_d is the corresponding displacement energy, a_0 is the Bohr radius, U_R the Rydberg energy (in J), $\alpha = Z/137$, and $\beta = v/c$ where v is the velocity of incident electrons. v can be calculated according to equation (5).

The displacement cross sections for direct interaction between incident 300 keV electrons and constituent lattice atoms in Li_2TiO_3, calculated using the maximum kinetic energy transfer corresponding to each of the previously detailed models, are shown in Table 5.4. Note that while values for the direct interaction cross section of titanium have been included for completeness, the value stated corresponds to the cross section for energy transfer only as opposed to displacement since insufficient energy is transferred to titanium lattice atoms to induce displacement from it's lattice site; as such the displacement cross section for titanium is in fact zero as the $P_d(T)$ term in Eq. (13) is always equal to zero.

Table 5.4: Displacement cross sections for Li, Ti and O lattice atoms in Li_2TiO_3 calculated using different models for T_{max} using Eq. (14). *Note that in the case of Ti, the value stated corresponds to the cross section for energy transfer only as insufficient energy is transferred to induce displacement.

Displacement cross section for direct interaction σ_d / Barns				
Lattice atom	σ_d (T_{max} Hobbs)	σ_d (T_{max} Sonder and Sibley)	σ_d (T_{max} Lehmann)	σ_d (T_{max} Binary collision)
O (σ_d)	27.25	14.13	21.90	21.90
Li (σ_d)	4.92	2.71	4.02	4.02
*Ti (σ_d)	14.12	37.27	21.70	21.71

Regardless of which model of kinetic energy transfer is used, the estimated displacement cross section for oxygen is consistently larger than that of lithium due to the relationship between atomic number, Z, and displacement cross section. This indicates that oxygen atom displacements are likely to occur more frequently than those of lithium atoms when exposed to the TEM electron beam under the conditions employed here. However, it is also noted that these approximations provide only an indication of the probability of displacement, and are not necessarily indicative of the defect concentration per incident electron since they do not account for recombination. Since there are three oxygen sites for every two lithium sites in Li_2TiO_3, a greater proportion of oxygen sites are available for recombination of oxygen Frenkel defects than those of lithium; thus the probability of oxygen defect recombination is greater than that of lithium defect recombination. As such, it not necessarily the case that the contribution of lithium defects to the observed vacancy-type defect formation and growth is lesser than that of oxygen defects.

Radiation induced cavity growth

Regarding the mechanisms of radiation induced cavity growth, one long-standing theory is that, following initial displacement and the associated formation of a Frenkel pair, interstitial defects are preferentially absorbed at dislocations due to the high elastic strains associated with self-interstitial atoms [29]. This results in vacancy supersaturation, and a net vacancy flow to vacancy clusters, which are relatively unstrained. Indeed, an atomic scale HRTEM experiment by Xu *et al*. [26] unequivocally showed the nucleation and growth of voids in the vicinity of self-interstitial atom (SIA) loops in Mg under electron irradiation. Void nucleation in this case was attributed to vacancy supersaturation

adjacent to SIA loops which acted as biased sinks for interstitial atoms. However, since no resolvable dislocations were observed in any of the Li_2TiO_3 samples studied here, and cavity growth was shown to occur across the entire area illuminated by the electron beam, an alternative mechanism is likely to be dominant.

The thermal migration energy of interstitials is generally significantly lower than that of vacancies in oxide ceramics [92]. Hence, mobile interstitial atoms migrate to the free surface of the TEM foil more readily than vacancies. Free surfaces act as efficient sinks for defects. Additionally, since surface atoms are not fully coordinated, and need only be supplied with sufficient energy to break the remaining bonds in order to be displaced, whereas bulk atoms must additionally receive sufficient energy to (i) break all bonds, and (ii) form a stable Frenkel pair [93]; the displacement energy of atoms at the surface is significantly lower than that of bulk lattice atoms. As such, surface interstitials are readily lost due to sputtering. To compound this effect, lithium is known to be volatile and as such may be lost to surface evaporation under the influence of the electron beam. This preferential loss of interstitial defects at the sample surface leaves behind an excess vacancy concentration. Subsequent migration of single vacancies and small vacancy clusters by a combination of thermal and ballistically induced processes results in a net vacancy flux to larger, less mobile clusters, leading to cavity growth.

As part of a computational modelling study designed to investigate point defect processes and lithium diffusion, Kuganathan *et al*. [94] evaluated the formation energies of intrinsic defects in Li_2TiO_3 by comparing a defective crystal to an ideal, non-defective, crystal (the defect formation parameters of which are interconnected by thermodynamic relations) using atomistic simulations. They reported that the defect formation energy for intrinsic Li Frenkel defects is significantly lower than that of oxygen Frenkel defects in Li_2TiO_3 under thermal equilibrium conditions. The presence of lithium vacancies is also believed to facilitate lithium diffusion [95]; hence lithium diffusion is likely to be enhanced under electron irradiation due to the increased vacancy concentration resulting from electron beam induced displacement damage. While comparatively few studies have been carried out on oxygen diffusion, it is likely that oxygen ions are less mobile than lithium ions due to the larger ionic radius of oxygen anions. Oyaidzu *et al.* [96] investigated the annihilation of radiation induced defects during isothermal annealing of neutron irradiated Li_2TiO_3 using Electron Spin Resonance (ESR) spectroscopy. They reported that defect annihilation consisted primarily of two processes; a fast process associated with lithium ion diffusion, and a slow process associated with the annihilation of

oxygen vacancies, with the slower kinetics of the latter process being attributed to low oxygen diffusivity. In light of these factors, it is likely that the diffusion and subsequent loss of lithium interstitials at the free surface of the TEM foil (resulting in the increased excess vacancy concentration responsible for cavity growth) is greater than the loss of oxygen interstitials due to the faster diffusion kinetics of Li.

Therefore, we propose that, despite possessing a smaller displacement cross section than oxygen, the contribution of vacancy defects originating from the electron beam induced displacement of lithium lattice atoms to the nucleation and growth of cavities in Li_2TiO_3 is likely to be greater than those originating from oxygen displacement.

Following initial nucleation, based on the defect size and number density data presented in Figure 5.6, growth of existing (defined here as TEM resolvable) defects was found to be favoured over the nucleation of additional defect aggregations at new sites. During the early stages of defect growth, it is proposed that ongoing displacement events induced by constant electron irradiation provide a net positive flux of vacancies to the walls of existing defects by Brownian motion. Subsequently, continued growth in conjunction with the close proximity of defects results in coalescence and the formation of larger cavities. Note that since the resolvable cavities were found to be largely immobile, coalescence events are believed to occur primarily as a result of impingement of the walls of neighbouring cavities on one another during growth, their close proximity negating the need for significant migration. This phenomenon was most apparent during the first 30 minutes of exposure to the electron beam, concurrent with the fastest rate of coarsening. Beyond 40 minutes of beam exposure, both number density and mean defect size began to stabilise as the occurrence of further coalescence events became less frequent. This is likely to be due to the further reduced mobility of larger, more stable cavities at ambient temperature, combined with the relatively large number of additional vacancies which would be required to induce a sufficient volume increase for further coalescence of larger contiguous cavities to occur without significant migration. Thus, in the absence of coalescence, further defect growth is abated as the process becomes predominantly reliant on diffusion of newly created vacancies to existing cavities. A cavity growth mechanism dominated by coalescence (as opposed to an Ostwald Ripening type mechanism) may also account for the irregular morphology of larger cavities; according to Muntifering *et al.* [32] cavity growth by coalescence was reportedly responsible for the non-spherical morphology of larger cavities in nanocrystalline Ni which had been implanted with helium and self-ions. Their findings, corroborated by a video recorded

during *in-situ* (TEM) annealing experiments, showed that only one side of some cavities expanded to combine with a neighbouring cavity, resulting in the formation of a larger, non-spherical cavity.

Given that small vacancy clusters readily collapse into dislocation loops or stacking fault tetrahedra [97-100], the homogeneous nucleation of voids by random coalescence of mobile vacancies is generally considered unlikely [101]; as such it has long been theorised that the presence of gas atoms is essential for void / cavity nucleation and subsequent growth [29]. Hence, the fact that electron beam induced vacancy-type defects in Li_2TiO_3 are observed to nucleate extensively and evolve into larger cavities (as opposed to collapsing or being absorbed by neutral defect sinks such as grain boundaries) may indicate the presence of a gaseous species which sufficiently stabilises the internal free surfaces of small clusters to facilitate growth. Formation of a Li_2CO_3 surface layer on Li_2TiO_3 due to exposure to atmospheric air under ambient conditions has been reported previously [57]; based on the behaviour of other lithium ceramics [58-62] surface reaction at ambient temperature likely occurs via an LiOH intermediate (resulting from initial reaction of Li_2TiO_3 with atmospheric water) which subsequently reacts with CO_2 to form Li_2CO_3. Figure 5.7 shows an X-ray diffraction pattern obtained from an Li_2TiO_3 pellet that had been exposed to ambient air for a period of several months. In addition to the peaks corresponding to the expected Li_2TiO_3 phase, peaks corresponding to Li_2CO_3 are present. This indicates the presence of a Li_2CO_3, the formation of which is attributed to the surface reaction of Li_2TiO_3 with atmospheric CO_2.
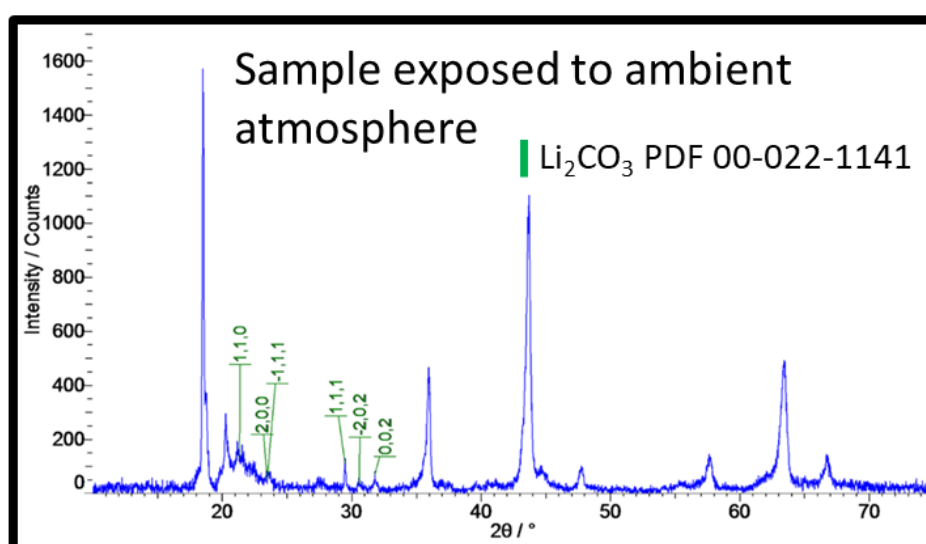
Figure 5.7: XRD pattern obtained from an atmospherically exposed Li_2TiO_3 pellet showing additional peaks corresponding to the presence of Li_2CO_3 in green. Indexed according to ICDD PDF no. 01-087-0728 [63].

Since the surface area of TEM specimens is very high, it is feasible that this reaction occurs to a significant extent during specimen preparation. Lin *et al.* [102] reported that the Li_2CO_3 surface reaction layer found on lithiated NiO nanosheets rapidly decomposed under the TEM electron beam during the acquisition of Electron Energy Loss Spectra (EELS). The decomposition of Li_2CO_3 is likely to evolve CO_2 according to the following reaction:

$$Li_2CO_3 \text{ (s)} \quad \rightarrow \quad Li_2O \text{ (s)} + CO_2 \text{ (g)}$$

Hence it is speculated that CO_2, evolved as a result of the decomposition of a Li_2CO_3 surface reaction layer under electron irradiation, may be responsible for the stabilisation of vacancy-type defects induced by the electron beam, thus facilitating the nucleation and growth of the observed cavities in Li_2TiO_3.

Electron beam induced damage – effect of ceramic microstructure

The effect of ceramic microstructure on electron irradiation induced defect formation and evolution was studied using the four pellets processed under different conditions as described in the Microstructure and Phase Analysis section. These processing conditions resulted in the production of ceramic samples which exhibited different grain sizes and densities, as described in Table 5.1 and variations in the extent of intrinsic crystallographic disorder attributed to stacking fault concentrations, as indicated in Figure 5.4. To investigate the effect of grain size and porosity on electron beam induced damage, thin film TEM specimens with the following grain sizes were examined, sintering conditions are detailed in brackets: High Porosity Sample A (900 °C, 3 h) 0.58 ± 0.11 nm; High Porosity Sample B (900 °C, 6 h) 0.75 ± 0.12 nm; Low Porosity Sample C (1000 °C, 2 h), 0.93 ± 0.12 nm; and Low Porosity Sample D (1100 °C, 6 h), 1.09 ± 0.08 nm. Bright field through-focal-series were taken at 10 minute intervals during the electron beam irradiation, up to a maximum of 30 minutes' beam exposure time. Figure 5.8 shows under-focussed bright field TEM micrographs of the samples before and after 30 minutes of exposure to the electron beam, the corresponding through-focal-series micrographs are inset. It is visually apparent that the specimens sintered at 900 °C (A and B) exhibit a higher concentration of cavities than the analogous specimens sintered at higher temperatures (C and D), indicating that samples sintered at higher temperature may be less susceptible to electron beam induced cavity formation.
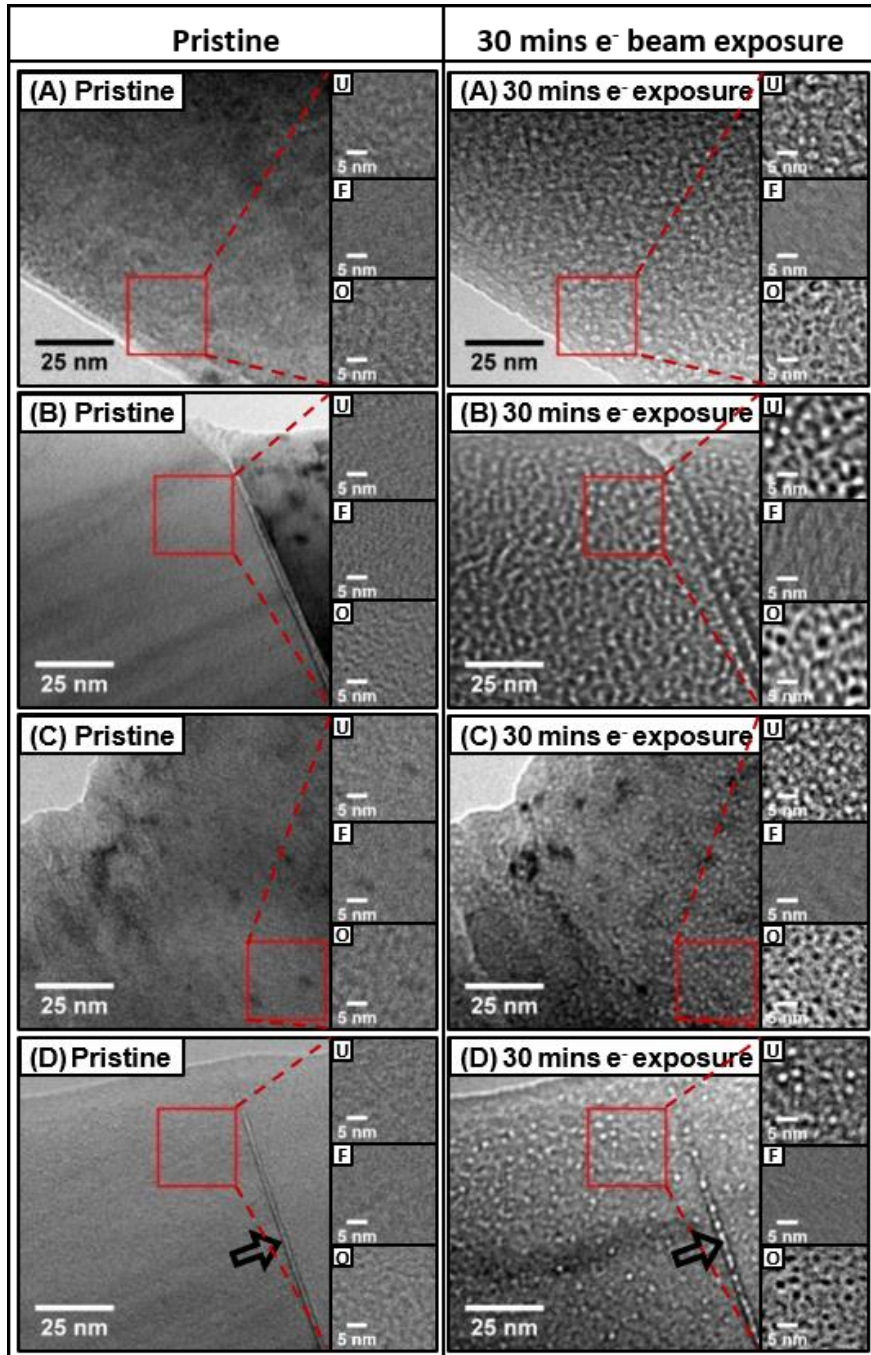
Figure 5.8: Under-focussed bright field TEM micrographs showing the difference in the size and number density of cavities observed in Li_2TiO_3 ceramics prepared under different conditions, before (pristine) and after 30 minutes of exposure to a 300kV electron beam at room temperature. Corresponding through-focal-series inset showing change in contrast in under-focused (U), in-focus (F) and over-focused (O) micrographs, characteristic of vacancy-type defects.

The size and number density of TEM resolvable vacancy-type defects were determined using the method described previously. Figure 5.9 shows the mean defect size and number density of electron beam induced cavities observed in Li_2TiO_3 specimens sintered under different conditions during the first 30 minutes of electron beam exposure. In each case, cavity growth and a concurrent decrease

in number density approximately commensurate with the degree of growth, was observed with increased electron beam exposure time. This suggests that the coarsening mechanisms proposed in the previous section are likely to be consistent for all of the samples examined in this study.
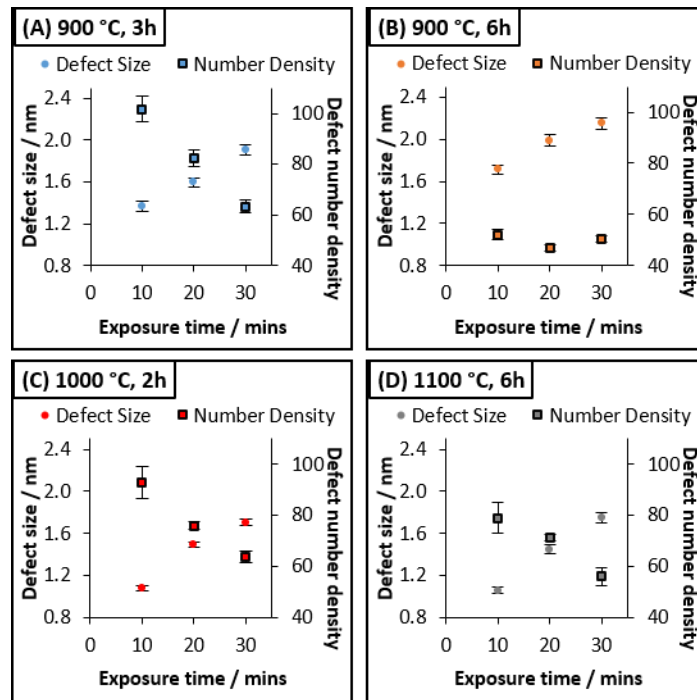
Figure 5.9: Mean average size and number density observed in Li_2TiO_3 ceramics prepared under different conditions (sintering conditions: (A): 900 °C, 3 hours; (B): 900 °C, 6 hours; (C): 1000 °C, 2 hours; (D): 1100 °C, 6 hours) after 30 minutes of exposure to a 300 keV electron beam at room temperature

It is noted that the high porosity sample (B) sintered for the longer of the two durations (900 °C, 6h) exhibited abnormally large cavities at significantly lower number density after only a short period of exposure to the electron beam when compared to other specimens. It is suspected that this is due to a difference in electron beam intensity between this experiment and those of the other specimens. As condenser lens settings were not explicitly monitored, the beam intensity may have inadvertently been greater in this case, resulting in accelerated cavity growth and stabilisation of number density over a shorter time period.

Comparison of the mean size and corresponding number density of cavities observed in the high porosity sample (A) with the smallest grain size (sintered at 900 °C, 3h), with those observed in the low porosity specimens with larger grains ((C) sintered at 1000 °C and (D) sintered at 1100 °C) reveals that sample A exhibited cavities that were both larger, and greater in number density than samples

C and D. Comparing the low porosity specimens (C and D), mean cavity size was shown to be comparable, but the sample with the larger of the two grain sizes ((D) sintered at 1100 °C, 6h) exhibited lower cavity number density. Hence, it is arguable that the microstructural properties of low porosity and large grain size reduce the susceptibility of Li_2TiO_3 to electron beam induced damage.

The influence of grain size on radiation induced damage accumulation and recovery has been investigated for numerous materials; the contrasting results of selected studies which have been conducted on oxide ceramics are briefly discussed forthwith.

A number of materials have been reported to have superior radiation stability in nanocrystalline form compared to their larger grained analogues, this effect was first highlighted by Rose *et al.* [31] who reported a linear correlation between grain size and defect number density in nanocrystalline ZrO_2 in the grain size range 18 - ~70nm, saturation of defect number density was apparently observed in grains 70 – 100 nm in size. They proposed that, since no resolvable defects were observed in grains smaller that 15nm, all point defects were absorbed at grain boundaries, which act efficient defect sinks. Agglomeration of defects in larger grains, leading to cluster formation, was attributed to the increased diffusion path length to grain boundaries. Enhanced radiation stability in the context of defect accumulation and amorphisation has also been reported for nanocrystalline $MgGa_2O_4$ [34], which was reported to remain crystalline at Kr^+ fluences approximately a factor of eight higher than the onset of amorphisation in large grained (~10 µm) polycrystalline counterparts; and $Gd_2Zr_2O_7$ [35], where a lesser proportion of samples consisting of 55 nm grains was reported to have amorphised than those consisting of 221 nm grains under He^+ irradiation. Dey *et al.[36]* reported that larger grained (220 nm) samples of yttria stabilised zirconia exhibited a higher number density of defects than those with smaller grains (25 – 38 nm) under Kr^+ irradiation; adding that both vacancy and interstitial clusters were observed in larger grained samples, where only vacancy-type defect clusters were observed in smaller grained samples. They attribute this observation to the preferential migration of interstitial defects to defect sinks at grain boundaries during the cascade. However, aside from the increased availability of defect sinks associated with the increased grain boundary area of smaller grained materials, their irradiation response can also be affected by competing effects which are detrimental to radiation damage tolerance. High surface energy associated with increased interfacial area enhances the driving force for structural modifications which reduce the free energy of the system, such as grain growth and phase transformations, which can reduce radiation stability

[38]. The highly localised energy deposition resulting from the increased confinement of excited phonons and electrons in small grains, where the dissipation of energy is impeded due to scattering at grain boundaries, can result in thermal spikes. In conjunction with the excess free energy of grain interfaces, these two factors reduce the energy difference between amorphous (disordered) and crystalline (ordered) states, lowering radiation damage resistance; as proposed by Lu *et al.* to explain the amorphisation of nanocrystalline monoclinic ZrO_2 under U^+ irradiation [103] when bulk ZrO_2 with ~ 0.2 μm grains could not be amorphised under similar irradiation conditions [104]. Other materials where larger grain size has been reported to improve radiation tolerance include ZrO_2-MgO composite ceramics [105], where larger grained samples exhibited increased resistance to phase transitions under Xe^+ irradiation; and UO_2, ThO_2 and CeO_2 [37], all of which showed increased volumetric swelling of unit cell parameters in nanocrystalline form (~20 nm grain size) as a result of Au^+ irradiation compared to microcrystalline analogues (~2 μm grain size).

Here, we propose that the shorter diffusion path length to grain boundaries and free surfaces, which act as sinks for defects, in the smaller grained specimens of higher porosity (A and B), results in greater losses of mobile interstitials produced as a result of electron beam induced displacement damage; thus lowering the probability of the annihilation of Frenkel defects by recombination. This in turn leads to a greater excess vacancy concentration within grains, facilitating cavity growth.

Preferential cavity formation at the grain boundary, where lattice atoms are less ordered and the concentration of intrinsic defects is greater, is also apparent in the low porosity specimen with the largest grains (see Figure 5.8D, marked with an arrow). This may indicate that cavity nucleation occurs preferentially at existing intrinsic defect sites.

XRD patterns obtained from the ceramic pellets from which the thin film TEM specimens were prepared (detailed previously, Figure 5.4) imply that the ideal, fully ordered Li_2TiO_3 structure was not completely formed at the lower end of the sintering temperatures employed. As such the degree of disorder, and consequently the concentration of intrinsic defect sites, is likely to be greater in specimens which had been sintered at lower temperatures. Hence, the greater number of sites available to facilitate cavity nucleation results in increased cavity number density in specimens sintered at lower temperature. It is therefore proposed that the apparently lesser susceptibility of Li_2TiO_3 specimens with lower porosity and larger grains to electron beam induced cavity formation

relative to analogous small grained specimens of high porosity, is due to a combination of crystallographic and microstructural contributions:

(i) The greater degree of crystallographic order present in specimens sintered at higher temperature results in fewer intrinsic defect sites to facilitate cavity nucleation, and thus reduced cavity number density.

(ii) The longer diffusion path to the surface of specimens with larger grains reduces the extent of interstitial defect losses due to sputtering and evaporation, thereby reducing the excess vacancy concentration responsible for cavity growth.

The combination of these two factors is believed to be responsible for the observation that electron beam induced cavities in samples which had been sintered at higher temperature, with larger grains and lower porosity, exhibit fewer cavities of smaller size than those observed in in smaller grained, high porosity samples sintered at lower temperature.

Conclusions

We have shown that Li_2TiO_3 is susceptible to beam damage under a conventional 300 keV TEM electron beam at room temperature. The damage induced by electron irradiation manifests itself as cavity formation, which is believed to be due to the aggregation of vacancy-type defects introduced as a result of displacement damage. While radiolytic displacement mechanisms may contribute to the induced damage, our calculations show that sufficient kinetic energy is transferred from 300 keV electrons to Li and O lattice atoms in Li_2TiO_3 via elastic interactions to induce their displacement from equilibrium positions; hence knock-on damage is proposed to be the primary damage mechanism. The effects of electron beam heating were found to be negligibly small. Cavity nucleation and growth is proposed to occur as a result of the preferential loss of interstitial defects, introduced as a result of electron beam induced displacements, from the surface of thin film specimens. Owing to the lesser thermal migration energy of interstitial defects compared to that of vacancies, it is theorised that the preferential loss of mobile interstitial defects at the specimen surface leaves behind an excess vacancy concentration which ultimately leads to vacancy supersaturation and the formation of vacancy clusters. Following the extensive nucleation in the first few minutes of electron irradiation, subsequent growth of nucleated clusters into TEM resolvable cavities is attributed to continued introduction of excess vacancy defects as a result of electron beam induced displacement and

preferential interstitial losses, resulting in a net influx of vacancies to the walls of vacancy clusters and small cavities. The initial stages of cavity growth are assumed to occur due to the net positive flux of excess vacancies, induced by ongoing displacement events and sustained loss of interstitial defects at the specimen surface under electron irradiation, to the walls of existing cavities by Brownian motion. The coalescence of contiguous cavities in close proximity as a result of impingement of the walls of neighbouring cavities on one another is proposed to be the dominant growth mechanism during subsequent stages of relatively rapid growth and concurrent coarsening, the rate of which was shown to slow or cease entirely after 40-60 minutes of electron beam exposure as the supply of vacancies required to facilitate further growth of larger, immobile cavities became increasingly reliant on Brownian motion of newly created Frenkel defects.

Despite possessing a lesser displacement cross section, the contribution of vacancies originating from lithium displacement to the total excess vacancy concentration responsible for cavity growth is speculated to be greater than that of oxygen. This is considered likely due to the combination of the faster diffusion kinetics of lithium, resulting in a greater extent of lithium interstitial loss at the surface, and the lesser proportion of available sites for defect recombination.

Cavity nucleation and growth in Li_2TiO_3 under electron irradiation may be facilitated by the stabilising effect of gaseous CO_2 produced as a result of the decomposition of an Li_2CO_3 surface reaction layer under the electron beam.

Specimens sintered at higher temperatures, which exhibited low porosity and larger grain size appear to be less susceptible to electron beam induced cavity formation than analogous high porosity specimens with smaller grains which had been sintered at lower temperatures. This is attributed to the former possessing a lesser number of intrinsic defects which may act as cavity nucleation sites, in conjunction with the lesser degree of interstitial losses from the specimen surface due to the longer diffusion path to the free surface in specimens with larger grains. These observations suggest that the properties of low porosity, large grain size and low intrinsic defect concentration may enhance the resistance of Li_2TiO_3 to electron irradiation damage and associated cavity formation and growth.

Cavities induced as a result of electron beam damage could easily be misinterpreted as damage and / or gas bubble formation induced by external radiation sources during the inspection thereof using TEM techniques; as such, caution is advised when interpreting the results of such experimental work

where Li_2TiO_3 or similar materials are concerned in order to avoid the unintentional reporting of erroneous findings. Given the proposed mechanism of cavity growth, the effects of electron irradiation on Li_2TiO_3 described in this work are likely to be exacerbated in thin film TEM specimens due to surface effects (i.e. very high surface area to volume ratio); it is also noted that the mechanisms of neutron damage differ significantly from that which is induced by electrons due to the significantly greater mass and neutral charge of the former particle. Nonetheless, in light of the high flux of high energy neutrons to which lithium titanate would be subjected in the breeder blanket of a working fusion reactor, if the cavity formation and growth observed in this study is indeed primarily due to a similar mechanism of knock-on displacement damage, further nanoscale investigation of the radiation tolerance of Li_2TiO_3 and other candidate ceramic breeder materials should be undertaken such that the composition and microstructural properties thereof can be tailored in such a way as to mitigate these effects as far as reasonably possible. The accompanying second part of this publication investigates the effect of temperature on the formation and growth of electron beam induced cavities in Li_2TiO_3 and the interaction of implanted helium therewith.

References (for Chapter 5 manuscript only)

[1]   N. T. Wu, H. Wu, H. Liu, and Y. Zhang, "Solvothermal coating $LiNi_{0.8}Co_{0.15}Al_{0.05}O_2$ microspheres with nanoscale Li_2TiO_3 shell for long lifespan Li-ion battery cathode materials," *Journal of Alloys and Compounds,* vol. 665, pp. 48-56, Apr 2016, doi: 10.1016/j.jallcom.2016.01.044.

[2]   L. Q. Zhang and H. Noguchi, "Novel layered Li-Cr-Ti-O cathode materials related to the $LiCrO_2$-Li_2TiO_3 solid solution," *Journal of the Electrochemical Society,* vol. 150, no. 5, pp. A601-A607, May 2003, doi: 10.1149/1.1566016.

[3]   K. Meng, Z. X. Wang, H. J. Guo, X. H. Li, and D. Wang, "Improving the cycling performance of $LiNi_{0.8}Co_{0.1}Mn_{0.1}O_2$ by surface coating with Li_2TiO_3," *Electrochimica Acta,* vol. 211, pp. 822-831, Sep 2016, doi: 10.1016/j.electacta.2016.06.110.

[4]   Y. W. Li *et al.*, "High performance Co_3O_4/Li_2TiO_3 composite hollow nanofibers as anode material for Li-ion batteries," *Journal of Materials Science-Materials in Electronics,* vol. 29, no. 16, pp. 14222-14231, Aug 2018, doi: 10.1007/s10854-018-9555-5.

[5]   Y. Wang, A. Zhou, X. Dai, L. Feng, J. Li, and J. Li, "Solid-state synthesis of submicron-sized $Li_4Ti_5O_{12}$/Li_2TiO_3 composites with rich grain boundaries for lithium ion batteries," *Journal of Power Sources,* vol. 266, pp. 114-120, 2014/11/15/ 2014, doi: https://doi.org/10.1016/j.jpowsour.2014.05.002.

[6]   H. S. Bhatti *et al.*, "Electrochemical Characteristics and Li^+ Ion Intercalation Kinetics of Dual-Phase $Li_4Ti_5O_{12}$/Li_2TiO_3 Composite in the Voltage Range 0-3 V," *Journal of Physical Chemistry C,* vol. 120, no. 18, pp. 9553-9561, May 2016, doi: 10.1021/acs.jpcc.5b12114.

[7]   A. Lakshmi-Narayana, M. Dhananjaya, N. Guru-Prakash, O. Hussain, A. Mauger, and C. Julien, "Li_2TiO_3/Graphene and Li_2TiO_3/CNT Composites as Anodes for High Power Li-Ion Batteries," *ChemistrySelect,* vol. 3, no. 31, pp. 9150-9158, 2018.

[8] Y.-z. Hao, Q.-l. Zhang, J. Zhang, C.-r. Xin, and H. Yang, "Enhanced sintering characteristics and microwave dielectric properties of Li_2TiO_3 due to nano-size and nonstoichiometry effect," *Journal of Materials Chemistry,* 10.1039/C2JM33788F vol. 22, no. 45, pp. 23885-23892, 2012, doi: 10.1039/C2JM33788F.

[9] Y.-Z. Hao, H. Yang, G.-H. Chen, and Q.-L. Zhang, "Microwave dielectric properties of Li_2TiO_3 ceramics doped with LiF for LTCC applications," *Journal of Alloys and Compounds,* vol. 552, pp. 173-179, 2013/03/05/ 2013, doi: https://doi.org/10.1016/j.jallcom.2012.10.110.

[10] V. C. Martins *et al.*, "High thermal stability OF Li_2TiO_3-Al_2O_3 composite in the microwave C-Band," *Journal of Physics and Chemistry of Solids,* vol. 125, pp. 51-56, 2019/02/01/ 2019, doi: https://doi.org/10.1016/j.jpcs.2018.10.011.

[11] A. Lakshmi Narayana, M. Dhananjaya, N. Guru Prakash, O. M. Hussain, and C. M. Julien, "Nanocrystalline Li_2TiO_3 electrodes for supercapattery application," *Ionics,* vol. 23, no. 12, pp. 3419-3428, 2017/12/01 2017, doi: 10.1007/s11581-017-2147-1.

[12] S. Liu *et al.*, "Conceptual design of the water cooled ceramic breeder blanket for CFETR based on pressurized water cooled reactor technology," *Fusion Engineering and Design,* vol. 124, pp. 865-870, 2017/11/01/ 2017, doi: https://doi.org/10.1016/j.fusengdes.2017.02.065.

[13] E. R. Kumar, K. N. Vyas, and T. Jayakumar, "Overview of LLCB TBM design and R&D activities in India," *Fusion Engineering and Design,* vol. 109-111, pp. 1522-1527, 2016/11/01/ 2016, doi: https://doi.org/10.1016/j.fusengdes.2015.11.038.

[14] Y. Kawamura *et al.*, "Status of water cooled ceramic breeder blanket development," *Fusion Engineering and Design,* vol. 136, pp. 1550-1556, 2018/11/01/ 2018, doi: https://doi.org/10.1016/j.fusengdes.2018.05.055.

[15] F. A. Hernández *et al.*, "An enhanced, near-term HCPB design as driver blanket for the EU DEMO," *Fusion Engineering and Design,* vol. 146, pp. 1186-1191, 2019/09/01/ 2019, doi: https://doi.org/10.1016/j.fusengdes.2019.02.037.

[16] R. Knitter, M. H. H. Kolb, U. Kaufmann, and A. A. Goraieb, "Fabrication of modified lithium orthosilicate pebbles by addition of titania," *Journal of Nuclear Materials,* vol. 442, no. 1-3, pp. S433-S436, Nov 2013, doi: 10.1016/j.jnucmat.2012.10.034.

[17] R. Knitter and B. Löbbecke, "Reprocessing of lithium orthosilicate breeder material by remelting," *Journal of Nuclear Materials,* vol. 361, no. 1, pp. 104-111, 2007/03/31/ 2007, doi: https://doi.org/10.1016/j.jnucmat.2006.11.005.

[18] J. Aktaa, M. Walter, E. Gaisina, M. H. H. Kolb, and R. Knitter, "Assessment of the chemical compatibility between EUROFER and ceramic breeder with respect to fatigue lifetime," *Fusion Engineering and Design,* vol. 157, p. 111732, 2020/08/01/ 2020, doi: https://doi.org/10.1016/j.fusengdes.2020.111732.

[19] J. M. Heuser, M. H. H. Kolb, T. Bergfeldt, and R. Knitter, "Long-term thermal stability of two-phased lithium orthosilicate/metatitanate ceramics," *Journal of Nuclear Materials,* vol. 507, pp. 396-402, 2018/08/15/ 2018, doi: https://doi.org/10.1016/j.jnucmat.2018.05.010.

[20] S. Pupeschi, R. Knitter, and M. Kamlah, "Effective thermal conductivity of advanced ceramic breeder pebble beds," *Fusion Engineering and Design,* vol. 116, pp. 73-80, Mar 2017, doi: 10.1016/j.fusengdes.2017.01.026.

[21] M. H. H. Kolb, R. Rolli, and R. Knitter, "Tritium adsorption/release behaviour of advanced EU breeder pebbles," *Journal of Nuclear Materials,* vol. 489, pp. 229-235, 2017/06/01/ 2017, doi: https://doi.org/10.1016/j.jnucmat.2017.03.051.

[22] J. M. Heuser, A. Zarins, L. Baumane, G. Kizane, and R. Knitter, "Radiation stability of long-term annealed bi-phasic advanced ceramic breeder pebbles," *Fusion Engineering and Design,* vol. 138, pp. 395-399, 2019/01/01/ 2019, doi: https://doi.org/10.1016/j.fusengdes.2018.12.034.

[23] M. Oyaidzu *et al.*, "Correlation between annihilation of radiation defects and tritium release in Li_2TiO_3," *Journal of Nuclear Materials,* vol. 329, pp. 1313-1317, Aug 2004, doi: 10.1016/j.jnucmat.2004.04.223.

[24]   M. Kobayashi, Y. Oya, K. Munakata, and K. Okuno, "Developing a tritium release model for Li_2TiO_3 with irradiation-induced defects," *Journal of Nuclear Materials,* vol. 458, pp. 22-28, Mar 2015, doi: 10.1016/j.jnucmat.2014.11.047.

[25]   K. Toda *et al.*, "Correlation between release of deuterium and annihilation of irradiation defects produced by gamma-ray in Li_2TiO_3," *Fusion Engineering and Design,* vol. 88, no. 9-10, pp. 2369-2372, Oct 2013, doi: 10.1016/j.fusengdes.2013.05.006.

[26]   W. Xu *et al.*, "In-situ atomic-scale observation of irradiation-induced void formation," *Nature Communications,* vol. 4, no. 1, p. 2288, 2013/08/05 2013, doi: 10.1038/ncomms3288.

[27]   L. W. Hobbs, "Transmission electron microscopy of defects in alkali halides," *Le Journal de Physique Colloques,* vol. 34, no. C9, pp. C9-227, 1973.

[28]   M. Klimenkov, E. Materna-Morris, and A. Moslang, "Characterization of radiation induced defects in EUROFER 97 after neutron irradiation," (in English), *Journal of Nuclear Materials,* Article; Proceedings Paper vol. 417, no. 1-3, pp. 124-126, Oct 2011, doi: 10.1016/j.jnucmat.2010.12.261.

[29]   R. M. Mayer and L. M. Brown, "Nucleation and growth of voids by radiation: I. Formulation of the problem," *Journal of Nuclear Materials,* vol. 95, no. 1, pp. 46-57, 1980/11/01/ 1980, doi: https://doi.org/10.1016/0022-3115(80)90079-3.

[30]   T. Koyanagi *et al.*, "Microstructural evolution of pure tungsten neutron irradiated with a mixed energy spectrum," *Journal of Nuclear Materials,* vol. 490, pp. 66-74, Jul 2017, doi: 10.1016/j.jnucmat.2017.04.010.

[31]   M. Rose, A. G. Balogh, and H. Hahn, "Instability of irradiation induced defects in nanostructured materials," *Nuclear Instruments and Methods in Physics Research Section B: Beam Interactions with Materials and Atoms,* vol. 127-128, pp. 119-122, 1997/05/02/ 1997, doi: https://doi.org/10.1016/S0168-583X(96)00863-4.

[32]   B. Muntifering *et al.*, "Cavity Evolution at Grain Boundaries as a Function of Radiation Damage and Thermal Conditions in Nanocrystalline Nickel," *Materials Research Letters,* vol. 4, no. 2, pp. 96-103, 2016, doi: 10.1080/21663831.2015.1121165.

[33]   X. M. Bai, A. F. Voter, R. G. Hoagland, M. Nastasi, and B. P. Uberuaga, "Efficient Annealing of Radiation Damage Near Grain Boundaries via Interstitial Emission," *Science,* vol. 327, no. 5973, pp. 1631-1634, Mar 2010, doi: 10.1126/science.1183723.

[34]   T. D. Shen, S. Feng, M. Tang, J. A. Valdez, Y. Wang, and K. E. Sickafus, "Enhanced radiation tolerance in nanocrystalline $MgGa_2O_4$," *Applied Physics Letters,* vol. 90, no. 26, Jun 2007, Art no. 263115, doi: 10.1063/1.2753098.

[35]   Z. Y. Huang *et al.*, "Defect-fluorite $Gd_2Zr_2O_7$ ceramics under helium irradiation: Amorphization, cell volume expansion, and multi-stage bubble formation," *Journal of the American Ceramic Society,* vol. 102, no. 8, pp. 4911-4918, Aug 2019, doi: 10.1111/jace.16364.

[36]   S. Dey *et al.*, "Radiation Tolerance of Nanocrystalline Ceramics: Insights from Yttria Stabilized Zirconia," *Scientific Reports,* vol. 5, Jan 2015, Art no. 7746, doi: 10.1038/srep07746.

[37]   W. F. Cureton *et al.*, "Grain size effects on irradiated CeO_2, ThO_2, and UO_2," *Acta Materialia,* vol. 160, pp. 47-56, Nov 2018, doi: 10.1016/j.actamat.2018.08.040.

[38]   W. B. Liu *et al.*, "Irradiation Induced Microstructure Evolution in Nanostructured Materials: A Review," *Materials,* vol. 9, no. 2, Feb 2016, Art no. 105, doi: 10.3390/ma9020105.

[39]   M. Klimenkov, P. Vladimirov, J. Hoffmann, N. Zimber, A. Moslang, and V. Kuksenko, "First simultaneous detection of helium and tritium inside bubbles in beryllium," *Micron,* vol. 127, Dec 2019, Art no. 102754, doi: 10.1016/j.micron.2019.102754.

[40]   V. I. Dubinko, A. G. Guglya, and S. E. Donnelly, "Radiation-induced formation, annealing and ordering of voids in crystals: Theory and experiment," *Nuclear Instruments and Methods in Physics Research Section B: Beam Interactions with Materials and Atoms,* vol. 269, no. 14, pp. 1634-1639, 2011/07/15/ 2011, doi: https://doi.org/10.1016/j.nimb.2010.12.012.

[41]   P. A. M. Dirac, *The principles of quantum mechanics*, Third ed. (no. Accessed from https://nla.gov.au/nla.cat-vn2391961). Oxford: Clarendon Press, 1947.

[42] L. W. Hobbs, "ELECTRON-BEAM SENSITIVITY IN INORGANIC SPECIMENS," *Ultramicroscopy,* vol. 23, no. 3-4, pp. 339-344, 1987, doi: 10.1016/0304-3991(87)90244-0.

[43] U. Jain and A. B. Lidiard, "GROWTH OF COLLOIDAL CENTERS IN IRRADIATED ALKALI-HALIDES," *Philosophical Magazine,* vol. 35, no. 1, pp. 245-259, 1977, doi: 10.1080/14786437708235986.

[44] Y. Ekmanis, "RADIOLYSIS BEHAVIOR IN ALKALI-HALIDE CRYSTALS," *Nuclear Instruments & Methods in Physics Research Section B-Beam Interactions with Materials and Atoms,* vol. 1, no. 2-3, pp. 473-474, 1984, doi: 10.1016/0168-583x(84)90111-3.

[45] V. I. Dubinko, A. A. Turkin, D. I. Vainshtein, and H. W. den Hartog, "A new mechanism for radiation damage processes in alkali halides," *Journal of Applied Physics,* vol. 86, no. 11, pp. 5957-5960, Dec 1999, doi: 10.1063/1.371639.

[46] V. I. Dubinko, A. A. Turkin, D. I. Vainshtein, and H. W. den Hartog, "Theory of the late stage of radiolysis of alkali halides," *Journal of Nuclear Materials,* vol. 277, no. 2-3, pp. 184-198, Feb 2000, doi: 10.1016/s0022-3115(99)00207-x.

[47] E. Johnson and L. T. Chadderton, "The void superlattice in fluorite," *Micron,* vol. 11, no. 3-4, pp. 247-250, 1980.

[48] P. J. Call, W. Hayes, J. P. Stott, and A. E. Hughes, "Radiolysis of alkaline-earth fluorides," *Journal of Physics C: Solid State Physics,* vol. 7, no. 14, pp. 2417-2428, 1974/07/21 1974, doi: 10.1088/0022-3719/7/14/006.

[49] L. W. Hobbs and M. R. Pascucci, "Radiolysis and defect structure in electron-irradiated α-quartz," *Le Journal de Physique Colloques,* vol. 41, no. C6, pp. C6-237, 1980.

[50] J. F. Denatale and D. G. Howitt, "A mechanism for radiation damage in silicate glasses," *Nuclear Instruments and Methods in Physics Research Section B: Beam Interactions with Materials and Atoms,* vol. 1, no. 2, pp. 489-497, 1984/02/01/ 1984, doi: https://doi.org/10.1016/0168-583X(84)90114-9.

[51] O. Ugurlu *et al.*, "Radiolysis to knock-on damage transition in zeolites under electron beam irradiation," *Physical Review B,* vol. 83, no. 11, Mar 2011, Art no. 113408, doi: 10.1103/PhysRevB.83.113408.

[52] D. J. Smith, M. R. McCartney, and L. A. Bursill, "The electron-beam-induced reduction of transition metal oxide surfaces to metallic lower oxides," *Ultramicroscopy,* vol. 23, no. 3, pp. 299-303, 1987/01/01/ 1987, doi: https://doi.org/10.1016/0304-3991(87)90239-7.

[53] H. J. Fan and L. D. Marks, "Phase transitions in V_2O_5 in a high resolution electron microscope," *Ultramicroscopy,* vol. 31, no. 4, pp. 357-364, 1989/12/01/ 1989, doi: https://doi.org/10.1016/0304-3991(89)90334-3.

[54] D. Wang, D. S. Su, and R. Schlogl, "Electron beam induced transformation of MoO_3 to MoO_2 and a new phase MoO," *Zeitschrift Fur Anorganische Und Allgemeine Chemie,* vol. 630, no. 7, pp. 1007-1014, 2004, doi: 10.1002/zaac.200400052.

[55] M. R. McCartney and D. J. Smith, "STUDIES OF ELECTRON-IRRADIATION AND ANNEALING EFFECTS ON TIO2 SURFACES IN ULTRAHIGH-VACUUM USING HIGH-RESOLUTION ELECTRON-MICROSCOPY," *Surface Science,* vol. 250, no. 1-3, pp. 169-178, Jul 1991, doi: 10.1016/0039-6028(91)90719-9.

[56] M. I. Buckett, J. Strane, D. E. Luzzi, J. P. Zhang, B. W. Wessels, and L. D. Marks, "Electron irradiation damage in oxides," *Ultramicroscopy,* vol. 29, no. 1, pp. 217-227, 1989/05/02/ 1989, doi: https://doi.org/10.1016/0304-3991(89)90249-0.

[57] Y. Furuyama, K. Yahata, R. Nakamori, A. Taniike, H. Samata, and A. Kitamura, "CO_2 absorption characteristics of a Li_2TiO_3 blanket material under atmospheric exposure," *Journal of Nuclear Materials,* vol. 455, no. 1, pp. 527-530, 2014/12/01/ 2014, doi: https://doi.org/10.1016/j.jnucmat.2014.08.007.

[58] T. L. Ávalos-Rendón and H. Pfeiffer, "High CO_2 Chemisorption in α-Li_5AlO_4 at Low Temperatures (30–80 °C): Effect of the Water Vapor Addition," *Energy & Fuels,* vol. 26, no. 5, pp. 3110-3114, 2012/05/17 2012, doi: 10.1021/ef3004416.

[59] L. Martínez-dlCruz and H. Pfeiffer, "Toward Understanding the Effect of Water Sorption on Lithium Zirconate (Li_2ZrO_3) during Its Carbonation Process at Low Temperatures," *The Journal of Physical Chemistry C,* vol. 114, no. 20, pp. 9453-9458, 2010/05/27 2010, doi: 10.1021/jp1020966.

[60] W. Xia *et al.*, "Reaction mechanisms of lithium garnet pellets in ambient air: The effect of humidity and CO_2," *Journal of the American Ceramic Society,* vol. 100, no. 7, pp. 2832-2839, 2017/07/01 2017, doi: 10.1111/jace.14865.

[61] I. Yanase, K. Sato, H. Kobayashi, T. Doe, and T. Naka, "CO_2 absorption property of Li_4SiO_4 in the presence of water vapor at room temperature," *Chemical Engineering Journal,* vol. 356, pp. 81-90, Jan 2019, doi: 10.1016/j.cej.2018.09.005.

[62] M. L. Grasso, P. A. Larochette, and F. C. Gennari, "CO_2 capture properties of Li_4SiO_4 after aging in air at room temperature," *Journal of CO_2 Utilization,* vol. 38, pp. 232-240, May 2020, doi: 10.1016/j.jcou.2020.02.002.

[63] S. Gates-Rector and T. Blanton, "The Powder Diffraction File: a quality materials characterization database," *Powder Diffraction,* vol. 34, no. 4, pp. 352-360, 2019, doi: 10.1017/S0885715619000812.

[64] C. A. Schneider, W. S. Rasband, and K. W. Eliceiri, "NIH Image to ImageJ: 25 years of image analysis," *Nature Methods,* vol. 9, no. 7, pp. 671-675, 2012/07/01 2012, doi: 10.1038/nmeth.2089.

[65] G. Greaves, A. H. Mir, R. W. Harrison, M. A. Tunes, S. E. Donnelly, and J. A. Hinks, "New Microscope and Ion Accelerators for Materials Investigations (MIAMI-2) system at the University of Huddersfield," *Nuclear Instruments and Methods in Physics Research Section A: Accelerators, Spectrometers, Detectors and Associated Equipment,* vol. 931, pp. 37-43, 2019/07/01/ 2019, doi: https://doi.org/10.1016/j.nima.2019.03.074.

[66] K. Kataoka *et al.*, "Crystal growth and structure refinement of monoclinic Li_2TiO_3," *Materials Research Bulletin,* vol. 44, no. 1, pp. 168-172, 1/8/ 2009, doi: http://doi.org/10.1016/j.materresbull.2008.03.015.

[67] A. Boulineau, L. Croguennec, C. Delmas, and F. Weill, "Structure of Li_2MnO_3 with different degrees of defects," *Solid State Ionics,* vol. 180, no. 40, pp. 1652-1659, 2010/01/29/ 2010, doi: https://doi.org/10.1016/j.ssi.2009.10.020.

[68] *Generated using CrystalDiffract®: a powder diffraction program for Mac and Windows. CrystalMaker Software Ltd, Oxford, England (www.crystalmaker.com).*

[69] S. J. Zinkle, "Effect of H and He irradiation on cavity formation and blistering in ceramics," *Nuclear Instruments & Methods in Physics Research Section B-Beam Interactions with Materials and Atoms,* vol. 286, pp. 4-19, Sep 2012, doi: 10.1016/j.nimb.2012.03.030.

[70] R. F. Egerton, P. Li, and M. Malac, "Radiation damage in the TEM and SEM," *Micron,* vol. 35, no. 6, pp. 399-409, 2004, doi: 10.1016/j.micron.2004.02.003.

[71] U. Fischer *et al.*, "Comparison of nuclear irradiation parameters of fusion breeder materials in high flux fission test reactors and a fusion power demonstration reactor," *Journal of Nuclear Materials,* vol. 280, no. 2, pp. 151-161, 2000/07/01/ 2000, doi: https://doi.org/10.1016/S0022-3115(00)00049-0.

[72] I. Jencic, M. W. Bench, I. M. Robertson, and M. A. Kirk, "ELECTRON-BEAM-INDUCED CRYSTALLIZATION OF ISOLATED AMORPHOUS REGIONS IN Si, Ge, GaP, AND GaAs," *Journal of Applied Physics,* vol. 78, no. 2, pp. 974-982, Jul 1995, doi: 10.1063/1.360764.

[73] P. D. Edmondson, W. J. Weber, F. Namavar, and Y. Zhang, "Determination of the displacement energies of O, Si and Zr under electron beam irradiation," *Journal of Nuclear Materials,* vol. 422, no. 1-3, pp. 86-91, Mar 2012, doi: 10.1016/j.jnucmat.2011.12.021.

[74] L. Reimer, "Scanning Electron Microscopy, Physics of Image Formation and Microanalysis " *Springer-Verlag Berlin Heidelberg*, 1985.

[75] S. M. Seltzer and M. J. Berger, "EVALUATION OF THE COLLISION STOPPING POWER OF ELEMENTS AND COMPOUNDS FOR ELECTRONS AND POSITRONS," *International Journal of Applied Radiation and Isotopes,* vol. 33, no. 11, pp. 1189-1218, 1982, doi: 10.1016/0020-708x(82)90244-7.

[76] S. Saito, K. Tsuchiya, H. Kawamura, T. Terai, and S. Tanaka, "Density dependence on thermal properties of Li_2TiO_3 pellets," *Journal of Nuclear Materials,* vol. 253, pp. 213-218, Mar 1998, doi: 10.1016/s0022-3115(97)00314-0.

[77] P. Gierszewski, "Review of properties of lithium metatitanate," *Fusion Engineering and Design,* vol. 39-40, pp. 739-743, Sep 1998, doi: 10.1016/s0920-3796(97)00168-3.

[78]   N. Roux, J. Avon, A. Floreancig, J. Mougin, B. Rasneur, and S. Ravel, "Low-temperature tritium releasing ceramics as potential materials for the ITER breeding blanket," *Journal of Nuclear Materials,* vol. 233, pp. 1431-1435, Oct 1996, doi: 10.1016/s0022-3115(96)00136-5.

[79]   D. B. Williams and C. B. Carter, *Transmission Electron Microscopy: A Textbook for Materials Science, Second Edition*. New York: Springer Science+Business Media, 2009.

[80]   L. W. Hobbs, "Radiation Effects in Analysis of Inorganic Specimens by TEM," in *Introduction to Analytical Electron Microscopy*, J. J. Hren Ed. New York: Springer Science+Business Media, 1979, p. 437.

[81]   R. F. Egerton, "Radiation damage to organic and inorganic specimens in the TEM," *Micron,* vol. 119, pp. 72-87, 2019/04/01/ 2019, doi: https://doi.org/10.1016/j.micron.2019.01.005.

[82]   M. L. Knotek and P. J. Feibelman, "STABILITY OF IONICALLY BONDED SURFACES IN IONIZING ENVIRONMENTS," *Surface Science,* vol. 90, no. 1, pp. 78-90, 1979, doi: 10.1016/0039-6028(79)90011-6.

[83]   G. Vitins, G. Kizane, A. Lusis, and J. Tiliks, "Electrical conductivity studies in the system Li_2TiO_3-$Li_{1.33}Ti_{1.67}O_4$," *Journal of Solid State Electrochemistry,* vol. 6, no. 5, pp. 311-319, Jun 2002, doi: 10.1007/s100080100239.

[84]   T. Fehr and E. Schmidbauer, "Electrical conductivity of Li_2TiO_3 ceramics," *Solid State Ionics,* vol. 178, no. 1-2, pp. 35-41, Jan 2007, doi: 10.1016/j.ssi.2006.11.002.

[85]   Z. Wan, Y. Yu, H. F. Zhang, T. Gao, X. J. Chen, and C. J. Xiao, "First-principles study of electronic, dynamical and thermodynamic properties of Li_2TiO_3," *European Physical Journal B,* vol. 85, no. 6, Jun 2012, Art no. 181, doi: 10.1140/epjb/e2012-20666-5.

[86]   E. Sonder and W. A. Sibley, "Defect Creation by Radiation in Polar Crystals," in *Point Defects in Solids*, J. H. Crawford and L. M. Silfkin Eds. Boston, MA: Springer, 1972, p. 437.

[87]   C. Lehmann, *Interaction of Radiation with Solids and Elementary Defect Production*. Amsterdam: North-Holland, 1977.

[88]   Z. L. Dong *et al.*, "Electron-beam radiation induced degradation of silicon nitride and its impact to semiconductor failure analysis by TEM," *AIP advances.,* vol. 8, no. 11, p. 115327, 2018, doi: 10.1063/1.5051813

[89]   H. Feshbach, W. A. McKinley, and H. Feshbach, "The Coulomb Scattering of Relativistic Electrons by Nuclei," *Physical review.,* vol. 74, no. 12, pp. 1759-1763, 1948, doi: 10.1103/PhysRev.74.1759

[90]   N. F. Mott and H. S. W. Massey, "The Theory of Atomic Collisions," *3rd Edition, Oxford University Press, London,* 1965.

[91]   J. Reyes-Gasga and R. Garcia-Garcia, "Analysis of the electron-beam radiation damage of TEM samples in the acceleration energy range from 0.1 to 2 MeV using the standard theory for fast electrons," *Radiation Physics and Chemistry,* vol. 64, no. 5-6, pp. 359-367, Aug 2002, Art no. Pii s0969-806x(01)00578-3, doi: 10.1016/s0969-806x(01)00578-3.

[92]   S. J. Zinkle and C. Kinoshita, "Defect production in ceramics," *Journal of Nuclear Materials,* vol. 251, pp. 200-217, 1997/11/11/ 1997, doi: https://doi.org/10.1016/S0022-3115(97)00224-9.

[93]   J. Strane, L. D. Marks, D. E. Luzzi, M. I. Buckett, J. P. Zhang, and B. W. Wessels, "ENCAPSULATION, DIFFUSION AND DIET IN THE ELECTRON-MICROSCOPE," *Ultramicroscopy,* vol. 25, no. 3, pp. 253-257, 1988, doi: 10.1016/0304-3991(88)90019-8.

[94]   N. Kuganathan, A. Kordatos, M. E. Fitzpatrick, R. V. Vovk, and A. Chroneos, "Defect process and lithium diffusion in Li_2TiO_3," *Solid State Ionics,* vol. 327, pp. 93-98, Dec 2018, doi: 10.1016/j.ssi.2018.10.030.

[95]   M. Vijayakumar *et al.*, "Combined $^{6,7}Li$ NMR and Molecular Dynamics Study of Li Diffusion in Li_2TiO_3," *Journal of Physical Chemistry C,* vol. 113, no. 46, pp. 20108-20116, Nov 2009, doi: 10.1021/jp9072125.

[96]   M. Oyaidzu *et al.*, "ESR study on annihilation process of radiation defects induced in solid tritium breeding materials by neutron irradiation," *Physica Scripta,* vol. T108, pp. 42-45, 2004.

[97]   V. Gavini, K. Bhattacharya, and M. Ortiz, "Vacancy clustering and prismatic dislocation loop formation in aluminum," *Physical Review B,* vol. 76, no. 18, Nov 2007, Art no. 180101, doi: 10.1103/PhysRevB.76.180101.

[98]   F. Gao, D. J. Bacon, L. M. Howe, and C. B. So, "Temperature-dependence of defect creation and clustering by displacement cascades in alpha-zirconium," *Journal of Nuclear Materials,* vol. 294, no. 3, pp. 288-298, Apr 2001, doi: 10.1016/s0022-3115(01)00483-4.

[99]   C. C. Matthai and D. J. Bacon, "THE COLLAPSE OF VACANCY CLUSTERS - A MOLECULAR-DYNAMICS STUDY," *Journal of Nuclear Materials,* vol. 135, no. 2-3, pp. 173-180, 1985, doi: 10.1016/0022-3115(85)90075-3.

[100]   S. J. Zinkle, L. E. Seitzman, and W. G. Wolfer, "STABILITY OF VACANCY CLUSTERS IN METALS .1. ENERGY CALCULATIONS FOR PURE METALS," *Philosophical Magazine a-Physics of Condensed Matter Structure Defects and Mechanical Properties,* vol. 55, no. 1, pp. 111-125, Jan 1987, doi: 10.1080/01418618708209803.

[101]   B. N. Singh and A. J. E. Foreman, "An assessment of void nucleation by gas atoms during irradiation," *Journal of Nuclear Materials,* vol. 104, pp. 1469-1474, 1981/01/01/ 1981, doi: https://doi.org/10.1016/0022-3115(82)90807-8.

[102]   F. Lin, I. M. Markus, M. M. Doeff, and H. L. L. Xin, "Chemical and Structural Stability of Lithium-Ion Battery Electrode Materials under Electron Beam," *Scientific Reports,* vol. 4, Jul 2014, Art no. 5694, doi: 10.1038/srep05694.

[103]   F. Y. Lu *et al.*, "Amorphization of nanocrystalline monoclinic ZrO_2 by swift heavy ion irradiation," *Physical Chemistry Chemical Physics,* vol. 14, no. 35, pp. 12295-12300, 2012, doi: 10.1039/c2cp41553d.

[104]   B. Schuster, M. Lang, R. Klein, C. Trautmann, R. Neumann, and A. Benyagoub, "Structural phase transition in ZrO_2 induced by swift heavy ion irradiation at high-pressure," *Nuclear Instruments & Methods in Physics Research Section B-Beam Interactions with Materials and Atoms,* vol. 267, no. 6, pp. 964-968, Mar 2009, doi: 10.1016/j.nimb.2009.02.046.

[105]   W. J. Qin *et al.*, "Different Radiation Tolerances of Ultrafine-Grained Zirconia-Magnesia Composite Ceramics with Different Grain Sizes," *Materials,* vol. 12, no. 17, Sep 2019, Art no. 2649, doi: 10.3390/ma12172649.

Chapter 6 - Thermal evolution of electron beam induced cavities in Li_2TiO_3 ceramics

Lithium metatitanate has previously been shown to be susceptible to electron beam induced damage, resulting in the formation of cavities at room temperature (see Chapter 5). The formation and growth of such cavities is believed to be due to the aggregation of vacancies produced as a result of displacement damage induced by the TEM electron beam. The mobility of vacancy and interstitial defects produced as a result of irradiation induced displacement events is known to be enhanced at elevated temperature; as such, the dynamics of cavity growth under irradiation can be strongly affected by temperature. In this chapter, the effects of elevated temperature and electron beam exposure time on cavity growth in Li_2TiO_3 ceramics with different microstructural properties (using samples with analogous microstructures to those discussed in the previous chapter) are discussed.

6.1 Effect of elevated temperature on electron beam induced cavity growth

An overview of the microstructures of the specific specimens examined in the first half of this chapter, which is concerned with the growth dynamics of electron beam induced cavities in Li_2TiO_3 as a function of temperature, is shown in Figure 6.1. The actual grains examined during in-situ thermal annealing experiments in their pristine state, along with the corresponding grain sizes measured from TEM micrographs are detailed. Grain size measurements and associated errors were calculated according to the method described previously.
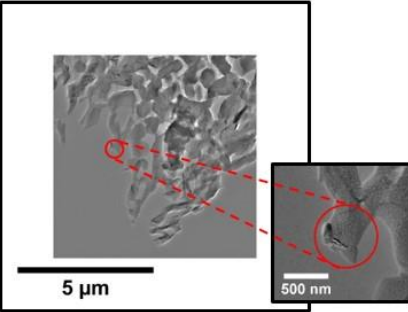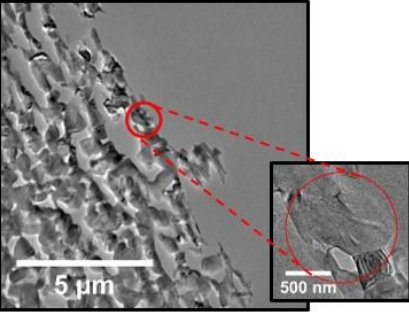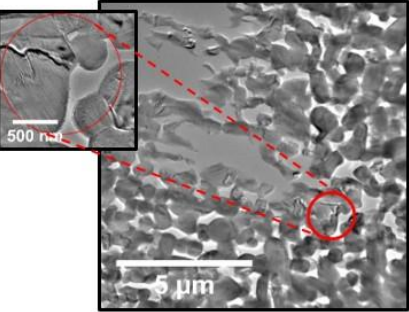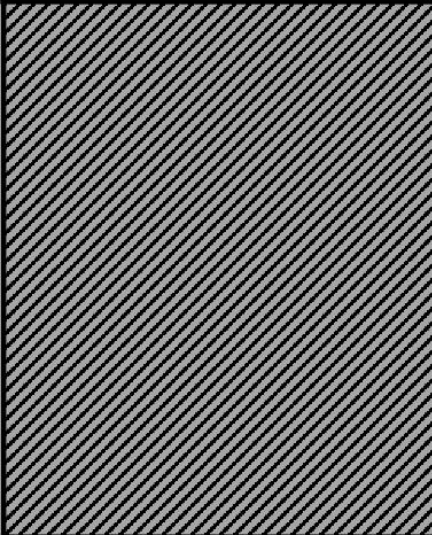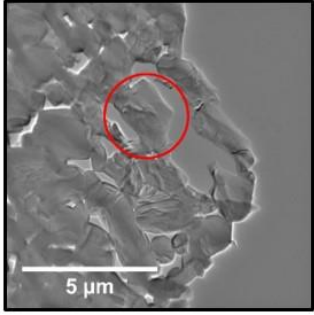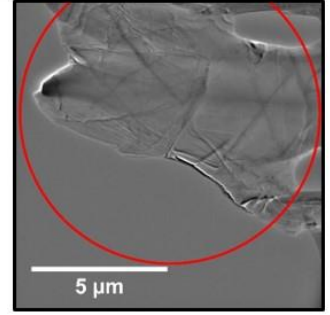
A: High porosity (900 °C, 3h) *Constant* beam exposure	A': High porosity (900 °C, 3h) *Minimised* beam exposure	B: High porosity (900 °C, 6h) *Minimised* beam exposure
Actual size of examined grain: 0.4 µm ± 0.1 µm	*Actual size of examined grain:* 0.9 µm ± 0.4 µm	*Actual size of examined grain:* 1.2 µm ± 0.4 µm

	C: Low porosity (1000 °C, 2h) *Minimised* beam exposure	D: Low porosity (1100 °C, 6h) *Minimised* beam exposure
	Actual size of examined grain: 2.2 µm ± 1.2 µm	*Actual size of examined grain:* 6.5 µm ± 2.6 µm

Figure 6.1: Low-magnification (overview) bright field TEM micrographs showing the specific grains examined in specimens A-D during in-situ annealing experiments. The corresponding grain sizes, measured from TEM micrographs, are listed below the respective image. Sintering conditions are shown in brackets.

Figure 6.2 shows the thermal evolution of electron beam induced cavities in specimen A (high porosity, smallest grain size) during in-situ thermal annealing under constant electron irradiation by a 300 keV TEM electron beam.
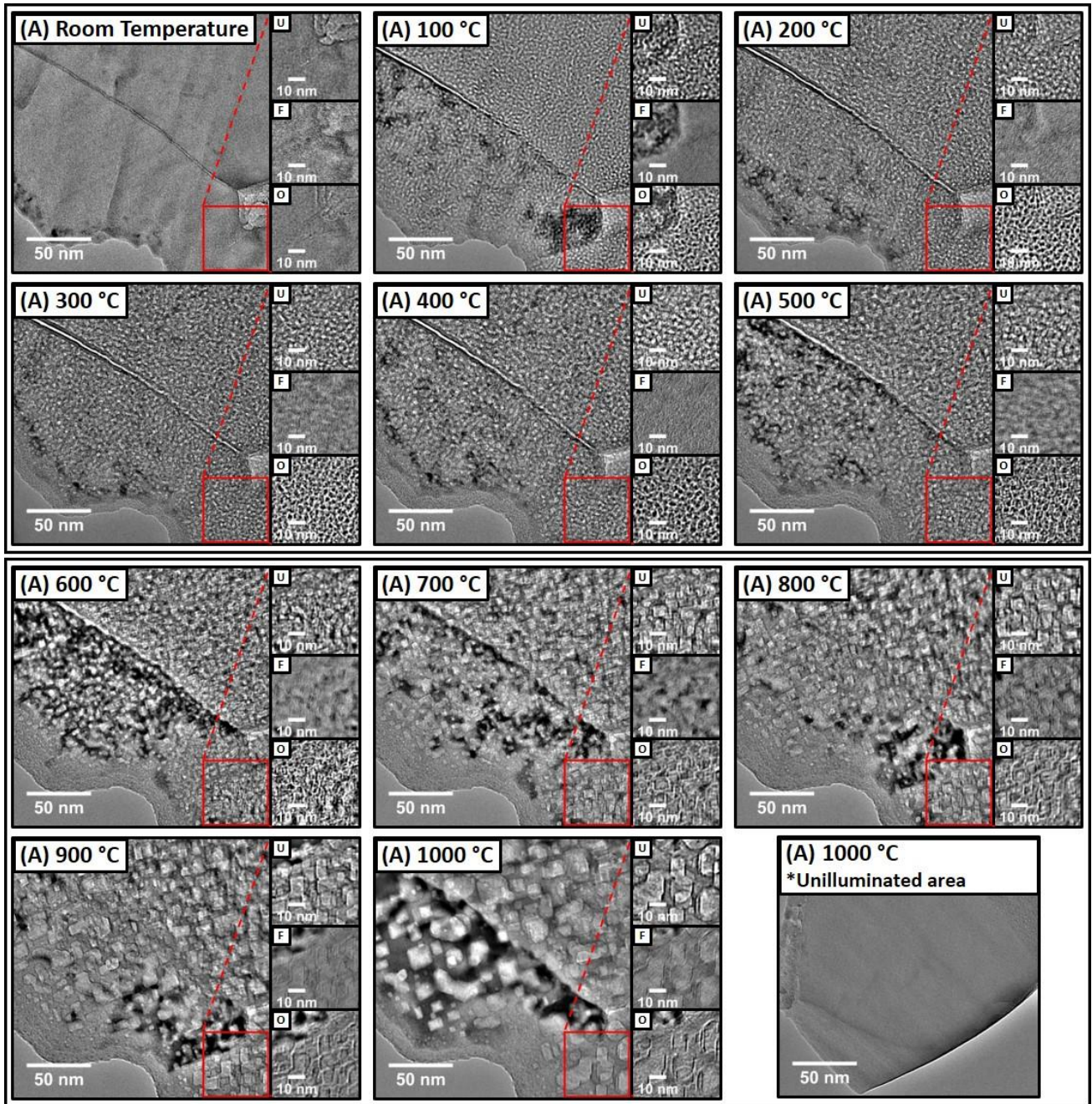
Figure 6.2: Bright field TEM micrographs showing the thermal evolution of electron beam induced cavities during in-situ annealing of Specimen A (high porosity, smallest grain size; sintered at 900 °C, 3h) under constant irradiation by a 300 keV electron beam.

After a short period of exposure to the electron beam (< 5 mins) at room temperature, no resolvable vacancy-type defects were observed in bright field through focal series micrographs of the pristine specimen in either under- or over-focus condition. Upon increasing the specimen temperature, small (<2 nm) bright features became clearly visible in under-focus condition after ~ 20 seconds at 100 °C (~ 3-4 mins total electron beam exposure time). Initially forming close to the edge of the specimen, these features were found to nucleate extensively across the bulk of grains in the area illuminated

126

by the electron beam over a period of 2-3 minutes. These features were identified as cavities by inspection of the change in Fresnel contrast (from bright features with dark fringes in under-focus condition, to dark features with bright fringes in over-focus condition) observed in through focal series micrographs.

After 10 minutes at 100 °C the mean size of 50 measured cavities was 1.7 ± 0.1 nm remaining stable within the error associated with measurement at 200 °C. Slow growth was observed at 300-400 °C, where mean cavity size increased by approximately 0.1 nm at each temperature increment. At 500 °C, mean cavity size increased by ~0.3 nm from 1.9 ± 0.1 nm to 2.2 nm ± 0.1nm, possibly indicating the onset of accelerated growth rate. Above 500 °C significant cavity growth occurred, with mean cavity size increasing sharply to 3.9 ± 0.2 nm and 4.3 ± 0.2 nm at 600 °C and 700 °C respectively. At such temperatures, many of the observed cavities had adopted a more faceted morphology due to the bounds imposed by the lattice planes of the crystalline matrix between which the cavities are accommodated. Such faceted morphology supposedly minimises the interfacial energy associated with voids and cavities more effectively than spherical forms [200]. Above 700 °C cavity growth was further enhanced, with growth rate increasing at each incremental temperature. The largest increase in cavity size was observed between 900 °C and the maximum temperature of 1000 °C, indicating that the fastest rate of cavity growth occurs at the highest temperature, where defect mobility is highest.

While large cavities up to ~36 nm in size were observed at the maximum temperature in areas of the specimen which had been exposed to the electron beam, no resolvable cavities were observed at equivalent temperature in areas of the specimen which had not been illuminated by the electron beam. This unequivocally shows that the observed cavity formation and growth of cavities in thin film specimens of Li_2TiO_3 occurs as a direct result of electron beam induced damage, and cannot be attributed to any peculiarity native to the properties of the material itself.
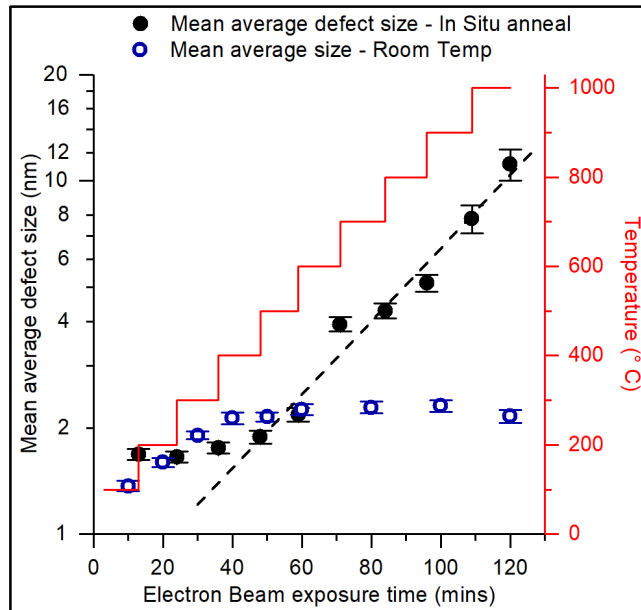
Figure 6.3: Mean average cavity size observed in Specimen A under constant irradiation by a 300 keV electron beam: (i) At room temperature (black), and (ii) During in-situ annealing (blue). Anneal temperature profile is shown in red, dashed blue line represents exponential fit of defect size during in-situ annealing at temperatures > 300 °C.

Figure 6.3 shows a graphical representation of the mean cavity size of 50 measured cavities as a function of electron beam exposure time under constant electron irradiation during in-situ annealing compared to those measured at room temperature. During the first 60 minutes of electron beam exposure, although the dynamics of cavity growth vary somewhat, the mean size of cavities observed during thermal annealing up to temperatures of 500 °C was found to be similar to those observed at room temperature. In both cases cavity growth was observed to be slow during the first 60 minutes of electron irradiation; as such mean cavity size remains relatively small (< 2.5 nm) regardless of temperature. However, where at room temperature the majority of cavity growth occurred in the early stages of exposure to the electron beam (stabilising after ~40 minutes) and mean cavity size reached a maximum of only 2.3 nm over the entire 120 minutes of electron irradiation; extensive growth occurred in the later stages of thermal annealing under constant electron irradiation. Mean cavity size reached 11.2 ± 1.1 nm at 1000 °C, almost five times larger than those observed at room temperature at comparable electron beam exposure time. Closer inspection of the cavity growth profile revealed that, at temperatures greater than 400 °C, mean cavity size under constant electron irradiation was shown to increase pseudo-exponentially with temperature (see Figure 6.3 exponential fit, note log y scale). This indicates that the growth of electron beam induced cavities in Li_2TiO_3 is enhanced at temperatures in excess of 400 °C under constant electron irradiation, and that

128

the rate of cavity growth is increasingly accelerated with increasing temperature above this threshold.

As proposed in the previous chapter, the nucleation and growth of electron beam induced cavities in Li_2TiO_3 is believed to occur due to the preferential loss of interstitial defects, introduced as a result of displacement damage, at the specimen surface due to the higher mobility of interstitials compared to that of vacancies. The preferential loss of interstitials leaves behind an excess vacancy concentration, which ultimately leads to vacancy supersaturation resulting in cavity formation and growth.

Enhanced cavity growth at elevated temperature is primarily attributed to the associated increase in defect mobility, which results in a faster rate of interstitial loss, and therefore increased excess vacancy concentration. In conjunction with this, the mobility of the corresponding vacancy defects is also increased, resulting in a higher flux of excess vacancies to the walls of existing cavities; thus exacerbating cavity growth.

6.2 Effect of reducing beam exposure during annealing on cavity growth

Figure 6.4 shows the thermal evolution of electron beam induced cavities in Li_2TiO_3 during in-situ thermal annealing under minimised exposure to the electron beam.

Figure 6.4: Bright field TEM micrographs showing the thermal evolution of electron beam induced cavities during in-situ annealing of Specimen A' (high porosity, smallest grain size; sintered at 900 °C, 3h) under a 300 keV electron beam where electron beam exposure time was minimised (beam switched off during isothermal dwell time at each incremental temperature).

The extent of cavity growth was found to be significantly reduced by switching off the TEM electron beam during the isothermal dwell time at each incremental temperature, thereby reducing the duration for which the specimen was exposed to the electron beam and thus reducing electron fluence. It is visually apparent that cavities were consistently smaller throughout the annealing process than those observed at equivalent temperature under constant electron irradiation. This is particularly noticeable at intermediate temperatures (500 – 600 °C); growth rate remained slow and cavities remained relatively small under minimised electron beam exposure, where under constant electron irradiation cavity growth had significantly accelerated at such temperatures. The onset of enhanced cavity growth appears delayed under minimised electron beam exposure, where rapid growth was not observed below 700 °C; at which temperature considerable growth was observed. Beyond 700 °C cavities continued to increase in size with increasing temperature up to the maximum of 1000 °C.
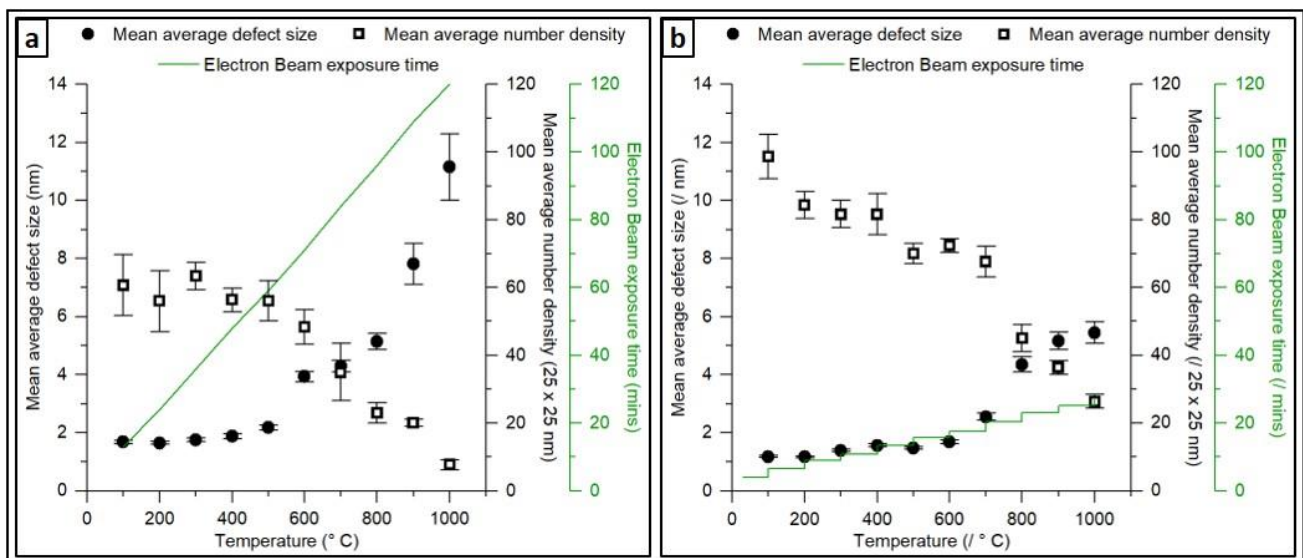
Figure 6.5: Mean average defect size observed at incrementally increasing temperatures during in-situ annealing. a) Under constant exposure to a 300 keV electron beam (Specimen A), and b) under minimised exposure to a 300 keV electron beam (Specimen A').

Figure 6.5 shows a graphical representation of the mean cavity size of 50 measured cavities as a function of temperature during in-situ annealing under constant electron irradiation compared to those measured when electron beam exposure was minimised. Concurrent with visual examination of TEM micrographs, inspection of mean cavity size statistics shows that cavities were found to be consistently smaller at equivalent temperature throughout the thermal annealing process under minimised electron beam exposure; showing a clear dependence of cavity size on electron fluence.

131

This is proposed to be primarily due to the reduction in vacancy defect production and thus lowered excess vacancy concentration associated with reduced electron fluence. Hence the lesser supply of vacancies results in a reduced flux of vacancies to cavity walls, and cavity growth occurs to a lesser extent.

The cavity growth profile under minimised electron beam exposure deviates significantly from that observed under constant electron irradiation. While the measured cavity sizes are similar at temperatures up to 400 °C, the thermal evolution behaviour of cavities subjected to different doses of electron irradiation is dramatically different above this temperature. Where cavity growth was approximately exponential with temperature above 400 °C under constant electron irradiation, when exposure to the electron beam was minimised the onset of accelerated cavity growth during thermal annealing was delayed until the specimen reached 700 °C. In this case significant cavity growth occurred only between 700 °C and 900 °C. The fastest rate of growth was observed at 800 °C, above which the growth rate slowed at both 900 °C and 1000 °C respectively.

This behaviour can be explained by variations in the factors affecting cavity growth. Two key temperature dependent factors are the vacancy diffusion coefficient and the equilibrium vacancy concentration [155]. At low temperature, cavity growth is limited by low defect mobility; hence the flux of vacancy defects to existing cavities is low, and growth is relatively slow. Additionally, since the migration energy of vacancies is generally greater than that of interstitials in oxide ceramics [157], vacancies are less mobile than interstitials. As such, at low temperatures where vacancies remain relatively immobile, mutual recombination with mobile interstitials may be favoured over the vacancy aggregation processes, further limiting cavity growth.

The equilibrium vacancy concentration, C_v^0, in a material varies proportionally with temperature, T, according to the approximate relationship [201]:

$$C_v^0 \propto \exp\left(\frac{-E_f^v}{k_b T}\right) \qquad (6.1)$$

Where E_f^v is the vacancy defect formation energy and k_b is the Boltzmann constant. As temperature increases, the magnitude of the negative exponent decreases, and consequently equilibrium vacancy concentration increases with temperature. Thus, at high temperature the degree of vacancy supersaturation is lessened as the thermal equilibrium vacancy concentration approaches the concentration of electron beam induced (vacancy) defects. Such diminution of supersaturation

results in a lesser supply of excess vacancies to facilitate cavity growth. Hence, it is proposed that under minimized electron beam exposure conditions, the introduction of extrinsic defects was sufficiently lessened for the thermal equilibrium vacancy concentration to become significant, resulting in retarded cavity growth at high temperature. Emission of vacancies by cavities may also increase at high temperature, contributing to reduced growth rate by partially counteracting the net vacancy influx. Hence, the most efficient cavity growth under minimised electron beam exposure was observed at intermediate temperature (in this case 700 – 900 °C); where vacancies were sufficiently mobile to allow rapid diffusion to the walls of existing cavies, and the equilibrium vacancy concentration was sufficiently low to maintain adequate supersaturation to facilitate growth.

The observation that the onset of accelerated cavity growth during thermal annealing was delayed until the specimen reached 700 °C when exposure to the electron beam was minimised (c.f. 400 - 500 °C under constant electron irradiation) indicates that a threshold vacancy concentration for efficient cavity growth exists. However, it is noted that this corresponds to a beam exposure time of ~20 minutes at 700 °C; significantly less than the exposure time at which accelerated growth rate was observed under constant electron irradiation at lower temperature (40-60 minutes). Hence, since a lesser electron fluence was required to promote efficient cavity growth at higher temperature, it is concluded that the aforementioned threshold vacancy concentration is temperature dependent. As such, it is clear that both electron fluence (and thus vacancy defect concentration) and specimen temperature (defect mobility) contribute to cavity growth dynamics, and the contributions of these two factors are interdependent.

The observation that cavities were consistently smaller under minimised electron beam exposure than those observed under constant electron irradiation at equivalent temperature shows that reducing electron fluence suppresses cavity growth to some extent regardless of specimen temperature. However, at low temperatures, it is proposed that cavity growth is primarily diffusion limited, as cavity size was similar up to 400 °C regardless of electron beam exposure time; cavities also remained significantly smaller at higher dose (>20 minutes' electron beam exposure time) under constant electron irradiation at low temperature than those observed at higher temperature and equivalent dose under minimised electron beam exposure. Accordingly, larger cavities were observed at equivalent doses at higher temperature; indicating that, beyond a threshold vacancy concentration required for efficient cavity growth, defect mobility has a greater influence than dose on cavity growth dynamics. Nonetheless, it was shown that the mean cavity size reached at the

maximum temperature is dramatically reduced from ~11.2 nm under constant electron irradiation to ~5.4 nm when beam exposure time was reduced; hence it is proposed that, at high temperature where defect mobility is high, cavity growth is primarily limited by the supply of electron beam induced vacancy defects (dose limited). Radiation enhanced diffusion of lattice atoms (and consequently enhanced diffusion the vacancy defects by which atomic diffusion is facilitated) due to increased point defect concentration [157, 202], and / or ionisation enhanced diffusion - by which the thermal activation energy input required for diffusion is potentially lowered due to the lower migration energy of ionised point defects [203] - may also contribute to the earlier onset of enhanced cavity growth occurring at lower temperatures under constant electron irradiation.

6.3 Effect of ceramic microstructure on the thermal evolution of electron beam induced cavities during thermal annealing

Figure 6.6, Figure 6.7 and Figure 6.8 show the thermal evolution of electron beam induced cavities in Li_2TiO_3 specimens with different microstructural properties (grain size and porosity) under minimised electron beam exposure.
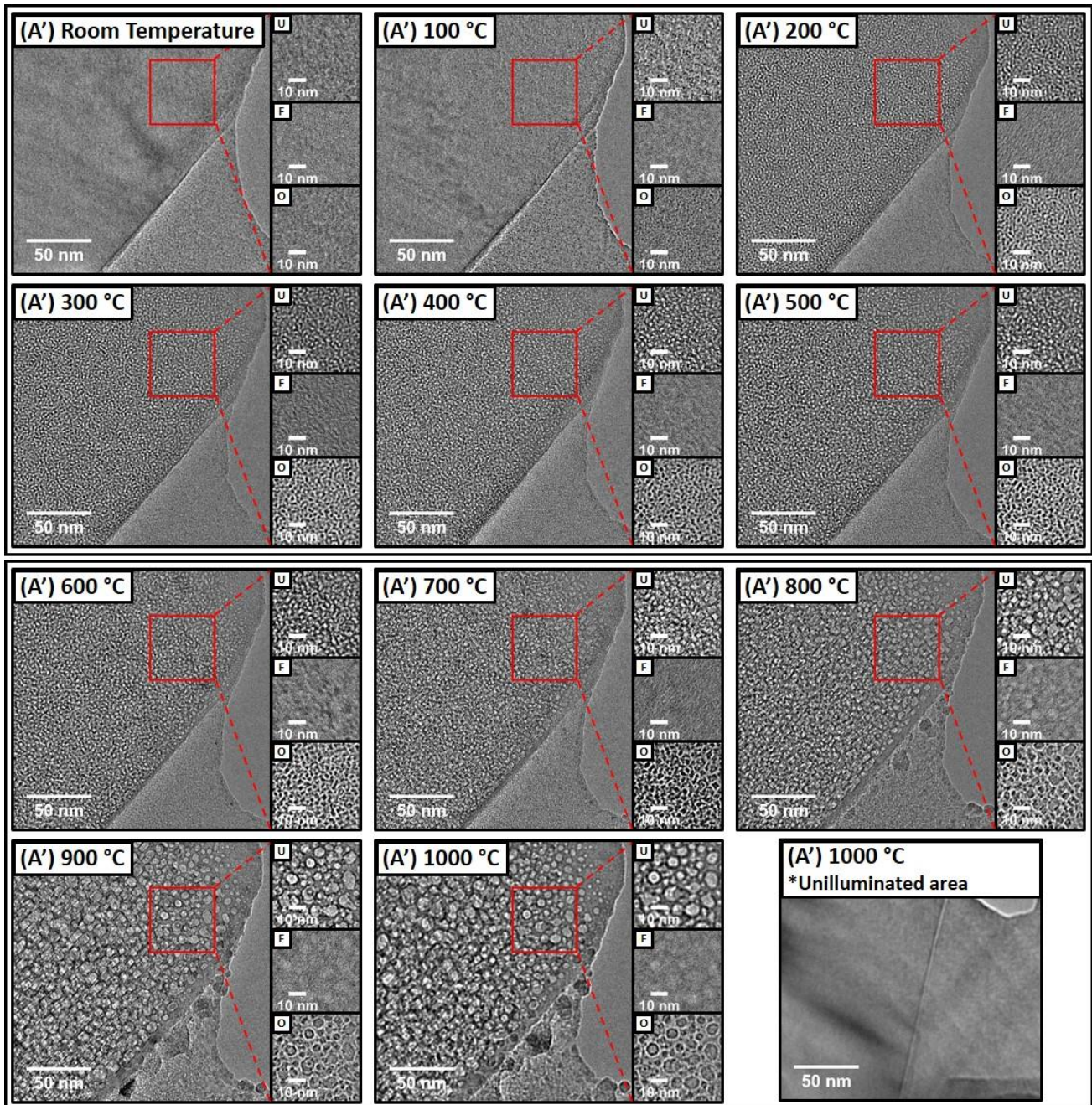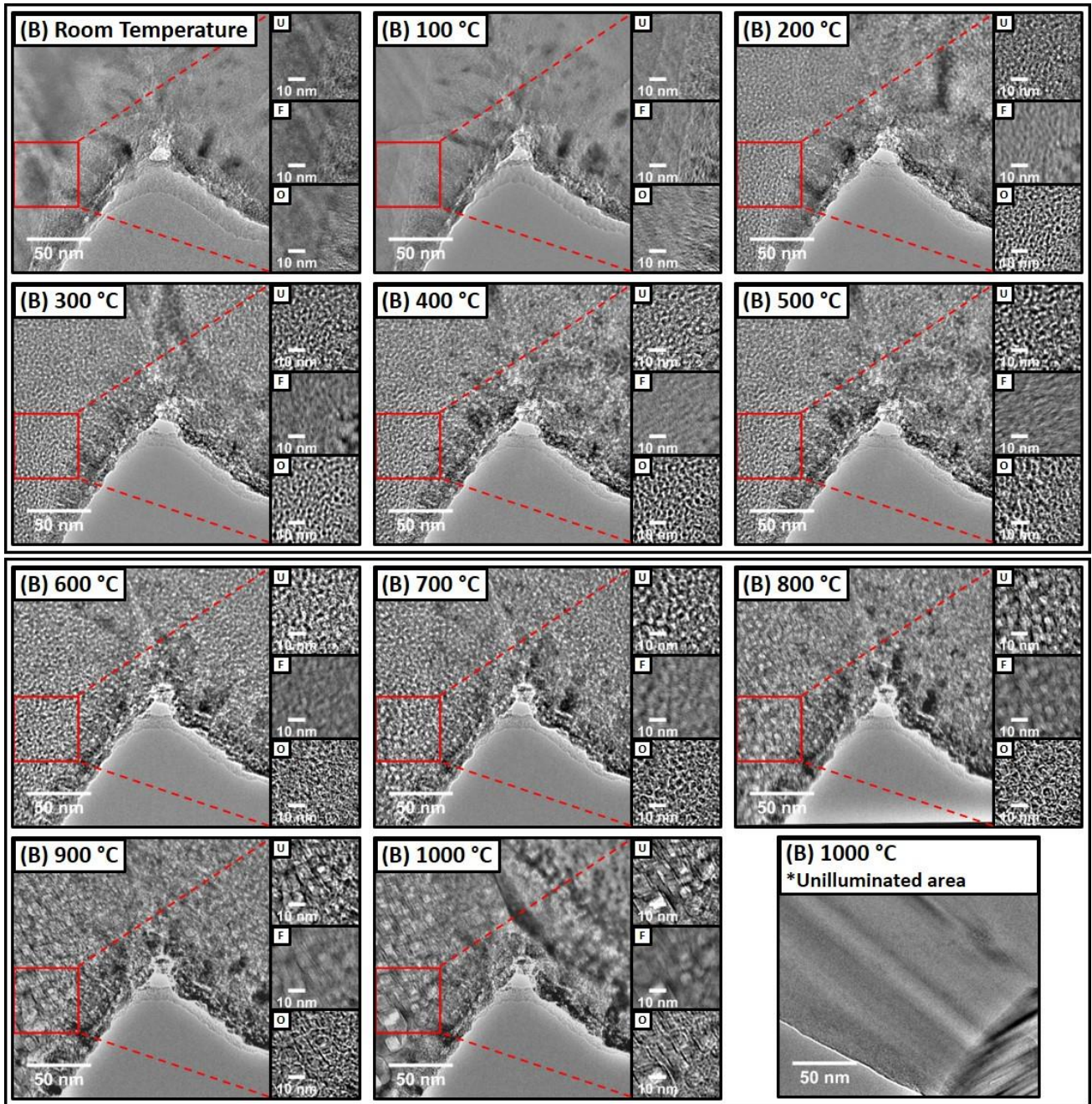
Figure 6.6: Bright field TEM micrographs showing the thermal evolution of electron beam induced cavities during in-situ annealing of Specimen B (high porosity, intermediate grain size [*Grain size: A'<B<C<D]; sintered at 900 °C, 6h) under a 300 keV electron beam where electron beam exposure time was minimised (beam switched off during isothermal dwell time at each incremental temperature).
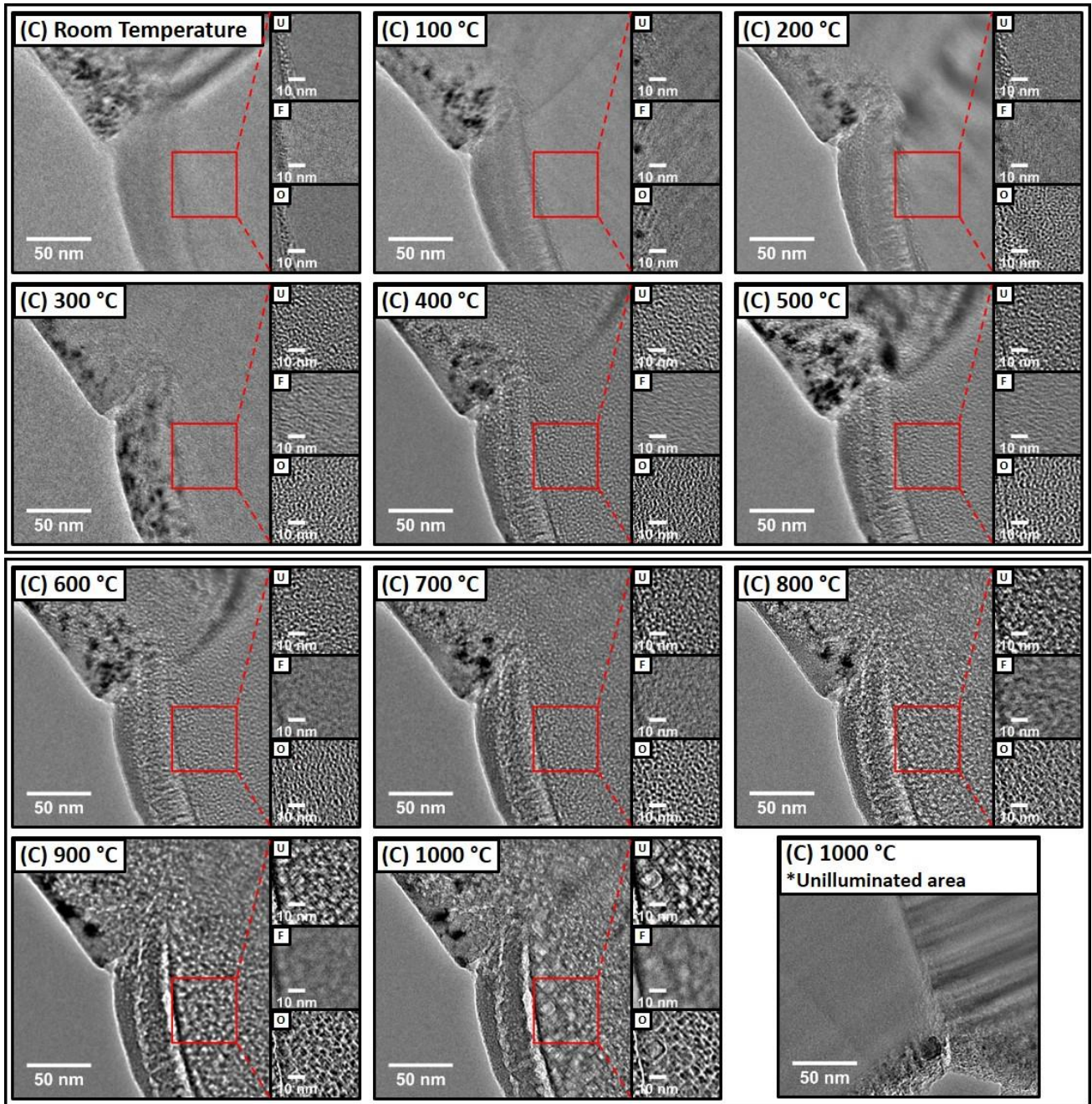
Figure 6.7: Bright field TEM micrographs showing the thermal evolution of electron beam induced cavities during in-situ annealing of Specimen C (low porosity, intermediate grain size [*Grain size: A'<B<C<D]; sintered at 1000 °C, 2h) under a 300 keV electron beam where electron beam exposure time was minimised (beam switched off during isothermal dwell time at each incremental temperature).
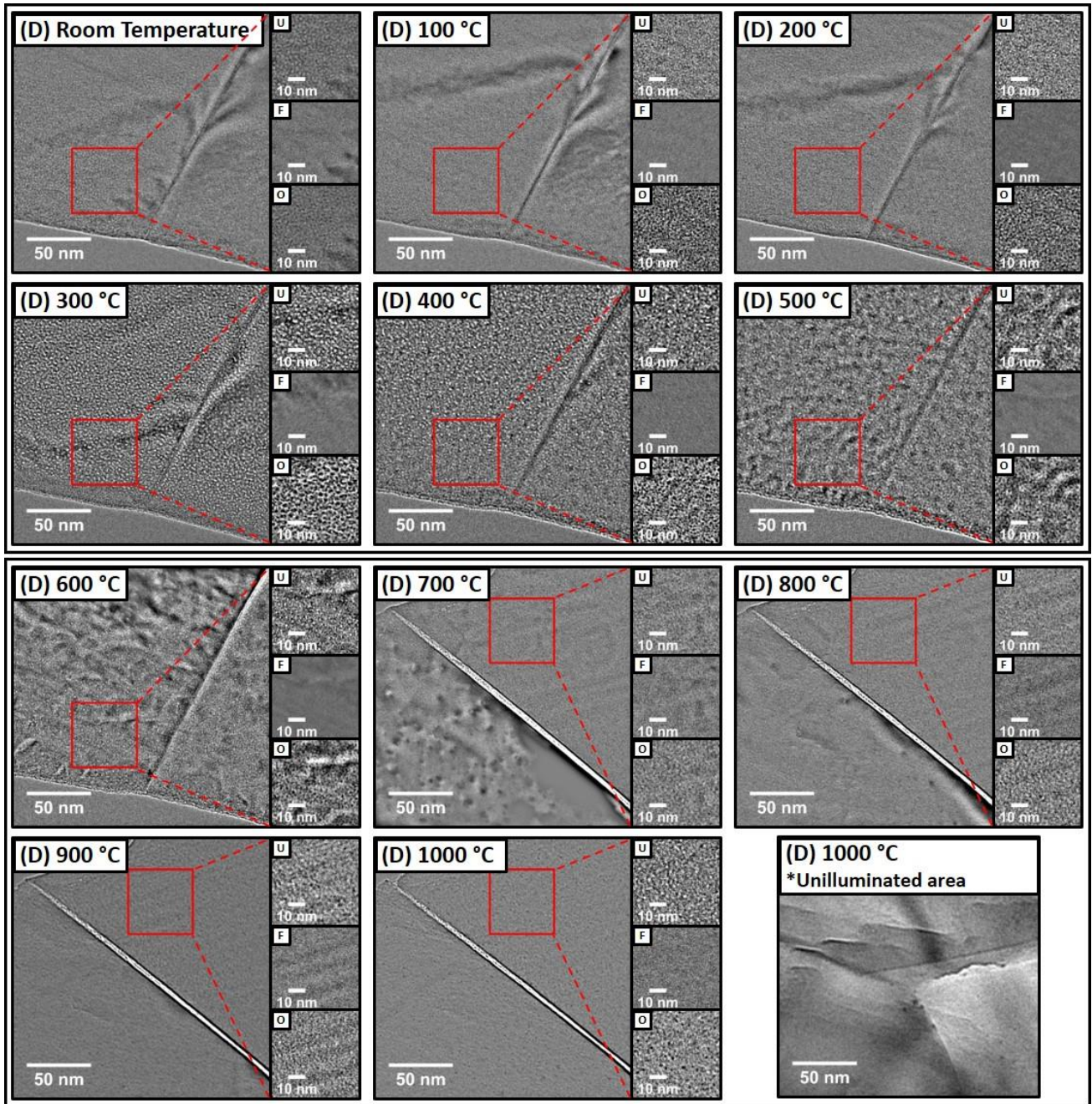
Figure 6.8: Bright field TEM micrographs showing the thermal evolution of electron beam induced cavities during in-situ annealing of Specimen D (low porosity, largest grain size; sintered at 1100 °C, 6h) under a 300 keV electron beam where electron beam exposure time was minimised (beam switched off during isothermal dwell time at each incremental temperature).

The primary purpose of these experiments was to determine the extent of electron beam damage leading to cavity formation and growth in microstructurally different specimens, such that the effects of the interactions of the electron beam with microstructurally analogous specimens could be taken into account in subsequent *in-situ* helium implantation and thermal annealing experiments, which will be discussed in Chapter 7.

Figure 6.6 corresponds to Specimen B, which was of similar porosity but larger grain size than that of Specimen A' (shown in Figure 6.4). Hereafter, these will be referred to as *high porosity* specimens. Figure 6.7 and Figure 6.8 correspond to Specimens C and D respectively, hereafter referred to as *low porosity* specimens, which were of lower porosity and larger grain size than that of Specimens A and B. Note also that the grain size of Specimen D was significantly larger than that of Specimen C; thus a significant difference in grain size existed within each suite of samples of comparable porosity.

The density, mean average grain size, and actual size of the grains examined during in-situ thermal annealing experiments (determined by manual density measurements, SEM image analysis, and analysis of TEM micrographs respectively) are summarised in Table 6.1. Values and associated errors were calculated according to the methods described in the previous chapter. Further details of specimen characteristics were presented in in Chapter 4.

Table 6.1: Mean average density and grain size (determined by SEM image analysis and manual density measurements respectively) of the Li_2TiO_3 samples shown in Figure 6.4, Figure 6.6, Figure 6.7, and Figure 6.8, and the actual size of the specific grains examined during electron beam irradiation (determined from TEM micrographs). Errors quoted were calculated according to Eq. (3.3) for density, 1 ESD for mean grain size, and half of the range of four measurements across each grain for actual grain size used in TEM experiments.

Corresponding figure	Sample ID and sintering conditions	Density (%TD)	Mean grain size (μm) from SEM analysis	Actual grain size used in TEM experiments (μm)
Figure 6.4	A' (900 °C, 3 hours)	65 ± 4	0.7 ± 0.3	0.9 ± 0.4
Figure 6.6	B (900 °C, 6 hours)	67 ± 3	1.0 ± 0.4	1.2 ± 0.4
Figure 6.7	C (1000 °C, 2 hours)	82 ± 2	1.6 ± 0.8	2.2 ± 1.2
Figure 6.8	D (1100 °C, 6 hours)	84 ± 2	3.4 ± 2.6	6.5 ± 2.6

Figure 6.9 shows a graphical representation of the mean cavity size of 50 cavities measured from micrographs of each specimen as a function of temperature during in-situ annealing under minimised electron beam exposure conditions. For ease of comparison, the data shown in Figure 6.5b is duplicated in Figure 6.9a.
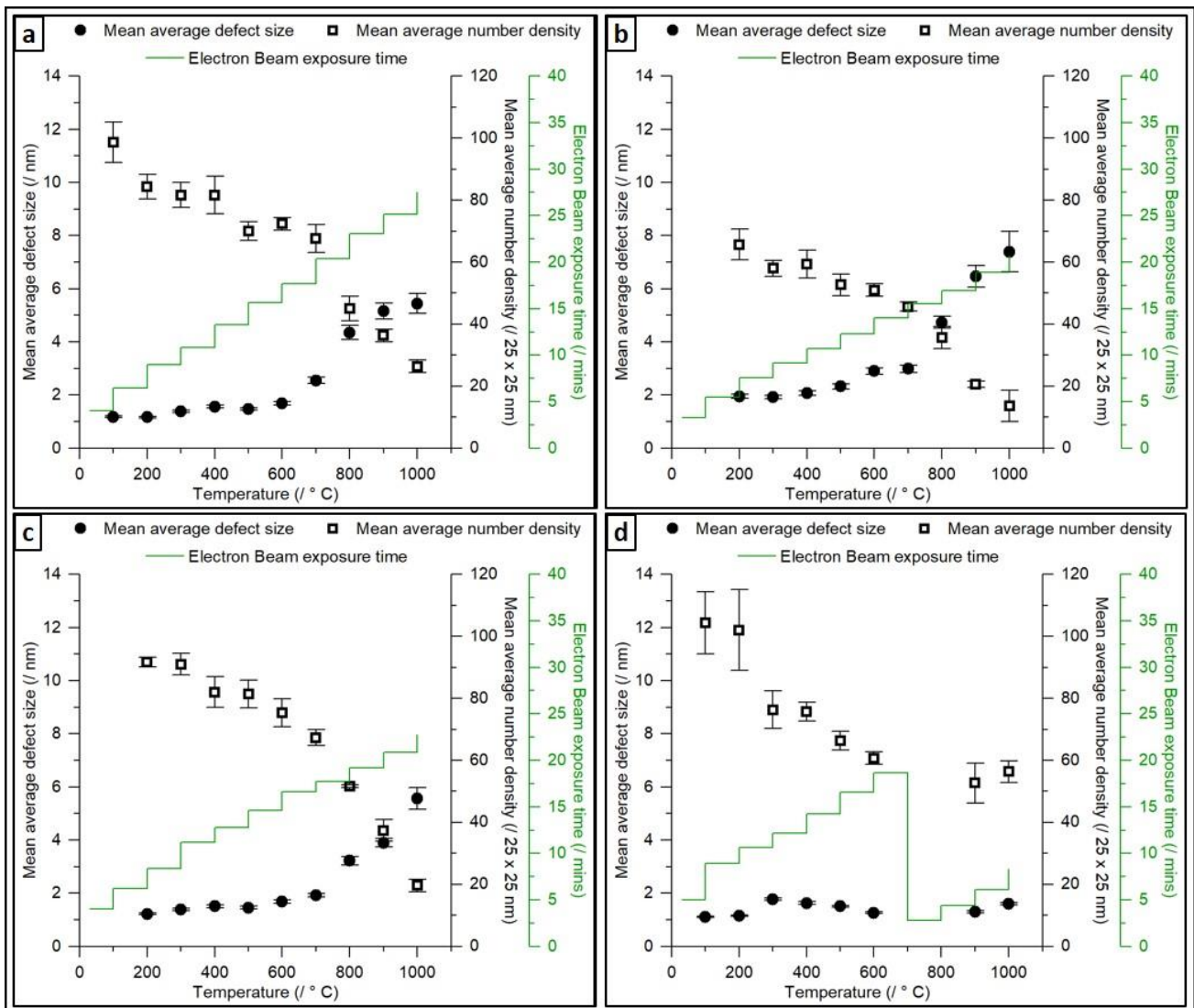
Figure 6.9: Mean average defect size and defect number density observed at incrementally increasing temperatures during in-situ annealing under minimised electron beam exposure. a) Specimen A' - high porosity, smallest grain size; b) Specimen B - high porosity, intermediate grain size; c) Specimen C - low porosity, intermediate grain size; d) Specimen D - low porosity, largest grain size.

Comparing the size of cavities exhibited in high porosity specimens, prepared from Li_2TiO_3 ceramic samples sintered at 900 °C for 3h and 6h (Figure 6.9a and b respectively), cavities were consistently larger in the larger grained specimen sintered for 6h despite lesser electron beam exposure time. The electron beam induced cavity growth behaviour exhibited by this specimen type was also shown to

139

be somewhat anomalous at room temperature (see Chapter 4). The reason for this remains unknown.

Although no resolvable cavities were observed at 100°C, the mean size and growth profile of cavities in the low porosity specimen with the smaller of the two grain sizes, prepared from an Li_2TiO_3 ceramic sample sintered at 1000 °C for 2h (Figure 6.9c), was remarkably similar to that of the high porosity specimen with the smallest grains (sintered at 900 °C for 3h, Figure 6.9a) at annealing temperatures of 200 °C - 600°C. In this temperature range cavity growth was relatively slow and cavities remained small, mean cavity size increased by only ~0.5 nm (from ~1.7 nm to ~2.2 nm). Although cavity growth was enhanced between 700 °C and 900 °C, which is proposed to be due mainly to enhanced defect mobility at such temperatures, the extent of growth was found to be less than that of the high porosity specimen with the smallest grains. It is probable that this is due to the slightly reduced electron beam exposure time in this temperature interval, in conjunction with the longer diffusion path required for interstitial defects to escape the specimen surface in the case of the low porosity specimen with larger grains, resulting in a reduction in the excess vacancy concentration responsible for cavity growth. Interestingly, the rate of cavity growth did not slow between 900 °C and 1000 °C in the low porosity specimen sintered at 1000 °C for 2h as it did in the high porosity specimen sintered at 900 °C for 3h; as a result, the mean cavity sizes at 1000 °C were similar (5.6 nm and 5.4 nm respectively) despite the former exhibiting slower growth at intermediate temperatures. This could be attributed to the lesser degree of vacancy defect loss to unbiased sinks at grain boundaries in specimens with larger grains; the result being that a higher vacancy excess, and thus a greater net influx of vacancies to existing cavities, is maintained despite increased equilibrium vacancy concentration at higher temperatures.

In contrast, the cavity growth dynamics of the low porosity specimen with the largest grain size, prepared from an Li_2TiO_3 ceramic sample sintered at 1100 °C for 6h, differ significantly from those exhibited by the other specimens investigated. Visual inspection of TEM micrographs (Figure 6.8) in conjunction with mean cavity size statistics (Figure 6.9c) reveals that some resolvable cavity formation was apparent at 100 °C – 200 °C, and measurable growth was observed at 300 °C (from 1.2 nm to 1.8 nm). A concurrent decrease in cavity number density was observed with cavity growth up to 300 °C, indicative of a coarsening process similar to that observed in other specimens. However, despite being subjected to the longest duration of electron beam exposure experienced by any of the specimens (at equivalent temperatures), mean cavity size reached a maximum at 300 °C, above

which cavity shrinkage occurred in the 400 °C – 600 °C temperature range. The observed shrinkage was accompanied by the continued reduction of cavity number density, indicating that some cavities had annealed out entirely. This was particularly apparent at 500 °C – 600 °C, at which temperature damage recovery processes resulting in the shrinkage and annihilation of cavities appear to outweigh further cavity nucleation and growth. Void shrinkage can be attributed to (i) a net absorption of interstitials by voids, (ii) the emission of vacancies by voids, or a combination of these two factors [204]. In this case, it is proposed that the longer diffusion path for interstitials to reach sinks at grain boundaries or escape from the surface of the specimen with the largest grains also results in a reduction of the extent of the preferential loss of interstitials, which in turn increases the probability of vacancy-interstitial recombination and thus reduces the excess vacancy concentration responsible for cavity formation and growth. The influence of the increased diffusion path length to surfaces / grain boundaries on excess vacancy concentration may be more significant at elevated temperature where defect mobility is enhanced.

The rate of thermal vacancy emission ($\dot{R}_v$) from voids or cavities increases with temperature (T), and can be described by [155]:

$$\dot{R}_v = \frac{D_v C_v^0}{R}\left[1 - exp\left(\frac{2\Omega\gamma}{k_b TR}\right)\right]$$
<div align="right">Eq. (6.2)</div>

Where D_v and C_v^0 are vacancy diffusivity and thermal equilibrium concentration respectively, R is the cavity radius, Ω is atomic volume and γ is the free surface energy. Hence it is suggested that cavity shrinkage at temperatures above 300 °C is due to a combination of two factors:

(i) The thermal equilibrium vacancy concentration (see eq. (6.1)) is sufficiently high to suppress further cavity growth in this specimen as the processes responsible for excess vacancy production are likely to be less efficient in specimens with large grains.

(ii) Increased thermal emission of vacancies from existing cavities and their subsequent diffusion away from the cavity where they may be accommodated in the bulk due to increased equilibrium vacancy concentration at elevated temperature.

Note from Eq. (6.2) that the rate of thermal emission of vacancies from voids or cavities is greater for cavities of smaller radius. Given the proposed reduction in excess vacancy concentration in the bulk of larger grained specimens due to the increased probability of defect recombination, it is feasible

that the rate of vacancy emission from existing small cavities at elevated temperature outweighs the influx of excess vacancies to cavity walls; resulting in the shrinkage and dissolution of cavities.

The observation of damage recovery in the form of cavity shrinkage in the 400 °C – 600°C temperature range, in conjunction with the relatively low number density of smaller cavities exhibited by the largest grained, low porosity specimen at 600 °C, indicates that this specimen is the most resistant to electron beam induced cavity formation, particularly at intermediate temperatures.

Unfortunately, mechanical failure of the thin film specimen at 700 °C forced the examination of an area which had not previously been illuminated by the electron beam at temperatures of 700 °C and above. No resolvable defects were observed at 700 °C and 800 °C (3 minutes and 4 minutes electron beam exposure time respectively). Sparingly resolvable defects were observed at 900 °C after ~6 minutes of electron beam exposure. Where significantly enhanced growth was observed in the other specimen types studied at such temperatures, minimal cavity growth of only 0.3 nm (from 1.3 nm to 1.6 nm) was observed in this specimen on increasing the temperature to 1000 °C and exposure time to 8 minutes. This is likely to be due to the reduced electron fluence (dose) experienced by this area of the specimen owing to the earlier mechanical failure; as such, the excess vacancy concentration responsible for cavity growth had not been previously allowed to build up at lower temperature, and hence the supply of vacancies to cavity walls was insufficient for efficient growth to occur despite the high temperatures. Notably however, the number density of resolvable defects observed at 900 °C – 1000 °C was approximately half that of defects observed at low temperature at approximately equivalent electron exposure time. This suggests that Li_2TiO_3 exhibits a greater resistance to electron beam induced damage when the associated electron irradiation is carried out at high temperature. The apparently lesser susceptibility of Li_2TiO_3 to electron beam induced cavity formation when irradiated at high temperature is proposed to be due to the higher recombination rate of electron beam induced Frenkel pairs at elevated temperature due to increased defect mobility; hence the excess vacancy concentration responsible for cavity growth builds up to a lesser extent and the extent of cavity formation and growth is reduced.

6.4 Possible influence of CO_2 release on cavity growth

It has long been established that the presence of gas atoms is considered essential for void/cavity nucleation and growth [18, 21, 22]. The presence of gas atoms reduces the surface energy associated with vacancy clusters, voids and cavities [145]; thereby stabilising the internal surfaces, in turn

preventing the collapse of small voids into dislocation loops and facilitating growth. Void number density has been reported to increase with gas concentration in irradiated metals, indicating that the gas acts as an efficient nucleating agent [146]. In addition to aiding nucleation, void embryos containing a sufficient quantity of gas have been reported to experience preferential growth, where void number density was significantly reduced or entirely absent in degassed specimens of the same material [145]. Once nucleated, growth of existing voids and cavities is generally believed to occur by the absorption of vacancies and gas atoms [18, 23]; the extent of (volumetric) growth is primarily dictated by the supply of vacancies, the net absorption of which may be driven by the internal pressure of the stabilising gas [147]. The pressure exerted by gases contained within cavities may also serve to reduce the thermal emission of vacancies [140], which would otherwise counter the net influx of vacancies responsible for cavity growth to a greater extent.

Li_2TiO_3 is known to absorb atmospheric water and CO_2 at room temperature, resulting in the formation of a Li_2CO_3 surface layer [205]. Evidence of Li_2CO_3 formation due to the reaction of the Li_2TiO_3 pellets used in this work with atmospheric CO_2 was shown previously in the XRD pattern obtained from a pellet which had been deliberately exposed to atmospheric air for a long period (see Figure 5.7, Chapter 5). While all specimens used in TEM experiments, and the pellets from which they were prepared, were stored under inert (dry argon) atmosphere in order to minimise atmospheric exposure as far as reasonably possible, some degree of surface reaction during sample preparation was inevitable. The results of thermal desorption spectroscopy (TDS) experiments designed to identify the gaseous species evolved from the pristine Li_2TiO_3 samples used in this work as a function of temperature are shown in Figure 6.10.
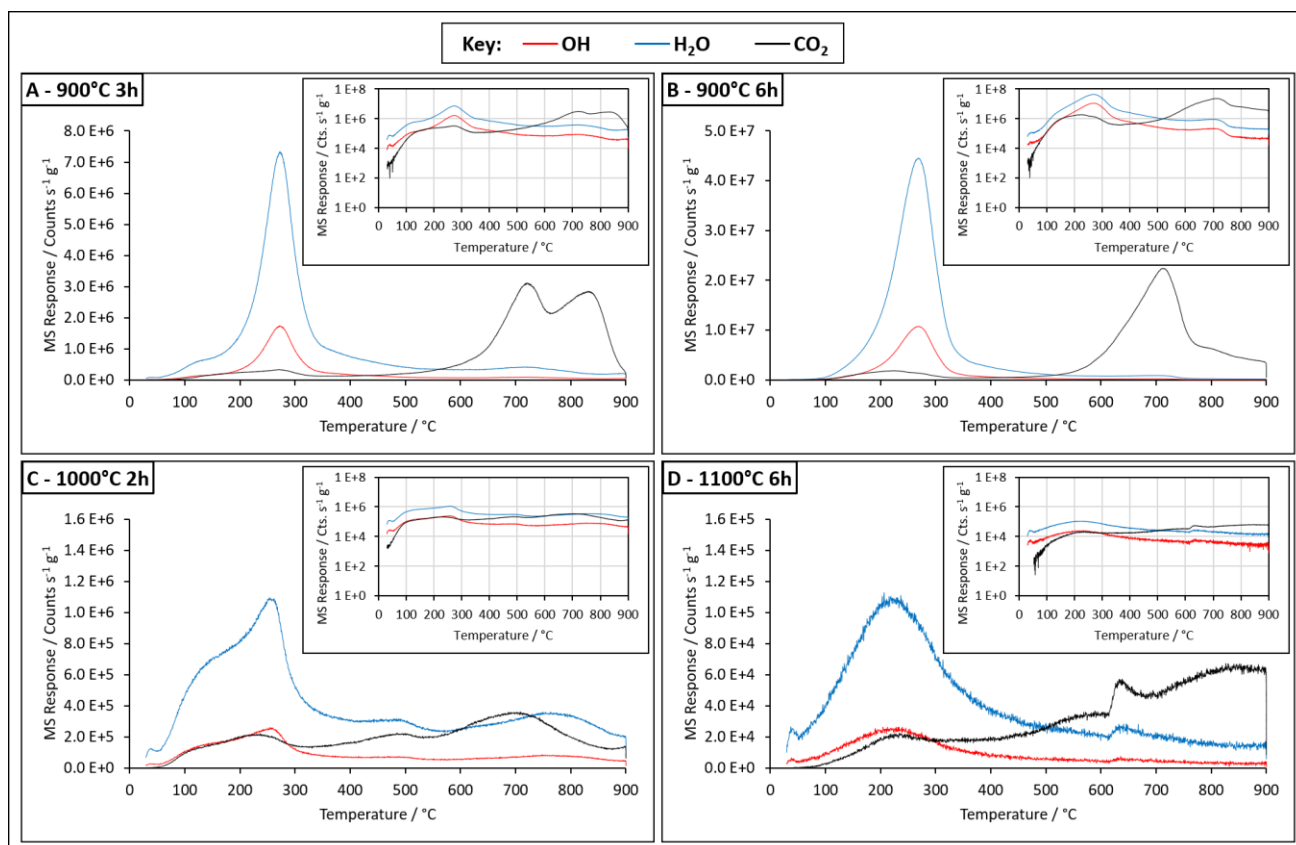
Figure 6.10: TDS spectra showing H_2O, OH and CO_2 release profiles obtained from "pristine" Li_2TiO_3 pellets sintered under different conditions as a function of temperature (using a constant heating rate of 10 °C min-1). Data shown has been background subtracted and normalised according to the mass of each sample. Main figures are plotted on an appropriate linear y scale to highlight key features in the gas desorption profiles of each sample; insets show identical data plotted on equivalent logarithmic y scales to enable the comparison of the desorption rates observed in the data obtained from different samples.

The TDS spectra obtained from pristine Li_2TiO_3 pellets were dominated by signals corresponding to H_2O, OH and CO_2 species, indicating that significant quantities of water and CO_2 had been absorbed in all cases. Peak positions and desorption profiles of H_2O and OH species were found to be very similar, with the latter scaling approximately to the former; hence it was concluded that both of these signals could be attributed to water desorption. The signal corresponding to OH is potentially due to fragmentation of H_2O as a result of the ionisation process associated with mass spectrometry.

All samples exhibited initial water and OH desorption events at low temperature (~40 °C), which was attributed to the desorption of weakly physisorbed surface water. Significant desorption of water from all samples was observed between ~50 °C and ~350 °C, which appears to occur in a two-stage process. Increased water release at slightly elevated temperatures (~50 – ~150 °C), which appears most clearly as a shoulder in the TDS spectra corresponding to samples A and C, was attributed to

desorption of weakly chemisorbed water at the sample surfaces; peak water desorption, which occurred at temperatures between 200 °C and 300 °C in each case, was attributed to the thermally activated desorption of chemisorbed water originating from further beneath the sample surfaces. It is noted that the magnitude of the main water desorption peak is significantly greater in the case of the high porosity samples (Figure 6.10, A and B) than those of the low porosity samples (Figure 6.10, C and D), indicating that the latter two samples absorbed less water during sample preparation and interim storage; this is proposed to be due to the lower accessible surface area of the low porosity samples resulting in lesser surface available for absorption of atmospheric moisture.

Minor CO_2 desorption peaks were also observed between ~50 °C and ~350 °C, concurrent with peak water release. This was attributed to the desorption of physisorbed and/or weakly chemisorbed CO_2, the release of which appears to have been assisted by the desorption of water, which may be acting as a carrier gas which assists the desorption of weakly bound CO_2 from the sample surface. The main CO_2 desorption events occur above 500 °C, with peak CO_2 release observed between ~640 °C and ~740 °C in each case. This temperature range coincides with the thermal decomposition temperature of Li_2CO_3 (~740 °C under ambient conditions) [82], the decomposition of which may occur at lower temperature when in contact with a catalysing surface [84], or may be slightly reduced under vacuum. Hence the major CO_2 desorption event is ascribed to the thermal decomposition of Li_2CO_3, formed as a result of surface reaction of Li_2TiO_3 with atmospheric CO_2 during sample preparation. Similarly to water desorption, CO_2 desorption from low porosity samples was significantly less than that of high porosity samples; peak CO_2 desorption from the sample of lowest porosity (Figure 6.10 D) was found to be approximately three orders of magnitude less than the maximum desorption observed from high porosity samples. Again this is attributed to the lower accessible surface area of low porosity samples, resulting in less surface availability for reaction with atmospheric CO_2; thus Li_2CO_3 formation occurs to a lesser extent in low porosity specimens.

According to Mayer *et al.* [146]*,* any gas is capable of stabilising voids and cavities. While diffusion processes associated with water desorption appear to have negligible effects on cavity growth in Li_2TiO_3, a distinct correlation exists between CO_2 desorption and the rate of cavity growth during thermal annealing under electron irradiation. Neglecting the cavity growth statistics for specimen D due to its mechanical failure, the fastest rate of cavity growth was observed at 700 °C - 800 °C in thin film specimens A - C during thermal annealing under electron irradiation; this correlates well to the peak CO_2 desorption temperatures observed in TDS data collected from the analogous pellet

samples. As CO_2 produced by the thermal decomposition of Li_2CO_3 diffuses through the thin film specimens, it will invariably meet the surfaces of cavities formed as a result of electron beam damage. Hence it is proposed that, while the majority of CO_2 escapes from the specimen surface, sufficient CO_2 is absorbed by existing cavities to further stabilise them by reducing the surface energy associated therewith; the internal gas pressure exerted also increases the driving force for vacancy absorption, resulting in enhanced cavity growth due to increased absorption of vacancies and gas atoms. The low levels of CO_2 release observed in TDS data obtained from sample D relative to that of the other samples may also contribute to the comparatively low number density of small cavities observed at high temperatures; it is feasible that insufficient gas atoms are present to stabilise the nucleation and growth of a large number of voids at such temperatures.

6.5 Conclusions of thermal evolution of electron beam induced cavities study

Li_2TiO_3 has previously been shown to be susceptible to electron beam induced damage, resulting in cavity formation (see Chapter 5). In this chapter effect of temperature on the evolution of electron beam induced damage was investigated; the growth of cavities under a 300 keV TEM electron beam was found to be significantly enhanced at elevated temperatures, relevant to the operating temperatures of ceramic breeder materials in a working fusion reactor. Under constant electron irradiation, the size of cavities was shown to increase exponentially with increasing temperature at temperatures in excess of 400 °C, this is primarily attributed to the enhanced mobility of irradiation induced defects at elevated temperatures.

Minimising exposure of thin-film specimens to the electron beam was found to significantly reduce the extent of cavity growth, particularly at high temperatures, indicating that cavity growth is strongly dependent on electron fluence. Based on the results of this study, it is proposed that cavity growth in Li_2TiO_3 under electron irradiation is diffusion limited at low temperatures, whereas at high temperatures, where the equilibrium vacancy concentration becomes significant by comparison to the number of additional vacancies introduced as a result of electron beam damage, the excess vacancy concentration (which correlates to electron irradiation dose) becomes the limiting factor for cavity growth. That said, beyond a threshold irradiation dose, defect mobility is proposed to have a greater overall influence on cavity growth dynamics than electron fluence.

The microstructure of Li_2TiO_3 ceramics was found to effect the growth dynamics of electron beam induced cavities as a function of temperature. The thin film specimen of low porosity with the largest

grain size showed cavity shrinkage at intermediate temperatures (400 °C – 600 °C) where continued growth of cavities was observed in all other specimens at equivalent temperatures; indicating that low porosity and large grain size may increase the resistance of Li_2TiO_3 to electron beam damage. This is attributed to the longer diffusion path to defect sinks associated with large grain size, resulting in a lesser degree of preferential interstitial loss and increased probability of defect recombination; thus reducing the excess vacancy concentration responsible for cavity growth in the bulk. Limited evidence, in the form of the significantly reduced number density of small cavities which formed at high temperature compared to those observed to nucleate at low temperature in the early stages of cavity formation, suggests that radiation damage recovery may be enhanced when electron irradiation of a pristine region of such specimens is carried out at high temperature.

A distinct correlation between the temperature at which significant quantities of CO_2 were released from bulk Li_2TiO_3 samples and accelerated cavity growth in thin film specimens was identified. Hence it is proposed that enhanced cavity growth under electron irradiation at elevated temperature in Li_2TiO_3 may be facilitated by CO_2 gas produced as a result of the thermal decomposition of an Li_2CO_3 surface reaction layer. The presence of CO_2 gas is proposed to enhance cavity growth by stabilising the internal free surfaces of cavities, and exerting pressure on cavity walls, which increases the driving force for vacancy absorption and reduces the rate of thermal emission of vacancies from existing cavities.

Chapter 7 - In-situ helium ion implantation and thermal annealing experiments

As stated in the previous section, the nucleation and growth of cavities is believed to be facilitated by gas atoms due to a combination of the stabilisation effect associated with the reduction of the free surface energy of internal cavity surfaces, and the pressure exerted by gas contained within cavities. Helium is known to be particularly efficient in its capacity to stabilise cavities; indeed vacancy defects, the aggregation of which is proposed to be the origin of cavity formation in Li_2TiO_3, have been described as an insaturable trap for helium due to the positive binding energy between interstitial helium atoms and helium-vacancy clusters [147]. As such, helium trapped within cavities can reach very high gas pressures, which in turn increases the driving force for vacancy absorption by existing helium filled cavities.

The results of room temperature in-situ helium ion implantation and subsequent thermal annealing experiments designed to investigate the thermal evolution of implanted helium in Li_2TiO_3 at temperatures relevant to breeder blanket operating temperatures are discussed in the following section. The main objectives of these experiments were to investigate the nature and extent of helium accumulation in Li_2TiO_3 samples with different microstructural properties as a function of temperature, and to determine the effects of the interactions of implanted helium with electron beam induced radiation defects.

7.1 Room temperature in-situ He$^+$ implantation

Prior to in-situ helium implantation experiments, in order to identify an appropriate ion energy such that the majority of implanted helium was deposited within thin film specimens of Li_2TiO_3, the ion implantation range and the associated displacement damage profile induced by implanted ions was simulated using SRIM [132]. The results of SRIM simulations corresponding to the implantation of 5.5 keV He$^+$ ions into Li_2TiO_3 using the *"Detailed Calculation with full Damage Cascades"* model are shown in Figure 7.1. The threshold displacement energies corresponding to each lattice atom type used in simulations were taken from the work of Fisher *et al. [206]*. The theoretical density of Li_2TiO_3 (3.43 g cm^{-3} [78]) was used in simulations since the regions of porosity in a thin film specimen are effectively empty space which the ions pass through unhindered, whereas the grains of ceramic with which the ion beam interacts are likely to possess a density approximately equal to the theoretical maximum. A total fluence of 10^{17} He$^+$ ions cm^{-2} was selected based on the fluence of helium which has been reported in the literature to result in helium bubble formation in other ceramics [37, 123, 127, 151].

Helium concentration and ion induced dpa profiles were calculated from SRIM outputs using equations 7.1 and 7.2 respectively:

$$[He] \, (atom \, \%) = \frac{He^+ \, Ions \, (Atoms \, cm^{-3} \, / \, Atoms \, cm^{-2}) \cdot Fluence \, (Ions \, cm^{-2})}{Target \, density, \rho \, (Atoms \, cm^{-3})} \qquad (7.1)$$

$$He^+ Induced \, dpa = \frac{Total \, He^+ \, Induced \, Vacancies \, (Vacancies \, Å^{-1} \, Ion^{-1}) \cdot Fluence \, (Ions \, cm^{-2})}{Target \, density, \rho \, (Atoms \, cm^{-3}) \cdot 10^{-8} \, (cm \, Å^{-1})} \qquad (7.2)$$

Where the *"He⁺ ions"* (in units of Atoms cm⁻³ / Atoms cm⁻²) and *"Total He⁺ Induced Vacancies"* (in units of vacancies Å⁻¹ Ion⁻¹) terms at a given range are direct outputs from SRIM, the latter of which was calculated from the sum of the outputs corresponding to each target atom type (Li, Ti and O).
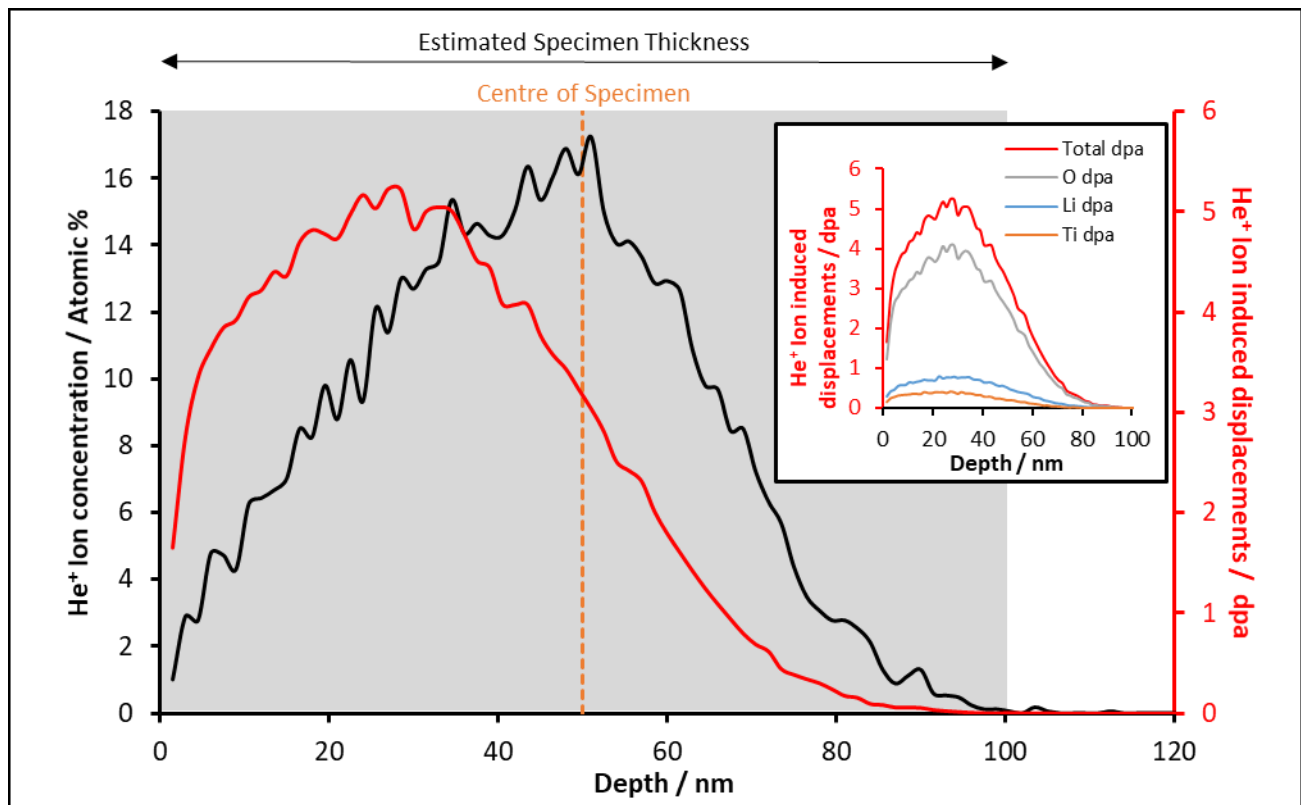
Figure 7.1: Ion range profile (black) and associated ion-induced displacement damage profile (red) of 5.5 keV He⁺ ions implanted into the surface of a Li$_2$TiO$_3$ thin film at 18.7° to the surface normal to a total fluence of 10^{17} He⁺ ions cm⁻²; simulated using SRIM [132]. Estimated specimen thickness is shown by the grey area, dashed orange line indicates the centre of the specimen in the plane parallel to the specimen surface. Inset shows the contributions of each lattice atom type to the total displacements per atom induced by implanted He⁺ ions.

As shown in Figure 7.1, assuming a specimen thickness of 100 nm, the maximum concentration of implanted helium coincides approximately with the centre of the specimens, and the implantation range of 5.5 keV He$^+$ ions is such that the majority of implanted helium was deposited within the thin film specimens. The results of SRIM simulations show that peak helium concentration theoretically reached ~17 atomic percent at the fluence employed in this work, and the mean average helium concentration over the depth of the specimens was ~8 atomic percent. Peak and average helium concentrations therefore correspond to the quantity of helium which would be produced as a result of ~52% and ~25% lithium burnup in Li_2TiO_3 during operation in a fusion reactor (according to the Li (n,α) reaction) respectively. For Li_2TiO_3, an end-of-life lithium burnup of ~17% in the EU DEMO fusion reactor is considered feasible [33]; simulations performed by Shimwell *et al.* [207] showed that the depletion of ^{6}Li (with which ceramic breeders have been proposed to be enriched to up to 90% of their total lithium content [12]) in Li_4SiO_4 due to burnup was estimated reach a maximum of 19 % after five years in operation. As such the helium concentration corresponding to the fluence used in this work is somewhat higher than that which is expected to be produced during the testing of ceramic breeder materials in the DEMO programme; however, considering that it is unlikely that all of the implanted helium was retained by the thin film specimens, and that thermal migration is likely to result in localised regions of high helium concentration under operational conditions in a working breeder blanket, it is reasonable to assume that the helium concentration resulting from the ion fluence used in this work is fairly representative of that which might occur under operational conditions.

The effects of helium ion implantation on the specimens is twofold; firstly, the implanted helium may act as a stabilising gas, facilitating cavity formation and growth, and / or accumulating to form helium bubbles due to its insolubility in most solids [19]. Secondly, as shown by the results of SRIM simulations, sufficient energy is transferred from incident helium ions to lattice atoms to induce a significant number atomic displacements, thereby introducing an appreciable amount of damage to the crystal structure. Peak ion induced damage was predicted to reach approximately 5 dpa at the maximum fluence used in this work according to SRIM simulations, the majority of which is supposedly due to displacements in the oxygen sublattice (see Figure 7.1, inset). It is noted however, that this is likely to be an overestimate of the actual extent of damage present in the specimen since SRIM simulations do not account for defect recombination; as such the number of "surviving" vacancies per Angstrom-Ion is likely to be significantly lower than that which is predicted using SRIM.

150

Nonetheless, a significant number of defects are expected to have been introduced as a result of displacement damage associated with the ion implantation process.

As such, in addition to potential gas bubble formation as a result of helium accumulation, and the facilitation of cavity nucleation and growth in Li_2TiO_3 specimens due to the stabilising effect of helium on the internal surfaces thereof; additional vacancies introduced as a result of displacement damage induced by helium ion implantation are expected to enhance cavity growth in areas exposed to the electron beam. The introduction of additional vacancies as a result of ion induced displacements increases the vacancy concentration, thus increasing the extent of vacancy supersaturation; this in turn results in a higher flux of vacancies to the walls of existing cavities which, in conjunction with by the concurrent absorption of gas atoms, is expected to enhance cavity growth.

Figure 7.2, Figure 7.3 and Figure 7.4 show cavity / helium bubble formation in Li_2TiO_3 specimens A (high porosity, smallest grains), C (low porosity, larger grains) and D (low porosity, largest grains) respectively at progressively increasing He^+ fluence during in-situ ion implantation at room temperature. The grain sizes of the specific grains examined in each specimen during in-situ helium ion implantation (and subsequent in-situ thermal annealing experiments), measured from TEM micrographs according to the method described previously, were as follows:

High porosity - Specimen A: 1.2 µm ± 0.5 µm

Low porosity - Specimen C: 2.8 µm ± 2.5 µm

Low porosity - Specimen D: 7.1 µm ± 2.8 µm

Electron beam exposure time was minimised as far as reasonably possible during ion implantation. The lower rightmost micrographs in each figure, which were taken at the end of the room temperature ion implantation process, correspond to an area of each specimen which had not previously been exposed to the electron beam during ion implantation; as such the formation of features observed in these regions was ascribed solely to the effects of the implanted helium. All other micrographs correspond to areas which had been subjected to the minimum possible electron exposure time which allowed the acquisition of through focal series micrographs at incrementally increasing ion fluence; hence the formation of features observed in these regions was attributed to effects arising due to a combination of ion implantation and electron beam damage.
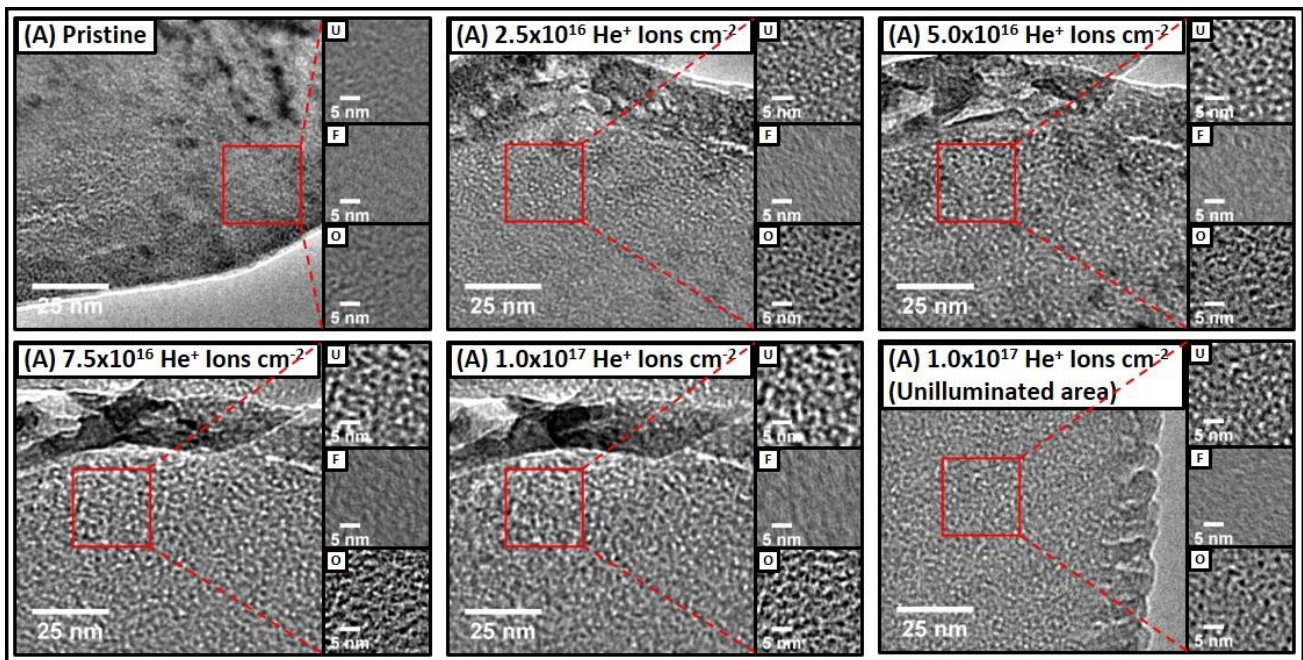
Figure 7.2: Bright field TEM micrographs showing the formation of cavities and/or helium bubbles with increasing fluence of 5.5 keV He+ ions during in-situ implantation of Li_2TiO_3 Specimen A (high porosity, smallest grain size; sintered at 900 °C, 3h) at room temperature.
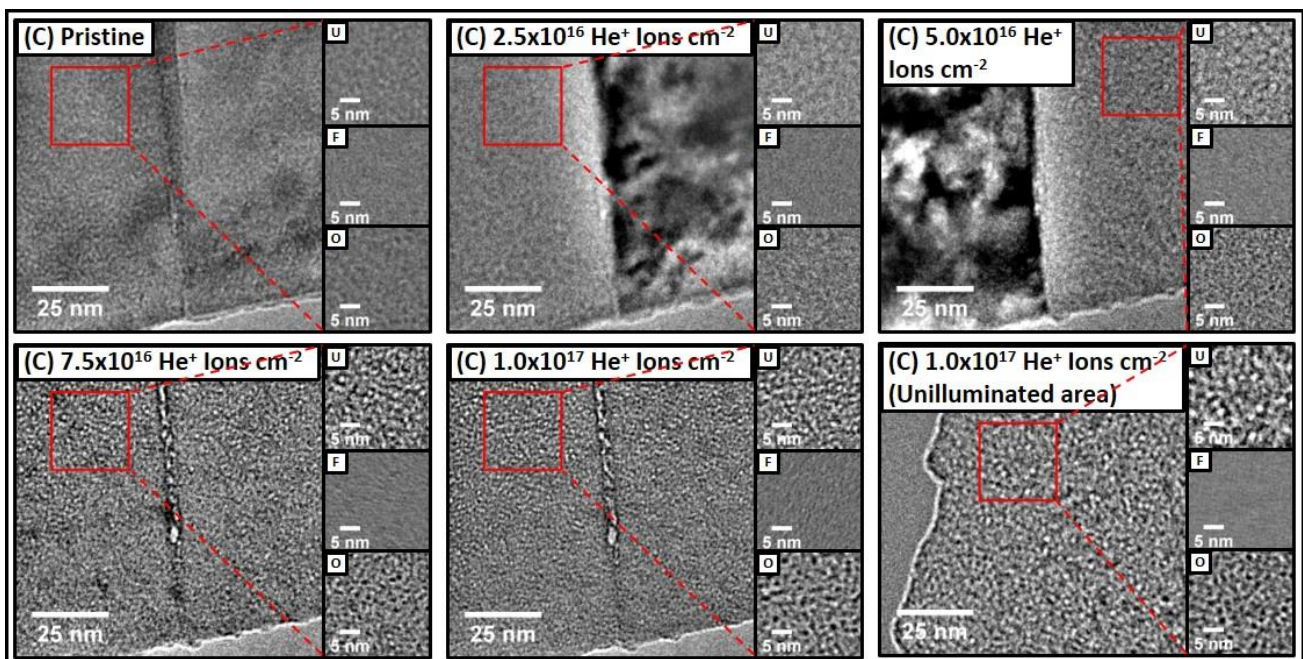
Figure 7.3: Bright field TEM micrographs showing the formation of cavities and/or helium bubbles with increasing fluence of 5.5 keV He+ ions during in-situ implantation of Li_2TiO_3 Specimen C (Low porosity, intermediate grain size; sintered at 1000 °C, 2h) at room temperature.
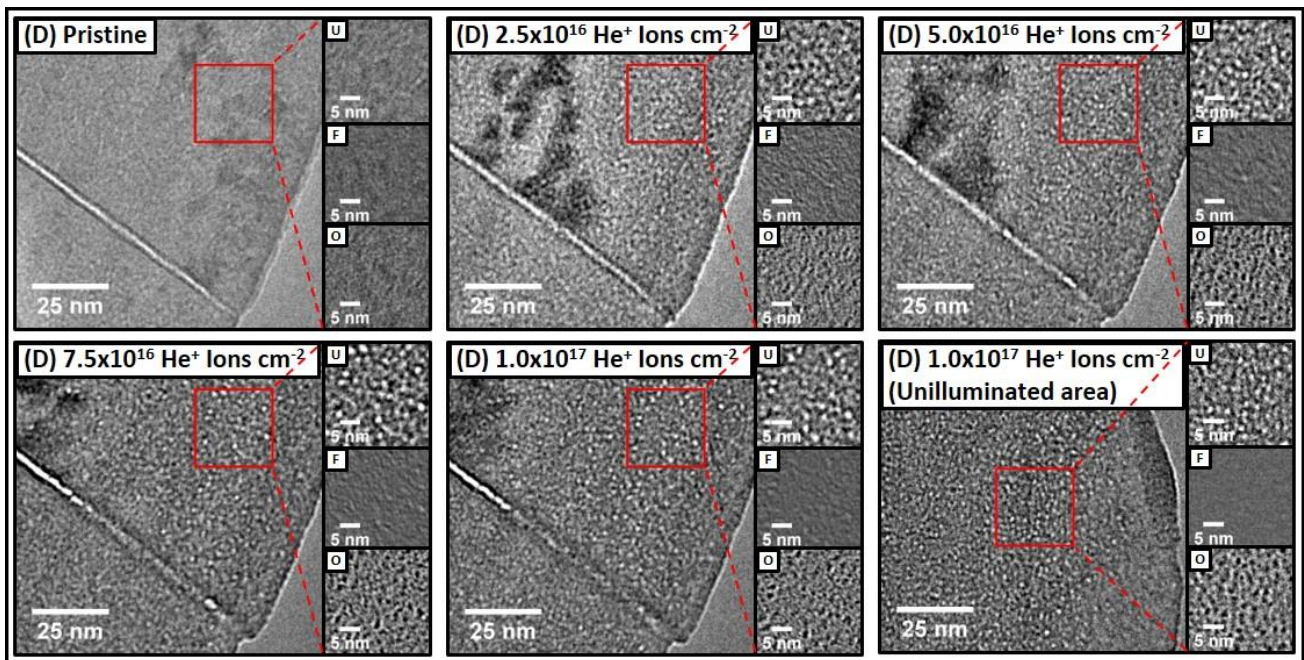
Figure 7.4: Bright field TEM micrographs showing the formation of cavities and/or helium bubbles with increasing fluence of 5.5 keV He+ ions during in-situ implantation of Li_2TiO_3 Specimen D (Low porosity, largest grain size; sintered at 1100 °C, 6h) at room temperature.

TEM resolvable cavities, possibly stabilised by the implanted helium, became visible in TEM micrographs of specimens A and D at the lowest incremental fluence (2.5×10^{16} He$^+$ ions cm^{-2}), at which point the regions from which through focal series micrographs were taken had been subjected to 4 minutes and 9 minutes of electron beam exposure respectively. Cavities began to become resolvable in specimen C at a fluence of 5×10^{16} He$^+$ ions cm^{-2}, corresponding to an electron beam exposure time of 11 minutes. Given the similarity of the cavities observed in specimen C to those observed in specimens A and D at higher fluences, this discrepancy is assumed to be an artefact of image acquisition parameters (i.e. focus) or a difference in specimen thickness affecting the quality of the micrographs obtained. Beyond the fluence at which cavities become resolvable, increasing helium fluence did not generally appear to have a dramatic effect on the size or number density of cavities at room temperature; although some cavity growth, accompanied with an increase cavity number density, appears to have occurred in specimen A with increasing fluence.

Based on the combined data available from all three samples, it is probable that the critical fluence for helium bubble formation in Li_2TiO_3 is less than or equal to 2.5×10^{16} He$^+$ ions cm^{-2}, corresponding to a peak helium concentration of ~4 atomic %; equivalent to the quantity of helium produced at a lithium burnup of ~ 13 %. It is noted however, that the cavities observed under in-situ helium implantation at room temperature are somewhat indiscernible from those observed under electron

irradiation at equivalent temperature; as such, the contribution of the effects of implanted helium to cavity nucleation and growth is not clear from regions of the specimen which were intermittently exposed to the electron beam during helium implantation. A high number density of similar cavities was observed to have formed in all specimens in regions which had not been previously exposed to the electron beam during ion implantation; these regions, far removed from the regions observed during ion implantations, had only been exposed to the electron beam for the minimum amount of time which allowed through focal series micrographs to be acquired after ion implantation was complete (~2 minutes). Since electron beam induced defects were not resolvable at room temperature until Li_2TiO_3 specimens had been exposed to the electron beam for 6-7 minutes in the absence of implanted helium (see chapter 6), the observation of cavities in these regions confirms that helium has accumulated to a sufficient extent in all specimens to result in the formation of a high number density of nanometre sized bubbles independently of electron beam induced defects.
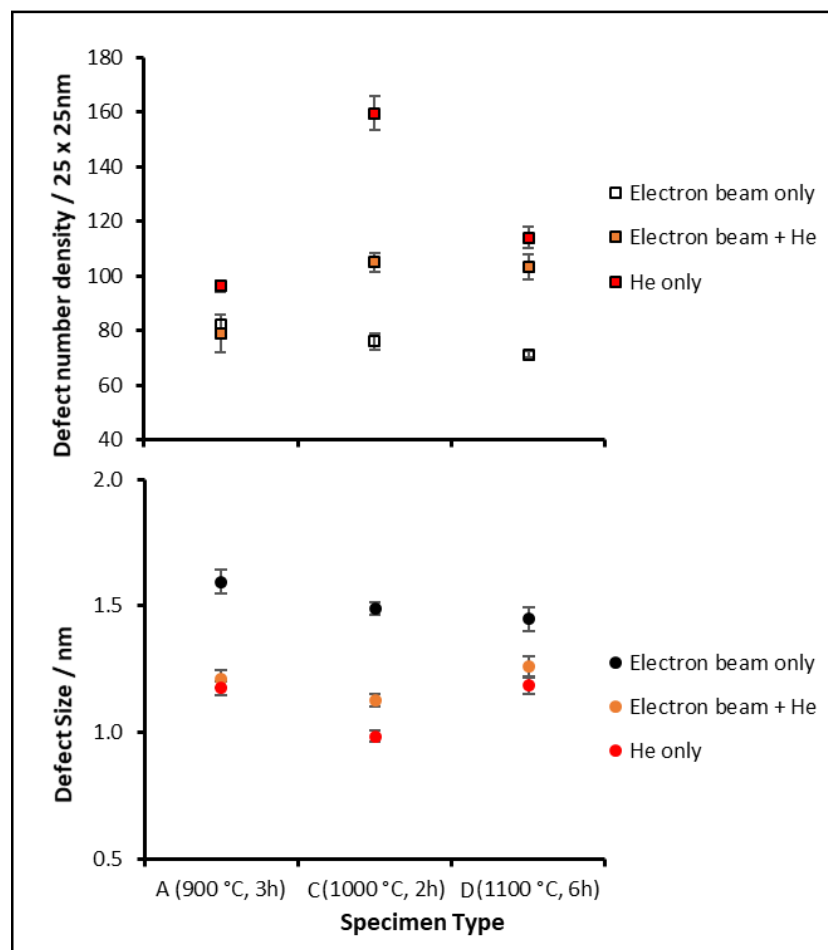
Figure 7.5: Comparison of the mean size (bottom) and number density (top) of bubbles / cavities observed in specimens A, C and D at room temperature as a result of (i) electron beam damage only

154

after 20 minutes electron beam exposure to a 300 keV electron beam (black data points); (ii) 5.5 keV He$^+$ ion implantation only ($\leq$ 2 minutes electron beam exposure) to a total fluence of 1×10^{17} He$^+$ions cm^{-2} (red data points); (iii) Combined He$^+$ ion implantation and electron beam damage (orange data points) at equivalent ion fluence (1×10^{17} 5.5 keV He$^+$ions cm^{-2}) and comparable electron beam exposure time (15.5 minutes $\pm$ 2.5 minutes exposure to a 300 KeV electron beam).

Figure 7.5 shows a graphical representation of the mean size and number density of cavities / helium bubbles observed in previously unilluminated regions of specimens A, C and D at room temperature following helium ion implantation to a total fluence of 1×10^{17} He$^+$ ions cm^{-2} ($\leq$ 2 minutes electron beam exposure) compared to those observed in regions of the same specimens which had been intermittently exposed to the electron beam during implantation (15.5 minutes $\pm$ 2.5 minutes electron beam exposure). The mean size and number density of cavities observed in analogous specimens at comparable electron beam exposure times (20 minutes) following room temperature electron irradiation in the absence of implanted helium are included for further comparison. Across the three specimens, cavities observed in regions of helium implanted specimens which had not previously been exposed to the electron beam were found to be consistently smaller, and higher in number density than those observed in specimens which had been electron irradiated in the absence of helium, suggesting that helium is acting as a nucleating agent for vacancy aggregation. Regions of helium implanted specimens which had been exposed to the electron beam during ion implantation typically exhibited intermediate cavity size and number density, with values lying between those obtained from regions where damage was associated solely with either helium implantation or electron irradiation. In these regions, cavity size was found to increase slightly compared to regions which had not been previously exposed to the electron beam; the concurrent decrease in cavity number density is characteristic of a coarsening process consistent with cavity growth. Hence it is proposed that implanted helium is primarily responsible for the increase in cavity number density compared to specimens which had been electron irradiated in the absence of helium; whereas increased cavity growth in regions which had been subjected to appreciable doses of electron irradiation is primarily attributed to a net influx of vacancies to the walls of stable cavities induced as a result of electron irradiation, which may be assisted by radiation enhanced diffusion effects.

7.2 Influence of implanted helium on cavity growth dynamics during thermal annealing

Figure 7.6 shows the thermal evolution of cavities during in-situ annealing of high porosity Specimen A (high porosity, smallest grains) following room temperature helium ion implantation. A graphical

representation of the corresponding mean cavity size and cavity number density at each incremental temperature is shown in Figure 7.7.

Figure 7.6: Bright field TEM micrographs showing the thermal evolution of cavities during in-situ annealing of Li_2TiO_3 Specimen A (high porosity, smallest grain size; sintered at 900 °C, 3h) following room temperature ion implantation to a total fluence of $1x10^{17}$ He^+ ions cm^{-2}.
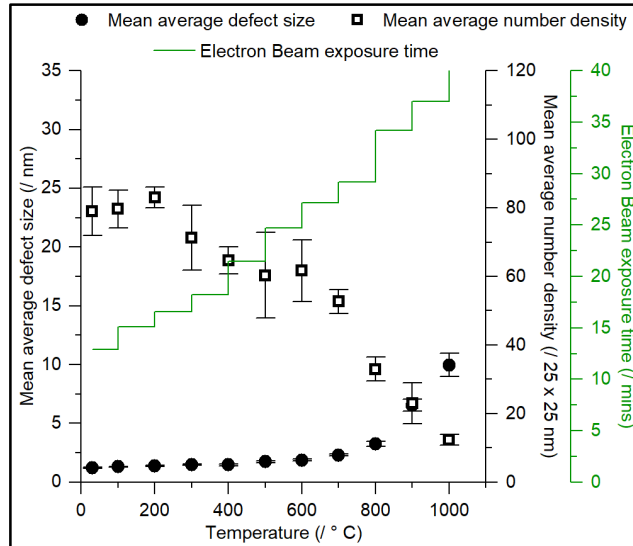
Figure 7.7: Mean average defect size and defect number density observed at incrementally increasing temperatures during in-situ annealing of specimen A following room temperature ion implantation to a total fluence of 1×10^{17} He$^+$ ions cm^{-2}.

The morphology of cavities observed during in-situ thermal annealing of specimen A following helium ion implantation was found to be very similar to those observed in the analogous un-implanted specimen which had been annealed under minimised electron beam exposure (see Figure 6.4, Chapter 6). Furthermore, at equivalent temperature, the number density of cavities observed in the helium implanted specimen was found to be comparable to that of the analogous un-implanted specimen throughout the thermal annealing process, and the respective mean cavity sizes were remarkably similar at equivalent temperatures up to 800 °C (see Figure 6.5b, Chapter 6. Note change of y scale). At temperatures in excess of 800 °C however, where cavity growth rate was found to progressively decrease in the un-implanted specimen, growth of cavities in the helium implanted specimen was observed to continue at an accelerated rate, which remained approximately constant rate up to the maximum temperature of 1000 °C. This continued growth may in part be facilitated by the absorption of helium atoms by cavities, and the resultant stabilising effect, in conjunction with the additional vacancies introduced as a result of ion implantation. However, in the interest of consistency, regions of helium implanted specimens observed during in-situ annealing were the same as those observed during room temperature ion implantation; as such the duration for which the regions observed during thermal the annealing of helium implanted specimens were exposed to the electron beam was slightly greater (11 minutes ± 3 minutes additional electron beam exposure time) than that of analogous un-implanted specimens at equivalent temperature. Hence it is possible that the additional vacancies produced due to a greater degree of electron beam damage contribute

significantly to the enhanced cavity growth at high temperature, particularly because the volume increase of cavities is dependent on vacancy supply [147]. Given the similarity of cavity size and number density observed in helium implanted and analogous un-implanted specimens up to 800 °C, and the previous observation that cavity growth was enhanced by increasing the total electron fluence at high temperatures (see Figure 6.5a c.f. Figure 6.5b, Chapter 6), it is equally likely that the enhanced growth observed at high temperature during the thermal annealing of specimen A following helium ion implantation compared to its un-implanted analogue is mainly due to increased electron beam exposure. Indeed, it is possible that the majority of implanted helium had escaped specimen A due to its high porosity and the relatively short diffusion path to the specimen surface associated with small grain size; hence the influence of helium on cavity growth dynamics may be minimal in this case.

The thermal evolution of cavities during in-situ annealing of low porosity Specimens C and D (low porosity, intermediate and largest grain sizes respectively) following room temperature helium ion implantation are shown in Figure 7.8 and Figure 7.9. A graphical representation of the corresponding mean cavity sizes and cavity number densities at each incremental temperature is shown in Figure 7.10.
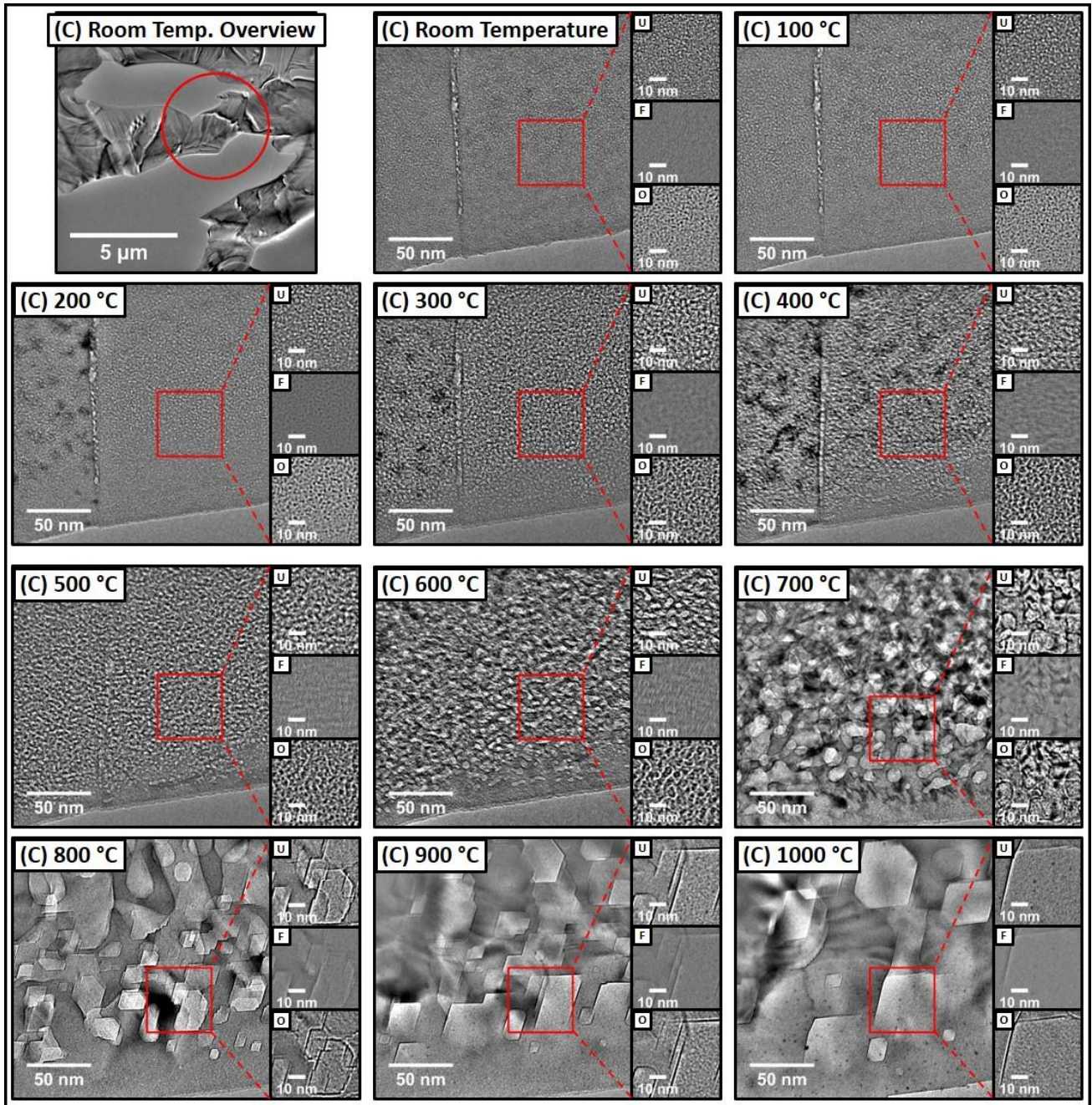
Figure 7.8: Bright field TEM micrographs showing the thermal evolution of cavities during in-situ annealing of Li$_2$TiO$_3$ Specimen C (Low porosity, intermediate grain size; sintered at 1000 °C, 2h) following room temperature ion implantation to a total fluence of 1x10^{17} He$^+$ ions cm^{-2}.
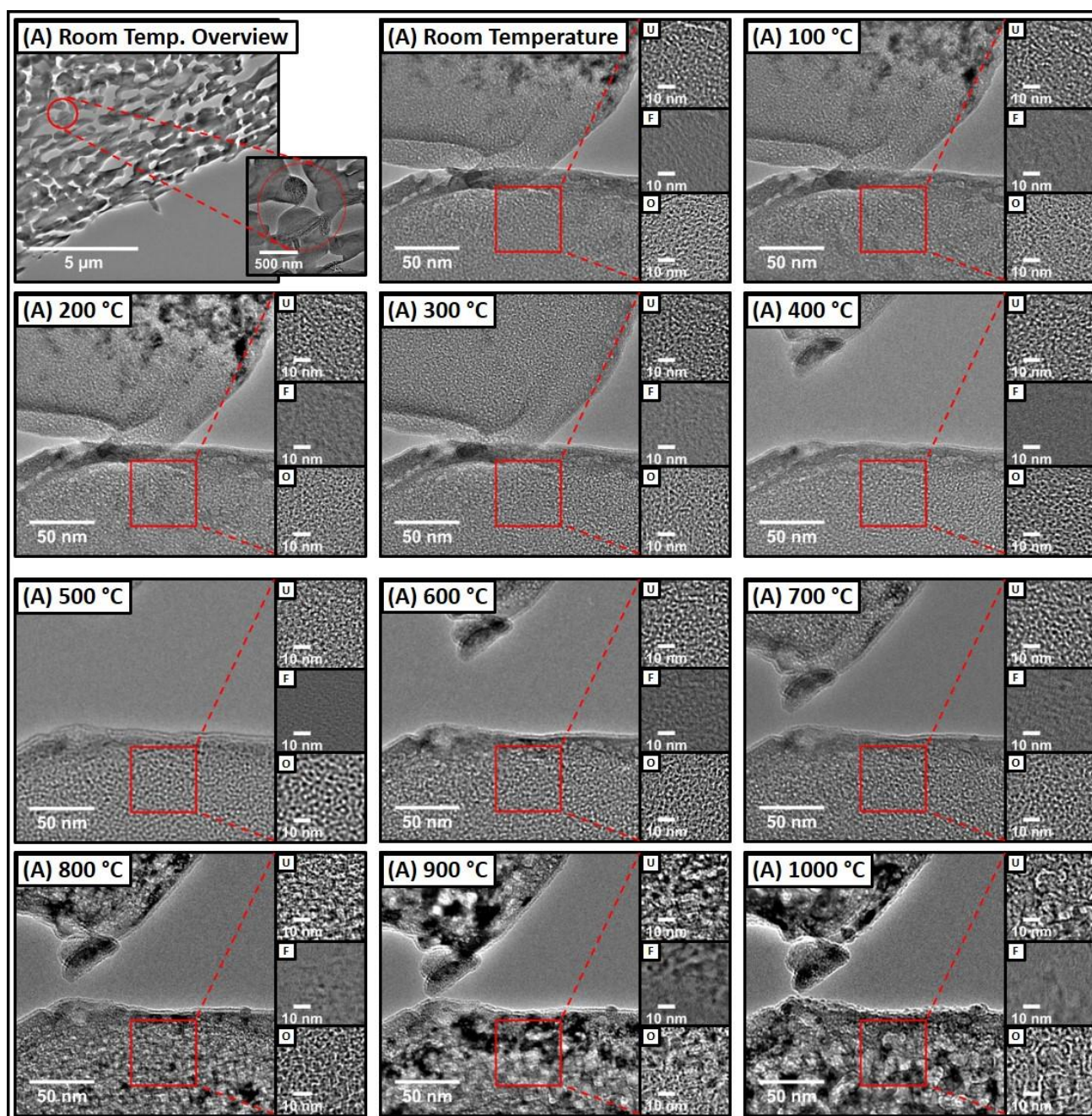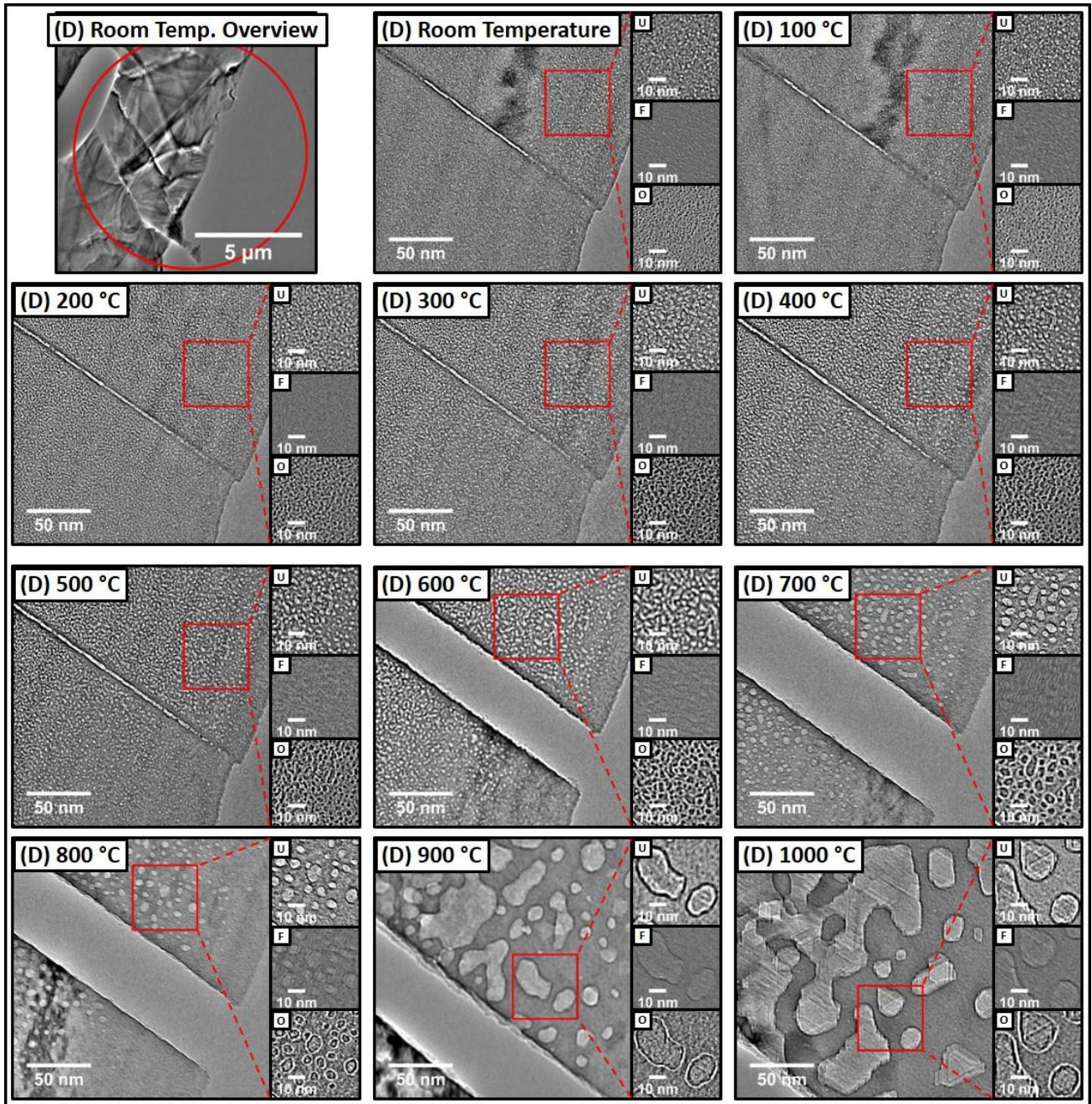
Figure 7.9: Bright field TEM micrographs showing the thermal evolution of cavities during in-situ annealing of Li_2TiO_3 Specimen D (Low porosity, largest grain size; sintered at 1100 °C, 6h) following room temperature ion implantation to a total fluence of $1x10^{17}$ He$^+$ ions cm^{-2}.
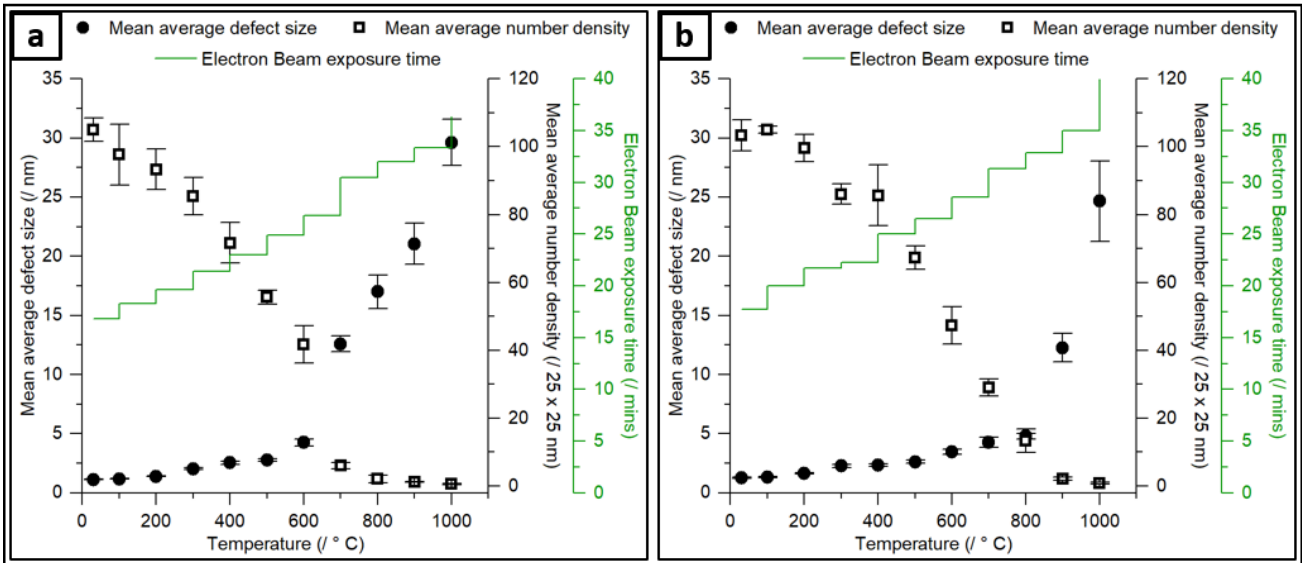
Figure 7.10: Mean average defect size and defect number density observed at incrementally increasing temperatures during in-situ annealing of a) specimen C (low porosity, intermediate grain size); and b) Specimen D (low porosity, largest grain size) following room temperature ion implantation to a total fluence of 1×10^{17} He$^+$ ions cm^{-2}.

Similarly to the behaviour of the high porosity specimen (specimen A), the size and number density of cavities observed in low porosity specimens C and D was found to be comparable to those observed in un-implanted analogues at low temperatures ($\leq$ 400 °C). However, in stark contrast to the behaviour of the high porosity specimen, the growth of cavities was found to be significantly enhanced in helium implanted specimens of low porosity compared to their respective un-implanted analogues at elevated temperatures; cavity sizes reached maximums in excess of five times the size of those observed in analogous un-implanted specimens (see Figure 6.9c and Figure 6.9d, Chapter 6). The difference in cavity size between those observed in helium implanted specimens and those observed in un-implanted analogues was shown to increase with increasing temperature, indicating that cavity growth is increasingly accelerated by the presence of helium as temperature increases. This is proposed to be due to the greater retention of implanted helium by low porosity specimens with larger grains as a result of the longer diffusion distance to grain boundaries or the sample surface, in conjunction with the enhanced mobility of defects (vacancies and interstitials induced by the combined effect of electron irradiation and ion implantation) and implanted helium atoms at elevated temperature. While the latter increases the flux of vacancies and gas atoms to the walls of existing cavities, and enhances the rate of interstitial defect loss to the surface, thereby increasing the excess vacancy concentration; the internal pressure exerted by helium contained within cavities increases the driving force for vacancy absorption. This effect is compounded by the reduction in the

161

rate of thermal emission of vacancies from cavities due to the opposing pressure of the gas, which would otherwise counter the net influx of vacancies responsible for cavity growth. Reduced thermal emission of vacancies from existing cavities also reduces the number of vacancies which may otherwise have escaped the confines of cavities, migrated to the specimen surface, and subsequently have been lost to the vacuum; thus the reduction in the rate of vacancy emission from cavities due to the presence of helium also contributes to maintaining the vacancy supersaturation responsible for cavity growth. The net result being the significant enhancement of cavity growth in implanted specimens which are proposed to have retained significant quantities of helium due to their low porosity and large grain size.

In both low porosity specimens, cavity growth is accompanied by concurrent decrease in cavity number density, again characteristic of a coarsening process. The absence of very small cavities at sufficiently elevated temperatures to promote efficient cavity growth, in conjunction with the observation that, at high temperatures, the largest cavities form in the vicinity of regions previously occupied by a greater number of cavities of intermediate size, suggests that the dominating mechanism of coarsening is coalescence as opposed to Ostwald ripening. The cavity growth dynamics of the two helium implanted low porosity specimens was found to be very similar at temperatures up to 600 °C. Beyond this temperature the cavity growth characteristics exhibited by the low porosity specimens vary significantly; similarly to the behaviour of its un-implanted analogue, cavity growth rate is significantly enhanced at 700 °C in helium implanted specimen C (low porosity, intermediate grain size), where rapid cavity growth continued up to 1000 °C. In the case of helium implanted specimen D, cavities continued to grow larger than those observed in its un-implanted analogue at temperatures in excess of 300 °C (as opposed to the shrinkage observed in the un-implanted specimen, as shown in Figure 6.9d, Chapter 6), confirming that the presence of helium facilitates cavity growth. However, the onset of significantly enhanced cavity growth occurred at 900 °C; 200 °C higher than the temperature at which rapid cavity growth was observed in specimen C. The mean cavity sizes observed in specimen D at temperatures in excess of 600 °C were also consistently smaller than those observed in specimen C at equivalent temperature despite specimen D having received a slightly higher dose of electron irradiation. Hence it is proposed that, while both low porosity specimens have retained sufficient helium to facilitate cavity growth, the shorter diffusion path to the specimen surface attributed to the smaller grains of specimen C results in a greater degree of preferential interstitial loss; this in turn results in a greater extent of vacancy supersaturation, and

thus a greater influx of vacancies to the walls of existing cavities which leads to enhanced cavity growth. Indeed, it was earlier proposed, with reference to electron irradiated specimens, that cavity growth at high temperature was likely to be dose limited; it is perhaps more correctly stated that the extent of cavity growth at high temperature is primarily limited by the extent of vacancy supersaturation; which itself is dose dependent, but also varies according to the microstructure of the material.
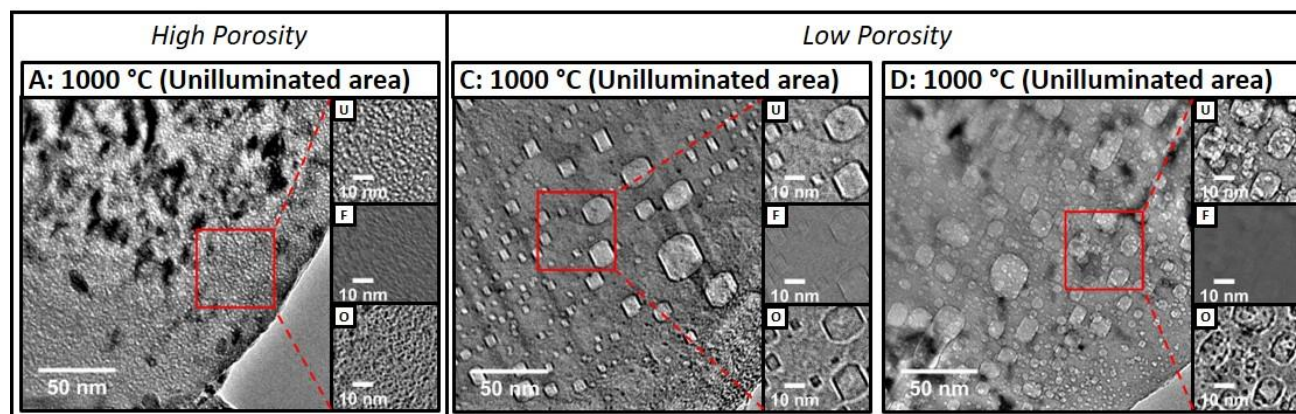
Figure 7.11: Bright field TEM micrographs showing helium bubbles observed in areas of Li_2TiO_3 Specimens A - C which had not previously been exposed to the electron beam. The micrographs shown were obtained at an annealing temperature of 1000 °C following room temperature ion implantation to a total fluence of 1×10^{17} He$^+$ ions cm^{-2}.

Cavity growth during thermal annealing was clearly exacerbated in low porosity specimens with relatively large grain size (specimen's C and D) as a result of helium implantation, whereas the effect of helium implantation on cavity growth has been shown to be significantly less pronounced in the high porosity specimen with small grains (specimen A). This was believed to be due to the higher retention of helium in low porosity specimens due to the longer diffusion path required for helium to escape from the free surfaces of specimens with lager grains, in conjunction with the lesser availability of free surfaces in low porosity specimens. Inspection of regions of helium implanted specimens which had not previously been exposed to the electron beam at the end of thermal annealing experiments confirmed that helium had indeed accumulated to a greater extent in low porosity specimens of Li_2TiO_3. As shown in Figure 7.11, a significant number density of relatively large helium bubbles clearly formed in regions of low porosity specimens far removed from the regions which were exposed to electron irradiation during thermal annealing. In contrast, the extent of helium bubble formation and growth in the high porosity specimen with the smallest grain size in the absence of the electron beam was found to be significantly lower, as indicated by the markedly

smaller defects observed in the corresponding TEM micrographs. This indicates that the majority of helium is likely to have escaped specimen A, and that a much greater proportion of helium was retained by specimen's C and D; which unequivocally confirms that helium accumulates to a greater extent in Li_2TiO_3 specimens of lower porosity and larger grain size.

This also accounts for the lesser degree of cavity growth enhancement observed in regions of the helium implanted high porosity specimen which had been intermittently exposed to the electron beam during thermal annealing (Figure 7.6) compared to those observed in low porosity specimens under comparable conditions (Figure 7.8 and Figure 7.9). It is also apparent that the extent of cavity growth in regions of helium implanted Li_2TiO_3 specimens which had been intermittently exposed to the electron beam during thermal annealing is significantly greater than that of helium bubbles formed in regions which had not previously been exposed to electron irradiation. This is clear evidence that defects induced by radiation induced displacement damage interact with implanted helium, resulting in enhanced cavity growth. This is consistent with the theory that cavity growth is primarily driven by the absorption of vacancies induced as a result of displacement damage, while implanted helium serves to stabilise cavities, increase the driving force for vacancy absorption, and increase the retention of vacancies by existing cavities due to the combination of internal gas pressure and the strength of vacancy-helium complexes.

7.3 Conclusions of In-situ helium ion implantation and thermal annealing study

Implantation of helium was found to have significant effects on cavity growth dynamics in Li_2TiO_3, particularly at high temperatures. Resolvable cavities were observed to form at room temperature in electron irradiated regions of helium implanted Li_2TiO_3 at fluences from 2.5×10^{16} He$^+$ ions cm^{-2} (equivalent to 4 atomic % He, or 13% lithium burnup). Helium bubbles observed to form independently of electron beam damage at a total fluence of 1×10^{17} He$^+$ ions cm^{-2} confirmed that helium accumulated to some degree in all specimens, regardless of their microstructural properties. The increased number density of smaller cavities observed in helium implanted specimens compared to those observed in un-implanted analogues indicates that helium acts as a nucleating agent for cavity formation.

Cavity growth has been shown to be significantly exacerbated by the presence of implanted helium, most notably at high temperatures (700 °C – 1000 °C). The extent of helium accumulation was found to be greater in specimens of low porosity, and large grain size; helium implanted specimens with

the aforementioned microstructural properties exhibited severely enhanced cavity growth, particularly in regions which were also subjected to electron beam damage. The enhancement of cavity growth in helium implanted specimens is proposed to be due to the stabilisation of cavities as a result of the reduction in surface free energy of cavities associated with helium contained therein. The pressure of helium contained within cavities can supposedly reach very high pressures as vacancies are thought to be an insaturable trap for helium atoms, and the strength of vacancy-helium complexes is reported to be high, limiting the emission of helium and vacancies from nucleated cavities. The pressure exerted by the gas is proposed to increase the driving force for vacancy absorption and reduce the rate of the thermal emission of vacancies from existing cavities, thus enhancing cavity growth.

Large cavities were observed in electron irradiated regions of helium implanted low porosity specimens with larger grain sizes, whereas the high porosity specimen with the smallest grain size exhibited comparably lesser enhancement of cavity growth as a result of helium implantation. This is attributed to the higher retention of implanted helium by specimens of low porosity and larger grain size due to the lesser availability of free surfaces from which helium can escape and the longer diffusion path to such free surfaces associated with larger grain size. However, the largest cavities were observed in electron irradiated regions of the helium implanted low porosity specimen with the smaller of the two grain sizes; this is attributed to high helium retention in conjunction with the shorter diffusion path for interstitial defects introduced as a result of displacement damage to escape the surface, resulting in increased preferential interstitial loss and thus increased excess vacancy concentration. The combination of these two factors results in the greatest degree of cavity growth.

The interactions of retained helium with defects introduced as a result of radiation induced displacement damage has been shown to significantly exacerbate the extent of cavity growth in Li_2TiO_3 at temperatures relevant to breeder blanket operating conditions. Such cavities have the potential to trap tritium in a working blanket, thereby impeding its release and increasing tritium inventory, both of which would be detrimental to material performance. In the absence of implanted helium, the microstructural properties of large grain size and low porosity appear to increase the radiation tolerance of Li_2TiO_3 to displacement damage induced by electron irradiation. However, since the presence of helium has been shown to severely exacerbate cavity growth in Li_2TiO_3, the increased helium retention by specimens of low porosity and large grain size and the influence of helium on the cavity growth dynamics thereof in fact resulted in a greater extent of cavity growth in

such specimens at temperatures relevant to breeder blanket operating conditions. As such, in spite of exhibiting an apparently lesser resistance to irradiation induced displacement damage in the absence of helium, when the effects of helium are taken into account the high porosity specimen with the smallest grain size showed the best overall performance in terms of cavity formation at breeder blanket operating temperatures.

It is therefore proposed that, given the high levels of neutron damage and helium production which are expected to occur in ceramic breeder materials during operation, the properties of *high* porosity and *small* grain size are likely to be beneficial for the optimisation of the performance of lithium titanate ceramic breeder materials from the perspective of overall radiation damage tolerance when the effects of helium are taken into account.

Chapter 8 - Conclusions and future work

8.1 Conclusions

The microstructural properties of Li_2TiO_3 ceramics prepared using solid state synthesis and conventional sintering methods were shown to be strongly dependent on post-synthesis processing conditions. The densification behaviour of Li_2TiO_3 was found to be strongly dependent on temperature, and relatively independent of sintering duration within the limits of the conditions studied. The extent of grain growth during sintering was shown to be affected by both the temperature and duration; hence, by adjusting the conditions employed, the microstructure of Li_2TiO_3 ceramics can be tuned in such a way that the contributions of porosity and grain size to the material's performance in different environments could be investigated. Temperature dependent crystallographic disorder, attributed to the presence of stacking faults and cation disorder has been identified in β- Li_2TiO_3 ceramics prepared by conventional solid state sintering; an inverse relationship between sintering temperature and the degree of deviation from the ideal structure was found to exist, suggesting that the concentration of intrinsic defects is likely to be greater in samples sintered at lower temperatures.

Two suites of Li_2TiO_3 samples, one "high porosity" suite and one "low porosity" suite, each comprising two sample types of comparable density but different grain size, were fabricated. These samples were subsequently used to independently investigate the effects of ceramic density (and porosity by association) and grain size on the behaviour of Li_2TiO_3 under electron irradiation in a conventional TEM. We have shown, for the first time, that Li_2TiO_3 is susceptible to electron beam damage, which is manifested as cavity formation and growth. Electron beam induced cavity formation in Li_2TiO_3 is proposed to be due to the aggregation of vacancy defects introduced as a result of displacement damage; the majority of damage is believed to be due to the displacement of Li and O lattice atoms via knock-on damage mechanisms, although radiolytic displacement mechanisms may also contribute. The build-up of an excess vacancy concentration, which leads to vacancy supersaturation, subsequent aggregation and cavity formation, is proposed to occur as a result of the preferential loss of interstitial defects at the specimen surface due to the higher mobility of interstitials compared to that of vacancies. Room temperature cavity nucleation and growth in Li_2TiO_3 under electron irradiation may be facilitated by the stabilising effect of gaseous CO_2 produced as a result of the decomposition of an Li_2CO_3 surface reaction layer under the electron beam. Specimens

which had been sintered at higher temperatures, which exhibited low porosity and larger grain size were found to be least susceptible to electron beam induced cavity formation at room temperature. This is proposed to be due to the lesser number of intrinsic defect sites available for cavity nucleation in samples sintered at higher temperature, in conjunction with the longer diffusion path for interstitials to escape the specimen surface; thereby reducing the preferential loss of interstitials, thus reducing the extent of vacancy supersaturation responsible for cavity growth. Hence it is suggested that the properties of low porosity, large grain size, and low intrinsic defect concentration increase the tolerance of Li_2TiO_3 to electron beam induced damage.

The cavities which were found to form in Li_2TiO_3 under a conventional TEM electron beam at room temperature could be easily misinterpreted as damage or gas bubble formation induced by an external radiation source. Hence, in order to avoid the unintentional reporting of erroneous results, extreme care should be taken when interpreting data on which scientific arguments are based where this data has been obtained using TEM techniques, particularly where Li_2TiO_3 or similar materials are the subject of experimental research.

Complimentary in-situ thermal annealing experiments, coupled with in-situ helium ion implantation studies were used to further investigate electron beam induced cavity growth in Li_2TiO_3, and the influence of implanted helium thereon, at temperatures relevant to breeder blanket operating conditions. The effects of ceramic grain size and porosity on the extent of cavity growth and helium accumulation, and the correlation between the latter two, at elevated temperatures was investigated using analogous specimens to those used in the prior room temperature electron irradiation study.

Growth of electron beam induced cavities in Li_2TiO_3 was found to be significantly enhanced at elevated temperature. Minimising the time for which thin film specimens were exposed to the electron beam has been shown to reduce the extent of cavity growth, indicating a clear dependence on irradiation dose. Where cavity growth is believed to be primarily limited by defect diffusion at low temperatures, growth of cavities is effectively dose limited at high temperatures. Beyond a threshold electron fluence, enhanced defect mobility at elevated temperature is proposed to have a greater overall effect on the extent of cavity growth than electron irradiation dose. In agreement with the room temperature electron irradiation study, the properties of low porosity and large grain size appear to improve the tolerance of Li_2TiO_3 ceramics to electron beam induced damage and cavity formation. The evolution of gaseous CO_2 as a result of the thermal decomposition of an Li_2CO_3 surface

reaction layer, and its subsequent capture by cavities, is proposed to have facilitated cavity growth during thermal annealing due to the stabilising effect of the gas and the increased driving force for vacancy absorption associated with the pressure exerted by the gas on cavity walls.

Helium, implanted to a total fluence of 1×10^{17} He^+ ions cm^{-2}, was shown to accumulate in Li_2TiO_3 to a sufficient degree to form bubbles at room temperature in all specimens. The extent of helium accumulation / retention at elevated temperature is proposed to be greater in low porosity specimens with larger grains, corroborated by the observation of significantly larger helium bubbles in areas of low porosity specimens with larger grain size which had not been previously exposed to the electron beam at the end of in-situ thermal annealing experiments compared to those observed in high porosity analogues with small grains. Cavity growth in electron irradiated regions was found to be significantly exacerbated by the presence of helium, particularly at high temperatures relevant to breeder blanket operating conditions. The enhancement of cavity growth in helium implanted specimens is proposed to be due to the stabilisation of cavities as a result of the reduction in surface free energy of cavities associated with helium contained therein, in conjunction with the increased driving force for vacancy absorption and reduced rate of thermal emission of vacancies from existing cavities associated with the pressure exerted by gaseous helium on cavity walls. Hence the greater degree of enhancement of cavity growth in low porosity specimens with large grains compared to that of analogous specimens of high porosity and small grain size is attributed to the increased helium retention of the former. Thus, it is proposed that the interactions of implanted helium with defects induced as a result of displacement damage dramatically enhance cavity growth; as a result of this, in spite of exhibiting an apparently lower resistance to irradiation induced displacement damage in the absence of helium, when the effects of helium are taken into account the high porosity specimen with the smallest grain size showed the best overall performance in terms of cavity formation at breeder blanket operating temperatures.

It is therefore proposed that the properties of *high* porosity and *small* grain size are likely to be beneficial for the optimisation of the performance of lithium titanate ceramic breeder materials from the perspective of overall radiation damage tolerance when the effects of helium are taken into account. In light of the findings of this project, further nanoscale investigation of the radiation tolerance of candidate ceramic breeder materials, and the interaction of radiation induced defects therein with helium is recommended. Tailoring the composition and microstructural properties of ceramic breeder materials may enable the mitigation of extensive cavity formation under irradiation

in a helium-rich environment, thus diminishing the potential for trapping of tritium therein and improving material performance.

8.2 Future work

In light of the findings of this project, it is suggested that further investigation into the mechanisms of electron beam induced damage under TEM electron beams in Li_2TiO_3 (and similar lithium ceramics) should be conducted such that the respective contributions of knock-on and radiolytic damage mechanisms can identified, and the contributions of damage corresponding to the displacement of each lattice atom type can be established. This could potentially be achieved by systematically reducing the accelerating voltage to such an extent that insufficient energy is transferred to lattice atoms of a particular type by a particular mechanism (i.e. knock-on) that only specific lattice atom types could theoretically be displaced. Observation of the formation of extended defects (or lack thereof) as a result of electron irradiation at progressively lower accelerating voltage may allow the identification of which displacement mechanism is dominant, and / or the displacement of which lattice atom type is responsible for the resulting cavity formation by process of elimination. Such investigations would potentially allow the optimisation of experimental parameters for use in TEM examination of lithium ceramics such that the effects of electron beam damage are mitigated or eliminated entirely; thereby allowing the unambiguous examination of the effects of externally induced radiation damage (or other pre-existing features) without the need to account for the effects of electron beam damage when interpreting results. Furthermore, the susceptibility of the latest generation of advanced dual-phase ceramic breeders proposed for testing in test blanket modules at ITER to electron beam damage should be investigated in order to avoid the erroneous reporting of the results of any future experimental work which utilises TEM techniques to characterise neutron damage where in these materials.

Pending the outcome such electron beam damage susceptibility experiments, and the optimisation of experimental parameters such that the effects of electron beam damage can be mitigated, further nanoscale investigation of helium accumulation in the latest generation of ceramic breeder materials using TEM techniques. The effects of irradiation temperature, and the interactions of helium with defects induced as a result of displacement damage should be further explored in these materials. This could be achieved by conducting dual-beam implantations with helium and heavy ions (using the latter to induce fusion-representative levels of displacement damage) and complimentary

thermal annealing experiments. If in-situ ion implantation is employed for this purpose, the results, (along with those detailed in this report) should be verified by conducting analogous experiments on bulk ceramic samples, followed by analysis using cross-sectional TEM. This would firstly allow the validity of results obtained from thin-film specimens in terms of their representativeness of the behaviour of bulk ceramics to be assessed, and secondly allow the contribution of surface effects associated with thin-film specimens to the observed behaviour to be evaluated.

The results of the work detailed in this report indicate that the degree of radiation tolerance and extent of helium accumulation in Li_2TiO_3 is affected by its microstructural properties. The combination of small grain size and high porosity was found to be beneficial in terms of reducing the extent of cavity / helium bubble formation at temperatures relevant to breeder blanket operating conditions when the effects of helium were taken into account. Nonetheless, on the grounds that high ceramic density is generally considered to be beneficial due the associated increase in TBR, further work could be carried out regarding the optimisation of the microstructural properties of ceramic breeder materials. Alternative synthesis methods to those used in this work, such as sol-gel methods which may afford a greater degree of control over the powder particle size, (thereby allowing the production of very small particles of precursor powder [45]) could be used in conjunction with novel densification techniques such as spark plasma sintering (which has been reported to allow full densification of some ceramics at lower temperatures than conventional methods while maintaining the original fine-grained structure of green bodies [208]) to produce high density lithium ceramics with small grain size. By variation of sintering conditions, larger grained samples of equivalent density could be produced. Comparison of the performance of the materials produced using these methods to higher porosity samples of comparable grain sizes, possibly prepared by more conventional methods such as those utilised in this work, would allow the individual contributions of porosity and grain size to helium accumulation, radiation tolerance and tritium release be further clarified according to the results of subsequent ion implantation / neutron irradiation studies. The microstructural properties of future ceramic breeder materials could then be optimised accordingly.

Finally, given that the current literature on the subject is currently very limited, the influence of helium on tritium release characteristics of candidate ceramic breeder materials could be further investigated using ion implantation and complementary thermal desorption spectroscopy techniques. The newly established TRiCEM system [209] at the UK Atomic Energy Authority Materials Research Facility allows actual tritium implantation (as opposed to the use of other hydrogen

isotopes as tritium simulants); this system, in conjunction with existing TDS capabilities at the same facility, could be used to further explore this concept.

References

[1]   C. L. Smith and S. Cowley, "The path to fusion power," *Philosophical Transactions of the Royal Society a-Mathematical Physical and Engineering Sciences,* vol. 368, no. 1914, pp. 1091-1108, Mar 2010, doi: 10.1098/rsta.2009.0216.

[2]   M. Kikuchi and K. Lackner, *Fusion Physics*. International Atomic Energy Agency (IAEA): IAEA, 2012.

[3]   L. V. Boccaccini *et al.*, "Objectives and status of EUROfusion DEMO blanket studies," *Fusion Engineering and Design,* vol. 109, pp. 1199-1206, Nov 2016, doi: 10.1016/j.fusengdes.2015.12.054.

[4]   F. A. Hern *et al.*, "Overview of the HCPB Research Activities in EUROfusion," *IEEE Transactions on Plasma Science,* vol. 46, no. 6, pp. 2247-2261, 2018, doi: 10.1109/TPS.2018.2830813.

[5]   F. A. Hernández *et al.*, "An enhanced, near-term HCPB design as driver blanket for the EU DEMO," *Fusion Engineering and Design,* vol. 146, pp. 1186-1191, 2019/09/01/ 2019, doi: https://doi.org/10.1016/j.fusengdes.2019.02.037.

[6]   G. Federici, L. Boccaccini, F. Cismondi, M. Gasparotto, Y. Poitevin, and I. Ricapito, "An overview of the EU breeding blanket design strategy as an integral part of the DEMO design effort," *Fusion Engineering and Design,* vol. 141, pp. 30-42, Apr 2019, doi: 10.1016/j.fusengdes.2019.01.141.

[7]   M. Abdou *et al.*, "Blanket/first wall challenges and required R&D on the pathway to DEMO," *Fusion Engineering and Design,* vol. 100, pp. 2-43, Nov 2015, doi: 10.1016/j.fusengdes.2015.07.021.

[8]   R. Knitter, M. H. H. Kolb, U. Kaufmann, and A. A. Goraieb, "Fabrication of modified lithium orthosilicate pebbles by addition of titania," *Journal of Nuclear Materials,* vol. 442, no. 1-3, pp. S433-S436, Nov 2013, doi: 10.1016/j.jnucmat.2012.10.034.

[9]   S. Liu *et al.*, "Conceptual design of the water cooled ceramic breeder blanket for CFETR based on pressurized water cooled reactor technology," *Fusion Engineering and Design,* vol. 124, pp. 865-870, 2017/11/01/ 2017, doi: https://doi.org/10.1016/j.fusengdes.2017.02.065.

[10]   E. R. Kumar, K. N. Vyas, and T. Jayakumar, "Overview of LLCB TBM design and R&D activities in India," *Fusion Engineering and Design,* vol. 109-111, pp. 1522-1527, 2016/11/01/ 2016, doi: https://doi.org/10.1016/j.fusengdes.2015.11.038.

[11]   Y. Kawamura *et al.*, "Status of water cooled ceramic breeder blanket development," *Fusion Engineering and Design,* vol. 136, pp. 1550-1556, 2018/11/01/ 2018, doi: https://doi.org/10.1016/j.fusengdes.2018.05.055.

[12]   R. Knitter, P. Chaudhuri, Y. J. Feng, T. Hoshino, and I. K. Yu, "Recent developments of solid breeder fabrication," *Journal of Nuclear Materials,* vol. 442, no. 1-3, pp. S420-S424, Nov 2013, doi: 10.1016/j.jnucmat.2013.02.060.

[13]   C. E. Kessel *et al.*, "Overview of the fusion nuclear science facility, a credible break-in step on the path to fusion energy," *Fusion Engineering and Design*, vol. 135, Part B, pp. 236-270, Oct 2018, doi: https://doi.org/10.1016/j.fusengdes.2017.05.081.

[14]   M. Oyaidzu *et al.*, "Correlation between annihilation of radiation defects and tritium release in Li_2TiO_3," *Journal of Nuclear Materials,* vol. 329, pp. 1313-1317, Aug 2004, doi: 10.1016/j.jnucmat.2004.04.223.

[15]   M. Kobayashi, Y. Oya, K. Munakata, and K. Okuno, "Developing a tritium release model for Li_2TiO_3 with irradiation-induced defects," *Journal of Nuclear Materials,* vol. 458, pp. 22-28, Mar 2015, doi: 10.1016/j.jnucmat.2014.11.047.

[16]   K. Toda *et al.*, "Correlation between release of deuterium and annihilation of irradiation defects produced by gamma-ray in Li_2TiO_3," *Fusion Engineering and Design,* vol. 88, no. 9-10, pp. 2369-2372, Oct 2013, doi: 10.1016/j.fusengdes.2013.05.006.

[17]   M. Klimenkov, E. Materna-Morris, and A. Moslang, "Characterization of radiation induced defects in EUROFER 97 after neutron irradiation," (in English), *Journal of Nuclear Materials,* Article; Proceedings Paper vol. 417, no. 1-3, pp. 124-126, Oct 2011, doi: 10.1016/j.jnucmat.2010.12.261.

[18]   R. M. Mayer and L. M. Brown, "Nucleation and growth of voids by radiation: I. Formulation of the problem," *Journal of Nuclear Materials,* vol. 95, no. 1, pp. 46-57, 1980/11/01/ 1980, doi: https://doi.org/10.1016/0022-3115(80)90079-3.

[19]   C. A. Taylor *et al.*, "Investigating Helium Bubble Nucleation and Growth through Simultaneous In-Situ Cryogenic, Ion Implantation, and Environmental Transmission Electron Microscopy," *Materials,* vol. 12, no. 16, Aug 2019, Art no. 2618, doi: 10.3390/ma12162618.

[20]   S. J. Zinkle, "Effect of H and He irradiation on cavity formation and blistering in ceramics," *Nuclear Instruments & Methods in Physics Research Section B-Beam Interactions with Materials and Atoms,* vol. 286, pp. 4-19, Sep 2012, doi: 10.1016/j.nimb.2012.03.030.

[21]   B. N. Singh and A. J. E. Foreman, "An assessment of void nucleation by gas atoms during irradiation," *Journal of Nuclear Materials,* vol. 104, pp. 1469-1474, 1981/01/01/ 1981, doi: https://doi.org/10.1016/0022-3115(82)90807-8.

[22]   R. M. Mayer, W. M. Stobbs, and P. R. Ward, "The effect of gas on the irradiation of aluminium inside a high voltage electron microscope," *Journal of Microscopy,* https://doi.org/10.1111/j.1365-2818.1975.tb04039.x vol. 105, no. 1, pp. 87-95, 1975/09/01 1975, doi: https://doi.org/10.1111/j.1365-2818.1975.tb04039.x.

[23]   R. E. Stoller, "THE INFLUENCE OF HELIUM ON MICROSTRUCTURAL EVOLUTION - IMPLICATIONS FOR DT FUSION-REACTORS," *Journal of Nuclear Materials,* vol. 174, no. 2-3, pp. 289-310, Nov 1990, doi: 10.1016/0022-3115(90)90242-f.

[24]   M. Kobayashi, H. Uchimura, K. Toda, and Y. Oya, "Effects of helium and ambient water vapor on tritium release from Li_2TiO_3," *Journal of Nuclear Materials,* vol. 455, no. 1-3, pp. 735-738, Dec 2014, doi: 10.1016/j.jnucmat.2014.08.058.

[25]   M. Rose, A. G. Balogh, and H. Hahn, "Instability of irradiation induced defects in nanostructured materials," *Nuclear Instruments and Methods in Physics Research Section B: Beam Interactions with Materials and Atoms,* vol. 127-128, pp. 119-122, 1997/05/02/ 1997, doi: https://doi.org/10.1016/S0168-583X(96)00863-4.

[26]   B. Muntifering *et al.*, "Cavity Evolution at Grain Boundaries as a Function of Radiation Damage and Thermal Conditions in Nanocrystalline Nickel," *Materials Research Letters,* vol. 4, no. 2, pp. 96-103, 2016, doi: 10.1080/21663831.2015.1121165.

[27]   X. M. Bai, A. F. Voter, R. G. Hoagland, M. Nastasi, and B. P. Uberuaga, "Efficient Annealing of Radiation Damage Near Grain Boundaries via Interstitial Emission," *Science,* vol. 327, no. 5973, pp. 1631-1634, Mar 2010, doi: 10.1126/science.1183723.

[28]   T. D. Shen, S. Feng, M. Tang, J. A. Valdez, Y. Wang, and K. E. Sickafus, "Enhanced radiation tolerance in nanocrystalline $MgGa_2O_4$," *Applied Physics Letters,* vol. 90, no. 26, Jun 2007, Art no. 263115, doi: 10.1063/1.2753098.

[29]   Z. Y. Huang *et al.*, "Defect-fluorite $Gd_2Zr_2O_7$ ceramics under helium irradiation: Amorphization, cell volume expansion, and multi-stage bubble formation," *Journal of the American Ceramic Society,* vol. 102, no. 8, pp. 4911-4918, Aug 2019, doi: 10.1111/jace.16364.

[30]   S. Dey *et al.*, "Radiation Tolerance of Nanocrystalline Ceramics: Insights from Yttria Stabilized Zirconia," *Scientific Reports,* vol. 5, Jan 2015, Art no. 7746, doi: 10.1038/srep07746.

[31]   W. F. Cureton *et al.*, "Grain size effects on irradiated CeO_2, ThO_2, and UO_2," *Acta Materialia,* vol. 160, pp. 47-56, Nov 2018, doi: 10.1016/j.actamat.2018.08.040.

[32]   O. El-Atwani *et al.*, "The role of grain size in He bubble formation: Implications for swelling resistance," *Journal of Nuclear Materials,* vol. 484, pp. 236-244, Feb 2017, doi: 10.1016/j.jnucmat.2016.12.003.

[33]   M. Zmitko *et al.*, "Development and qualification of functional materials for the EU Test Blanket Modules: Strategy and R&D activities," *Journal of Nuclear Materials,* vol. 417, no. 1-3, pp. 678-683, Oct 2011, doi: 10.1016/j.jnucmat.2011.02.009.

[34]   A. Zarins *et al.*, "Behaviour of advanced tritium breeder pebbles under simultaneous action of accelerated electrons and high temperature," *Fusion Engineering and Design,* vol. 121, pp. 167-173, 2017/10/01/ 2017, doi: https://doi.org/10.1016/j.fusengdes.2017.06.033.

[35]   M. Lang *et al.*, "Swift heavy ion-induced amorphization of $CaZrO_3$ perovskite," *Nuclear Instruments and Methods in Physics Research Section B: Beam Interactions with Materials and Atoms,* vol. 286, pp. 271-276, 2012/09/01/ 2012, doi: https://doi.org/10.1016/j.nimb.2011.12.028.

[36]   M. Klimenkov, P. Vladimirov, J. Hoffmann, N. Zimber, A. Moslang, and V. Kuksenko, "First simultaneous detection of helium and tritium inside bubbles in beryllium," *Micron,* vol. 127, Dec 2019, Art no. 102754, doi: 10.1016/j.micron.2019.102754.

[37]   N. Sasajima, T. Matsui, S. Furuno, K. Hojou, and H. Otsu, "Damage accumulation in Al_2O_3 during H_2^+ or He^+ ion irradiation," *Nuclear Instruments and Methods in Physics Research Section B: Beam Interactions with Materials and Atoms,* vol. 148, no. 1, pp. 745-751, 1999/01/02/ 1999, doi: https://doi.org/10.1016/S0168-583X(98)00810-6.

[38]   N. T. Wu, H. Wu, H. Liu, and Y. Zhang, "Solvothermal coating $LiNi_{0.8}Co_{0.15}Al_{0.05}O_2$ microspheres with nanoscale Li_2TiO_3 shell for long lifespan Li-ion battery cathode materials," *Journal of Alloys and Compounds,* vol. 665, pp. 48-56, Apr 2016, doi: 10.1016/j.jallcom.2016.01.044.

[39]   L. Q. Zhang and H. Noguchi, "Novel layered Li-Cr-Ti-O cathode materials related to the $LiCrO_2$-Li_2TiO_3 solid solution," *Journal of the Electrochemical Society,* vol. 150, no. 5, pp. A601-A607, May 2003, doi: 10.1149/1.1566016.

[40]   K. Meng, Z. X. Wang, H. J. Guo, X. H. Li, and D. Wang, "Improving the cycling performance of $LiNi_{0.8}Co_{0.1}Mn_{0.1}O_2$ by surface coating with Li_2TiO_3," *Electrochimica Acta,* vol. 211, pp. 822-831, Sep 2016, doi: 10.1016/j.electacta.2016.06.110.

[41]   Y. W. Li *et al.*, "High performance Co_3O_4/Li_2TiO_3 composite hollow nanofibers as anode material for Li-ion batteries," *Journal of Materials Science-Materials in Electronics,* vol. 29, no. 16, pp. 14222-14231, Aug 2018, doi: 10.1007/s10854-018-9555-5.

[42]   Y. Wang, A. Zhou, X. Dai, L. Feng, J. Li, and J. Li, "Solid-state synthesis of submicron-sized $Li_4Ti_5O_{12}$/Li_2TiO_3 composites with rich grain boundaries for lithium ion batteries," *Journal of Power Sources,* vol. 266, pp. 114-120, 2014/11/15/ 2014, doi: https://doi.org/10.1016/j.jpowsour.2014.05.002.

[43]   H. S. Bhatti *et al.*, "Electrochemical Characteristics and Li^+ Ion Intercalation Kinetics of Dual-Phase $Li_4Ti_5O_{12}$/Li_2TiO_3 Composite in the Voltage Range 0-3 V," *Journal of Physical Chemistry C,* vol. 120, no. 18, pp. 9553-9561, May 2016, doi: 10.1021/acs.jpcc.5b12114.

[44]   A. Lakshmi-Narayana, M. Dhananjaya, N. Guru-Prakash, O. Hussain, A. Mauger, and C. Julien, "Li_2TiO_3/Graphene and Li_2TiO_3/CNT Composites as Anodes for High Power Li-Ion Batteries," *ChemistrySelect,* vol. 3, no. 31, pp. 9150-9158, 2018.

[45]   Y.-z. Hao, Q.-l. Zhang, J. Zhang, C.-r. Xin, and H. Yang, "Enhanced sintering characteristics and microwave dielectric properties of Li_2TiO_3 due to nano-size and nonstoichiometry effect," *Journal of Materials Chemistry,* 10.1039/C2JM33788F vol. 22, no. 45, pp. 23885-23892, 2012, doi: 10.1039/C2JM33788F.

[46]   Y.-Z. Hao, H. Yang, G.-H. Chen, and Q.-L. Zhang, "Microwave dielectric properties of Li_2TiO_3 ceramics doped with LiF for LTCC applications," *Journal of Alloys and Compounds,* vol. 552, pp. 173-179, 2013/03/05/ 2013, doi: https://doi.org/10.1016/j.jallcom.2012.10.110.

[47]   V. C. Martins *et al.*, "High thermal stability of Li_2TiO_3-Al_2O_3 composite in the microwave C-Band," *Journal of Physics and Chemistry of Solids,* vol. 125, pp. 51-56, 2019/02/01/ 2019, doi: https://doi.org/10.1016/j.jpcs.2018.10.011.

[48]   A. Lakshmi Narayana, M. Dhananjaya, N. Guru Prakash, O. M. Hussain, and C. M. Julien, "Nanocrystalline Li_2TiO_3 electrodes for supercapattery application," *Ionics,* vol. 23, no. 12, pp. 3419-3428, 2017/12/01 2017, doi: 10.1007/s11581-017-2147-1.

[49]   C. E. Johnson, K. R. Kummerer, and E. Roth, "CERAMIC BREEDER MATERIALS," *Journal of Nuclear Materials,* vol. 155, pp. 188-201, Jul 1988, doi: 10.1016/0022-3115(88)90240-1.

[50]   https://www.iter.org/sci/Fusion

[51]   A. Donato, "A critical review of Li_2O ceramic breeder material properties correlations and data," *Fusion Engineering and Design,* vol. 38, no. 4, pp. 369-392, Feb 1998, doi: 10.1016/s0920-3796(97)00123-3.

[52]   F. A. Hernández and P. Pereslavtsev, "First principles review of options for tritium breeder and neutron multiplier materials for breeding blankets in fusion reactors," *Fusion Engineering and Design,* vol. 137, pp. 243-256, 2018/12/01/ 2018, doi: https://doi.org/10.1016/j.fusengdes.2018.09.014.

[53]   S. Cho *et al.*, "Investigation of technical gaps between DEMO blanket and HCCR TBM," *Fusion Engineering and Design,* vol. 136, pp. 190-198, 2018/11/01/ 2018, doi: https://doi.org/10.1016/j.fusengdes.2018.01.050.

[54]   Y. Kawamura *et al.*, "Progress of R&D on water cooled ceramic breeder for ITER test blanket system and DEMO," *Fusion Engineering and Design,* vol. 109-111, pp. 1637-1643, 2016/11/01/ 2016, doi: https://doi.org/10.1016/j.fusengdes.2015.11.002.

[55]   T. Hoshino, "Pebble fabrication of super advanced tritium breeders using a solid solution of $Li_{2+x}TiO_{3+y}$ with Li_2ZrO_3," *Nuclear Materials and Energy,* vol. 9, pp. 221-226, 2016/12/01/ 2016, doi: https://doi.org/10.1016/j.nme.2016.05.004.

[56]   R. Knitter and B. Löbbecke, "Reprocessing of lithium orthosilicate breeder material by remelting," *Journal of Nuclear Materials,* vol. 361, no. 1, pp. 104-111, 2007/03/31/ 2007, doi: https://doi.org/10.1016/j.jnucmat.2006.11.005.

[57]   H. Kleykamp, "Phase equilibria in the Li-Ti-O system and physical properties of Li_2TiO_3," *Fusion Engineering and Design,* vol. 61-62, pp. 361-366, Nov 2002, Art no. Pii s0920-3796(02)00120-5, doi: 10.1016/s0920-3796(02)00120-5.

[58]   A. Laumann *et al.*, "In-situ Synchrotron X-ray Diffraction Study of the Formation of Cubic Li_2TiO_3 Under Hydrothermal Conditions," *European Journal of Inorganic Chemistry,* no. 14, pp. 2221-2226, May 2011, doi: 10.1002/ejic.201001133.

[59]   G. Izquierdo and A. R. West, "PHASE-EQUILIBRIA IN THE SYSTEM Li_2O-TiO_2," *Materials Research Bulletin,* vol. 15, no. 11, pp. 1655-1660, 1980, doi: 10.1016/0025-5408(80)90248-2.

[60]   M. Zmitko *et al.*, "Development and qualification of functional materials for the European HCPB TBM," *Fusion Engineering and Design,* vol. 136, pp. 1376-1385, Nov 2018, doi: 10.1016/j.fusengdes.2018.05.014.

[61]   K. Kataoka *et al.*, "Crystal growth and structure refinement of monoclinic Li_2TiO_3," *Materials Research Bulletin,* vol. 44, no. 1, pp. 168-172, 1/8/ 2009, doi: http://doi.org/10.1016/j.materresbull.2008.03.015.

[62]   J. F. Dorrian and R. E. Newnham, "Refinement of the structure of Li_2TiO_3," *Materials Research Bulletin,* vol. 4, no. 3, pp. 179-183, 3// 1969, doi: http://doi.org/10.1016/0025-5408(69)90054-3.

[63]   *Images generated using CrystalMaker®: a crystal and molecular structures program for Mac and Windows. CrystalMaker Software Ltd, Oxford, England (www.crystalmaker.com)*

[64]   D. Tranqui, R. D. Shannon, H. Y. Chen, S. Iijima, and W. H. Baur, "CRYSTAL-STRUCTURE OF ORDERED Li_4SiO_4," (in English), *Acta Crystallographica Section B-Structural Science,* Article vol. 35, no. NOV, pp. 2479-2487, 1979, doi: 10.1107/s0567740879009730.

[65]   B. Dejong, D. Ellerbroek, and A. L. Spek, "LOW-TEMPERATURE STRUCTURE OF LITHIUM NESOSILICATE, Li_4SiO_4, AND ITS Li_{1S} AND O_{1S} X-RAY PHOTOELECTRON-SPECTRUM," *Acta Crystallographica Section B-Structural Science,* vol. 50, pp. 511-518, Oct 1994, doi: 10.1107/s0108768194002375.

[66]   H. Migge, "ESTIMATION OF FREE-ENERGIES FOR Li_8SiO_6 AND Li_4SiO_4 AND CALCULATION OF THE PHASE-DIAGRAM OF THE Li-Si-O SYSTEM," *Journal of Nuclear Materials,* vol. 151, no. 2, pp. 101-107, Jan 1988, doi: 10.1016/0022-3115(88)90061-x.

[67]   G. W. Hollenberg, "A TRANSFORMATION IN LITHIUM ORTHOSILICATE," *Journal of Nuclear Materials,* vol. 103, no. 1-3, pp. 591-595, 1982.

[68]   P. C. Soares, E. D. Zanotto, V. M. Fokin, and H. Jain, "TEM and XRD study of early crystallization of lithium disilicate glasses," *Journal of Non-Crystalline Solids,* vol. 331, no. 1-3, pp. 217-227, Dec 2003, doi: 10.1016/j.jnoncrysol.2003.08.075.

[69]   D. Vollath and H. Wedemeyer, "ON THE PREPARATION OF THE LITHIUM SILICATES SERIES FROM Li_2SiO_3 TO Li_8SiO_6 IN ALCOHOLIC MEDIA," *Journal of Nuclear Materials,* vol. 141, pp. 334-338, Nov-Dec 1986, doi: 10.1016/s0022-3115(86)80060-5.

[70]   S. Claus, H. Kleykamp, and W. SmykatzKloss, "Phase equilibria in the Li_4SiO_4-Li_2SiO_3 region of the pseudobinary Li_2O-SiO_2 system," *Journal of Nuclear Materials,* vol. 230, no. 1, pp. 8-11, May 1996, doi: 10.1016/0022-3115(96)00022-0.

[71]   S. Pupeschi, R. Knitter, and M. Kamlah, "Effective thermal conductivity of advanced ceramic breeder pebble beds," *Fusion Engineering and Design,* vol. 116, pp. 73-80, Mar 2017, doi: 10.1016/j.fusengdes.2017.01.026.

[72]   A. Ying *et al.*, "Status and perspective of the R&D on ceramic breeder materials for testing in ITER," *Journal of Nuclear Materials,* vol. 367–370, Part B, pp. 1281-1286, 8/1/ 2007, doi: http://doi.org/10.1016/j.jnucmat.2007.03.240.

[73]   K. F. Hesse, "REFINEMENT OF CRYSTAL-STRUCTURE OF LITHIUM POLYSILICATE," *Acta Crystallographica Section B-Structural Science,* vol. 33, no. MAR15, pp. 901-902, 1977, doi: 10.1107/s0567740877004932.

[74]   S. Kutolin and N. Druz, "Effect of synthesis conditions on the structure and properties of lithium metazirconate," *Inorg. Mater,* vol. 1, pp. 1590-1592, 1965.

[75]   G. P. Wyers and E. H. P. Cordfunke, "PHASE-RELATIONS IN THE SYSTEM Li_2O ZrO_2," *Journal of Nuclear Materials,* vol. 168, no. 1-2, pp. 24-30, Oct-Nov 1989, doi: 10.1016/0022-3115(89)90560-6.

[76]   H. Pfeiffer and K. M. Knowles, "Reaction mechanisms and kinetics of the synthesis and decomposition of lithium metazirconate through solid-state reaction," *Journal of the European Ceramic Society,* vol. 24, no. 8, pp. 2433-2443, Jul 2004, doi: 10.1016/s0955-2219(03)00630-7.

[77]   J. L. Hodeau, M. Marezio, A. Santoro, and R. S. Roth, "NEUTRON PROFILE REFINEMENT OF THE STRUCTURES OF Li_2SnO_3 AND Li_2ZrO_3," *Journal of Solid State Chemistry,* vol. 45, no. 2, pp. 170-179, 1982, doi: 10.1016/0022-4596(82)90273-0.

[78]   N. Roux, J. Avon, A. Floreancig, J. Mougin, B. Rasneur, and S. Ravel, "Low-temperature tritium releasing ceramics as potential materials for the ITER breeding blanket," *Journal of Nuclear Materials,* vol. 233, pp. 1431-1435, Oct 1996, doi: 10.1016/s0022-3115(96)00136-5.

[79]   A. R. West, "Solid state chemistry and its applications 2014," John Wiley & Sons pp. 187-197.

[80]   H. L. Xu *et al.*, "Effect of the Particle Size of Quartz Powder on the Synthesis and CO_2 Absorption Properties of Li_4SiO_4 at High Temperature," *Industrial & Engineering Chemistry Research,* vol. 52, no. 5, pp. 1886-1891, Feb 2013, doi: 10.1021/ie301178p.

[81]   M. Q. Xiang, Y. C. Zhang, Y. Zhang, S. Y. Liu, H. Liu, and C. F. Wang, "Fabrication and Characterization of Li_2TiO_3-Li_4SiO_4 Pebbles for Tritium Breeder," *Journal of Fusion Energy,* vol. 34, no. 6, pp. 1341-1347, Dec 2015, doi: 10.1007/s10894-015-9967-7.

[82]   D. Mandal, D. Sathiyamoorthy, and V. G. Rao, "Preparation and characterization of lithium-titanate pebbles by solid-state reaction extrusion and spherodization techniques for fusion reactor," *Fusion Engineering and Design,* vol. 87, no. 1, pp. 7-12, Jan 2012, doi: 10.1016/j.fusengdes.2011.08.006.

[83]   R. Padhy, A. N. Rao, S. K. S. Parashar, K. Parashar, and P. Chaudhuri, "Sintering effect on electrical properties of Li_2TiO_3," *Solid State Ionics,* vol. 256, pp. 29-37, Mar 2014, doi: 10.1016/j.ssi.2013.12.031.

[84]   S. Sonak, U. Jain, A. K. Sahu, S. Kumar, and N. Krishnamurthy, "Thermogravimetric analysis and kinetic study of formation of lithium titanate by solid state route," *Journal of Nuclear Materials,* vol. 457, pp. 88-93, Feb 2015, doi: 10.1016/j.jnucmat.2014.11.016.

[85]   A. V. Zhukov, S. V. Chizhevskaya, and A. O. Merkushkin, "Solid-Phase Synthesis of Li_2TiO_3," *Glass and Ceramics,* vol. 72, no. 9-10, pp. 327-330, Jan 2016, doi: 10.1007/s10717-016-9784-0.

[86]   T. Tang, Z. Zhang, J. B. Meng, and D. L. Luo, "Synthesis and characterization of lithium silicate powders," *Fusion Engineering and Design,* vol. 84, no. 12, pp. 2124-2130, Dec 2009, doi: 10.1016/j.fusengdes.2009.02.017.

[87]   J. M. Miller, H. B. Hamilton, and J. D. Sullivan, "TESTING OF LITHIUM TITANATE AS AN ALTERNATE BLANKET MATERIAL," *Journal of Nuclear Materials,* vol. 212, pp. 877-880, Sep 1994, doi: 10.1016/0022-3115(94)90961-x.

[88] L. DeJonghe and M. Rahaman, "Handbook of Advanced Ceramics," Elsevier Inc., Marquis one, Atlanta. pp. 187-188., 2003.

[89] H. Kimura, M. Asano, and K. Kubo, "THERMOCHEMICAL STUDY OF THE VAPORIZATION OF $LI_2O(c)$ BY MASS-SPECTROMETRIC KNUDSEN EFFUSION METHOD," *Journal of Nuclear Materials,* vol. 92, no. 2-3, pp. 221-228, 1980, doi: 10.1016/0022-3115(80)90106-3.

[90] Y. Ikeda, H. Ito, G. Matsumoto, and H. Hayashi, "THE VAPORIZATION AND THERMOCHEMICAL STABILITY OF LITHIUM ALUMINATES," *Journal of Nuclear Materials,* vol. 97, no. 1-2, pp. 47-58, 1981, doi: 10.1016/0022-3115(81)90417-7.

[91] H. Pfeiffer and P. Bosch, "Thermal stability and high-temperature carbon dioxide sorption on hexa-lithium zirconate ($Li_6Zr_2O_7$)," *Chemistry of Materials,* vol. 17, no. 7, pp. 1704-1710, Apr 2005, doi: 10.1021/cm047897+.

[92] H. Nakagawa, M. Asano, and K. Kubo, "MASS-SPECTROMETRIC INVESTIGATION OF THE VAPORIZATION OF $Li_2TiO_{3(s)}$," *Journal of Nuclear Materials,* vol. 110, no. 2-3, pp. 158-163, 1982, doi: 10.1016/0022-3115(82)90141-6.

[93] D. Cruz, S. Bulbulian, E. Lima, and H. Pfeiffer, "Kinetic analysis of the thermal stability of lithium silicates (Li_4SiO_4 and Li_2SiO_3)," *Journal of Solid State Chemistry,* vol. 179, no. 3, pp. 909-916, Mar 2006, doi: 10.1016/j.jssc.2005.12.020.

[94] S. Saito, K. Tsuchiya, H. Kawamura, T. Terai, and S. Tanaka, "Density dependence on thermal properties of Li_2TiO_3 pellets," *Journal of Nuclear Materials,* vol. 253, pp. 213-218, Mar 1998, doi: 10.1016/s0022-3115(97)00314-0.

[95] M. Xiang, Y. Zhang, Y. Zhang, C. Wang, W. Liu, and Y. Yu, "Effects of grain size and porosity on strength of Li_2TiO_3 tritium breeding pebbles and its grain growth behavior," *Journal of Nuclear Materials,* vol. 482, pp. 163-169, 2016/12/15/ 2016, doi: https://doi.org/10.1016/j.jnucmat.2016.10.027.

[96] A. E. Danks, S. R. Hall, and Z. Schnepp, "The evolution of 'sol-gel' chemistry as a technique for materials synthesis," *Materials Horizons,* vol. 3, no. 2, pp. 91-112, Mar 2016, doi: 10.1039/c5mh00260e.

[97] L. C. Klein, "SOL-GEL PROCESSING OF IONIC CONDUCTORS," *Solid State Ionics,* vol. 32-3, pp. 639-645, Feb-Mar 1989, doi: 10.1016/0167-2738(89)90339-1.

[98] O. Renoult, J. P. Boilot, J. P. Korb, and M. Boncoeur, "LITHIUM SOL-GEL CERAMICS FOR TRITIUM BREEDING APPLICATION," *Journal of Nuclear Materials,* vol. 223, no. 2, pp. 126-134, May 1995, doi: 10.1016/0022-3115(95)00018-6.

[99] X. H. Yu *et al.*, "Fabrication of Li_4SiO_4 pebbles by wet method with modified powders synthesized via sol-gel process," *Journal of Nuclear Materials,* vol. 456, pp. 455-460, Jan 2015, doi: 10.1016/j.jnucmat.2014.10.030.

[100] X. W. Wu, Z. Y. Wen, X. G. Xu, J. D. Han, and B. Lin, "Fabrication and improvement of the density of Li_2TiO_3 pebbles by the optimization of a sol-gel method," *Journal of Nuclear Materials,* vol. 393, no. 1, pp. 186-191, Aug 2009, doi: 10.1016/j.jnucmat.2009.06.002.

[101] M. H. H. Kolb, R. Knitter, U. Kaufmann, and D. Mundt, "Enhanced fabrication process for lithium orthosilicate pebbles as breeding material," *Fusion Engineering and Design,* vol. 86, no. 9-11, pp. 2148-2151, Oct 2011, doi: 10.1016/j.fusengdes.2011.01.104.

[102] J. F. Ziegler, "The electronic and nuclear stopping of energetic ions," *Applied Physics Letters,* vol. 31, no. 8, pp. 544-546, 1977/10/15 1977, doi: 10.1063/1.89771.

[103] G. H. Kinchin and R. S. Pease, "The Displacement of Atoms in Solids by Radiation," *Reports on Progress in Physics,* vol. 18, no. 1, pp. 1-51, 1955/01/01 1955, doi: 10.1088/0034-4885/18/1/301.

[104] L. W. Hobbs, "Radiation Effects in Analysis of Inorganic Specimens by TEM," in *Introduction to Analytical Electron Microscopy*, J. J. Hren Ed. New York: Springer Science+Business Media, 1979, p. 437.

[105] C. E. Johnson, "CERAMIC BREEDER MATERIALS," *Ceramics International,* vol. 17, no. 4, pp. 253-258, 1991, doi: 10.1016/0272-8842(91)90019-v.

[106] U. Jain and A. B. Lidiard, "GROWTH OF COLLOIDAL CENTERS IN IRRADIATED ALKALI-HALIDES," *Philosophical Magazine,* vol. 35, no. 1, pp. 245-259, 1977, doi: 10.1080/14786437708235986.

[107] Y. Ekmanis, "RADIOLYSIS BEHAVIOR IN ALKALI-HALIDE CRYSTALS," *Nuclear Instruments & Methods in Physics Research Section B-Beam Interactions with Materials and Atoms,* vol. 1, no. 2-3, pp. 473-474, 1984, doi: 10.1016/0168-583x(84)90111-3.

[108] V. I. Dubinko, A. A. Turkin, D. I. Vainshtein, and H. W. den Hartog, "A new mechanism for radiation damage processes in alkali halides," *Journal of Applied Physics,* vol. 86, no. 11, pp. 5957-5960, Dec 1999, doi: 10.1063/1.371639.

[109] E. Johnson and L. T. Chadderton, "The void superlattice in fluorite," *Micron,* vol. 11, no. 3-4, pp. 247-250, 1980.

[110] P. J. Call, W. Hayes, J. P. Stott, and A. E. Hughes, "Radiolysis of alkaline-earth fluorides," *Journal of Physics C: Solid State Physics,* vol. 7, no. 14, pp. 2417-2428, 1974/07/21 1974, doi: 10.1088/0022-3719/7/14/006.

[111] L. W. Hobbs and M. R. Pascucci, "Radiolysis and defect structure in electron-irradiated α-quartz," *Le Journal de Physique Colloques,* vol. 41, no. C6, pp. C6-237, 1980.

[112] J. F. Denatale and D. G. Howitt, "A mechanism for radiation damage in silicate glasses," *Nuclear Instruments and Methods in Physics Research Section B: Beam Interactions with Materials and Atoms,* vol. 1, no. 2, pp. 489-497, 1984/02/01/ 1984, doi: https://doi.org/10.1016/0168-583X(84)90114-9.

[113] L. W. Hobbs, "ELECTRON-BEAM SENSITIVITY IN INORGANIC SPECIMENS," *Ultramicroscopy,* vol. 23, no. 3-4, pp. 339-344, 1987, doi: 10.1016/0304-3991(87)90244-0.

[114] M. L. Knotek and P. J. Feibelman, "STABILITY OF IONICALLY BONDED SURFACES IN IONIZING ENVIRONMENTS," *Surface Science,* vol. 90, no. 1, pp. 78-90, 1979, doi: 10.1016/0039-6028(79)90011-6.

[115] R. A. Verrall, J. M. Miller, and P. Gierszewski, "Performance of a Li_2TiO_3 pebble-bed in the CRITIC-III irradiation," *Journal of Nuclear Materials,* vol. 281, no. 1, pp. 71-79, Sep 2000, doi: 10.1016/s0022-3115(00)00057-x.

[116] G. Piazza, F. Scaffidi-Argentina, and H. Werle, "Post-irradiation examinations of Li_4SiO_4 pebbles irradiated in the EXOTIC-7 experiment," *Journal of Nuclear Materials,* vol. 283, pp. 1396-1400, Dec 2000, doi: 10.1016/s0022-3115(00)00300-7.

[117] G. Piazza, A. Erbe, R. Rolli, and O. Romer, "Post-irradiation examinations of Li_4SiO_4 pebbles irradiated in the EXOTIC-8 experiment," *Journal of Nuclear Materials,* vol. 329, pp. 1260-1265, Aug 2004, doi: 10.1016/j.jnucmat.2004.04.235.

[118] M. Oyaidzu *et al.*, "ESR study on annihilation process of radiation defects induced in solid tritium breeding materials by neutron irradiation," *Physica Scripta,* vol. T108, pp. 42-45, 2004.

[119] G. M. Ran *et al.*, "Annihilation behavior of irradiation defects in Li_4SiO_4 irradiated with high thermal neutron fluence," *Journal of Nuclear Materials,* vol. 491, pp. 43-47, Aug 2017, doi: 10.1016/j.jnucmat.2017.04.055.

[120] Q. L. Zhou *et al.*, "Release kinetics of tritium generation in neutron irradiated biphasic Li_2TiO_3-Li_4SiO_4 ceramic breeder," *Journal of Nuclear Materials,* vol. 522, pp. 286-293, Aug 2019, doi: 10.1016/j.jnucmat.2019.05.033.

[121] M. H. H. Kolb, J. M. Heuser, R. Rolli, H. C. Schneider, R. Knitter, and M. Zmitko, "The HICU PIE results of EU ceramic breeder pebbles: General characterization," *Journal of Nuclear Materials,* vol. 531, Apr 2020, Art no. 152023, doi: 10.1016/j.jnucmat.2020.152023.

[122] T. Nakazawa *et al.*, "High energy heavy ion induced structural disorder in Li_2TiO_3," *Journal of Nuclear Materials,* vol. 367-370, pp. 1398-1403, 2007/08/01/ 2007, doi: https://doi.org/10.1016/j.jnucmat.2007.04.003.

[123] M. A. van Huis *et al.*, "Formation, growth and dissociation of He bubbles in Al_2O_3," *Nuclear Instruments & Methods in Physics Research Section B-Beam Interactions with Materials and Atoms,* vol. 216, pp. 149-155, Feb 2004, doi: 10.1016/j.nimb.2003.11.071.

[124] J. Wang *et al.*, "Release behavior of hydrogen isotopes in deuterium-irradiated Li_2TiO_3," *Fusion Engineering and Design,* vol. 113, pp. 318-323, Dec 2016, doi: 10.1016/j.fusengdes.2016.05.022.

[125] E. Carella, M. Gonzalez, and R. Gonzalez-Arrabal, "D-depth profiling in as-implanted and annealed Li-based breeder blanket ceramics," *Journal of Nuclear Materials,* vol. 438, no. 1-3, pp. 193-198, Jul 2013, doi: 10.1016/j.jnucmat.2013.02.073.

[126] M. Kobayashi, Y. Oya, and K. Okuno, "Migration of hydrogen isotopes in lithium metatitanate," *Journal of Nuclear Materials,* vol. 439, no. 1-3, pp. 159-167, Aug 2013, doi: 10.1016/j.jnucmat.2013.04.020.

[127] C. A. Taylor *et al.*, "Combined effects of radiation damage and He accumulation on bubble nucleation in $Gd_2Ti_2O_7$," *Journal of Nuclear Materials,* vol. 479, pp. 542-547, Oct 2016, doi: 10.1016/j.jnucmat.2016.07.043.

[128] G. Greaves, A. H. Mir, R. W. Harrison, M. A. Tunes, S. E. Donnelly, and J. A. Hinks, "New Microscope and Ion Accelerators for Materials Investigations (MIAMI-2) system at the University of Huddersfield," *Nuclear Instruments and Methods in Physics Research Section A: Accelerators, Spectrometers, Detectors and Associated Equipment,* vol. 931, pp. 37-43, 2019/07/01/ 2019, doi: https://doi.org/10.1016/j.nima.2019.03.074.

[129] K. Ono, M. Miyamoto, H. Kurata, M. Haruta, and A. Yatomi, "Dynamic behavior of helium bubbles at high temperature in Si studied by in situ TEM, STEM-EELS, and TDS," *Journal of Applied Physics,* vol. 126, no. 13, Oct 2019, Art no. 135104, doi: 10.1063/1.5118684.

[130] S. M. González de Vicente, J.-L. Boutard, S.J. Zinkle and H. Tanigawa, "Materials testing facilities and programmes for fission and ion implantation damage," *Nuclear Fusion,* vol. 57, no. 9, p. 092011, 2017.

[131] S. J. Zinkle and L. L. Snead, "Opportunities and limitations for ion beams in radiation effects studies: Bridging critical gaps between charged particle and neutron irradiations," *Scripta Materialia,* vol. 143, pp. 154-160, Jan 2018, doi: 10.1016/j.scriptamat.2017.06.041.

[132] J. F. Ziegler, M. D. Ziegler, and J. P. Biersack, "SRIM – The stopping and range of ions in matter (2010)," *Nuclear Instruments and Methods in Physics Research Section B: Beam Interactions with Materials and Atoms,* vol. 268, no. 11, pp. 1818-1823, 2010/06/01/ 2010, doi: https://doi.org/10.1016/j.nimb.2010.02.091.

[133] Y. Li *et al.*, "In-situ TEM investigation of 30 keV He^+ irradiated tungsten: Effects of temperature, fluence, and sample thickness on dislocation loop evolution," *Acta Materialia,* vol. 206, p. 116618, 2021/03/01/ 2021, doi: https://doi.org/10.1016/j.actamat.2020.116618.

[134] L. F. He *et al.*, "In situ TEM observation of dislocation evolution in Kr-irradiated UO_2 single crystal," *Journal of Nuclear Materials,* vol. 443, no. 1, pp. 71-77, 2013/11/01/ 2013, doi: https://doi.org/10.1016/j.jnucmat.2013.06.050.

[135] M. P. Short, D. R. Gaston, M. Jin, L. Shao, and F. A. Garner, "Modeling injected interstitial effects on void swelling in self-ion irradiation experiments," *Journal of Nuclear Materials,* vol. 471, pp. 200-207, 2016/04/01/ 2016, doi: https://doi.org/10.1016/j.jnucmat.2015.10.002.

[136] W. Xu *et al.*, "In-situ atomic-scale observation of irradiation-induced void formation," *Nature Communications,* vol. 4, no. 1, p. 2288, 2013/08/05 2013, doi: 10.1038/ncomms3288.

[137] L. W. Hobbs, "Transmission electron microscopy of defects in alkali halides," *Le Journal de Physique Colloques,* vol. 34, no. C9, pp. C9-227, 1973.

[138] T. Koyanagi *et al.*, "Microstructural evolution of pure tungsten neutron irradiated with a mixed energy spectrum," *Journal of Nuclear Materials,* vol. 490, pp. 66-74, Jul 2017, doi: 10.1016/j.jnucmat.2017.04.010.

[139] H. Trinkaus and B. N. Singh, "Modeling of void nucleation under cascade damage conditions," *Journal of Nuclear Materials,* vol. 307, pp. 900-906, Dec 2002, Art no. Pii s0022-3115(02)01120-0, doi: 10.1016/s0022-3115(02)01120-0.

[140] S. Jublot-Leclerc, X. Li, L. Legras, F. Fortuna, and A. Gentils, "Cavity nucleation and growth in dual beam irradiated 316L industrial austenitic stainless steel," *Journal of Nuclear Materials,* vol. 494, pp. 240-251, Oct 2017, doi: 10.1016/j.jnucmat.2017.07.038.

[141] V. Gavini, K. Bhattacharya, and M. Ortiz, "Vacancy clustering and prismatic dislocation loop formation in aluminum," *Physical Review B,* vol. 76, no. 18, Nov 2007, Art no. 180101, doi: 10.1103/PhysRevB.76.180101.

[142] F. Gao, D. J. Bacon, L. M. Howe, and C. B. So, "Temperature-dependence of defect creation and clustering by displacement cascades in alpha-zirconium," *Journal of Nuclear Materials,* vol. 294, no. 3, pp. 288-298, Apr 2001, doi: 10.1016/s0022-3115(01)00483-4.

[143] C. C. Matthai and D. J. Bacon, "THE COLLAPSE OF VACANCY CLUSTERS - A MOLECULAR-DYNAMICS STUDY," *Journal of Nuclear Materials,* vol. 135, no. 2-3, pp. 173-180, 1985, doi: 10.1016/0022-3115(85)90075-3.

[144] S. J. Zinkle, L. E. Seitzman, and W. G. Wolfer, "STABILITY OF VACANCY CLUSTERS IN METALS .1. ENERGY CALCULATIONS FOR PURE METALS," *Philosophical Magazine a-Physics of Condensed Matter Structure Defects and Mechanical Properties,* vol. 55, no. 1, pp. 111-125, Jan 1987, doi: 10.1080/01418618708209803.

[145] S. J. Zinkle and E. H. Lee, "EFFECT OF OXYGEN ON VACANCY CLUSTER MORPHOLOGY IN METALS," *Metallurgical Transactions a-Physical Metallurgy and Materials Science,* vol. 21, no. 5, pp. 1037-1051, May 1990, doi: 10.1007/bf02656525.

[146] R. M. Mayer, "NUCLEATION AND GROWTH OF VOIDS BY RADIATION .5. ROLE OF GAS," *Journal of Nuclear Materials,* vol. 95, no. 1-2, pp. 83-91, 1980, doi: 10.1016/0022-3115(80)90083-5.

[147] P. J. Goodhew, "Inert gas bubbles," *Materials Science and Technology,* vol. 6, no. 10, pp. 950-952, 1990/10/01 1990, doi: 10.1179/026708390790189597.

[148] D. E. Rimmer and A. H. Cottrell, "The solution of inert gas atoms in metals," *The Philosophical Magazine: A Journal of Theoretical Experimental and Applied Physics,* vol. 2, no. 23, pp. 1345-1353, 1957/11/01 1957, doi: 10.1080/14786435708243211.

[149] B. Kaiser *et al.*, "TEM study and modeling of bubble formation in dual-beam He^+/Fe^{3+} ion irradiated EUROFER 97," *Journal of Nuclear Materials,* vol. 484, pp. 59-67, Feb 2017, doi: 10.1016/j.jnucmat.2016.11.014.

[150] T. F. Yang *et al.*, "Effects of He Irradiation on Yttria-Stabilized Zirconia Ceramics," *Journal of the American Ceramic Society,* vol. 98, no. 4, pp. 1314-1322, Apr 2015, doi: 10.1111/jace.13423.

[151] C. A. Taylor *et al.*, "Bubble formation and lattice parameter changes resulting from He irradiation of defect-fluorite $Gd_2Zr_2O_7$," *Acta Materialia,* vol. 115, pp. 115-122, Aug 2016, doi: 10.1016/j.actamat.2016.05.045.

[152] G. Gutierrez *et al.*, "Helium bubble formation in nuclear glass by in-situ TEM ion implantation," *Journal of Nuclear Materials,* vol. 452, no. 1-3, pp. 565-568, Sep 2014, doi: 10.1016/j.jnucmat.2014.06.010.

[153] P. J. Goodhew, "CAVITY GROWTH-MECHANISM MAPS," *Scripta Metallurgica,* vol. 18, no. 10, pp. 1069-1073, 1984, doi: 10.1016/0036-9748(84)90180-7.

[154] S. K. Tyler and P. J. Goodhew, "Direct evidence for the Brownian motion of helium bubbles," *Journal of Nuclear Materials,* vol. 92, no. 2, pp. 201-206, 1980/09/01 1980, doi: https://doi.org/10.1016/0022-3115(80)90103-8.

[155] G. S. Was, *Fundamentals of Radiation Materials Science. Metals and Alloys*, 1st ed. Springer-Verlag Berlin Heidelberg, 2007.

[156] H. Trinkaus and B. N. Singh, "Helium accumulation in metals during irradiation – where do we stand?," *Journal of Nuclear Materials,* vol. 323, no. 2, pp. 229-242, 2003/12/01 2003, doi: https://doi.org/10.1016/j.jnucmat.2003.09.001.

[157] S. J. Zinkle and C. Kinoshita, "Defect production in ceramics," *Journal of Nuclear Materials,* vol. 251, pp. 200-217, 1997/11/11 1997, doi: https://doi.org/10.1016/S0022-3115(97)00224-9.

[158] H. Schroeder and P. F. P. Fichtner, "ON THE COARSENING MECHANISMS OF HELIUM BUBBLES - OSTWALD RIPENING VERSUS MIGRATION AND COALESCENCE," *Journal of Nuclear Materials,* vol. 179, pp. 1007-1010, Mar-Apr 1991, doi: 10.1016/0022-3115(91)90261-5.

[159] J. H. Evans, "Mechanisms of void coarsening in helium implanted silicon," *Nuclear Instruments & Methods in Physics Research Section B-Beam Interactions with Materials and Atoms,* vol. 196, no. 1-2, pp. 125-134, Nov 2002, Art no. Pii s0168-583x(02)01290-9, doi: 10.1016/s0168-583x(02)01290-9.

[160] S. Furuno *et al.*, "Ion irradiation and annealing effects in Al_2O_3 and $MgAl_2O_4$," *Nuclear Instruments and Methods in Physics Research Section B: Beam Interactions with Materials and Atoms,* vol. 127-128, pp. 181-185, 1997/05/02 1997, doi: https://doi.org/10.1016/S0168-583X(97)00066-9.

[161] A. Ofan *et al.*, "Spherical solid He nanometer bubbles in an anisotropic complex oxide," *Physical Review B,* vol. 82, no. 10, Sep 2010, Art no. 104113, doi: 10.1103/PhysRevB.82.104113.

[162] C. A. Taylor, J. D. Sugar, D. B. Robinson, N. C. Bartelt, R. B. Sills, and K. Hattar, "Using In Situ TEM Helium Implantation and Annealing to Study Cavity Nucleation and Growth," *Jom,* vol. 72, no. 5, pp. 2032-2041, May 2020, doi: 10.1007/s11837-020-04117-4.

[163] V. N. Chernikov, H. Trinkaus, P. Jung, and H. Ullmaier, "THE FORMATION OF HELIUM BUBBLES NEAR THE SURFACE AND IN THE BULK IN NICKEL DURING POST-IMPLANTATION ANNEALING," *Journal of Nuclear Materials,* vol. 170, no. 1, pp. 31-38, Jan 1990, doi: 10.1016/0022-3115(90)90323-f.

[164] J. Strane, L. D. Marks, D. E. Luzzi, M. I. Buckett, J. P. Zhang, and B. W. Wessels, "ENCAPSULATION, DIFFUSION AND DIET IN THE ELECTRON-MICROSCOPE," *Ultramicroscopy,* vol. 25, no. 3, pp. 253-257, 1988, doi: 10.1016/0304-3991(88)90019-8.

[165] M. R. McCartney and D. J. Smith, "STUDIES OF ELECTRON-IRRADIATION AND ANNEALING EFFECTS ON TIO_2 SURFACES IN ULTRAHIGH-VACUUM USING HIGH-RESOLUTION ELECTRON-MICROSCOPY," *Surface Science,* vol. 250, no. 1-3, pp. 169-178, Jul 1991, doi: 10.1016/0039-6028(91)90719-9.

[166] W. B. Liu *et al.*, "Irradiation Induced Microstructure Evolution in Nanostructured Materials: A Review," *Materials,* vol. 9, no. 2, Feb 2016, Art no. 105, doi: 10.3390/ma9020105.

[167] F. Y. Lu *et al.*, "Amorphization of nanocrystalline monoclinic ZrO_2 by swift heavy ion irradiation," *Physical Chemistry Chemical Physics,* vol. 14, no. 35, pp. 12295-12300, 2012, doi: 10.1039/c2cp41553d.

[168] B. Schuster, M. Lang, R. Klein, C. Trautmann, R. Neumann, and A. Benyagoub, "Structural phase transition in ZrO_2 induced by swift heavy ion irradiation at high-pressure," *Nuclear Instruments & Methods in Physics Research Section B-Beam Interactions with Materials and Atoms,* vol. 267, no. 6, pp. 964-968, Mar 2009, doi: 10.1016/j.nimb.2009.02.046.

[169] W. J. Qin *et al.*, "Different Radiation Tolerances of Ultrafine-Grained Zirconia-Magnesia Composite Ceramics with Different Grain Sizes," *Materials,* vol. 12, no. 17, Sep 2019, Art no. 2649, doi: 10.3390/ma12172649.

[170] T. Nakazawa, V. Grismanovs, D. Yamaki, Y. Katano, and T. Aruga, "Disordering in Li_2TiO_3 irradiated with high energy ions," *Nuclear Instruments and Methods in Physics Research Section B: Beam Interactions with Materials and Atoms,* vol. 206, pp. 166-170, 2003/05/01/ 2003, doi: https://doi.org/10.1016/S0168-583X(03)00712-2.

[171] Q. L. Zhou, Y. Oya, T. Chikada, W. Zhang, L. H. Xue, and Y. W. Yan, "Preparation of Li_2TiO_3 by hydrothermal synthesis and its structure evolution under high energy Ar^+ irradiation," *Journal of the European Ceramic Society,* vol. 37, no. 15, pp. 4955-4961, Dec 2017, doi: 10.1016/j.jeurceramsoc.2017.06.032.

[172] N. M. Masaki, K. Noda, H. Watanabe, R. G. Clemmer, and G. W. Hollenberg, "SPECTROSCOPIC STUDY OF LITHIUM-OXIDE IRRADIATED BY FAST-NEUTRONS," *Journal of Nuclear Materials,* vol. 212, pp. 908-911, Sep 1994, doi: 10.1016/0022-3115(94)90967-9.

[173] J. Tiliks, G. Kizane, A. Vitins, G. Vitins, and J. Meisters, "Physicochemical processes in blanket ceramic materials," *Fusion Engineering and Design,* vol. 69, no. 1-4, pp. 519-522, Sep 2003, doi: 10.1016/s0920-3796(03)00120-0.

[174] A. Zarins, A. Supe, G. Kizane, R. Knitter, and L. Baumane, "Accumulation of radiation defects and products of radiolysis in lithium orthosilicate pebbles with silicon dioxide additions under action of high absorbed doses and high temperature in air and inert atmosphere," *Journal of Nuclear Materials,* vol. 429, no. 1-3, pp. 34-39, Oct 2012, doi: 10.1016/j.jnucmat.2012.05.028.

[175] R. A. Verrall, D. H. Rose, J. M. Miller, I. J. Hastings, and D. S. Macdonald, "BUBBLE FORMATION IN IRRADIATED LI_2O," *Journal of Nuclear Materials,* vol. 179, pp. 855-858, Mar-Apr 1991, doi: 10.1016/0022-3115(91)90223-t.

[176] G. Hollenberg and D. Baldwin, "The effect of irradiation on four solid breeder materials," *Journal of nuclear materials,* vol. 133, pp. 242-245, 1985.

[177] E. Carella, T. Sauvage, R. Bes, B. Courtois, and M. Gonzalez, "Nuclear reaction analysis as a tool for the ^{3}He thermal evolution in Li_2TiO_3 ceramics," *Nuclear Instruments & Methods in Physics Research Section*

B-Beam Interactions with Materials and Atoms, vol. 332, pp. 85-89, Aug 2014, doi: 10.1016/j.nimb.2014.02.035.

[178]   L. J. Zhao *et al.*, "Tritium release in Li_4SiO_4 and $Li_{4.2}Si_{0.8}Al_{0.2}O_4$ ceramics," *Journal of Nuclear Materials,* vol. 482, pp. 42-46, Dec 2016, doi: 10.1016/j.jnucmat.2016.10.009.

[179]   C. E. Johnson, "Tritium behavior in lithium ceramics," *Journal of Nuclear Materials,* vol. 270, no. 1-2, pp. 212-220, Apr 1999, doi: 10.1016/s0022-3115(98)00905-2.

[180]   N. Roux, G. Hollenberg, C. Johnson, K. Noda, and R. Verrall, "SUMMARY OF EXPERIMENTAL RESULTS FOR CERAMIC BREEDER MATERIALS," *Fusion Engineering and Design,* vol. 27, pp. 154-166, Mar 1995, doi: 10.1016/0920-3796(95)90123-x.

[181]   R. E. Avila, L. A. Pena, and J. C. Jimenez, "Surface desorption and bulk diffusion models of tritium release from Li_2TiO_3 and Li_2ZrO_3 pebbles," *Journal of Nuclear Materials,* vol. 405, no. 3, pp. 244-251, Oct 2010, doi: 10.1016/j.jnucmat.2010.08.009.

[182]   J. G. van der Laan, H. Kawamura, N. Roux, and D. Yamaki, "Ceramic breeder research and development: progress and focus," *Journal of Nuclear Materials,* vol. 283, pp. 99-109, Dec 2000, doi: 10.1016/s0022-3115(00)00352-4.

[183]   H. Wedemeyer, H. Werle, and E. Gunther, "INFLUENCE OF GRAIN-SIZE AND CARBONATE IMPURITIES ON THE TRITIUM RELEASE FROM LITHIUM ORTHOSILICATE," *Journal of Nuclear Materials,* vol. 191, pp. 240-242, Sep 1992.

[184]   M. M. W. Peeters, A. J. Magielsen, M. P. Stijkel, and J. G. van der Laan, "In-pile tritium release behaviour of lithium metatitanate produced by extrusion-spheroidisation-sintering process in EXOTIC-9/1 in the high flux reactor, Petten," *Fusion Engineering and Design,* vol. 82, no. 15-24, pp. 2318-2325, Oct 2007, doi: 10.1016/j.fusengdes.2007.05.036.

[185]   J. M. Heuser, M. H. H. Kolb, R. Rolli, H. C. Schneider, R. Knitter, and M. Zmitko, "The HICU PIE results of EU ceramic breeder pebbles: Tritium release properties," *Journal of Nuclear Materials,* vol. 531, Apr 2020, Art no. 152024, doi: 10.1016/j.jnucmat.2020.152024.

[186]   M. Kobayashi, K. Toda, Y. Oya, and K. Okuno, "Dependency of irradiation damage density on tritium migration behaviors in Li_2TiO_3," *Journal of Nuclear Materials,* vol. 447, no. 1-3, pp. 1-8, Apr 2014, doi: 10.1016/j.jnucmat.2013.12.001.

[187]   J. K. Cockcroft, P. Barnes, M. Attfield, and H. Driessen, "Powder Diffraction on the Web," http://pd.chem.ucl.ac.uk/, (c) 1997 - 2006.

[188]   C. A. Schneider, W. S. Rasband, and K. W. Eliceiri, "NIH Image to ImageJ: 25 years of image analysis," *Nature Methods,* vol. 9, no. 7, pp. 671-675, 2012/07/01 2012, doi: 10.1038/nmeth.2089.

[189]   D. B. Williams and C. B. Carter, *Transmission Electron Microscopy: A Textbook for Materials Science, Second Edition*. New York: Springer Science+Business Media, 2009.

[190]   "OriginPro, Version 2017 . OriginLab Corporation, Northampton, MA, USA.,"

[191]   A. Baron-Wiechec *et al.*, "Thermal desorption spectrometry of beryllium plasma facing tiles exposed in the JET tokamak," *Fusion Engineering and Design,* vol. 133, pp. 135-141, 2018/08/01/ 2018, doi: https://doi.org/10.1016/j.fusengdes.2018.05.075.

[192]   R. Smith, "MRF Tritium Capability," (Presentation slides, July 2015) Personal communication.

[193]   "ASTM E112-10, Standard Test Methods for Determining Average Grain Size," PA: ASTM International, West Conshohocken, 2010.

[194]   M. I. Mendelson, "AVERAGE GRAIN SIZE IN POLYCRYSTALLINE CERAMICS," *Journal of the American Ceramic Society,* vol. 52, no. 8, pp. 443-+, 1969, doi: 10.1111/j.1151-2916.1969.tb11975.x.

[195]   A. R. C. Gerlt, A. K. Criner, L. Semiatin, and E. J. Payton, "On the grain size proportionality constants calculated in MI Mendelson's "Average Grain Size in Polycrystalline Ceramics"," *Journal of the American Ceramic Society,* vol. 102, no. 1, pp. 37-41, Jan 2019, doi: 10.1111/jace.15950.

[196]   J. C. Wurst and J. A. Nelson, "LINEAR INTERCEPT TECHNIQUE FOR MEASURING GRAIN-SIZE IN 2-PHASE POLYCRYSTALLINE CERAMICS," *Journal of the American Ceramic Society,* vol. 55, no. 2, pp. 109-&, 1972, doi: 10.1111/j.1151-2916.1972.tb11224.x.

[197]   R. Knitter, B. Alm, and G. Roth, "Crystallisation and microstructure of lithium orthosilicate pebbles," *Journal of Nuclear Materials,* vol. 367, pp. 1387-1392, Aug 2007, doi: 10.1016/j.jnucmat.2007.04.002.

[198] I. M. Lifshitz and V. V. Slyozov, "The kinetics of precipitation from supersaturated solid solutions," *Journal of Physics and Chemistry of Solids,* vol. 19, no. 1, pp. 35-50, 1961/04/01/ 1961, doi: https://doi.org/10.1016/0022-3697(61)90054-3.

[199] C. Wagner, "THEORIE DER ALTERUNG VON NIEDERSCHLAGEN DURCH UMLOSEN (OSTWALD-REIFUNG)," *Zeitschrift Fur Elektrochemie,* vol. 65, no. 7-8, pp. 581-591, 1961.

[200] E. Snoeck, J. Majimel, M. O. Ruault, and M. J. Hytch, "Characterization of helium bubble size and faceting by electron holography," *Journal of Applied Physics,* vol. 100, no. 2, Jul 2006, Art no. 023519, doi: 10.1063/1.2216791.

[201] S. T. Murphy and N. D. M. Hine, "Point Defects and Non-stoichiometry in Li_2TiO_3," *Chemistry of Materials,* vol. 26, no. 4, pp. 1629-1638, 2014/02/25 2014, doi: 10.1021/cm4038473.

[202] A. I. Van Sambeek, R. S. Averback, C. P. Flynn, and M. H. Yang, "Radiation enhanced diffusion in MgO," in *Symposium on Microstructure of Irradiated Materials, at the 1994 MRS Fall Meeting*, Boston, Ma, Nov 29-Dec 01 1994, vol. 373, in Materials Research Society Symposium Proceedings, 1995, pp. 293-298. [Online]. Available: <Go to ISI>://WOS:A1995BD31C00043

[203] J. C. Bourgoin, J. W. Corbett, and H. L. Frisch, "IONIZATION ENHANCED DIFFUSION," *Journal of Chemical Physics,* vol. 59, no. 8, pp. 4042-4046, 1973, doi: 10.1063/1.1680596.

[204] C. Fan *et al.*, "Irradiation induced void spheroidization, shrinkage and migration in Cu at elevated temperatures: An in situ study," *Acta Materialia,* vol. 201, pp. 504-516, 2020/12/01/ 2020, doi: https://doi.org/10.1016/j.actamat.2020.10.008.

[205] Y. Furuyama, K. Yahata, R. Nakamori, A. Taniike, H. Samata, and A. Kitamura, "CO_2 absorption characteristics of a Li_2TiO_3 blanket material under atmospheric exposure," *Journal of Nuclear Materials,* vol. 455, no. 1, pp. 527-530, 2014/12/01/ 2014, doi: https://doi.org/10.1016/j.jnucmat.2014.08.007.

[206] U. Fischer *et al.*, "Comparison of nuclear irradiation parameters of fusion breeder materials in high flux fission test reactors and a fusion power demonstration reactor," *Journal of Nuclear Materials,* vol. 280, no. 2, pp. 151-161, 2000/07/01/ 2000, doi: https://doi.org/10.1016/S0022-3115(00)00049-0.

[207] J. Shimwell *et al.*, "Spatially and temporally varying tritium generation in solid-type breeder blankets," *Fusion Engineering and Design,* vol. 98-99, pp. 1868-1871, Oct 2015, doi: 10.1016/j.fusengdes.2015.04.018.

[208] Z. Shen, M. Johnsson, Z. Zhao, and M. Nygren, "Spark Plasma Sintering of Alumina," *Journal of the American Ceramic Society,* https://doi.org/10.1111/j.1151-2916.2002.tb00381.x vol. 85, no. 8, pp. 1921-1927, 2002/08/01 2002, doi: https://doi.org/10.1111/j.1151-2916.2002.tb00381.x.

[209] A. Hollingsworth *et al.*, "Comparative study of deuterium retention in irradiated Eurofer and Fe-Cr from a new ion implantation materials facility," *Nuclear Fusion,* vol. 60, no. 1, Jan 2020, Art no. 016024, doi: 10.1088/1741-4326/ab546e.